Probing the Nature of Dark Energy with 21-cm Intensity Mapping

by

Elimboto Mwiki Yohana

A Thesis Submitted to the College of Agriculture, Engineering and Science
in partial fulfillment of the requirements for the degree of
Doctor of Philosophy
at the
University of KwaZulu-Natal

Supervised by Professor Yin-Zhe Ma

Abstract

Two approaches to measure the BAOs (baryon acoustic oscillations) with optical and radio telescopes, namely; galaxy redshift and intensity mapping (IM) surveys have been introduced and discussed in the literature. Among the two methods, the galaxy redshift survey has been used to great effect and is based on the detection and survey of millions of individual galaxies and measuring their redshifts by comparing templates of the spectral energy distributions of the light emitted from the galaxies with optical lines. IM is novel but a robust approach that focuses on surveys of extremely large volumes of galaxies without resolving each individual galaxy and can efficiently probe scales over redshift ranges inaccessible to the current galaxy redshift surveys. However, the IM survey has promisingly shown to have better overall sensitivity to the BAOs than the galaxy redshift survey but has a number of serious issues to be quantified. The most obvious of these issues is the presence of foreground contaminants from the Milky Way galaxy and extragalactic point sources which strongly dominate the neutral hydrogen (HI) signal of our interest.

Under this study, we are interested to realize the IM approach, pave the pathway, and optimize the scientific outputs of future radio experiments. We, therefore, carry out simulations and present forecasts of the cosmological constraints by employing HI IM technique with three near-term radio telescopes by assuming 1 year of observational time. The telescopes considered here are Five-hundred-meter Aperture Spherical radio Telescope (FAST), BAOs In Neutral Gas Observations (BINGO), and Square Kilometre Array Phase I (SKA-I) single-dish experiments. We further forecast the combined constraints of the three radio telescopes with *Planck* measurements.

In order to tackle the foreground challenge, we develop strategies to model various sky components and employ an approach to clean them from our Milky Way galaxy and extragalactic point sources by considering a typical single-dish radio telescope. Particularly, the Principal Component Analysis foreground separation approach considered can indeed recover the cosmological HI signal to high precision. We show that, although the approach may face some challenges, it can be fully realized on the selected range of angular scales.

Declaration

I, the undersigned, hereby declare that this thesis entitled "Probing the Nature of Dark Energy with 21-cm Intensity Mapping" is my own work and that any work done by others has been acknowledged and referenced accordingly. This thesis is being submitted for the candidacy in the Degree of Doctor of Philosophy at the University of KwaZulu-Natal, Durban, South Africa. The thesis has not been submitted elsewhere in wholly or partly for any degree, diploma, examination or other qualification. However, no part of this thesis has already been, or is concurrently being, submitted to any university for any of the aforementioned qualifications. Most of the original materials in this thesis are based on two papers that have been published/submitted for publication as follows:

1. Elimboto Yohana, Yi-Chao Li, and Yin-Zhe Ma. Forecasts of cosmological constraints from HI intensity mapping with FAST, BINGO and SKA-I. *Research in Astronomy and Astrophysics*, Vol. 19, No. 12 (2019);

2. Elimboto Yohana, Yin-Zhe Ma, Di Li, and Xuelei Chen. Recovering 21-cm signal from simulated FAST intensity maps. Submitted to MNRAS.

Although a significant amount of the original work has been done in collaboration as described in the list above, most of it has been carried out by myself. Several figures in the text have been taken from the works authored by others, just for illustration and/or discussion. Such figures are credited in the respective/associated captions.

Elimboto Yohana, March 12, 2020

Acknowledgement

I, Elimboto Yohana, sincerely acknowledge for financial support from DAAD and AIMS Scholarship, and thanks to the University of KwaZulu-Natal for providing a conducive learning environment; and for the financial support which facilitated my attendance at various conferences, summer schools, and workshops, from which my participation has gained experiences and skills that greatly contributed to this study. I also thank my employer, the Dar Es Salaam University College of Education, a Constituent College of the University of Dar Es salaam, for granting me leave in order to pursue Ph.D. studies.

With great sincerity and due respect, I'm conveying my thanks to all those who in different ways contributed towards the accomplishment of this project. My grateful thanks are directed to my supervisor, Professor Yin-Zhe Ma, for his outstanding contribution in terms of ideas, skills, proper guidance, recommendations and motivation during the whole period of research. I extend my sincere thanks to our research group, dubbed NAOC-UKZN Computational Astrophysics Centre (NUCAC) under Professor Yin-Zhe Ma, in particular, thanks to Antony Walters, Ayodeji Ibitoye, Chandan Ganjigere Nagarajappa, Denis Tramonte, Mthokozisi Mdlalose, Phumlani Nkuthalo Phakathi, Piyanat (Boom) Kittiwist, and Wei-ming Dai, from which a lot of ideas generated during our very long weekly meetings have emanated to the fashioning of this thesis. Thanks to my co-supervisor, Professor Kavilan Moodley, for his useful advises, that greatly contributed in many ways towards the accomplishment of this study. Special thanks to Dr. Yi-Chao Li, whose technical skills and valuable time spent during a lot of problem-solving discussions we had together steadily propelled my study. I also extend my thanks to Richard Shaw from UBC and Stuart Harper from Manchester University for sacrificing their valuable times by engaging in technical discussions that we have had through emails; they were really insightful and helpful. Many thanks especially, to Astrophysics & Cosmology Research Unit (ACRU) team which contributed to this thesis in various ways, including, but not limited to, seminars, public talks, weekly presentations, and postgraduates and postdoctoral weekly picnic meetings. I highly recognize the contribution given by my family, with special respect and thanks to my beloved wife Hamida, and my son Yohana, for being highly patient and tolerant during their very long lonely and tough times for the entire duration I have been away from them; my parents, brothers and sisters in terms of advice, encouragement, and prayers. Since when I joined the education system, unquestionably, any success in my academic advancement has their full hands.

Special thanks to friends and fellows in Christ from various assemblies who have been close to

me during the entire duration of my study; they have always been so helpful, physically, socially and spiritually; their prayers, advice, and willingness to help will always make me remember them. Some of these folks include: Henry and Christina Sunpathy, Conrad and Nerusha, Victor and Doll Narainsamy, Clement and Vanishree, Philip and Karen, Sagren and Priscilla, Zohor and Savy, Marco and Acsah, Ashish and Caitlin, Ricardo, Hannah, Ludfia, and Elisha, all from Chatsworth Assembly; Daniel from La Mercy Assembly; Thabo and Siphelele Goba from KwaMashu, Brian and Lali Ganessan from Asherville Christian Brethren; Greg and Bernice from Wynberg Gospel Hall in Cape Town; Emmanuel and Anne Kasembe, Wilbert and Sophia Manjonda, Mathew and Christina, and Dastan Kamanzi, from Keko Juu Assembly in Dar Es Salam; Kaumba and Eva Kapaku, Evaristo and Esther Yamboto, from Lusaka Gospel Assembly. All these contributions collectively amounted to a lenient conducting of my research. Finally, I convey my gratitude to the Almighty God with due thanksgiving, for giving me strength and health during the whole period of my stay at the University of KwaZulu-Natal, and for continually guiding and protecting my family, my wife and my son.

Contents

List of Tables

List of Figures

1

Introduction

1.1 The Isotropic and Homogeneous Universe

Cosmological studies are very ancient and have largely been propelled by the human inquisitive mind to understand the Universe. But, only around the 1920s and increasingly, in recent years, the study of cosmology has progressively received its due attention, when rigorous theoretical developments, scientific observations, and experiments started to be employed to study the Universe as a whole. Today, cosmology continues steadily to be an active study and research area, marked with spectacular discoveries and breakthroughs. The study of this fascinating field has gone through many reformations at different epochs, often influenced by culture, religion, and philosophy. Steady theoretical framework developments pushed to the state-of-the-art cosmology which started with Einstein's advancement of the general relativity (GR) theory around 1915. Out of GR, Einstein developed field equations about the cosmos which implied the Universe was evolving.

It was not until 1929 when Hubble made a paradigm shift by observationally convincing the community of astronomers that the Universe was actually expanding. This discovery marked the beginning of modern cosmology and was followed by a myriad theoretical and observational advancements to study the Universe. Cosmic propositions such as the Big Bang theory and steady-state Universe were born, their perspectives rigorously challenged and have since then been very hot topics in cosmology. Countless debates due to different cosmological perspectives continued to streamline and fashion the study of cosmology, increasing its precision. As a result, two antagonistic schools of thought emerged, one a proponent of the static universe, and another one supporting the evolutionary state of the universe. These contentious ideas continued to revolve, until 1965, when to a great extent the dispute was resolved following a serendipitous discovery of the Cosmic Microwave Background (CMB). Thus, CMB discovery was seen as another good evidence to support the evolution of cosmic structure. The observed redshifted wavelengths of primordial photons in the electromagnetic spectrum is believed to be the effect of the cosmic expansion as these photons travel through space. This observation cemented and favoured the proposition that the past very hot and dense universe originated from the Big

Bang, has been expanding, reasonably marking the beginning of physical cosmology. What followed then was a parade of studies attempting to answer numerous cosmological questions, such as how possible the clumpy and highly structured Universe we see today was remarkably smooth as evidenced by the CMB that formed few thousand hundred years from the Big Bang, what forces drive the expansion of the cosmic structure, and the possibility that the Universe could have undergone rapid expansion (inflation) in the past, just a minute fraction of a second after the Big Bang, and how all these processes independently and collectively account for the structure formation and the dynamics of the evolving Universe. The cosmological studies thus attempt to provide a scientific account of the history and prospects of the Universe since its inception and predict its future trends. Cosmology is an evolutionary field of study, it continues to grow perpetually, battling to answer many fundamental questions of nature, and in doing so it opens avenues for the new scope of exciting ideas. Nevertheless, the power of observational techniques boosted by revolutionary cosmological experiments, such as a large number of galaxy redshift surveys, cosmic microwave background, and 21-cm experiments have opened doors to test many cosmological theories and models, and the degree of agreement between models and data is greatly astonishing.

Cosmology is thus a scientific investigation and analysis of the origin, history, structures, and dynamics of the Universe, and its ultimate fate, and it deals with the Universe as a whole and its phenomena at largest scales. Due to very large-scales, cosmological observations are generally very challenging because the majority of the vast cosmos of spacetime we are observing is very far from us. However, distant sources used to probe the cosmic are very dim. For this reason, the study of the Universe is paralleled by the development and advancement of the new generation of instruments, usually large optical telescopes with more sensitive detectors. The discipline of cosmology has progressively matured over decades, and today, many of its theoretical predictions are no longer speculations but have been diversely tested experimentally and confirmed to be true. For decades, enormous advancements have been made in studying and understanding our Universe, and today increasingly, numerous observations and experiments are being developed and/or commissioned to survey the Universe. This is the era of high fidelity cosmology, and we can now provide solutions to long-standing puzzles with high precision and unprecedented accuracy.

Large-scale Universe structures contain predominantly a collection of galaxies. Each of these galaxies, for example, our Milky Way galaxy, contains gravitationally bound large number of stars spanning up to $\sim 10^{11}$. Galaxies naturally occur in groups called clusters, with each cluster containing up to a few thousand galaxies. Rarely, clusters group to form clusters of clusters. There is however little possibility for the existence of high hierarchies such as clusters of clusters of clusters. The Universe also contains empty regions, which together with superclusters have recently been one of the major research focus in cosmology.

Studies have shown that on **sufficiently large scale**, that is much larger than the typical clustering scale (which is also much larger than the typical distance between any two nearest

galaxies), galaxies are not randomly cluttered but their distribution on average uniformly spread throughout the cosmic structure at any given time. Thus, different patches of the Universe with the same volume however on sufficiently large scale contain roughly the same number of galaxies at any given time, which changes accordingly with time following the dynamic state of the Universe.

Edwin Hubble discovered around 1930s that distant galaxies were moving further away from us (the Milky Way galaxy) and from each other. He further found that such galaxies were receding from each other with recession velocities roughly proportional to their distances apart at any given time. This discovery is called Hubble's Law and we quantitatively describe it below.

Let $r(t)$ denote the radius of the balloon at any given time t, and consider an angle θ_{AB} at the center of the balloon subtended by two dots denoted by A and B. Then $\mathrm{d}_{AB} = \theta_{AB} r(t)$ is the distance between the dots on a great circle. Furthermore, as dots A and B move relative to each other, their speed is given by $v_{AB} = \dot{\mathrm{d}}_{AB} = \theta_{AB}\dot{r}(t) = \mathrm{d}_{AB}(\dot{r}(t)/r(t))$, where $\dot{r} = \mathrm{d}r(t)/\mathrm{d}t$. This implies that $v_{AB} \propto \mathrm{d}_{AB}$, with $\dot{r}/r$ being the proportionality factor. If distances change between A and B by some factor at any time t, in that period of time, the distances between any pairs of dots change by the same factor.

We can conclude that any two pairs of dots A and B around a great circle will move with a relative speed that increases with their distance of separation as the balloon expands. The uniform expansion of this spherically perfect uniformly dotted balloon gives us an approximate analogy of a relative distribution and motions of galaxies in an expanding cosmological principle universe model. If we denote the proportionality constant, $\dot{r}/r$ by H and generalize the notion for any two arbitrary objects (in this case galaxies), that recede with a speed v proportional to the distance d between them, we can write $v = Hd$, and this equality applied at the present time t_0 is

$$v = H_0 d, \tag{1.1.1}$$

known as the Hubble's Law, where H_0 is the Hubble constant given by $H_0 = 100h\,\mathrm{km\,s^{-1}\,Mpc^{-1}}$, and h is the dimensionless constant. The Hubble constant has a close relationship with other two concepts, namely; the Hubble time and the Hubble radius. Hubble time, $t_H = 1/H_0$, is the measure of the time for which the expanding universe at the present rate, doubles its size; and Hubble radius, approximated by $c/H_0 \simeq 4300\,\mathrm{Mpc}$ (where c is the speed of light) is the radius of the presently observable universe.

There has been an ongoing dispute regarding the exact measurement of the Hubble constant; this, in turn, has constantly led to its improvements over time, as astronomers advance their knowledge and instruments to constrain the parameter with an ever-increasing precision in measurements and data acquisition. Several measurements have determined the Hubble constant in the range $65 - 75\,\mathrm{km\,s^{-1}\,Mpc^{-1}}$.

The most recent measurement of Hubble constant was carried out through calibration of the Tip of the Red Giant Branch (TRGB) applied to Type Ia Supernovae (SNeIa) which estimated the

Hubble constant to be $H_0 = 69.8 \pm 0.8\,\mathrm{km\,s^{-1}\,Mpc^{-1}}$, from observations made by NASA/ESA Hubble Space Telescope (Freedman et al., 2019). This measurement is relatively lower compared to the value of $74.03 \pm 1.42\,\mathrm{km\,s^{-1}\,Mpc^{-1}}$ recently reported by the Hubble SH0ES (Supernovae H_0 for the Equation of State), carried out by observing pulsating stars called Cepheid variables in a neighbouring satellite galaxy known as the Large Magellanic Cloud (Riess et al., 2019). The pre-existed Hubble constant estimation from the more distant background universe by the European Space Agency's *Planck* satellite constrained the parameter from CMB measurements (by assuming the standard ΛCDM model) to be $67.4 \pm 0.5\,\mathrm{km\,s^{-1}\,Mpc^{-1}}$ (Planck Collaboration et al., 2018). Other significant earlier reports on the Hubble constant measurements in a series can be found in various references mentioned in Planck Collaboration et al. (2018); Riess et al. (2019); Freedman et al. (2019).

Although, currently, there is no agreement on the exact value of Hubble constant between different measurements, such disparity in no way contradicts the observed phenomenon that the Universe is expanding. Therefore, it turns out that, in the distant past, at a later stage of their development, galaxies must have been very close to each other, about one billion years after a universal explosion at some initial point of the Universe which violently threw the matter, the assumed phenomenon for the origin of the Universe, commonly known as the Big Bang.

1.1.1 Friedmann Equations

General Relativity (Quigg, 2013; Bernstein, 1988; Peacock, 1998; Coles and Lucchin, 1995) is the modern treatment of gravity and has become one of the prominent tools for studying the late-time physical cosmology, providing us with the most suitable approach to describing the geometry of curved spacetime. What follows, we present a schema for obtaining the Friedman equations from Einstein's field equations adopted from Mo et al. (2010); Carroll (2003).

In the ΛCDM cosmology, the Universe's matter-energy content can be used to determine the geometry of spacetime via Einstein's field equations. The metric that relates the geometry of spacetime and mass-energy distribution evolves according to Einstein's field equations

$$G_{\mu\nu} - g_{\mu\nu}\Lambda = \frac{8\pi G}{c^4} T_{\mu\nu}, \tag{1.1.2}$$

where

$$G_{\mu\nu} \equiv R_{\mu\nu} - \frac{1}{2} R g_{\mu\nu} \tag{1.1.3}$$

is called the Einstein tensor, $R_{\mu\nu}$ and R are, respectively, called Ricci tensor and Ricci scalar (curvature scalar), and $g_{\mu\nu}$ is the metric tensor. Here, Λ is the usual cosmological constant, currently believed to be responsible for the accelerated cosmic expansion. Einstein introduced this constant when he was solving the field equations with an intention to yield a static universe. $T_{\mu\nu}$ is the energy-momentum tensor or sometimes referred to as the stress-energy tensor of the matter content of the Universe, G is Newton's constant of gravitation and c is the light speed. The Ricci tensor, $R_{\mu\nu}$, tells us about the local curvature of spacetime, and the Ricci scalar,

R is responsible for determining the effect of mass and energy distribution on the curvature of spacetime. The momentum and energy of the matter fields are a source of gravity, and all information regarding them are encoded in the energy-momentum tensor.

The metric, $g_{\mu\nu}$, is very important in cosmology, it contains all information about the geometry of spacetime. Metric tensors generally depend on the location and the geometry of space/spacetime for a given coordinate system x^α, and can be described by the metric $g_{\mu\nu} = g_{\mu\nu}(x^\alpha)$. Such a metric is general, and the information it encodes regarding the topology and geometry of spacetime is not known a priori, and thus can only be discovered by careful analysis. In the ΛCDM cosmology, we have assumed our Universe to be homogeneous, so the metric associated with such universe is independent of location, and hence $g_{\mu\nu}(x^\alpha) = g_{\mu\nu}$. The choice of the coordinate system determines numerical values for metric tensors. Ricci scalar can be deduced from the trace of Ricci tensor

$$R = R^\lambda_\lambda = g^{\mu\nu} R_{\mu\nu}, \tag{1.1.4}$$

and both the Ricci and the energy-momentum tensors are symmetric, that is $R_{\mu\nu} = R_{\nu\mu}$, $T_{\mu\nu} = T_{\nu\mu}$. We see how components of the Einstein's field equations (1.1.2) have different characterization, as a result they are split into components which either measure the curvature of spacetime or the energy contained in it.

We can contract (1.1.2) with a contravariant metric $g^{\mu\nu}$ to obtain the trace of the field equations,

$$R + 4\Lambda = -\frac{8\pi G}{c^4} T \tag{1.1.5}$$

where $T = T^\lambda_\lambda$. This enables us to re-write the field equations as

$$R_{\mu\nu} + g_{\mu\nu}\Lambda = \frac{8\pi G}{c^4}\left(T_{\mu\nu} - \frac{1}{2} g_{\mu\nu} T\right). \tag{1.1.6}$$

For a perfect fluid – the fluid in which there is no heat flow or viscosity, but entirely specified by both the rest-frames, energy density and (isotropic) pressure, the energy-momentum becomes

$$T^{\mu\nu} = \left(\rho + \frac{p}{c^2}\right) U^\mu U^\nu - g^{\mu\nu} p, \tag{1.1.7}$$

where ρc^2 is the energy density, U^μ and U^ν are the four-velocities of the fluid, with

$$U^\mu = c\frac{\mathrm{d}x^\mu}{\mathrm{d}s}. \tag{1.1.8}$$

Note that

$$T_{\mu\nu} = \left(\rho + \frac{p}{c^2}\right) U_\mu U_\nu - g_{\mu\nu} p. \tag{1.1.9}$$

The density and pressure solely depend on the cosmic time in an isotropic and homogeneous universe. That means there is no peculiar motion, and so the four-velocity is given by

$$U^\mu = (c, 0, 0, 0). \tag{1.1.10}$$

This further yields

$$T^{\mu}_{\nu} = \begin{pmatrix} \rho c^2 & 0 & 0 & 0 \\ 0 & -p & 0 & 0 \\ 0 & 0 & -p & 0 \\ 0 & 0 & 0 & -p \end{pmatrix} \tag{1.1.11}$$

with $T = \rho c^2 - 3p$.

The constituents of the metric tensor $g_{\mu\nu}$ can be obtained from the Friedmann-Robertson-Walker metric (FRWM) for a homogeneous and isotropic universe. The FRWM enables us to re-write using the scale factor $a(t)$ and the curvature signature k, the Ricci tensor R and the Ricci scalar $R_{\mu\nu}$. Now, if we plug the results obtained above into Equation (1.1.6) and apply the energy-momentum tensor (1.1.7) we obtain equations

$$\frac{\ddot{a}}{a} = -\frac{4\pi G}{3}\left(\rho + 3\frac{p}{c^2}\right) + \frac{\Lambda c^2}{3} \tag{1.1.12}$$

and

$$\frac{\ddot{a}}{a} + 2\frac{\dot{a}^2}{a^2} + 2\frac{kc^2}{a^2} = 4\pi G\left(\rho - \frac{p}{c^2}\right) + \Lambda c^2. \tag{1.1.13}$$

Equations (1.1.12) and (1.1.13), are, respectively, from the time-time (00) and the space-space (ii) components of the Einstein's field equations. Substituting Equation (1.1.12) into Equation (1.1.13) we obtain the Friedmann equation:

$$\left(\frac{\dot{a}}{a}\right)^2 = \frac{8\pi G}{3}\rho - \frac{kc^2}{a^2} + \frac{\Lambda c^2}{3}. \tag{1.1.14}$$

The cosmological constant Λ can be thought of an energy component of mass density $\rho_\Lambda = \Lambda c^2/8\pi G$ and pressure $p_\Lambda = -\rho_\Lambda c^2$; these terms can then be incorporated on the right-hand side of Equation (1.1.2) as part of energy-momentum tensor, $T_{\mu\nu} = (c^4\Lambda/8\pi G)g_{\mu\nu}$, see Mo et al. (2010).

Next, we introduce the FRW universe metric that takes the form (Kiefer and Polarski (2008))

$$(\mathrm{d}s)^2 = (c\mathrm{d}t)^2 - a^2(t)\left[\left(\frac{\mathrm{d}x}{\sqrt{1-kx^2}}\right)^2 + (x\mathrm{d}\theta)^2 + (x\sin\theta\mathrm{d}\phi)^2\right], \tag{1.1.15}$$

which can also be re-written as

$$(\mathrm{d}s)^2 = (c\mathrm{d}t)^2 - a^2(t)\left[\frac{\mathrm{d}r^2}{1-kr^2} + r^2\left(\mathrm{d}\theta^2 + \sin^2\theta\mathrm{d}\phi^2\right)\right]. \tag{1.1.16}$$

It is conventional and standard in cosmology to introduce new units such that the speed of light, $c = 1$; to require that speeds are measured in units of the light speed, and the Equation (1.1.16) translates into

$$\mathrm{d}s^2 = \mathrm{d}t^2 - a^2(t)\left[\frac{\mathrm{d}r^2}{1-kr^2} + r^2\left(\mathrm{d}\theta^2 + \sin^2\theta\mathrm{d}\phi^2\right)\right], \tag{1.1.17}$$

the Friedmann-Robertson-Walker (FRW) metric.

Here, (r, θ, ϕ) are the time-independent dimensionless comoving coordinates, with $r \in [0, 1]$, hence do not change as the Universe expands or contracts. These coordinates label a fundamental observer. In an unperturbed (homogeneous) FRW metric, a fundamental observer will always observe the Universe to be isotropic. The parameter t (in units of time) is called proper time – the time on a fundamental observer's standard clock. The parameter k is responsible for determining the global curvature of spacetime, and it is restricted to only take the values -1, 0 and $+1$.

1.1.2 The Redshift, Scale Factor, and Galaxy Velocity Measurements

Velocity measurements of the distant galaxies divided by the respective galaxy distances from us can be used to determine the expansion rate and consequently enable us to infer how rapid the cosmic is expanding. Such expansion determines how fast the distant galaxy recedes from us according to Hubble's law. A receding object such as galaxy will emit sound or light wavelength that is stretched out at the time it reaches an observer. As a result, the wavelength of sound or light as measured by an observer will be longer compared to the emitted one.

Let us formally derive the scale factor, redshift, and the line emission relationships and see how we can use the results to estimate the recession velocities of the distant galaxies. We consider the constant coordinates x^i for which in the FRW universe are the comoving coordinates (r, θ, ϕ) (see Subsection 1.1.1). Suppose that an arbitrary galaxy G, each defined in terms of this coordinate frame, that is $G(r, \theta, \phi)$, called the cosmological rest-frame is a basic unit in the cosmos. Similarly, an observer in our Galaxy (Milky Way) will have his/her own comoving coordinates, here denoted by $\mathbb{O}(r, \theta, \phi)$. Let us assume no preferred position for an observer, and place him/her at the center of the Universe ($r = 0$) for convenience. Suppose further that a sample distant galaxy $G(r, \theta, \phi)$ emits light towards us, such that t_{emit} is the time when the emitted light leaves the galaxy G and $t = t_{\text{obs}}$ is the present epoch time corresponding to the light reaching an observer at $r = 0$.

Light path is a null geodesic according to the theory of general relativity, which means $\mathrm{d}s^2 = 0$. θ and ϕ remains constant as there is no spatial distortion along the null geodesic, and hence the FRW metric (1.1.16) becomes

$$0 = c^2\mathrm{d}t^2 - a(t)^2\frac{\mathrm{d}r^2}{(1 - kr^2)} + 0 + 0, \tag{1.1.18}$$

which implies

$$c\mathrm{d}t = \pm a(t)\frac{\mathrm{d}r}{\sqrt{1 - kr^2}}; \tag{1.1.19}$$

we will consider

$$\frac{c\mathrm{d}t}{a(t)} = \frac{\mathrm{d}r}{\sqrt{1 - kr^2}}. \tag{1.1.20}$$

Since as time t increases, r decreases, we have

$$\int_{t_{\text{emit}}}^{t_{\text{obs}}} \frac{c\mathrm{d}t}{a(t)} = -\int_{r_{\text{emit}}}^{r=0} \frac{\mathrm{d}r}{\sqrt{1-kr^2}} \equiv \int_{r=0}^{r_{\text{emit}}} \frac{\mathrm{d}r}{\sqrt{1-kr^2}}. \tag{1.1.21}$$

Proper knowledge of the parameters a and k is required to solve (1.1.21), but we can in our case apply some approximations for such a solution. Suppose two successive peaks of the light wave emitted by the galaxy G are separated by $a(t)$ intervals, that is the two successive peaks emitted by G at times t_{emit} and $t_{\text{emit}} + \delta t_{\text{emit}}$ are respectively received by an observer $\mathbb{O}$ at times t_{obs} and $t_{\text{obs}} + \delta t_{\text{obs}}$, so that Equation (1.1.21) becomes

$$\int_{t_{\text{emit}}+\triangle t_{\text{emit}}}^{t_{\text{obs}}+\triangle t_{\text{obs}}} \frac{c\mathrm{d}t}{a(t)} = \int_{0}^{r} \frac{\mathrm{d}r}{\sqrt{1-kr^2}}. \tag{1.1.22}$$

We further assume that the scale factor $a(t)$ varies slowly with time, and hence in the time intervals, $\triangle t_{\text{emit}}$ and $\triangle t_{\text{obs}}$, $a(t)$ practically remains unchanged, thus upon subtracting (1.1.21) from (1.1.22), we have

$$\frac{c\triangle t_{\text{obs}}}{c\triangle t_{\text{emit}}} = \frac{a(t_{\text{obs}})}{a(t_{\text{emit}})}. \tag{1.1.23}$$

The factor at which the wavelength is stretched is called the redshift and is defined by

$$z \equiv \frac{\lambda_{\text{obs}} - \lambda_{\text{emit}}}{\lambda_{\text{emit}}}. \tag{1.1.24}$$

This is the factor by which the wavelength of light increases as it traverses space from the galaxy G to the observer $\mathbb{O}$. Since

$$\frac{c\triangle t_{\text{obs}}}{c\triangle t_{\text{emit}}} \equiv \frac{\lambda_{\text{obs}}}{\lambda_{\text{emit}}}, \tag{1.1.25}$$

the redshift is then related to the expansion factor as

$$1 + z \equiv \frac{\lambda_{\text{obs}}}{\lambda_{\text{emit}}} = \frac{a(t_{\text{obs}})}{a(t_{\text{emit}})}, \tag{1.1.26}$$

where respectively, λ_{obs} and λ_{emit} are the observed and emitted wavelengths of the sound or light from a receding object, $z = z_{\text{emit}}$ is the redshift of an object at the time it emits light of photon wavelength λ_{emit}. Redshift is simply a fractional change in the λ between an object and an observer. For present-day observation, $a(t_{\text{obs}}) \equiv a_{\text{obs}} = a_0 = 1$, and so

$$a_{\text{emit}} = \frac{1}{1 + z_{\text{emit}}}, \tag{1.1.27}$$

where a_{emit} and a_{obs} are respectively, the scale factors corresponding to the time a photon was emitted and the time it reaches an observer.

The integral on the right-hand side of (1.1.22) is called the co-moving distance, r_{com}. The multiplication of the comoving distance with the expansion factor a is called physical/proper distance, i.e. $r = ar_{\text{com}}$. Presently, the expansion factor is usually normalized to 1, making the proper distance and the co-moving distance the same. The proper distance progressively

decreases with the scale factor from the present moving back in time, but the co-moving distance does not change.

Growth of the structures in the Universe, set forth by small inhomogeneities in the background energy density induced velocities that deviate from the systematic expansion of the Universe. Such velocities are called peculiar and are relative to the fundamental observers' cosmological rest-frame. With respect to the fundamental observer (situated at the origin), the proper velocity of a particle (object) is defined by $v = \mathrm{d}l/\mathrm{d}t$, where $l(t)$ (see Eq. (1.1.38)) is the proper length between an observer and the object. For the component of the velocity due to universal systematic expansion, $v_{\mathrm{exp}} = H(t)/l(t)$ and the peculiar velocity v_{pec}, we can write (using Eq. (1.1.38))

$$v(t) = \dot{a}(t)\chi(t) + a(t)\dot{\chi}(t) = v_{\mathrm{exp}} + v_{\mathrm{pec}}. \tag{1.1.28}$$

Now, suppose a particle at the same location as a fundamental observer has a peculiar velocity v_{pec} relative to the fundamental observer. The geometry at the fundamental observer is locally a Minkowski space, and the fundamental observer will observe from a particle, a light with a Doppler redshift, z_{pec} given by

$$1 + z_{\mathrm{pec}} = \frac{\sqrt{1 + v_{\mathrm{pec}}/c}}{\sqrt{1 - v_{\mathrm{pec}}/c}}. \tag{1.1.29}$$

Assuming that two observers are separated by some proper distance from each other, and suppose further that a particle moves with a peculiar velocity along the geodesic connecting the two fundamental observers, we can write (using the redshift definition Eq. (1.1.26))

$$1 + z_{\mathrm{obs}} = \frac{\lambda_2}{\lambda_{\mathrm{p}}} = \frac{\lambda_1\lambda_2}{\lambda_{\mathrm{p}}\lambda_1} \tag{1.1.30}$$

where λ_{p} is the particle-emitted wavelength; λ_1 and λ_2 are the wavelengths observed respectively by the first and the second fundamental observers. The relation (1.1.30) above reduces to

$$1 + z_{\mathrm{obs}} = (1 + z_{\mathrm{pec}})(1 + z_{\mathrm{exp}}), \tag{1.1.31}$$

which implies that the observed redshift of any object, z_{obs} is a contribution of redshift due to the universal systematic expansion z_{exp} and the redshift due to the peculiar velocity of the object z_{pec} along the line-of-sight. Equation (1.1.29) can be approximated by $z_{\mathrm{pec}} \approx v_{\mathrm{pec}}/c$ in a non-relativistic case, and Equation (1.1.31) reduces to

$$z_{\mathrm{obs}} = z_{\mathrm{exp}} + \frac{v_{\mathrm{pec}}}{c}(1 + z_{\mathrm{exp}}). \tag{1.1.32}$$

For galaxies cluster at redshift z,

$$\sigma_v = \sigma_z \frac{c}{(1+z)}, \tag{1.1.33}$$

for which σ_v is the peculiar velocity dispersion of galaxies, and σ_z is the observed dispersion in the redshift.

It can be shown that for a free, non-relativistic particle with peculiar velocity $v_{\rm pec}$ and a momentum p,

$$v_{\rm pec} \propto a^{-1}(t), \text{ implying } p(t) \propto a^{-1}(t). \tag{1.1.34}$$

Again, since $pc = E = h_{\rm p}c$ for photons with rest mass, then $\nu \propto a^{-1}$ and the decay law $p \propto a^{-1}$ is true for both photons and massive particles.

The standard Doppler formula $z \simeq v/c$ is applied at low redshifts, and using the Hubble's law $v = H_0 d$, where the constant of proportionality, H_0 is the Hubble constant, and d is the distance of separation between the galaxy and an observer, we can write

$$z = \frac{H_0}{c} d. \tag{1.1.35}$$

Hubble's constant has units of time inverse ($\rm s^{-1}$), usually written as $H_0 = 100h\ \rm kms^{-1}Mpc^{-1}$, where the dimensionless parameter h, with a more often chosen fiducial value of $h = 0.7$ is introduced to account for uncertainties in the measurements of the Hubble constant, since various probes came up with varying values of this constant.

The Hubble rate tells us how rapidly the scale factor changes and the change in the scale factor describes the evolution of various Universe mass-energy contents. Therefore, measuring the amount of redshift in the emission or absorption lines, can inform us about the rate of recession from us (our own galaxy) of the structures in which they reside.

1.1.3 The Angular-diameter and the Luminosity Distances, Volumes and Redshift Relations

The Friedmann-Robertson-Walker (FRW) four-metric of spacetime, for a line element (metric), $\rm d\mathit{l}^2$ (see proof Weinberg (1972)) of a homogeneous and isotropic three-dimensional (3-D) hypersurface is given by (we adopt materials from Mo et al. (2010))

$$\begin{aligned} \rm d\mathit{s}^2 &= c^2 \rm dt^2 - d\mathit{l}^2 \\ &= c^2 \rm dt^2 - a^2(t) \left[\frac{dr^2}{1-kr^2} + r^2 \left(d\theta^2 + \sin^2\theta d\phi^2 \right) \right], \end{aligned} \tag{1.1.36}$$

where t is the constant cosmic time and c is the speed of light. Here, the cosmic time t becomes the proper time of all fundamental observers, if we define as the observer's proper time, the time recorded by the standard clock at rest with the observer. At any given time t, for any two fundamental observers, a proper distance l is defined as

$$l = \int \rm d\mathit{l}. \tag{1.1.37}$$

We label fundamental observers by the comoving coordinates (r, θ, ϕ) and assume that one observer is placed at the origin ($r = 0$) and the other at (r_1, θ, ϕ). We can then write a proper distance as

$$l = a(t) \int_0^{r_1} \frac{dr}{\sqrt{1-kr^2}} = a(t)\chi(r_1) \tag{1.1.38}$$

where χ is the proper distance l measured in units of the scale factor, called the co-moving distance between the two observers, and is defined as

$$\chi(r) = \begin{cases} \sin^{-1} r, & \text{for } k = +1 \\ r, & \text{for } k = 0 \\ \sinh^{-1} r, & \text{for } k = -1. \end{cases} \tag{1.1.39}$$

It follows that the rate of change of proper distance l at time t between any two fundamental observers in units of l is given by

$$\frac{\mathrm{d}l}{\mathrm{d}t} = H(t)l \tag{1.1.40}$$

where $H(t)$ is the Hubble rate (a function of cosmic time t):

$$H(t) = \frac{\mathrm{d}l}{l\mathrm{d}t} = \frac{\dot{a}(t)}{a(t)}. \tag{1.1.41}$$

Usually, time variables are changed from proper time to conformal time

$$\tau(t) = \int_0^t \frac{c\mathrm{d}t'}{a(t')}. \tag{1.1.42}$$

We can use τ and χ to write the FRW metric in the form that is more handy for gaining insights of the spacetime causal properties:

$$\mathrm{d}s^2 = a^2(\tau)\Big[\mathrm{d}\tau^2 - \mathrm{d}\chi^2 - f_k^2(\chi)\left(\mathrm{d}\theta^2 + \sin^2\theta \mathrm{d}\phi^2\right)\Big] \tag{1.1.43}$$

where

$$f_k(\chi) = \left\{ \begin{array}{ll} \sin\chi, & \text{for } k = +1 \\ \chi, & \text{for } \quad k = 0 \\ \sinh\chi, & \text{for } k = -1 \end{array} \right\} = r. \tag{1.1.44}$$

We will now derive the relationships between the angular-diameter and the luminosity distances, following this argument: the light we observe at the present time was emitted at an earlier time from a distant source, as a result, the proper and the co-moving distances cannot be observed directly. We, therefore, have to consider other cosmological distances that we can directly measure from astronomical observations.

Let the observable properties of the object with known physical (proper) size D, intrinsic luminosity L at some distance d be the object's angular extent θ' subtended by the object and the flux F. The angular-diameter and the luminosity distances, d_A and d_L, are, respectively given by

$$d_A = \frac{D}{\theta'} \tag{1.1.45}$$

for small values of θ', and

$$d_L^2 = \frac{4\pi F}{L}. \tag{1.1.46}$$

In a static space, $d_A = d_L = d$, but these values differ when we consider cosmic distances in an expanding universe. By the definition of the angular-diameter distance, the angular extent of the object decreases by the same factor that will decrease the d_A. Suppose at a given cosmic time $t_{\rm emit}$, there exist two points with the same radial coordinate $r_{\rm emit}$ (where in FRW metric $\mathrm{d}\theta = \mathrm{d}\phi = 0$), such that two light signals reaching us today at time $t_{\rm obs}$ originate from the two points, and the distance between the two light signals equals the proper size D of an object. In FRW metric, the proper size of an object is then given by the integral over the transverse direction of $\mathrm{d}l$ (Eq. (1.1.36))

$$D = a_{\rm emit} r_{\rm emit} \int d\theta' = \frac{a(t_{\rm obs}) r_{\rm emit}}{1+z} \theta' \tag{1.1.47}$$

and can be thought as the distance between the two signals. This means

$$d_A = \frac{a(t_{\rm obs}) r_{\rm emit}}{1+z_{\rm emit}} = a(t_{\rm emit}) r_{\rm emit}, \tag{1.1.48}$$

where $a(t_{\rm obs}) r_{\rm emit}$ is interpreted as the proper distance from an observer at the time of observation to the object, for flat universe.

Following the arguments given in Mo et al. (2010), the flux and the luminosity distance defined in Equation (1.1.46), can respectively, be written as

$$F = \frac{L}{4\pi \Big[a(t_{\rm obs}) r_{\rm emit}(1+z)\Big]^2} \tag{1.1.49}$$

and

$$d_L = a(t_{\rm obs}) r_{\rm emit}(1+z). \tag{1.1.50}$$

It can further be shown that the luminosity distance and the apparent surface brightness (SB) of an object are related as

$$\mathrm{SB} \equiv \frac{4F}{\pi\theta^2} = \frac{L}{\pi^2 D^2}(1+z)^{-4}, \tag{1.1.51}$$

and that if the Universe is not expanding,

$$d_L = a(t_{\rm obs}) r_{\rm emit}(1+z) = d_A(1+z)^2. \tag{1.1.52}$$

The apparent surface brightness (Eq. (1.1.51)), unlike d_A and d_L, is independent of the relationships involving $a(t_{\rm obs}) r_{\rm emit}$, $z_{\rm emit}$ and a dynamical evolution of the expansion factor $a(t)$, it only relies on the radiation field local thermodynamics conditions, a fact that follows directly from $\mathrm{SB} \propto T^4$.

It is necessary to transform an unobservable coordinate r into a function of redshift z so that we can express the luminosity and the angular-diameter distances, d_L and d_A in terms of the quantities that we can observe. However, understanding the propagation of light signals in an isotropic and homogeneous universe is equally important because almost all astronomical

object observations are facilitated by light signals. We know that photons propagate along null geodesics for which $\mathrm{d}s = 0$, and thus if we consider photon signals traveling towards the origin along the radial direction ($\mathrm{d}\theta = \mathrm{d}\phi = 0$), we can write their trajectories as

$$\mathrm{d}\tau = \mathrm{d}\chi; \tag{1.1.53}$$

this follows from Equation (1.1.43). If from a fundamental observer $(r_{\mathrm{emit}}, \theta_{\mathrm{emit}}, \phi_{\mathrm{emit}})$ at time t_{emit} a wave crest is emitted, it will reach us in the origin at time t_{obs} given by

$$\tau(t_{\mathrm{obs}}) - \tau(t_{\mathrm{emit}}) = \chi(r_{\mathrm{emit}}) - \chi(r_{\mathrm{obs}}) = \chi(r_{\mathrm{emit}}) \equiv \chi(r), \tag{1.1.54}$$

where $r_{\mathrm{obs}} = 0$, and $\chi(r)$ is the comoving distance (that traverses between the fundamental observer and the observer at the origin (us)). We see that between the fundamental observer and the origin, the comoving distance does not change with time.

Now, suppose a light signal (an event) that originates at cosmic time t_{emit} and reaching an observer at the origin at the present time t_{obs} has a comoving coordinate $r(t)$. It follows from (1.1.54) (and making use of the conformal time (Eq. (1.1.42)) and the fact $\mathrm{d}t = \mathrm{d}a/\dot{a}$) that

$$\chi(r) = \tau(t_{\mathrm{obs}}) - \tau(t_{\mathrm{emit}}) = c\int_{a(t_{\mathrm{emit}})}^{a(t_{\mathrm{obs}})} \frac{\mathrm{d}a}{a\dot{a}} \tag{1.1.55}$$

is the comoving distance corresponding to r. Speaking in more general terms, by setting $a(t_{\mathrm{obs}}) \equiv a_0$ – the present time scale factor, and $a(t) \equiv a$, we can write Equation (1.1.55) as

$$\chi(r) = \frac{c}{H_0 a_0}\int_0^z \frac{dz}{E(z)}, \tag{1.1.56}$$

where we have employed the fact that $a(z) = a_0/(1+z)$ and Equation (1.1.133), such that $E(z)$ is given by Equation (1.1.138). In general, if provided with the required set of cosmological parameters, the equation above can be integrated numerically. Using Equation (1.1.39) and Equation (1.1.44), we obtain the angular-diameter distance in the comoving units, r, given by

$$r = f_k\left[\frac{c}{H_0 a_0}\int_0^z \frac{dz}{E(z)}\right]. \tag{1.1.57}$$

For $z << z_{\mathrm{eq}}$ and $\Omega_{\Lambda,0}$ we can derive from Equation (1.1.56) for all three values of k, that is, $k = \{-1, 0, +1\}$, an analytical expression known as Mattig's formula (Mo et al. (2010)):

$$a_0 r = \frac{2c}{H_0}\frac{\Omega_0 z + (2-\Omega_0)\left[1 - (\Omega_0 z + 1)^{1/2}\right]}{\Omega_0^2(1+z)}. \tag{1.1.58}$$

When $z << z_{\mathrm{eq}}$ for flat universe ($\Omega_{\mathrm{m},0} + \Omega_{\Lambda,0} = 1$), $r = \chi$,

$$a_0 r = \frac{c}{H_0}\int_0^z \frac{dz}{\left[\Omega_{\Lambda,0} + \Omega_{\mathrm{m},0}(1+z)^3\right]^{1/2}}. \tag{1.1.59}$$

From Equation (1.1.56), we can get the proper distance per unit redshift at redshift z,

$$\frac{\mathrm{d}l}{\mathrm{d}z} = \frac{c}{H_0}\frac{1}{(1+z)}\frac{1}{E(z)}, \tag{1.1.60}$$

where

$$dl = a(t)\mathrm{d}\chi \tag{1.1.61}$$

is the proper length/distance element at time t (in the radial direction). We shall use these results in a sequel.

For a measured flux $F_{\rm obs}$ as observed by an observer, it can be shown that

$$d_L^2 = \frac{L_{\rm emit}}{4\pi F_{\rm obs}}. \tag{1.1.62}$$

If an astronomical object has a known intrinsic luminosity (or equivalently proper size), its luminosity or angular-diameter distance can be measured directly from it. Such sources with known or calibrated/intrinsic luminosities are called standard candles/rulers. Astrophysical objects such as Type Ia Supernovae (SNeIa) and a class of pulsating stars known as Cepheid variables are often used as standard candles due to characteristic qualities they possess. Supernovae results from stars, usually of mass at least 5 times to 20 times larger compared to that of the sun, exhausting their nuclei fuel, suddenly collapsing and ejecting huge amounts of heavy elements into interstellar space, the process known as supernovae explosion. SNeIa have been widely deployed to probe the cosmic, and the most breakthrough record we have today is the study carried by two independent teams, using a class of distant SNeIa, which led to the empirical discovery that the Universe expansion is accelerating (Riess et al., 1998; Perlmutter et al., 1999). Well-known relationships between distances and the intrinsic brightness of supernovae which are almost the same, and the changes in their colors with redshift due to the cosmic expansion, can be used to measure distances between them and us, and when these distances are compared to the supernovae cosmological redshifts, they can tell us how much the Universe has expanded since the occurrence of such supernovae.

Similarly, Cepheid variable stars have mean intrinsic luminosities that strongly correlate to their pulsation periods, the more luminous the Cepheid star, the longer the pulsation period. Such stars vary in brightness and temperature as they pulsate radially, and the variations produce changes in their brightness with stable periods and amplitude that are well-defined. Thus Cepheid variables luminosities have direct and strong relationships to their pulsation periods, making them useful benchmarks of cosmological distance measures. By simply observing their pulsation periods, one can establish their true luminosities, and by comparing their known luminosities to their observed brightness, distances to these stars can be determined.

Using distance-redshift relations, estimates of cosmological parameters, e.g., H_0, $\Omega_{\rm m,0}$ and Ω_Λ can be obtained through redshift measurements of properly calibrated standard candles.

The Hubble Space Telescope used Cepheids to successfully measure distances out to $\sim$ 10 Mpc. Linearity still applies for luminosity distance-redshift relations within such distances, where $d_L \approx cz/H_0$, and constraints can only be obtained for H_0. For example, Freedman et al. (2001) reported estimates of $H_0 = 72 \pm 8$ kms^{-1}Mpc^{-1}. SNeIa are usually employed to obtain measurements of more distant objects.

Let us now consider object populations. Suppose

$$n(z) = n_0(z)(1+z)^3 \tag{1.1.63}$$

is a proper number density of some objects population, where for conserved number of objects, n_0 is constant; and $\sigma(z)$ is the average proper cross-section of such population, then (using Eq. (1.1.60)), in a unit redshift interval around z,

$$\frac{\mathrm{d}N_{\rm en}}{dz} = n_0(z)(1+z)^3\frac{\mathrm{d}l}{\mathrm{d}z} = n_0(z)\sigma(z)\frac{c}{H_0}\frac{(1+z)^2}{E(z)} \tag{1.1.64}$$

is the number of intersections between a line-of-sight and such population of objects (Mo et al., 2010). For the objects intersection up to redshift z, the optical depth is calculated as

$$\tau(z) = \int_0^z \mathrm{d}N_{\rm en} = \frac{c}{H_0}\int_0^z n_0(z)\sigma(z)\frac{(1+z)^2}{E(z)}\mathrm{d}z. \tag{1.1.65}$$

Here, $\mathrm{d}N_{\rm en}/\mathrm{d}z$ is the expected number of absorption system per unit redshift. The two latter equations have various applications, where the meanings of $n_0(z)$ and $\sigma(z)$ have different interpretations depending on where they are applied, as summarized in the table below (see Mo et al. (2010) for full details).

	Quasi-stellar objects absorption line systems	Interpretations of the observed number of gravitational lensing events caused by foreground objects	Scattering of microwave background by ionized intergalactic gas
$n_0(z)$	Comoving number density	Comoving number density of lenses	Comoving number density of free electrons
$\sigma(z)$	Average absorption cross-section of absorbers	Average lensing cross-section	Thomson cross-section

Next we consider at a redshift z related to a depth $\mathrm{d}z$ and a solid angle $\mathrm{d}\Omega = \mathrm{d}\theta^2$, the proper-volume element given by

$$\mathrm{d}^2V_{\rm p} = a^3(t)r^2\mathrm{d}\chi\mathrm{d}\Omega = \frac{c}{H_0}\frac{\mathrm{d}z}{(1+z)E(z)}\frac{[a_0 r(z)]^2\,\mathrm{d}\Omega}{(1+z)^2}, \tag{1.1.66}$$

where an angle element $\mathrm{d}\theta$ subtends the proper distance $a(t)r\mathrm{d}\theta$, and Equation (1.1.57) relates r to z. The total objects number in a unit volume can be computed using this equation. However, out to redshift z, the total, proper-volume given by

$$\begin{aligned} V_{\rm p}(z) \quad &= 4\pi a^3(t)\int_0^{r(z)} r'^2\frac{\mathrm{d}r'}{\sqrt{1-kr'^2}} \\ &= \begin{cases} 2\pi a^3(t)\Big(\sin^{-1}r - r\sqrt{1-r^2}\Big), & \text{for } k=+1 \\ \frac{4\pi}{3}a^3(t)r^3, & \text{for } k=0 \\ 2\pi a^3(t)\Big(r\sqrt{1+r^2} - \sinh^{-1}r\Big), & \text{for } k=-1, \end{cases} \end{aligned} \tag{1.1.67}$$

can be obtained using Equation (1.1.66). Assuming that at redshift z the proper number density of objects is given by Equation (1.1.63), then we can compute per units of both redshift and solid angle, the predicted count of objects

$$\frac{\mathrm{d}^2N}{\mathrm{d}z\mathrm{d}\Omega} = n(z)\frac{\mathrm{d}^2V_\mathrm{p}}{\mathrm{d}z\mathrm{d}\Omega} = n_0(z)\frac{c}{H_0}\frac{\Big[a_0 r(z)\Big]^2}{E(z)}. \tag{1.1.68}$$

Just by counting sources as a function of z (for known value of n_0 at z), this equation can be used to put bounds on the cosmological parameters.

Let us now consider in the FRW metric, a comoving distance between two objects. Suppose an angle α on the sky separates two objects situated at redshifts z_1 and z_2, then the Equation (1.1.55) gives the comoving distances, here denoted by χ_1 and χ_2 of the two objects, as seen by an observer who is at the origin. For $k = +1$, the distance between two points on the unit sphere, where χ_1, χ_2 are the polar angles of the two points such that these points make azimuthal angles that differ by α, is a measure of the comoving distance χ_{12} between the two objects, see Mo et al. (2010). In summary, the comoving distance equations corresponding to $k = +1, 0, -1$ are respectively:

$$\mathrm{cos}\chi_{12} = \mathrm{cos}\chi_1\mathrm{cos}\chi_2 + \mathrm{sin}\chi_1\mathrm{sin}\chi_2\mathrm{cos}\alpha; \tag{1.1.69}$$

$$\chi_{12}^2 = \chi_1^2 + \chi_2^2 - 2\chi_1\chi_2\mathrm{cos}\alpha; \tag{1.1.70}$$

and

$$\mathrm{cosh}\chi_{12} = \mathrm{cosh}\chi_1\mathrm{cosh}\chi_2 - \mathrm{sinh}\chi_1\mathrm{sinh}\chi_2\mathrm{cos}\alpha. \tag{1.1.71}$$

In the case where the angle α is zero or very small, the angular-diameter distance measured from the first to the second object is given by

$$\mathrm{d}_{A,12} = \frac{a_0 r_{12}}{1+z_2}, \tag{1.1.72}$$

where

$$r_{12} \equiv f_k(\chi_{12}) = f_k(\chi_2 - \chi_1) = r(z_2)\sqrt{1-kr^2(z_1)} - r(z_1)\sqrt{1-kr^2(z_2)}; \tag{1.1.73}$$

and for the case when $\Omega_{\Lambda,0} = 0$,

$$\mathrm{d}_{A,12} = \frac{2c}{H_0}\frac{\sqrt{1+\Omega_0 z_1}\Big(2-\Omega_0+\Omega_0 z_2\Big) - \sqrt{1+\Omega_0 z_2}\Big(2-\Omega_0-\Omega_0 z_1\Big)}{\Omega_0^2(1+z_2)^2(1+z_1)}. \tag{1.1.74}$$

The role played by Equation (1.1.74) in gravitational lensing is important, with the source and the lens redshifts respectively given by z_2 and z_1. For $z_1 = 0$, Equation (1.1.74) reduces to Mattig's formula. Note that $|\mathrm{d}_{A,12}| \neq |\mathrm{d}_{A,21}|$.

1.1.4 Big Bang ΛCDM Model of Cosmology

It took astronomers several decades before they started to be convinced that the gravity of the normal visible matter was not sufficiently strong to form and hold together the complex Universe structures in existence today, such as galaxies and clusters of galaxies. Through decades, a number of astrophysical problems have been identified, and with time, the predicted existence of dark matter started to be seen as one possible candidate solution to such problems (Trimble, 1987). It was around the 1980s when most astronomers started to realize that an invisible form of matter may exist around galaxies and clusters of galaxies (Faber and Gallagher, 1979). A possible non-luminous matter detection through gravitational effects may go as far as 1840s (Trimble, 1987). Early attempts hinted that galaxies behave strangely and the known amount of visible matter content in the Universe could not account for the observed phenomena in which motions of galaxies do not obey fundamental laws of physics.

These big cosmological puzzles, in particular, missing mass around galaxies and clusters of galaxies, and the expansion of the Universe as was observed by Edwin Hubble through studying motions of galaxies (Hubble, 1929), led to the proposition of the standard ΛCDM model of cosmology around 2000s. The ΛCDM provides a reasonable account of large-scale structures of the galaxy and matter distribution in the Universe, the existence and structure of the cosmic microwave background (CMB) radiation as observed today, the accelerated expansion of the Universe, and the amount of hydrogen distributed throughout the cosmic; which are very important cosmology phenomenological properties of the Universe. A spatially-flat ΛCDM universe model is derived from general relativity, where Λ stands for a cosmological constant that was introduced by Einstein and has been associated to a special type of energy called dark energy (Mannheim, 2006) (the energy which keeps the Universe accelerated expanding (Riess et al., 1998)), and CDM is a shorthand for cold dark matter, a hypothetical type of non atomic matter.

Dark matter is an unknown and invisible substance that is thought to make up a significantly large fraction of the Universe's matter-energy content budget. The first attempt to describe the existence of this invisible form of matter that pervades most of the space in the Universe points back to the 1930s. The disproportionate account on the visible mass and observed very high velocities in galaxy clusters inspired Fritz Zwicky, a Swiss astronomer, who is one of the pioneers of modern astronomy, to carry out real major galaxy surveys and first postulated the existence of Dark matter (Andernach and Zwicky, 2017) (original paper was published in German (Zwicky, 1933)). Using the Coma cluster of galaxies, Zwicky observed very fast velocities of galaxies within the cluster, and realized that the amount of visible matter within the cluster was not sufficient to account for the very high velocities he noticed. In particular, he studied galaxy motions within the Coma cluster, and measured how fast with respect to us the galaxies were moving, and discovered that galaxies motions were remarkably fast $\sim 1000\,\mathrm{km}\,s^{-1}$ relative to each other, and concluded that such motions were too high for the galaxies to remain confined by the gravitational field of other galaxies within the Coma cluster. This was a puzzle

because the observed amount of matter would not be sufficient to hold together very fast-moving galaxies, instead, they were expected to stream away from each other. Zwicky then hypothesized that, in addition to the luminous galaxies that could be seen, the Coma cluster was filled with a mysterious type of matter (dark matter) that bound the galaxies together by exerting a gravitational pull and kept them from flying off into space. Zwicky was the first to study the concept of dark matter in detail using the virial theorem of classical mechanics to infer its existence (Andernach and Zwicky, 2017; Zwicky, 1937; de Swart et al., 2017).

Through studying the motion of stars within individual galaxies, M33 and Andromeda (M31), several astronomers such as Vera Rubin and Kent Ford (Rubin and Ford, 1970) could observe/describe similar "missing mass" phenomenon. According to Newton's Second Law of motion, motions of stars were expected to decrease with an increase in their distances from the center of the galaxy, since stars far away from the center would experience less gravitational pull as compared to those close to the center. This expectation is in contrast to what has actually been observed: the measured rotation speeds of orbiting stars as a function of the distance from the center of the M33 galaxy observed to be increasing with distances (or stayed constant) from the center to much high values than would be expected from the gravity of stars (contained within the galaxy) at the far edges of the M33 galaxy. Just as Zwicky concluded, this was another evidence that the bulk of matter within such galaxy was in fact contained as some broader distribution of dark matter and not in the luminous stars that could be seen. Similar studies were carried using two galaxies NGC 300 and M33 by Freeman where velocity maxima at a very large radius than photometrically predicted values were observed, something that could hint for the existence of a new form of undetected matter (Freeman, 1970; de Swart et al., 2017). A number of other probes have been reported, that studied the gravitational systems in relation to the stellar motions of galaxies and stars on very large length scales to affirm and/or address the dark matter problem (de Swart et al., 2017).

The invention of the general theory of relativity by Albert Einstein has changed our notion of how gravity works. It tells us that matter and energy curve spacetime and light rays bend in a gravitational field due to the curvature of spacetime. For example, massive stars attract nearby objects by distorting spacetime, causing other objects including light to move along the curved spacetime. In summary, according to GR, any massive object warps the space and time around it, and as a result, light rays will take an apparent turn around the object rather than traveling in a straight line. This observation provides other means of describing the dark matter phenomenon. By looking at a distant galaxy behind a foreground concentration of mass, for example, a cluster of galaxies, the shape of that distant galaxy will look distorted because the light rays from the distant galaxy coming towards us get bent by the gravitational field of the background galaxy cluster, and warp to form a ring around it. This ring is a highly distorted image of the distant galaxy behind the background cluster. The light bends because the mass within the foreground galaxy is far more than that contained in the luminous stars. This phenomenon is called gravitational lensing (Schneider et al., 1992) and has been studied using the SDSS and Hubble Space Telescope and a number of ground-based probes. Gravitational

lensing provides another evidence of dark matter existence and can be used to infer (using distant galaxy images) the distribution of mass in the cluster of galaxies. These observations have established that galaxies in the clusters are embedded within the dark matter distribution. Gravitational lensing can as well be applied to infer the existence of dark matter within an individual galaxy where also distant galaxies are used as lenses.

Weak lensing by galaxies or galaxy-galaxy lensing, a statistical approach in some sense is another lensing technique, it allows imaging the shape of galaxies behind thousand of foreground galaxies. The method probes the average mass of galaxy populations instead of probing individual galaxies, by measuring a large sample of distant background galaxies, for which weakly distorted distant galaxies images by the dark matter halos of a foreground population of galaxies are obtained. It was found through this approach that, extended massive dark matter halos always surround luminous galaxies.

In summary, the discovery of dark matter is a result of the idea that forces we can see are not sufficient to account for the existence of galaxies and other large-scale structures of the Universe. This has been backed up by theoretical calculations which have shown that the gravity of normal matter cannot generate enough gravity to form and hold the giant complex structures we see today, such as galaxies, stars, quasars, supernovae, pulsars, clusters of galaxies, and so on. Moreover, theoretical prospects show that dark matter influence can be detected by observing how places assumed to have a high dark matter concentration (such as giant galaxy clusters) curve the space, leading to bending and distortion of light from distant objects (e.g., galaxies) as the light traveling towards us passes nearby or behind them. Furthermore, dark matter has been contrasted to other types of matter such as a cloud of normal matter without stars and antimatter (made up of antiparticles), although the most common view is that dark matter could be made up of some foreign materials such as axions or WIMPS (weakly interacting massive particles).

Several alternatives to dark matter theories have been projected, but the notable one is the Modified Newtonian Dynamics (MOND) (Milgrom, 1983a,b,c; Famaey and McGaugh, 2012), which suggests that different laws of gravity can explain the discrepancy between the matter contents of the Universe and dynamics of galaxies. The theory asserts that, at regions where the gravitational pull is weak, such as in the far edges of galaxies (or galaxy clusters), Newton's law of gravity becomes irregular, so modification can be made to explain the phenomena without the need of dark matter. Recently, another approach has been suggested, it tries to modify the laws of gravity under the assumption of the phenomenon known as Vainshtein Screening (Platscher et al., 2018). Nevertheless, the dark matter theory has matured over time and plays a very significant role in galaxy formation, see Subsection 1.2.2.

Dark energy is another strange but abundant component of the Universe, which can neither be detected nor tested, but we can only see its effect. It is because of the dark energy that the late-time universe has been observed to be accelerated expanding (Perlmutter et al., 1997; Riess et al., 1998; Perlmutter et al., 1999), and the redshift in galaxies motions occur because the

Universe stretches the light wavelengths as it expands. Dark energy seems to be a function of empty space, as more space comes into existence this energy is not diluted, instead, the rate of the Universe expansion increases, which means the energy proportionally increases with the vacuum. This discovery is implied by Hubble's law which also supports a theory that had been projected by Georges LeMaitre in 1927. Understanding the late-time accelerated expansion of the Universe has been one of the major challenges in cosmology for about two decades (Riess et al., 1998; Perlmutter et al., 1999).

We can partly describe the fate of the Universe by measuring its density as the Universe's future expansion rate depends on it. But, there is more to consider than just the density of the Universe to account for its expansion rate. To address this challenge dark energy represented by the cosmological constant Λ, has been introduced in the FRW equations to describe the observed geometrically spatially-flat infinitely expanding universe. The parameter Λ, together with other parameters, constitute what is called the ΛCDM standard model of cosmology.

The ΛCDM model of cosmology is simply a dark matter and dark energy dominated spatially-flat universe which started as an abrupt expanding spacetime from hot and dense Big Bang singularity. The model assumes that the large structures that we observe today are a result of Gaussian fluctuations which have been amplified by gravity. The term Concordance Model is used for ΛCDM to mean it is the currently acceptable and the most commonly used model of cosmology. The ΛCDM assumes a 13.8 billion years old Universe with compositions, 4% baryonic (ordinary) matter – the matter that makes us, stars and planets; 23% dark matter, and 73% dark energy; all these derived from CMB radiation observations by *WMAP* satellite.

The standard ΛCDM model is currently extended to six parameters which have been found to successfully describe the Universe, namely, the present-day Hubble parameter, $H_0 = 100h\,\mathrm{km\,s^{-1}\,Mpc^{-1}}$, the cosmological constant energy-density, Ω_Λ, the baryons density, $\Omega_\mathrm{b}h^2$, the linear amplitude of density fluctuations, σ_8, the index of the power spectrum of primordial density fluctuations, n_s, and the optical depth to last scattering, τ (Spergel et al., 2007). Here the cosmological constant density, Ω_Λ and the curvature parameter, Ω_k are related to the total matter density (Cold Dark Matter + baryons) by $\Omega_\mathrm{m} = 1 - \Omega_\mathrm{k} - \Omega_\Lambda$, see Subsection 1.1.5. A number of alternative models have been extrapolated from the standard ΛCDM, for example by extending it with parameters such as w_0, w_a, Ω_k, and the growth index, γ.

1.1.5 Cosmic Evolution and Expansion History

The dynamics of the Universe can be described well by the Friedmann equations which is the subject of our discussion. However, two parameters, namely, the scale factor $a(t)$ and the current expansion rate, the Hubble constant, $H_0 = 100h\,\mathrm{km\,s^{-1}\,Mpc^{-1}}$ with $h = 0.7$ (Freedman et al., 2001) are in most cases able to describe the expansion of the Universe. Here, $100h\,\mathrm{km\,s^{-1}\,Mpc^{-1}}$ means at a distance of 1 Mpc from us, galaxies recede with a speed of $100h$ km per second. The discussion in Chen et al. (2017) points out a number of reported deviations in the measurement of the Hubble Parameter.

The scale factor is set to unity today. The curvature of the Universe is determined by the relationship between the total density of the cosmic and the critical density. The Universe is spatially-flat if its total density, ρ is equal to the critical density $\rho_{\rm crt}$ (a function of time), has negative curvature (open – hyperbolic universe) if $\rho < \rho_{\rm crt}$, and positive curvature (closed – elliptic universe) if $\rho > \rho_{\rm crt}$. The scale factor $a(t)$ is regulated by the different Universe density components, and its evolution is modelled by the equation of state (EoS) $w_i = p_i/\rho_i$, with p_i being the pressure of the $i^{\rm th}$ Universe density component, ρ_i. Various Universe density components today, are defined in terms of critical density. In general for different energy density components of the Universe, $\Omega = \rho/\rho_{\rm crt}$, where ρ is the total Universe density made up of the mixture of different materials in the Universe. Each of the components (baryons, photons, and so on) in the mixture has its own density usually normalized relative to $\rho_{\rm crt}$, thus each component has its own Ω, with Ω_0 being the current value. Below, we describe these concepts quantitatively.

Consider the fluid Equation (1.1.82), in which density ρ and pressure p are functions of scale factor a, and the EoS parameter w, given by

$$p(\rho) = w\rho c^2. \tag{1.1.75}$$

We can use these two equations, together with the Friedmann equation (FRW) (Eq. (1.1.14)) to determine the relationship between time and other properties of the Universe, such as scale factor, density, and pressure and describe the cosmic evolution.

Applying approximations in Quasi-Newtonian fashion as described in Liddle and Lyth (2000), we can recover the FRW equation

$$\left(\frac{\dot{a}}{a}\right)^2 = \frac{8\pi G\rho}{3} - \frac{k}{a^2}, \tag{1.1.76}$$

which is basically the FRW Equation (1.1.14) without the Λ term.

To describe the dynamics of the isotropic and homogeneous universe, we need the fluid equation, so we adopt the approach by Liddle and Lyth (2000) and make use of the first law of thermodynamics

$$\mathrm{d}E + p\mathrm{d}V = T\mathrm{d}S, \tag{1.1.77}$$

applied to a unit co-moving radius volume V that is expanding, similar to applying thermodynamics to a gas in a piston. Energy is transferred as work but not as heat in adiabatic process, so the energy is given by

$$E = mc^2 \ (= cp) = \frac{4}{3}\pi a^3 \rho a^3 \ (m = V \times \rho), \tag{1.1.78}$$

where a is the physical radius of the volume. Using the chain rule, change of energy in a time $\mathrm{d}t$ is given by

$$\frac{\mathrm{d}E}{dt} = 4\pi a^2 \rho c^2 \frac{\mathrm{d}a}{\mathrm{d}t} + \frac{4}{3}\pi a^3 c^2 \frac{\mathrm{d}\rho}{\mathrm{d}t}, \tag{1.1.79}$$

and the volume change is

$$\frac{\mathrm{d}V}{\mathrm{d}t} = 4\pi a^2 \frac{\mathrm{d}a}{\mathrm{d}t}. \tag{1.1.80}$$

We assume a reversible expansion, and thus,

$$4\pi a^2 \rho c^2 \dot{a} + \frac{4}{3}\pi a^3 c^2 \dot{\rho} + p 4\pi a^2 \dot{a} = 0, \tag{1.1.81}$$

and finally obtain the fluid equation

$$\dot{\rho} + 3\frac{\dot{a}}{a}\left(\rho + \frac{p}{c^2}\right) = 0. \tag{1.1.82}$$

p/c^2 signifies the loss of energy as a result of work done by pressure due to the increase in the Universe volume. ρ is the dilution in the density following volume increase. The conservation of energy applies, since energy equivalent to the amount of work done has been lost from the fluid and transferred into gravitational potential.

Next we consider the acceleration equation. Using the FRW Equation (1.1.76) and the fluid Equation (1.1.82) we can obtain another equation

$$\frac{\ddot{a}}{a} = -\frac{4\pi G}{3}\left(\rho + \frac{3p}{c^2}\right), \tag{1.1.83}$$

which describes the acceleration of the scale factor. This equation is called acceleration equation and it implies an increase in pressure will increase gravitational force resulting in decelerated expansion.

The compositions of the density (ρ) parameter that appears in the Friedmann (FRW) equation can be a non-relativistic matter component, a radiation component, and a plausible vacuum energy or cosmological constant component. These components change with a scale factor a in different ways as the Universe expands, depending on the dominance of a certain component in a particular regime, as discussed below.

We first consider a **matter-dominated universe** by approximating the Universe as an ideal gas during this epoch in order to describe the evolution of ρ (and possibly pressure p and temperature T). For an ideal gas with N number of atoms (derivation adopted from Mo et al. (2010)) in a volume V,

$$pV = Nk_{\mathrm{b}}T, \tag{1.1.84}$$

where k_{B} is the Boltzmann constant. Then we have

$$\rho_{\mathrm{m}} = m\frac{N}{V}, \tag{1.1.85}$$

as an equation for (ideal) monatomic gas (atoms are not bound together), consisting of particles of mass m. Using relations (1.1.84 & 1.1.85) above, we get

$$p_{\mathrm{m}} = \frac{k_{\mathrm{B}}T}{m}\rho_{\mathrm{m}}. \tag{1.1.86}$$

Note that $\rho_{\rm m}$ and $p_{\rm m}$ are, respectively, the energy density and pressure of cold dust in the matter-dominated universe, and are different from ρ and p.

As a function of adiabatic index γ, the EoS can be written as (Mo et al., 2010)

$$p_{\rm m} = (\gamma - 1)(\rho - \rho_{\rm m})c^2, \tag{1.1.87}$$

where $\gamma = 5/3$ for monatomic gas. This equation is useful for determining the true EoS parameter w. We can then write

$$w = w(T) = \frac{k_{\rm B}T}{mc^2}\left(1 + \frac{1}{\gamma - 1}\frac{k_{\rm B}T}{mc^2}\right)^{-1} \tag{1.1.88}$$

by using (1.1.86) and (1.1.87). Then, we see that $w(T) << 1$ immediately follows from $k_{\rm B}T << mc^2$. Clearly, the rest-mass energy does not contribute to the gas pressure in the non-relativistic limit.

Therefore, a zero pressure ($w = 0$, the dimensionless number) well approximates a non-relativistic matter/gas, often referred to as cold dust fluid.

This means we can now model a non-relativistic matter-dominated universe for a cold dust, where $p = 0$; $\rho_m >> \rho_r$; $\Lambda = 0$ (the rate of expansion increases with a positive Λ term), and hence Equation (1.1.12) becomes

$$\frac{\ddot{a}}{a} + \frac{4\pi G}{3}\rho = 0, \tag{1.1.89}$$

$$-H^2\left(\frac{-\ddot{a}}{H^2 a}\right) + \frac{4\pi G}{3}\rho = 0, \tag{1.1.90}$$

$$-H^2 q + \frac{4\pi G}{3}\rho = 0, \tag{1.1.91}$$

$$\implies \rho = \frac{3H^2}{4\pi G}q. \tag{1.1.92}$$

Substituting (1.1.92) into Equation (1.1.76), we have

$$H^2 - 2H^2 q = -\frac{k}{a^2} \implies a^2H^2(1 - 2q) = -k. \tag{1.1.93}$$

Since for spatially-flat universe $k = 0$, and both $H,\ a \neq 0 \implies 1 - 2q = 0$ and so $q = \frac{1}{2}$. For closed universe, $k = 1, \implies q > \frac{1}{2}$, and for open universe, $k = -1, \implies q < \frac{1}{2}$.

From the relation (1.1.92), we get the critical density,

$$\rho_{\rm crt} = \frac{3H^2}{8\pi G}. \tag{1.1.94}$$

Critical density is defined as the density required to make the Universe flat. As a consequence of this density to the cosmic, the kinetic energy and the gravitational potential in the Universe would balance if it uniformly self-gravitates and isotropically expands at a rate H as if it is a

sphere of density $\rho_{\rm crt}$. Furthermore, the Universe and the critical densities are related by the parameter q as $\rho/\rho_{\rm crt} = 1/2q$, which implies $q = \rho/2\rho_{\rm crt}$. A universe with a density, $\rho = \rho_{\rm crt}$ and an expansion rate H is called an *Einstein de Sitter* universe. This universe model has $\Omega = 1$ at all times.

Continuing with our derivation, the fluid Equation (1.1.82) for the matter-dominated universe becomes

$$\dot{\rho} + 3\frac{\dot{a}}{a}\rho = 0; \tag{1.1.95}$$

multiplying by a^3,

$$a^3\dot{\rho} + 3\dot{a}a^2\rho = 0. \tag{1.1.96}$$

In differential form,

$$\frac{d}{dt}\left(a^3\rho\right) = 0, \tag{1.1.97}$$

implying

$$a^3\rho = \text{constant} = a_0^3\rho_0. \tag{1.1.98}$$

We can model the **radiation-dominated universe** as perfect/ideal fluid approximation with $p = \frac{1}{3}\rho$. Substituting $p = \frac{1}{3}\rho$ into the fluid Equation (1.1.82),

$$\frac{\mathrm{d}\rho}{\mathrm{d}t} + 3(\rho + p)\frac{\dot{a}}{a} = 0, \tag{1.1.99}$$

we obtain

$$\frac{\mathrm{d}}{\mathrm{d}t}(a^4\rho) = 0 \implies a^4\rho = a_0^4\rho_0 = \text{constant}. \tag{1.1.100}$$

According to the Hubble's expansion law, the galaxy's recession velocity increases with the distance from the observer. This means at the present time, $H_0 = \dot{a_0}/a_0$, where H_0 (Hubble's constant) is the current value of Hubble's parameter H.

Next, we model the **Λ-dominated universe** by introducing the parameter $\Omega_k(a) = \rho_k(a)/\rho_{\rm crt}(a)$ (curvature density, defined in terms of a) and consider the Friedmann equation at the present time

$$H_0^2 = H_0^2(\Omega_{\rm m,0} + \Omega_{\rm r,0} + \Omega_{\Lambda,0}) - kc^2, \tag{1.1.101}$$

from which we can write the curvature

$$kc^2 = H_0^2(\Omega_{\rm m,0} + \Omega_{\rm r,0} + \Omega_{\Lambda,0} - 1). \tag{1.1.102}$$

Introducing the curvature parameter, $\Omega_{k,0}$ (see also Equation (1.1.130)), we have

$$\Omega_{k,0} \equiv -\frac{kc^2}{H_0^2} = 1 - (\Omega_{\rm m,0} + \Omega_{\rm r,0} + \Omega_{\Lambda,0}). \tag{1.1.103}$$

Various energy densities scale differently with a scale factor a, in which the matter density scales as $1/a^3$, radiation as $1/a^4$, Ω_k as $1/a^2$ – according to the Equation (1.1.103), and Ω_Λ stays constant. Thus, we can write

$$H^2 = H_0^2 \left(\frac{\Omega_{\mathrm{m},0}}{a^3} + \frac{\Omega_{\mathrm{r},0}}{a^4} + \Omega_{\Lambda,0} + \frac{\Omega_{k,0}}{a^2} \right) = H_0^2 E^2(a), \tag{1.1.104}$$

where we have defined $E(a) = H(a)/H_0$ to be the dimensionless Hubble function, and at the present time, $a = 1$. If $\Omega_{\Lambda,0} = 1$ and $\Omega_{\mathrm{m},0} = \Omega_{\mathrm{r},0} = \Omega_{k,0} = 0$, then the Equation (1.1.104) becomes

$$\frac{\dot{a}}{a} = H_0, \tag{1.1.105}$$

and we see that the resulting equation above has no solution for $a = 0$ at $t = 0$, instead it yields a Universe that expands exponentially:

$$a(t) = e^{H_0 t}. \tag{1.1.106}$$

If we take $t = 0$ to be the present day time, the equation above implies the Universe's age is infinite in this case.

The recent measurements by *Planck* satellite shows that the spatial curvature is very small, therefore, the k term in the FRW Equation (1.1.76) can be neglected (or equivalently neglecting both the k and Λ terms in Equation (1.1.14)), and using the resulting equation together with the EoS (1.1.75) which accounts for the pressure in mass-density, we can solve the fluid Equation (1.1.82) to have

$$\ln(\rho) = \ln(c/a)^{3(1+w)} \implies \rho \propto a^{-3(1+w)}. \tag{1.1.107}$$

We see that, for radiation, matter and Λ dominated universes, respectively, density varies with the scale factor as $\rho \propto a^{-4}$ ($w = 1/3$), $\rho \propto a^{-3}$ ($w = 0$), and $\rho \propto a^0$ ($w = -1$) $\implies$ $\rho =$ constant. Substituting the relation (1.1.107) into Equation (1.1.76) (without the k term), we have

$$\left(\frac{\dot{a}}{a} \right)^2 = \frac{8\pi G}{3}\rho = \frac{8\pi G}{3} \cdot c a^{-3(1+w)} = c a^{-3(1+w)}, \tag{1.1.108}$$

where solving this equation and applying initial conditions, at the Big Bang ($t = 0$, $a = 0$), results into

$$a^{\frac{3}{2}(w+1)} = \frac{2}{3(w+1)} ct. \tag{1.1.109}$$

Again, for radiation, matter and Λ dominated universes, we have respectively,

$a^2 = (1/2)ct$, implying $a \propto t^{(1/2)}$; $a^{(3/2)} = (2/3)ct$, implying $a \propto t^{(2/3)}$; and $a \propto e^{H_0 t}$ (see arguments that results into Equation (1.1.106) above). Since the universe is homogeneous and isotropic, we can generalize these derivations to the Universe as a whole although they originate from applying thermodynamics to a small patch of the Universe. Let us summarize our results

obtained so far in the table below.

Radiation-dominated universe	Matter-dominated universe	Λ-dominated universe
$w = \frac{1}{3}$	$w = 0$	$w = -1$
$\rho_{\rm r} \propto a^{-4}$	$\rho_{\rm m} \propto a^{-3}$	$\rho_\Lambda \propto a^0$
$a \propto t^{\frac{1}{2}}$	$a \propto t^{\frac{2}{3}}$	$a \sim e^{H_0 t}$
$H \sim \frac{1}{2} t^{-1}$	$H \sim \frac{2}{3} t^{-1}$	$H \sim H_0$

Taking an example of the matter-dominated universe such that the redshift to a galaxy at some distance D is given by

$$a(t) = \frac{1}{1+z}, \tag{1.1.110}$$

$$\frac{a(t_0)}{t_0^{2/3}} = \frac{a(t)}{t^{2/3}} = \frac{(1+z)^{-1}}{t^{2/3}} \implies \frac{t}{t_0} = (1+z)^{-3/2}, \tag{1.1.111}$$

since the present day value of $a(t)$ is $a(t_0) = 1$. This implies the *Einstein de Sitter* universe in the past at some redshift z was equivalent to the universe when its age was a fraction $t/t_0 = (1+z)^{-3/2}$, where t_0 is the today's age of the Universe. The matter-dominated universe expands as $t^{2/3}$, and thus

$$H = \frac{\dot{a}}{a} = \frac{2}{3t}, \tag{1.1.112}$$

where t is the approximate age of the Universe. This means as $a \to 0,\ t \to 0,\ \rho \to \infty$. Therefore, the Universe was in an extremely dense condition in the beginning.

Next, we briefly describe a photon energy denoted by E, so that

$$E = h_{\rm p}\nu = h_{\rm p}\frac{c}{\lambda} \implies E \propto \frac{1}{\lambda},\ (h_{\rm p},\ c \text{ are constants}). \tag{1.1.113}$$

Here $h_{\rm p}$ is the Planck's constant, ν is the frequency, λ is the photon wavelength and c is the speed of light. The photon wavelength expands with the Universe. Therefore, as the Universe expands, each photon energy in the Universe (analogous to a 3-D cube), $E \propto c/a$, and the total energy density $\propto c/aa^3 = c/a^4$. We can then conclude as follows:

- As a increases, λ increases, energy decreases.
- As the Universe expands, photon energy scales as $1/a$.
- As the Universe expands, energy of all photons in it varies as $1/a^4$.

As we have already seen, for radiation-dominated universe, $a \propto t^{1/2}$, thus when an object is slow, its energy and rest-mass are the same.

The energy densities, contained in ρ that appears in the Friedmann equation are usually expressed in terms of mass densities, and we can, respectively, denote matter, radiation and cosmological constant compositions at any time t by $\rho_{\rm m},\ \rho_{\rm r},\ \rho_\Lambda$. This allows us to re-write the Friedmann Equation (1.1.14) for a scale factor $a_0 = a(t_0)$ with

$$\rho_{\rm m}(t) = \rho_{\rm m,0} a^{-3}(t);\ \rho_{\rm r}(t) = \rho_{\rm r,0} a^{-4}(t);\ \text{and}\ \rho_\Lambda(t) = \rho_\Lambda = \text{constant}, \tag{1.1.114}$$

at the present time as

$$\left(\frac{\dot{a}}{a}\right)^2 \equiv H^2(t) = \frac{8\pi G}{3}\left[\rho_{\rm m,0}\left(\frac{a_0}{a}\right)^3 + \rho_{\rm r,0}\left(\frac{a_0}{a}\right)^4 + \rho_{\Lambda,0}\right] - \frac{kc^2}{a^2}, \tag{1.1.115}$$

where the index "0" denotes the current time, $t = t_0$.

Since the Universe is in present time expanding, it is obvious that the Hubble constant today, $H_0 = \dot{a}_0/a_0 > 0$, and we see that by looking at the equation above, we can without necessarily solving the Friedmann equation explicitly, examine the different cases of the behaviours of $a(t)$ (see Mo et al. (2010)).

From the Friedmann Equation (1.1.14),

$$\begin{aligned} H^2 &= \frac{8\pi G}{3}\left(\rho + \frac{\Lambda c^2}{8\pi G}\right) - \frac{kc^2}{a^2} \\ &= \frac{8\pi G}{3}\left(\rho + \rho_\Lambda\right) - \frac{kc^2}{a^2}, \end{aligned} \tag{1.1.116}$$

where $H = \dot{a}/a$ and $\rho_\Lambda = \Lambda c^2/8\pi G$. We can write the density $\rho = \rho_{\rm m} + \rho_{\rm r}$, where $\rho_{\rm m}$ is the contribution from matter (baryons and cold dark matter), and $\rho_{\rm r}$ is the contribution from radiation.

We can think of matter density as composed of baryons matter $\rho_{\rm b}$ and cold dark matter $\rho_{\rm c}$ and write

$$\rho_{\rm m} = \rho_{\rm b} + \rho_{\rm c}, \tag{1.1.117}$$

and further write the radiation density as constituted of photons ρ_γ and neutrinos ρ_ν, thus

$$\rho_{\rm r} = \rho_\gamma + \rho_\nu. \tag{1.1.118}$$

In consideration of their scaling with a scale factor $a(t)$, the baryons density and the cold dark matter density behave identically; similarly, photons and neutrinos densities behave in a similar manner, so instead of splitting $\rho_{\rm m}$ and $\rho_{\rm r}$ into components, we retain $\rho_{\rm m}$ and $\rho_{\rm r}$ and re-write the Friedmann Equation (1.1.116) as

$$H^2 = \frac{8\pi G}{3}\left(\rho_{\rm m} + \rho_r + \rho_\Lambda\right) - \frac{kc^2}{a^2}. \tag{1.1.119}$$

If the total density $\rho_{\rm m} + \rho_r + \rho_\Lambda$ equals the critical density (1.1.94), then $k = 0$, implying that the Universe is spatially-flat. This also implies the Universe expands critically, following the

equivalence of the expansion rate and the curvature, k. Therefore, at the critical density, the Universe expands critically for a given value of H. Usually, H_0 and $\rho_{\mathrm{crt},0}$ denote the Hubble constant and the critical density at the present time, such that $\Omega_{\mathrm{i}}(a) = \rho_{\mathrm{i}}(a)/\rho_{\mathrm{crt}}(a)$ represents the values of different Universe mass-density quantities with respect to critical density, and the matter, radiation and Λ values at the present time are respectively; $\Omega_{\mathrm{m},0},\ \Omega_{\mathrm{r},0}$ and $\Omega_{\Lambda,0}$.

It is conventional to express the non-relativistic matter total rest-mass density in the Universe today as

$$\rho_{\mathrm{m},0} = \Omega_{\mathrm{m},0}\rho_{\mathrm{crt},0} \approx 1.88 \times 10^{-29}\Omega_{\mathrm{m},0}h^2\mathrm{gcm}^{-3}, \tag{1.1.120}$$

such that $\Omega_{\mathrm{m},0}$ is the non-relativistic matter dimensionless cosmic density parameter at the present time, and h is the reduced Hubble parameter given by

$$h \equiv \frac{H_0}{100\mathrm{kms}^{-1}\mathrm{Mpc}^{-1}}. \tag{1.1.121}$$

Some recent observational constraints estimate

$$\Omega_{\mathrm{m},0} = 0.27 \pm 0.05;\ h = 0.72 \pm 0.05. \tag{1.1.122}$$

The total relativistic component (CMB radiation, neutrinos) density is given by

$$\rho_{\mathrm{r},0} \approx 7.8 \times 10^{-34}\mathrm{gcm}^{-3};\ \Longrightarrow\ \Omega_{\mathrm{r},0} \simeq 1.68\Omega_{\mathrm{CMB}} \approx 4.2 \times 10^{-5}h^{-2}, \tag{1.1.123}$$

where $\Omega_{\mathrm{CMB}} \simeq 2.4 \times 10^{-5}h^{-2}$. CMB, a blackbody radiation at a temperature $T_\gamma = 2.725\,\mathrm{K}$ seems to dominate the present day non-relativistic component density.

We can express the redshift variation of the non-relativistic and relativistic energy densities ratio as

$$\frac{\rho_{\mathrm{m}}}{\rho_{\mathrm{r}}} \approx 2.4 \times 10^4\Omega_{\mathrm{m},0}h^2(1+z)^{-1}, \tag{1.1.124}$$

and at the matter-radiation equality, $\rho_{\mathrm{m}} = \rho_{\mathrm{r}}$, the corresponding redshift, z_{eq} is given by

$$1 + z_{\mathrm{eq}} \approx 2.4 \times 10^4\Omega_{\mathrm{m},0}h^2. \tag{1.1.125}$$

It turns out that the Universe had been matter-dominated since the epoch corresponding to z_{eq}, assuming that the Universe did not bounce in the recent past, for example, due to large cosmological constant, Λ.

The radiation density ρ_{r} evolves faster with the scale factor a than ρ_{m}, and similarly, at an epoch where the scale factor was

$$a_{\mathrm{eq}} = \frac{\Omega_{\mathrm{r}}}{\Omega_{\mathrm{m}}} \approx 4.2 \times 10^{-5}(\Omega_{\mathrm{m}}h^2)^{-1}, \tag{1.1.126}$$

matter and radiation had the same energy density. The redshift z_{eq}, a scale factor a_{eq} and their corresponding epochs have important roles to play in the cosmic history of the Universe's structure evolution as we shall see later.

Let us now re-write Equation (1.1.115) for any cosmic time t as

$$H^2(t) = H_0^2\left[\frac{\Omega_{\rm r}}{a^4(t)} + \frac{\Omega_{\rm m}}{a^3(t)} - \frac{kc^2}{H_0^2a^2(t)} + \Omega_\Lambda\right], \tag{1.1.127}$$

and then substitute the equation (see Schneider (2006)),

$$\begin{aligned} k &= \left(\frac{H_0}{c}\right)^2(\Omega_0 - 1) = \left(\frac{H_0}{c}\right)^2(\Omega_{\rm m} + \Omega_\Lambda + \Omega_{\rm r} - 1) \\ &\approx \left(\frac{H_0}{c}\right)^2(\Omega_{\rm m} + \Omega_\Lambda - 1), \end{aligned} \tag{1.1.128}$$

into Equation (1.1.127) above to yield

$$\begin{aligned} \left(\frac{\dot{a}}{a}\right)^2 &\equiv H^2(t) = H_0^2\left[\frac{\Omega_{\rm r}}{a^4(t)} + \frac{\Omega_{\rm m}}{a^3(t)} + \frac{(1-\Omega_{\rm m}-\Omega_\Lambda)}{a^2(t)} + \Omega_\Lambda\right] \\ &\equiv H_0^2E^2(t). \end{aligned} \tag{1.1.129}$$

We can equivalently use the curvature equation

$$\Omega_{k,0} = -\frac{kc^2}{H_0^2a_0^2} = 1 - \Omega_0, \tag{1.1.130}$$

for $\Omega_0 = \Omega_{\rm m,0} + \Omega_{\rm r,0} + \Omega_{\Lambda,0}$ and write

$$H^2(a) = H_0^2\left(\frac{\Omega_{\rm r,0}}{a^4} + \frac{\Omega_{\rm m,0}}{a^3} + \frac{\Omega_{k,0}}{a^2} + \Omega_{\Lambda,0}\right) \equiv H_0^2E^2(a). \tag{1.1.131}$$

From above, we see explicitly how each term on the right-hand side of Equation (1.1.129) variably depends on the scale factor a; this enables us to draw the following remarks:

- The first term becomes dominant for very small values of a, and the Universe is then radiation-dominated during that particular epochs.
- For slightly larger $a > a_{\rm eq}$ the Universe is matter-dominated, since during such epoch the pressureless term dominates.
- Universe can be curvature-dominated if $k \neq 0$ for larger values of a, since under such conditions, the third (the curvature) term dominates.
- The Universe will be vacuum energy (or cosmological constant)-dominated for very large values of a, since Λ dominates provided that it is not zero.

Again, we can draw a number of conclusions on the evolution and the expansion history of the cosmic by qualitatively analyzing and relating the different behaviours of the function $a(t)$ to the spatial/spacetime curvature k and various energy densities of the Universe.

Furthermore, upon substituting (1.1.130) into Equation (1.1.115), we get

$$\left(\frac{\dot{a}}{a}\right)^2 = \frac{H_0^2 8\pi G}{3H_0^2}\left[\rho_{\rm m,0}\left(\frac{a_0}{a}\right)^3 + \rho_{\rm r,0}\left(\frac{a_0}{a}\right)^4 + \rho_{\Lambda,0}\right] + H_0^2(1-\Omega_0)\left(\frac{a_0}{a}\right)^2. \tag{1.1.132}$$

Making the use of $a(z) = 1/(1+z)$ and considering the fact that at present time $a = a_0 = 1$, the equation above gives

$$\begin{aligned} H(z) \equiv \left(\frac{\dot{a}}{a}\right)(z) \quad &= H_0 \left[\Omega_{\Lambda,0} + (1-\Omega_0)(1+z)^2 + \Omega_{\mathrm{m},0}(1+z)^3 + \Omega_{\mathrm{r},0}(1+z)^4\right]^{1/2} \\ &= H_0 E(z). \end{aligned} \tag{1.1.133}$$

We can further define the cosmic density parameters at cosmic time t as

$$\Omega(t) = \frac{\rho(t)}{\rho_{\mathrm{crt}}(t)}, \tag{1.1.134}$$

and since $H^2(z) = H_0^2(z)E^2(z)$, by also considering how different energy densities scale with a scale factor, a, we have

$$\Omega_\Lambda(z) \equiv \frac{\rho_\Lambda(t)}{\rho_{\mathrm{crt}}(t)} = \frac{8\pi G}{3H^2}\rho_\Lambda = \frac{8\pi G}{3H_0^2 E^2(z)}\rho_\Lambda = \frac{\Omega_{\Lambda,0}}{E^2(z)}; \tag{1.1.135}$$

similarly,

$$\Omega_{\mathrm{m}}(z) = \frac{\Omega_{\mathrm{m},0}(1+z)^3}{E^2(z)}, \text{ and } \Omega_{\mathrm{r}}(z) = \frac{\Omega_{\mathrm{r},0}(1+z)^4}{E^2(z)}. \tag{1.1.136}$$

We can use Equations (1.1.133) - (1.1.136) to calculate at any given redshift, values of the parameters H, Ω_Λ, Ω_{m} and Ω_{r}, once we know their values at the present time.

However, we can write

$$\Omega(z) = \frac{1}{E^2(z)}\left[\Omega_{\Lambda,0} + \Omega_{\mathrm{m},0}(1+z)^3 + \Omega_{\mathrm{r}}(1+z)^4\right], \tag{1.1.137}$$

and from (1.1.133),

$$E^2(z) = \Omega_{\Lambda,0} + (1-\Omega_0)(1+z)^2 + \Omega_{\mathrm{m},0}(1+z)^3 + \Omega_{\mathrm{r},0}(1+z)^4, \tag{1.1.138}$$

where we finally arrive at

$$\begin{aligned} E^2(z)(1-\Omega(z)) \quad &= (1-\Omega_0)(1+z)^2 \\ &\implies \Omega(z) = \frac{(\Omega_0 - 1)(1+z)^2}{E^z}. \end{aligned} \tag{1.1.139}$$

It can be shown that $\Omega(z)$ tends close to unity at high redshifts provided that $\Omega_{\mathrm{m},0}$ or $\Omega_{\mathrm{r},0}$ are not zero, and this behaviour of $\Omega(z)$ approaching unity at high redshifts does not depend at all on the present day values of H_0, $\Omega_{\Lambda,0}$, $\Omega_{\mathrm{m},0}$, and $\Omega_{\mathrm{r},0}$. This suggests that, a total density parameter, $\Omega_0 \sim 1$ must had characterized in the beginning any non-zero matter or radiation content FRW universe, as we shall see under Subsection (1.1.6).

1.1.6 Inflation, the Horizon and the Flatness Problems

Inflation (Linde, 1982; Hawking, 1993; Kofman et al., 2002; Linde, 2005b,a) is a radical extension of the standard Big Bang model of the origin, evolutionary state and the fate of the Universe

hypothesized by a physicist Alan Guth in early 1980s (Guth, 1981). Inflation matches the time when the size of the Universe expansion actually accelerated, i.e., it quickly grew exponentially. Inflation lasted within the amount of time required to satisfy the observable universe conditions.

Inflation is currently seen and commonly considered as part or extension of the Big Bang, depicted as the period during which establishment of the preceding dynamics for the Big Bang, especially, the conditions of the hot tightly coupled early plasma of ions came into play (Tsujikawa, 2003). It was already accepted in the standard Big Bang cosmology, that the Universe expands uniformly (Freedman et al., 2001). But, in 1981 Guth proposed that when the Universe was about 10^{-36}s old, it inflated by a factor of 10^{26} – beyond the current size of the observable universe in a mere duration of about 10^{-33} to 10^{-32} seconds. This perplexing hypothetical radical expansion of the Universe phenomenon is famously known as **cosmic inflation**.

Inflation was purposefully introduced to address the problems found in the Big Bang cosmology, including, but not limited to the horizon and flatness problems (Guth, 1981; Linde, 1982; Hawking, 1993; East et al., 2016).

Light has a finite speed, this means our ability to observe the Universe is limited to a finite volume of the cosmos called the observable universe. Observable universe is thus comprised of the regions from which light originating from them can reach us after it travels a finite amount of time t_0. On average, the light that reaches us after traveling for time up to $t_0 \approx 13.8$ Gyr would be coming from the visible region of the Universe. This roughly marks the radius of the observable universe to be around 13.8 billion light-years. As a result, we will not be able to observe the part of the Universe which is more distant beyond this limit, i.e., from regions for which light emitted will never reach us. This region of the Universe beyond our observance experience is called a horizon. This scenario introduces some crucial problems in the Big Bang cosmology, and for this reason, inflation was introduced to rectify some of these overarching problems as we shall see subsequently. One of such problems is a horizon problem which we explain quantitatively (we adopt the approach by Schneider (2006); Mo et al. (2010)) as follows.

Light will travel a distance $c\mathrm{d}t$, where $\mathrm{d}t$ is a time interval and c is the speed of light. This distance is equivalent to a comoving distance

$$\mathrm{d}\chi = \frac{c\mathrm{d}t}{a}, \tag{1.1.140}$$

where a is a scale factor. Now, suppose that from the Big Bang to some redshift z equivalent to a physical time t, the comoving distance corresponding to a horizon distance H, that a light traverses is given by

$$r_{\mathrm{H,com}}(z) = \int_0^t \frac{c\mathrm{d}t}{a(t)}. \tag{1.1.141}$$

Since

$$\dot{a} = \frac{\mathrm{d}a}{\mathrm{d}t} \implies \mathrm{d}t = \frac{\mathrm{d}a}{\dot{a}} = \frac{\mathrm{d}a}{aH}, \tag{1.1.142}$$

we re-write the integral above as

$$r_{\mathrm{H,com}}(z) = \int_0^a \frac{c\mathrm{d}a}{a^2 H(a)} \equiv \int_0^{(1+z)^{-1}} \frac{c\mathrm{d}a}{a^2 H(a)}. \tag{1.1.143}$$

At some cosmic epoch where $z_{\mathrm{eq}} >> z >> 0$, the expansion rate H was dominated by the energy density corresponding to such regime, which is pressureless matter energy, and as a result, the integral (1.1.143) will have much of its contribution from times or equivalently values of a when matter dominates the Universe. It follows from Equation (1.1.131) that

$$H(a) \approx H_0 \sqrt{\Omega_m} a^{-3/2}, \tag{1.1.144}$$

and upon substituting this into (1.1.143), we get

$$r_{\mathrm{H,com}}(z) \approx 2\frac{c}{H_0}\frac{1}{\sqrt{(1+z)\Omega_{\mathrm{m}}}};\ z_{\mathrm{eq}} >> z >> 0. \tag{1.1.145}$$

In a like manner, expansion rate H is radiation-dominated at earlier times corresponding to $z >> z_{\mathrm{eq}}$, and hence during the time when the Universe is dominated by radiation,

$$H(a) \approx H_0 \frac{\sqrt{\Omega_{\mathrm{r}}}}{a^2}, \tag{1.1.146}$$

and thus the integral (1.1.143) yields

$$r_{\mathrm{H,com}}(z) \approx \frac{c}{H_0\sqrt{\Omega_{\mathrm{r}}}}\frac{1}{(1+z)};\ z >> z_{\mathrm{eq}}. \tag{1.1.147}$$

We should notice that during very earlier times corresponding to large values of z, the comoving horizon distance was smaller compared to that at later times.

Now, let us consider a physical proper length $r_{\mathrm{H,prop}}$ corresponding to the comoving distance $r_{\mathrm{H,com}}$, for which at recombination ($z = z_{\mathrm{rec}}$) the physical proper distance (horizon length at recombination) is given by

$$r_{\mathrm{H,prop}}(z_{\mathrm{rec}}) = a r_{\mathrm{H,com}}(z_{\mathrm{rec}}) = 2\frac{c}{H_0}\Omega_{\mathrm{m}}^{-1/2}(1+z_{\mathrm{rec}})^{-3/2}. \tag{1.1.148}$$

We want to calculate the sky angular size, $\theta_{\mathrm{H,rec}}$ corresponding to the proper length $r_{\mathrm{H,prop}}(z_{\mathrm{rec}})$, before we do so, let us lay down the underlying formalism.

We establish that, the angular-diameter distance of a distant object whose radius is R and covering a solid angle Ω is given by (Schneider, 2006)

$$D_{\mathrm{A}}(z) = \sqrt{\frac{R^2\pi}{\Omega}}. \tag{1.1.149}$$

The angular-diameter distance and other distance-redshift measurements are cosmological parameters dependent, and we can use this fact to determine the angular-diameter distance specifically for a particular model of the Universe. For a Universe model without a cosmological constant ($\Lambda = 0$) (Schneider, 2006),

$$D_{\mathrm{A}}(z) = \frac{c}{H_0}\frac{2}{\Omega_{\mathrm{m}}^2(1+z)^2} \times \left[\Omega_{\mathrm{m}} z + (\Omega_{\mathrm{m}} - 2)\left(\sqrt{1+\Omega_{\mathrm{m}}} - 1\right)\right]. \tag{1.1.150}$$

For the angular-diameter distance (1.1.149), in which here $D_{\rm A}$ is taken to the CMB surface of last scattering (recombination), the horizon length at recombination will correspond to the angular size on the sky given by

$$\theta_{\rm H,rec} = \frac{r_{\rm H,prop}(z_{\rm rec})}{D_{\rm A}(z_{\rm rec})}. \tag{1.1.151}$$

Using (1.1.150) for the case in which $\Omega_\Lambda = 0$ results to

$$D_{\rm A}(z) \approx \frac{c}{H_0}\frac{2}{\Omega_{\rm m} z}, \text{ for } z >> 1, \tag{1.1.152}$$

and therefore at the recombination epoch, $z_{\rm rec} \sim 1000$, we have

$$\theta_{\rm H,rec} \approx \sqrt{\frac{\Omega_{\rm m}}{z_{\rm rec}}} = \sqrt{\frac{\Omega_{\rm m}}{1000}} \simeq \sqrt{\Omega_{\rm m}} 2^\circ, \text{ for } \Omega_\Lambda = 0. \tag{1.1.153}$$

This means at recombination, the angle subtended by the horizon length on the sky is about 1°. It implies that, at early times, before recombination, many regions of the presently observable universe may not have been in causal contact. By causal contact, we mean these regions did not know each other, and hence there was no information exchange between them that could have influenced onto them similar conditions. We see that two regions that were able to exchange information before recombination, had spatially very smaller radius of separation compared to the region of space at recombination. Interestingly, during the time when the CMB photons lastly had interaction with matter, there was no exchange of information, for example, about temperatures, between the regions that were spatially separated by much larger radius, but surprisingly, the CMB temperature anisotropies measured today from these regions show the same fluctuations $\triangle T/T \sim 10^{-5}$, see more in Schneider (2006). This scenario is known as the horizon problem.

To address the horizon problem, we consider the inflationary theory which assumes that the vacuum energy density dominated the Hubble expansion during early epochs and it was very much larger compared to today. Thus, during such time when the vacuum energy and the Hubble expansion dominated the Universe, we obtain

$$\left(\frac{\dot{a}}{a}\right)^2 = \frac{\Lambda c^2}{3} \tag{1.1.154}$$

from the Friedmann Equation (1.1.14), which implies the Universe is exponentially expanding,

$$a(t) = A\exp\left(c\sqrt{\frac{\Lambda}{3}}t\right), \tag{1.1.155}$$

where A is some constant. It is assumed that the phase transition (reheating) occurred at some epoch in the distant past where there was a transformation from vacuum energy to radiation and normal matter, ending the exponential expansion of the Universe, and marking the inception of the FRW universe evolution.

Next we consider the flatness problem (adopted from Schneider (2006)). We can generalize the definition of the cosmic density (1.1.134) parameter for different time epochs corresponding to an arbitrary redshift z,

$$\Omega_0(z) = \frac{\rho_{\rm m}(z) + \rho_{\rm r}(z) + \rho_\Lambda}{\rho_{\rm crt}(z)}, \tag{1.1.156}$$

where at various epochs we would assume different values of the Hubble expansion rate and the energy densities. Note that the critical density

$$\rho_{\rm crt} = \frac{3H^2(z)}{8\pi G} \tag{1.1.157}$$

is also a function of redshift z. Substituting the scale factor-energy densities relations (1.1.114) into (1.1.156), we obtain

$$\Omega_0(z) = \left(\frac{H_0}{H}\right)^2 \left(\frac{\Omega_{\rm r}}{a^4} + \frac{\Omega_{\rm m}}{a^3} + \Omega_\Lambda\right), \tag{1.1.158}$$

where using (1.1.129) we finally get

$$1 - \Omega_0(z) = F[1 - \Omega_0(0)], \tag{1.1.159}$$

such that

$$F = \left(\frac{H_0}{aH(a)}\right)^2, \tag{1.1.160}$$

and $\Omega_0(0)$ is the total cosmic density parameter today.

Close examination of (1.1.159) suggests that for all values of a, $F > 0$, and consequently, for all cosmic epochs up to today, the sign of the quantity $(\Omega_0 - 1)$ will be the same and preserved throughout the cosmic evolution. It then follows from (1.1.128) that the sign of $(\Omega_0 - 1)$ determines the sign of curvature which is also preserved throughout the cosmic history. It can be established from the analysis of F that at early times, for example, $z >> z_{\rm eq}$ to radiation-dominated universe, the Universe will be flat, however, the curvature of the closed universe for which $k > 0$ will always remain positive. As as result F becomes extremely small at early epochs, evidenced by (1.1.129) which yields

$$F = \frac{1}{\Omega_{\rm r}(1+z)^2}. \tag{1.1.161}$$

Therefore, very small values of F at high redshifts, require the condition that $\Omega_0(z)$ was very close to unity at early times to hold. At $z \sim 10^{10}$, for example, the condition $|\Omega_0 - 1| \lesssim 10^{-15}$ must hold. Flatness problem therefore calls for a fine tuning of the cosmic density parameter, for which at earlier ages it must had been very close to 1 if its order today has to be unity.

Inflation solves the flatness problem as well since any initial curvature will be flattened due to the radical expansion of the Universe. We thus have

$$\Omega_\Lambda = \frac{\Lambda}{3H^2} = 1 \tag{1.1.162}$$

during the inflationary phase. For complete dominance of the vacuum energy during such epoch, it is assumed that the inflation had to last long enough, where $\Omega_0 = 1$ by the time it halts, hence making the Universe flat as expected.

1.2 Large-Scale Structures of the Universe

A spatially-flat universe is largely composed of dark matter and dark energy, with a little amount of baryonic matter. The Universe's rich structure formation is a result of generation and amplified evolution of gravitational instability seeded by quantum mechanical perturbations when the Universe's age was a tiny fraction of a second old (Kiefer and Polarski, 2008).

Although today's description of structure formation is classical fluctuations, the primordial inflationary perturbations are assumed to be quantum. This is seemingly a contradictory scenario, but the paradigm shift in view of the structure formation from the physics that set forth incredibly small fluctuations to classical treatment of the subject has been explained in Kiefer and Polarski (2008). The inflationary model is an attempt to provide solutions to a number of fundamental problems arising from the Big Bang cosmology (Liddle and Lyth, 2000).

The inflationary theory prediction is somewhat supported by current observations, and yet to be vigorously tested observationally by future experiments. A well-established gravity theory of general relativity expounds how the present observable universe structures: galaxies, galaxy groups, galaxy clusters, and galaxy superclusters emanated from small inhomogeneities. The clearly inhomogeneous Universe as seen today is evidenced by among other things, the presence of uneven distribution and clustering of galaxies. However, lack of knowledge of the true nature of the major Universe energy density compositions, namely dark energy and dark matter makes this theory uncertain. The gravitational amplification of the structure depends on the dark energy EoS, (dark) matter content, and their properties such as the pressure forces. The discovery of nonluminous constituents in the Universe energy density composition such as the dark energy candidate follows an assertion that the Universe contains more components than the baryonic matter that we can see as probed by the distant supernovae measurements of accelerated expansion of the Universe (Riess et al., 1998; Perlmutter et al., 1999) and redshifted galaxies as seen by Edwin Hubble in 1929. The best candidate that explains the structure growth is the linear perturbation theory (Mukhanov et al., 1992; Bernardeau et al., 2002).

Most of the cosmological tests are conducted based on the geometry and growth of the structure. These prominent approaches use luminosity distances and angular diameter distances. Major probes include Type Ia Supernovae and CMB which rely on the geometry of the Universe; and baryonic acoustic oscillations (BAOs) (the imprints of the oscillatory patterns (fluctuations) of the acoustic waves on both CMB and the galaxy distribution), secondary anisotropies, cluster counts and clustering, relativistic effects such as redshift space distortions (RSDs), and weak gravitational lensing which are based on the structure growth, although some of these approaches include geometry implicitly. RSDs use information on how galaxies move. See galaxy formation and evolution by Mo et al. (2010).

A nearly perfect Gaussian spectrum of primordial fluctuations has been predicted by standard inflationary models with a single inflaton potential (Guth and Pi, 1982; Starobinsky, 1982; Bardeen et al., 1983; Mukhanov et al., 1992). Therefore, a complete description of the Gaussian

random fields can be given by the statistics of the two-point correlation function in real space and power spectrum in Fourier space, which have been widely applied to study the early universe physics from the CMB measurements and large-scale structures (Yoo et al., 2009).

Let us now consider a random field $f(\vec{x})$, where $\vec{x}$ denotes comoving spatial positions, in which at each point $f(\vec{x})$, $\langle f(\vec{x})\rangle = 0$ is some random number whose ensemble average is zero. If $P[f(\vec{x})]$ is a functional probability of some field configuration realization, we can define the two-point correlator as follows:

$$\xi(\vec{x}_i, \vec{x}_j) \equiv \langle f(\vec{x}_i) f(\vec{x}_j)\rangle = \int DP[f] f(\vec{x}_i) f(\vec{x}_j), \tag{1.2.1}$$

where on the right-hand side of (1.2.1) we have applied over field configuration a functional (path) integral. Statistical homogeneity implies invariance under spatial translation, so the translated field

$$T_a f(\vec{x}) \equiv f(\vec{x} - a) \tag{1.2.2}$$

and the original field have the same statistical properties, that is

$$P[f(\vec{x})] = P[T_a f(\vec{x})]. \tag{1.2.3}$$

Such statistical properties are also preserved for the two-point correlation function, thus

$$\xi(\vec{x}_i, \vec{x}_j) = \xi(\vec{x}_i - a, \vec{x}_j - a) \text{ for all } a; \implies \xi(\vec{x}_i, \vec{x}_j) = \xi(\vec{x}_i - \vec{x}_j). \tag{1.2.4}$$

Similarly, statistical invariance to spatial rotation applies, where the rotated field (R is a rotation matrix)

$$Rf(\vec{x}) \equiv f(R^{-1}\vec{x}) \tag{1.2.5}$$

has the same statistical properties as the original field, that is

$$P[f(\vec{x})] = P[Rf(\vec{x})], \tag{1.2.6}$$

and the two point correlator becomes

$$\xi(\vec{x}_i, \vec{x}_j) = \xi\Big(R^{-1}\vec{x}_i, R^{-1}\vec{x}_j\Big) \ \forall R. \tag{1.2.7}$$

Finally, combining statistical invariance under spatial translation and spatial rotation, we have

$$\xi(\vec{x}_i, \vec{x}_j) = \xi\Big(R^{-1}(\vec{x}_i, \vec{x}_j)\Big) \ \forall R; \implies \xi(\vec{x}_i, \vec{x}_j) = \xi(|\vec{x}_i - \vec{x}_j|). \tag{1.2.8}$$

This means the two-point correlation function will only depend on the separation distance between the two points.

The power spectrum (in Fourier space) or power spectral density and the two-point correlation (in real space) function are the quadratic statistics that can be used to measure the spatial clustering of galaxies (see early advancements on spatial clustering (Neyman and Scott, 1952)).

Spatial $\xi(r)$ or angular $\omega(\theta)$ galaxies distribution as the degree of clustering is measured by a galaxy correlation function (Postman et al., 1998; Alexander et al., 2012). We will see in a sequel that the matter (angular) power spectrum is the Fourier transform of this correlation function or equally, the correlation function is the inverse Fourier transform of the matter power spectrum (Mo et al., 2010). The spatial two-point correlation or autocorrelation function, $\xi(r)$ is defined as the probability over the expected unclustered random Poisson probability distribution, of finding a pair of galaxies, one in an element of volume δV_1 and another in an element of volume δV_2 where δV_1 and δV_2 are separated by a physical distance r (Coil et al., 2004; Alexander et al., 2012). To quantitatively grasp the concept of galaxy clustering correlation function, suppose that two small regions, δV_1, δV_2 separated by a physical distance r_{12}, each contains one galaxy in them, then the excess probability over the expected number of galaxy pairs is given

$$\langle n_{\text{pair}} \rangle \equiv \delta P = \bar{n}^2 \Big[1 + \xi(r_{12})\Big] \delta V_1 \delta V_2, \tag{1.2.9}$$

where $\bar{n}$ is the mean number of galaxies per unit volume. Galaxies are clustered if $\xi(r) = 0$, and on such scale, δP (expected number of pairs) simply becomes the product of the expected number of galaxies in the two regions, δV_1 and δV_2. Galaxy strong clustering and anti-clustering, respectively, correspond to $\xi(r) > 0$ and $\xi(r) < 0$, see Coil et al. (2004); Alexander et al. (2012); Coil (2013) and the references therein.

The spatial correlation function can be described in terms of a simple power law

$$\xi(r) = \left(\frac{r_0}{r}\right)^{-\gamma}, \tag{1.2.10}$$

on small scales $\sim 0.1h^{-1}\,\text{Mpc} \leq r \leq 10h^{-1}\,\text{Mpc}$, where the slope $\gamma \sim 1.8$ and correlation length $r_0 \sim 5h^{-1}\,\text{Mpc}$ (Zehavi et al., 2005; Alexander et al., 2012).

Angular galaxy distribution and clustering is measured by the two-point angular correlation function, $\omega(\theta)$. For the solid angle elements $\delta\Omega_1$ and $\delta\Omega_2$ separated by an angle θ, Georgakakis et al. (2000) defines the two-point angular correlation function as the joint probability δP of finding sources within such solid angle elements, given by

$$\delta P = N^2 \Big(1 + \omega(\theta)\Big) \delta\Omega_1 \delta\Omega_2 \tag{1.2.11}$$

where N is the galaxies' mean surface density. Similar to the two-point spatial correlation function, the angular correlation function measures the excess probability of the galaxy density over that expected for a random distribution (Georgakakis et al., 2000). $\omega(\theta) = 0$, implies sources are randomly distributed. Where an amplitude A_ω depends on the galaxy sample depth, the two-point angular correlation function can also be described by variants of a power law (Maddox et al., 1990; Postman et al., 1998; Georgakakis et al., 2000), more or less similar to

$$\omega(\theta) = A_\omega \theta^{1-\gamma}. \tag{1.2.12}$$

See also calculations of the angular autocorrelation function $\omega(\theta)$ using the Landy & Szalay (1993) estimator (Postman et al., 1998; Georgakakis et al., 2000; Coil et al., 2004; Alexander et al., 2012).

Next, we adopt the discussion presented in Mo et al. (2010) to derive/devise a way of describing the cosmological overdensity field $\rho(\vec{x})$ at some particular (random) epoch of time. Let us translate the observed galaxy density field $\rho(\vec{x})$ to dimensionless overdensity

$$\delta(\vec{x}) = \frac{\rho(\vec{x})}{\bar{\rho}(\vec{x})} - 1 \tag{1.2.13}$$

where $\bar{\rho}(\vec{x})$ is the background mean (the expected mean density). The idea is to find an approach to describing the cosmological overdensity field $\delta(\vec{x}, t)$ without going through a labourers work of determining the actual value of δ at each spatial location in the spacetime (x, t). Therefore, we can describe the density field $\delta(\vec{x}, t)$ by using the probability distribution

$$P(\delta_1, \delta_1, \ldots, \delta_N)\mathrm{d}\delta_1\mathrm{d}\delta_2 \ldots \mathrm{d}\delta_N, \tag{1.2.14}$$

such that $\delta_1 = \delta(\vec{x}_1),\ \delta_2 = \delta(\vec{x}_2),\ \ldots, \delta_N = \delta(\vec{x}_N)$.

The rather complicated probability distribution function (1.2.14) – bearing in mind N is infinitely very large, can describe the random processes underlying the density field $\delta(\vec{x})$.

This is especially possible because the cosmological (over)density field $\delta(\vec{x})$ is assumed to be a result of some random processes in the early universe, the most viable candidate being quantum fluctuations during inflation. Instead of directly using the probability distribution, a simple approach would then be to equivalently use the moments of this probability distribution function to describe the density field. In a statistical sense, we can therefore completely specify the distribution function (1.2.14) using infinitely many number of moments

$$\delta_1^{l_1},\ \delta_2^{l_2}, \ldots, \delta_N^{l_N} \tag{1.2.15}$$

of the probability distribution P by applying the relation

$$\langle \delta_1^{l_1}\delta_2^{l_2} \ldots \delta_N^{l_N} \rangle = \int \delta_1^{l_1}\delta_2^{l_2} \ldots \delta_N^{l_N} P(\delta_1, \delta_2, \ldots, \delta_N)\mathrm{d}\delta_1\mathrm{d}\delta_2, \ldots \mathrm{d}\delta_N. \tag{1.2.16}$$

We could describe the probability distribution for the average overdensity at each spatial location $\delta(\vec{x})$ of this field over which such random process realizations occurred if we had many universes. But, we only have one Universe realization of the random process. So, in the context of the Ergodic hypothesis, the ensemble average is equivalent to spatially averaging over one random field realization. This ensemble average as stipulated by the Ergodic hypothesis can be thought of as an average over independent sub-volumes of the same Universe. We can think of the ensemble average, $\langle \delta \rangle$ as an expectation value, quantum expectation value or an average over a classical ensemble.

Now, the first moment that specifies the probability distribution function above in regard to the Ergodic hypothesis which requires sufficiently rapidly decaying in spatial correlations as the separation increases so that many volumes V that are statistically independent may exist in one realization of the Universe (Mo et al., 2010) is given by

$$\langle \delta \rangle = \int \delta P(\delta)\mathrm{d}\delta = \frac{1}{V}\int_V \delta(\vec{x})\mathrm{d}\vec{x} = 0. \tag{1.2.17}$$

As stated above, this hypothesis simply allows for the existence of many statistically independent volumes in one realization. However, we would in principle require infinitely many moments to completely describe the probability distribution function of the cosmological density field $\delta(\vec{x})$. To make this requirement less tedious, we will adopt a somewhat scientifically substantiated belief that the initial cosmological density field was a random Gaussian field. This assumption takes us to the next step about explaining this field.

A Gaussian random field $\delta(\vec{x})$ values are distributed at an arbitrary set of N points as a multivariate (an N-variate) Gaussian. We can define a Gaussian random field as

$$P(\delta_1, \delta_2, \ldots, \delta_N) = \frac{e^{-Q}}{[(2\pi)^N \det(C)]^{1/2}} \tag{1.2.18}$$

where $Q = 1/2 \sum_{i,j} \delta_i (C^{-1})_{ij} \delta_j$ is computed as a sum over all possible pairs of points i, j, and C is just a covariance matrix, which is basically a second moment, and is related to the two-point correlation function as

$$C_{ij} = \langle \delta_i \delta_j \rangle \equiv \xi(r_{ij}), \tag{1.2.19}$$

where the two-point correlation function has been defined as $\xi(\vec{r}) = \langle \delta(\vec{x}) \delta(\vec{x} + \vec{r}) \rangle$, and for isotropic and homogeneous field, $r_{12} = |\vec{x}_1 - \vec{x}_2|$, meaning that the correlation function only relies on separation between two points, and not the absolute positions in the coordinate system. This correlation function only holds for a continuous field $\delta(\vec{x})$. In practice, galaxy distribution which is of our interest, is to a large extent a discrete field (rather than continuous), thus the two-point correlation function for the galaxy pointwise distribution is given by (recall the previous discussion under this Section),

$$1 + \xi(r) = \frac{n_{\text{pair}}(r \pm \mathrm{d}r)}{n_{\text{random}}(r \pm \mathrm{d}r)}, \tag{1.2.20}$$

where n_{pair} and n_{random}, respectively, denotes the expected number of galaxy pair distribution and the expected random distribution of galaxy pairs.

We see that the covariance matrix is simply given another name, the two-point correlation function. So the N-point probability distribution function, $P(\delta_1, \delta_2, \ldots, \delta_N)$ that would need to be represented by an infinite number of moments is now completely replaced by only a second moment, which is the two-point correlation function.

Let us under this Section, finally consider the matter power spectrum. The matter power spectrum (Kolb and Turner, 1990; Dodelson, 2003) is a prominent tool for describing the density contrast field of the Universe in terms of scale (such as angular scale). As previously pointed, this is the Fourier transform of the matter correlation function which we can use to model the amplitudes of the primordial fluctuations.

On large scales, there is a trade-off between gravity and the cosmic expansion, and structures growth seem to follow a linear theory, the density contrast field is assumed to be Gaussian and can be correctly described by the matter power spectrum. Description of the full field at small

scales requires higher-order statistics. CMB Planck spectrum, for example, carries primordial fluctuation information that informs us about matter density perturbations at $z \sim 1100$.

In general, statistical properties such as the power spectrum can be used to describe the matter density fluctuations. These fluctuations can be the matter-energy density of the Universe, $\rho(\vec{x})$, the temperature, T or the gravitational potential, Φ.

Let the Fourier transform of the mass-energy distribution density field $f(\vec{x})$ be defined by

$$F(\vec{k}) = \int \frac{\mathrm{d}^3\vec{x}}{(2\pi)^{3/2}} f(\vec{x}) e^{-i\vec{k}\cdot\vec{x}}. \tag{1.2.21}$$

Here, $F(k)$ has dimensions of Length^3, and for real fields, $F(\vec{k}) = F^*(-\vec{k})$. Let us also define the corresponding Fourier inverse transform as

$$f(\vec{x}) = \int \frac{\mathrm{d}^3\vec{k}}{(2\pi)^{3/2}} F(\vec{k}) e^{i\vec{k}\cdot\vec{x}}, \tag{1.2.22}$$

where $f(\vec{x})$ is dimensionless. Then the Fourier transform for the two-point correlation function is given by

$$\langle f(\vec{x}) f(\vec{y})\rangle = \int \frac{\mathrm{d}^3\vec{k}}{(2\pi)^{3/2}} \frac{\mathrm{d}^3\vec{k}'}{(2\pi)^{3/2}} \langle F(\vec{k}) F^*(\vec{k}')\rangle e^{i\vec{k}\cdot\vec{x}} e^{-i\vec{k}'\cdot\vec{y}}. \tag{1.2.23}$$

One can admit that, the power spectrum $P(k)$ of a rotational invariant and a translational invariant Universe's mass-energy distribution density field, $f(\vec{x})$ is defined by the relation

$$\langle F(\vec{k}) F^*(\vec{k}')\rangle = \frac{2\pi^2}{k^3} P(k) \delta^D(\vec{k} - \vec{k}'), \tag{1.2.24}$$

where the Dirac delta function, $\delta^D(\vec{k} - \vec{k}')$ is expressed as

$$\delta^D(\vec{k} - \vec{k}') = \frac{1}{(2\pi)^3} \int e^{\pm i(\vec{k}-\vec{k}')\cdot\vec{x}} \mathrm{d}^3\vec{x}. \tag{1.2.25}$$

From the power spectrum definition (1.2.24), k-modes are uncorrelated, the normalization factor $2\pi^2/k^3$ is conventional, and has a role of making $P(k)$ dimensionless, just as the field$f(\vec{x})$.

It can further be deduced that

$$\xi(r) = \langle f(\vec{x}) f(\vec{y})\rangle = \int \mathrm{d}k k^2 P(k) \frac{\sin(kr)}{kr}, \tag{1.2.26}$$

where $j_0(kr) = \sin(kr)/kr$ is the spherical Bessel function of the first kind of order zero.

We conclude that, in general, the coefficient $P(k)$ in the Fourier transform of the two-point correlation function to k-space ($k = 2\pi/\lambda$), with $r = 0$ or equivalently $\vec{x} = \vec{y}$ is called power spectrum. That is, the two-point correlation function is the Fourier transform of the matter power spectrum.

In cosmology, the notation $\xi(r) = \langle \delta(\vec{x})\delta(\vec{y})\rangle$ is commonly favored instead of $\xi(r) = \langle f(\vec{x}) f(\vec{y})\rangle$. Thus, for density field $\delta(\vec{x}, t)$, it is often convenient to work with Fourier components, denoted

by δ. Using this preferred convention, it can be equivalently shown that, the matter power spectrum is the Fourier transform of the two-point correlation function:

$$\begin{aligned} P(\vec{k}) &\equiv V\langle|\delta_{\vec{k}}|^2\rangle \\ &= \int \xi(\vec{x})e^{-i\vec{k}\cdot\vec{x}}\mathrm{d}^3\vec{x} \\ &= 4\pi\int \xi(r)\frac{\sin(kr)}{kr}r^2\mathrm{d}r, \end{aligned} \tag{1.2.27}$$

where for the volume V at which the Universe is assumed to be periodic,

$$\delta_{\vec{k}} = \frac{1}{V}\int \delta(\vec{x})e^{-i\vec{k}\cdot\vec{x}}\mathrm{d}^3\vec{x}, \tag{1.2.28}$$

such that the perturbed density field written as a sum of plane waves (of different wave numbers k, called modes) is given by

$$\delta(\vec{x}) = \sum_k \delta_{\vec{k}}e^{+i\vec{k}\cdot\vec{x}}. \tag{1.2.29}$$

As we have already assumed, we see that, at early times or equivalently on large Universe scales, the density field $\delta(\vec{x},t)$ has a distribution that has been predicted to be Gaussian random, and thus it can completely be described by either, the power spectrum $P(k)$ (has units of volume) or in the same manner by the two-point correlation function $\xi(r)$, see Einasto et al. (1993).

Let us now use the standard conventions used in cosmology to describe the matter density field, $\delta(\vec{x})$ at any epoch of time, t, or equivalently, z or a. We can always express the Universe matter density fluctuation in terms of the average density and the local density, given by $\rho(\vec{x}) = \bar{\rho}(1+\delta(\vec{x}))$, where $\bar{\rho}$ is the mean density, and the density contrast

$$\delta(\vec{x}) = \frac{\rho(\vec{x})-\bar{\rho}}{\bar{\rho}}, \tag{1.2.30}$$

can be expanded in Fourier modes as

$$\delta(\vec{x}) \equiv \frac{V}{(2\pi)^3}\int_{\mathrm{vol}} \delta(\vec{k})e^{-i\vec{k}\cdot\vec{x}}\mathrm{d}^3\vec{k}, \tag{1.2.31}$$

such that

$$\delta(\vec{k}) \equiv \frac{1}{V}\int_{\mathrm{vol}} \mathrm{d}^3\vec{x}\delta(\vec{x})e^{+i\vec{k}\cdot\vec{x}}, \tag{1.2.32}$$

and $\vec{x}$ are the co-moving coordinates. We can then define the power spectrum using the auto-correlation function $\delta(\vec{x})$ via the relation

$$\langle\delta(\vec{x})\delta(\vec{x})\rangle \quad = \frac{1}{V}\int_0^\infty \frac{\mathrm{d}k}{k}\frac{k^3|\delta^2(\vec{k})|}{2\pi^2}, \tag{1.2.33}$$

$$= \frac{1}{V}\int_0^\infty \frac{\mathrm{d}k}{k}\frac{k^3P(k)}{2\pi^2} = \frac{1}{V}\int \frac{\mathrm{d}k}{k}\triangle^2(k), \tag{1.2.34}$$

where $\triangle^2(k)$ is called the dimensionless power spectrum. In the theory of structure formation, the dimensionless power spectrum has a virtue of measuring perturbations contribution to the fractional variance in the matter density fluctuations, per unit logarithmic interval at wavenumber k (see Peacock and Nicholson (1991)).

Instead of using Fourier transform conventions to work with infinite space, we can consider a finitely large volume V of the Universe with periodic boundary conditions and then decompose $\delta(\vec{x}, t)$ in terms of plane waves

$$\delta(\vec{x}, t) = \frac{V}{(2\pi)^3} \sum \delta_{\vec{k}} e^{i\vec{k}\cdot\vec{x}}. \tag{1.2.35}$$

Thus the matter density field in Fourier space is given by

$$\delta(\vec{k}, t) = \int \mathrm{d}^3\vec{x}\delta(\vec{x}, t)e^{-i\vec{k}\cdot\vec{x}} \equiv \frac{V}{(2\pi)^3} \sum_{\vec{k}'} \delta_{\vec{k}'}(t) \int \mathrm{d}^3\vec{x} e^{i(\vec{k}'-\vec{k})\cdot\vec{x}}. \tag{1.2.36}$$

Using the Dirac delta function

$$\delta^D(\vec{p}) = \frac{1}{(2\pi)^3} \int \mathrm{d}^3\vec{x} e^{-i\vec{p}\cdot\vec{x}}, \tag{1.2.37}$$

we get the Fourier transform of the density contrast,

$$\delta_{\vec{k}}(t) = \frac{1}{V} \int \delta(\vec{x}, t)e^{-i\vec{k}\cdot\vec{x}} \mathrm{d}^3\vec{x}, \tag{1.2.38}$$

where the density contrast power spectrum is

$$P(k, t) = |\delta_{\vec{k}}(t)|^2, \tag{1.2.39}$$

and since we have assumed a homogeneous universe, the power spectrum is a function of k. For a wavelength λ_{eq} matching the size of horizon at the matter-radiation equality time t_{eq}, the power spectrum is expected to have a peak at $k_{\mathrm{eq}} = 2\pi/\lambda_{\mathrm{eq}}$.

Under the assumption of homogeneity, the equivalent two-point correlation function as for the power spectrum $P(k)$ is a function of r (not $\vec{r}$) and is given by

$$\xi(r) = \frac{1}{V} \int \mathrm{d}^3\vec{x}\delta^*(\vec{x} - \vec{r})\delta(\vec{x}). \tag{1.2.40}$$

The two-point correlation function as we have previously seen is the inverse Fourier transform of the power spectrum:

$$\xi(r) = \frac{V}{(2\pi)^3} \sum_{\vec{k}} P(k)e^{-i\vec{k}\cdot\vec{r}}. \tag{1.2.41}$$

Note that both $\delta(\vec{x})$ and $\delta_{\vec{k}}$ are unitless. Furthermore, the cosmological matter density field becomes a discrete sum over Fourier modes $\delta_{\vec{k}} = a_{\vec{k}} + ib_{\vec{k}} = |\delta_{\vec{k}}|e^{i\theta_k}$; $|\delta_{\vec{k}}|$ are amplitudes, θ_k are phases which make the field Gaussian if they are uncorrelated, where $\vec{k} = 2\pi/L(i_x, i_y, i_z)$, $i = 1, 2, \ldots, N$. Since $\delta(\vec{x})$ is real, it follows that $\delta^*_{\vec{k}} = \delta_{\vec{k}}$, and thus $a_{\vec{k}} = a_{-\vec{k}}$, $b_{\vec{k}} = -b_{-\vec{k}}$, implying that we can fully describe the cosmological density field $\delta(\vec{x})$ by only using Fourier modes in the upper-half of the space, $[0, \infty)$. Note also that, $\delta^*_{\vec{k}}$ is a complex conjugate of $\delta_{\vec{k}}$.

The power spectrum models the density field fluctuations root mean square (*rms*), $(\delta\rho/\rho)^2$ as a function of scale, making it a tool that measures directly how different scales contribute to the $(\delta\rho/\rho)$. $P(k)$ is fundamental, and in a Gaussian random fluctuation field, it can describe any statistical quantity. For example, the one-point distribution of the density field $\delta(\vec{x})$ is Gaussian,

$$P(\delta) = \left(2\pi\sigma^2\right)^{-1/2} e^{-\delta^2/2\sigma^2}, \tag{1.2.42}$$

where the variance of the density perturbation field is given by

$$\sigma^2 = \langle\delta^2\rangle = \int_0^\infty 4\pi k^2 P(k)\mathrm{d}k = \xi(0). \tag{1.2.43}$$

We can determine whether and when perturbations started to grow into non-linear stage by monitoring the evolution of the density field via power spectrum. For example, the analysis of the Jeans equations (Bonnor, 1957) in the expanding universe indicates that perturbations started to grow into structures when $|\delta_{\vec{k}}|^2 > 1$. It can be found that, growing modes solutions exist for $k < k_J$ which offer the possibility of describing the large-scale structures of the Universe observed today (Bretón et al., 2004).

For a particular perturbation mode λ related to a co-moving wavenumber $k = 2\pi/\lambda$, the *rms* for the density fluctuation $\delta\rho/\rho$ can be written as

$$\left(\frac{\delta\rho}{\rho}\right)^2 \equiv \langle\delta(\vec{x})\delta(\vec{x})\rangle = \frac{1}{V}\int_0^\infty \frac{k^3|\delta_{\vec{k}}|^2}{2\pi^2}\frac{\mathrm{d}k}{k}, \tag{1.2.44}$$

and corresponding to the density contrast is a mass fluctuation, δ_M whose *rms*

$$\left(\frac{\delta_M}{M}\right)_\lambda^2 = \frac{1}{(2\pi)^2}\frac{1}{VV_W}\int P(k)|W(k)|^2\mathrm{d}^3k, \tag{1.2.45}$$

where we define the window function (in most cases Gaussian), $W(k) = V_W e^{-k^2r^2/2}$ for a radius r within which the mass M is enclosed, and $V_W = (2\pi)^{3/2}r^3$ is its volume.

Without specified overall normalization amplitude for λ, *rms* mass perturbation at a given λ,

$$\left(\frac{\delta_M}{M}\right)_\lambda^2 \sim k^3P(k) \sim k^{3+n_\mathrm{s}}. \tag{1.2.46}$$

Here, n_s is a constant, called spectra index. For more detailed discussion, see Kolb and Turner (1990); Bretón et al. (2004).

On the largest scales (see Einasto et al. (1993); Kashlinsky (1992)), the power spectrum has theoretically been assumed to have the form (mostly shape and not the amplitude)

$$P(k) = Ak^{n_s} \tag{1.2.47}$$

for the primordial fluctuations; predicted independently by Harrison (Harrison, 1970) and Zeldovich (Zeldovich, 1972). Here, A is constant, and with the popular choice of the spectra index $n_s = 1$, the Harrison-Zeldovich $P(k) \propto k$. $n_\mathrm{s} = 1$ reflects a scale-invariant primordial power spectrum. However, $P(k) \propto k$ on large scales (small k) and $P(k) \propto k^{-3}$ on small scales (large k) from the theoretical point of view, see some discussion on small scale power spectrum in Widrow et al. (2009). Figure 1.1 shows linear and non-linear matter density power spectra at redshifts $z = 0.0$ and $z = 0.8$.

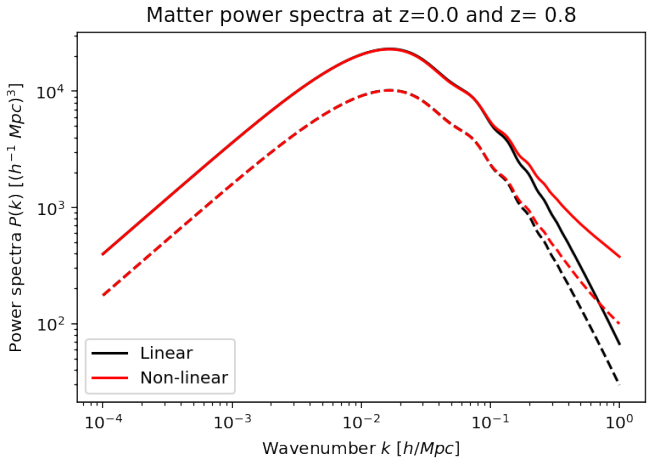

Figure 1.1: Linear and non-linear matter power spectra versus wavenumber at $z = 0$ (higher amplitude) and $z = 0.8$ (lower amplitude).

1.2.1 The Cosmic Microwave Background Radiation

The early universe was hot and dense, and thus neutral hydrogen atom could not exist. The temperature was so high and it could ionize any material that filled the universe. As a result, the early universe was opaque due to big plasma, mostly composed of tightly coupled nuclei, photons, and electrons. At this time there was a very high number density of free electrons causing extremely short photons' Thomson scattering mean free path. As the Universe expanded, it cooled down, causing the average photon energy to decrease; then primordial photons and electrons started to coalesce to form hydrogen and helium atoms (recombination), and the Universe became transparent. The Universe transitioned from radiation to matter-dominated, and the process took place at a time when the Universe temperature was about 3000 K. As a consequence of recombination, photons were no longer tightly held together with the charged particles, and were thus able to free-stream, and their mean free path quickly increased to approximately the size of the observable universe. These photons cooled off from 3000 K to 2.73 K as they traveled through space, and we see such photons today as Cosmic Microwave Background (CMB). The surface where the transition from opaque to transparent occurred is called the Surface of Last Scattering.

CMB is thus the oldest light that traveled towards us on its 13.8 billion years journey. We can, therefore, capture the history of the Universe by using this light. When looking at CMB, we see the Universe when it was just 380, 000 years old. Following recombination in a cosmic history is Dark Ages. We call such period Dark Ages because during that time luminous objects were not yet formed. Figure 1.2 depicts different phases of the Universe evolution history.

Therefore, the information encoded in the CMB spectrum which was discovered serendipitously by Bell Labs radio astronomers Arno Penzias and Robert Wilson in 1964 (Wilson and Penzias, 1965) provides a wealthy amount of imprints on the origin, evolution and expansion history of the

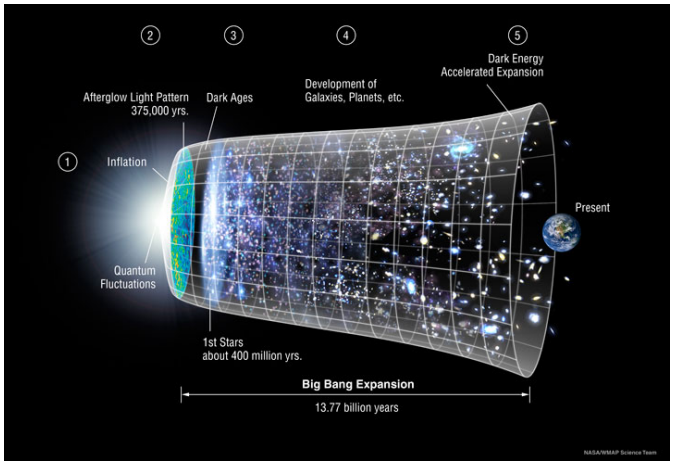

Figure 1.2: ΛCDM model of cosmology showing a Universe evolution timeline from quantum fluctuations and inflation to the present time. The figure is taken from NASA web page.

Universe. The CMB imprints have radiation nature that survived ages since the early universe, dating back to recombination ($z \sim 1100$). This radiation points back to the time when the Universe became transparent to CMB photons, and photons mainly free streamed. We can thus use the CMB light to trace signatures of small fluctuations (growth of small inhomogeneities) that set forth both dynamics and geometry of the expanding universe, which then triggered formation of the large-scale structures (LSSs). Before recombination when the Universe was very hot – above 3000 K, and opaque, these packets of light (photons) could not get far because they kept bouncing off all the free electrons.

This CMB momentous discovery was later followed by observations using FIRAS instruments on the *Cosmic Background Explorer* (*COBE*, 1992) satellite, which confirmed its radiation as having a characteristic continuous position and temperature dependent frequency spectrum, namely, Planck spectrum with an approximate temperature, $T = 2.726$ K (White et al., 1994; Mather et al., 1994). For the baryonic matter dominated universe, about 4 - 5 decades ago and more recently, sophisticated theoretical calculations, backed up by advanced sensitive experiments implied fluctuations in remote CMB of the order of 1 part out of 10^4 (i.e., $\triangle T/T = 10^{-4}$) (Peebles and Yu, 1970; Doroshkevich et al., 1978; Wilson and Silk, 1981). Later on, *COBE DMR* certainly detected CMB temperature fluctuations of order 10^{-5} across the sky (Smoot et al., 1992). These fluctuations give us information about density perturbations at $z \sim 1000$ (close to the Big Bang). *Wilkinson Microwave Anisotropy Probe* (*WMAP*, 2003), from NASA improved sensitivity after *COBE* and detected CMB temperature of 2.725 K with variation of 1 part in $100,000$, see the *WMAP* CMB temperature fluctuation sky map Figure 1.3. Such variation in the temperature of the Universe and hence its density at 1 part in 10^5 is a property of the Universe at a very early time, just when it was only $380,000$ years old. It turns out that the angular power spectrum (C_ℓ) of the temperature fluctuations is an important observable for the Universe's LSSs study.

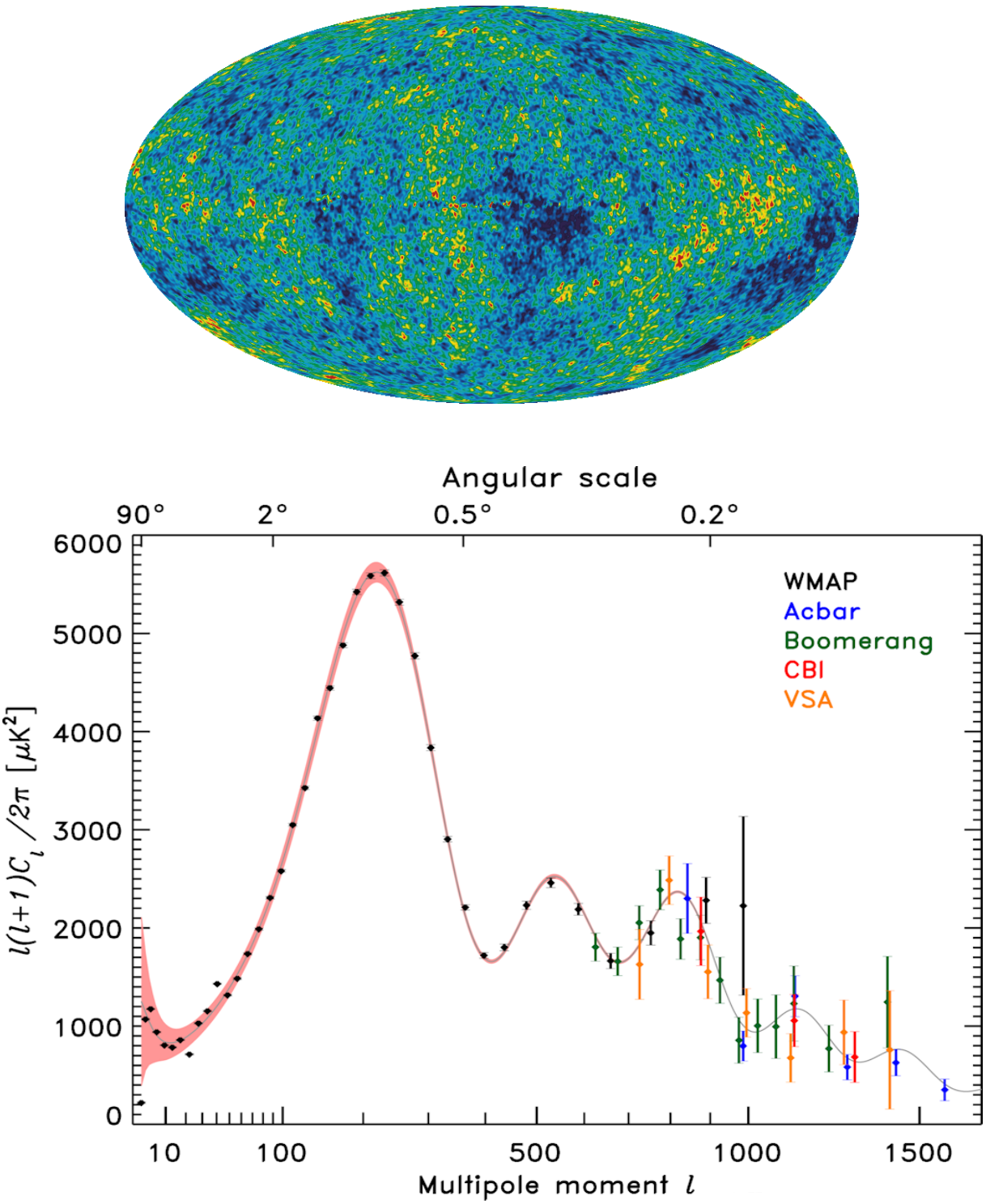

Figure 1.3: CMB temperature anisotropies/fluctuations (top) determined from five years of *WMAP* satellite data, with an approximate average temperature of 2.725 K, and the CMB angular power spectra (bottom) as measured by various probes. The map is taken from Ref. Hinshaw et al. (2009) and the power spectra figure is taken from Ref. D'Onofrio and Burigana (November, 2014).

More recently, rigorous dark-matter aided theoretical predictions certainly confirm relic fluctuations, $\triangle T/T$, that precursored the largest structures of the Universe to have the magnitude of 1 part in 10^5. Today, CMB can be used as a look-back probe to study the early universe, and the subsequent epochs. As experiments progressively advanced, *Planck* (2013) measured CMB with extreme sensitivity and resolution, however, providing rigorous predictions of parameter composition densities and quantities of our ΛCDM, the standard model of cosmology. The evolution of the Universe has given us clues that can be expressed mathematically and transformed into the data that we can obtain by looking out into space.

The CMB temperature fluctuations are Gaussian random fluctuations of the first order, with a temperature $\triangle T = 100\ \mu$K. For the photons, temperature fluctuations are simply a CMB intensity characterizing different sky positions/directions. CMB spectrum has nearly constant temperature across the sky and is a good blackbody (Fixsen et al., 1996). This observable can generally, precisely and quantitatively be described by temperature fluctuations $\triangle T/\overline{T}$.

In order to describe quantitatively the CMB power spectrum, we need the knowledge of mathematics over the sphere. The CMB anisotropy (temperature fluctuations) is defined as $\triangle T/\overline{T} \in \mathbb{S}^2$, and is a function that should depend on spatial position, $\vec{x}$, time t and a unit vector depicting photon direction, $\hat{\mathbf{n}}$. Since we are dealing with fields that are statistically homogeneous and statistically isotropic, we can safely assume that the statistical distribution of the CMB anisotropy $\triangle T/\overline{T}(\hat{\mathbf{n}})$ is the same in all positions and directions.

Assuming Gaussian fluctuations, we can make a spherical harmonic decomposition, i.e., Fourier decomposition in 2-dimension of these multipole moments of temperature field over a sphere characterized by the angular position (θ, ϕ) as

$$\frac{\triangle T}{\overline{T}}(\hat{\mathbf{n}}) = \sum_{\ell=1}^{\infty} \sum_{m=-\ell}^{+\ell} T_{\ell m} Y_{\ell m}(\hat{\mathbf{n}}), \tag{1.2.48}$$

where we have neglected spatial position and time in our expression.

Here, $Y_{\ell m}$ are the spherical harmonics (for angular position (θ, ϕ)),

$$Y_{\ell m}(\theta, \phi) = N e^{im\phi} P_\ell^m(\cos\theta), \tag{1.2.49}$$

such that

$$N = (-1)^m \sqrt{\frac{(2\ell+1)(\ell-m)!}{4\pi(\ell+1)!}} \tag{1.2.50}$$

is a constant which ensures the orthonormality of the spherical harmonics:

$$\int Y_{\ell m}(\theta, \phi) Y^*_{\ell' m'}(\theta, \phi) \mathrm{d}\Omega \equiv \int \mathrm{d}\hat{\mathbf{n}} Y_{\ell m}(\hat{\mathbf{n}}) Y^*_{\ell' m'}(\hat{\mathbf{n}}) = \delta_{\ell\ell'}\delta_{mm'} \text{ and} \tag{1.2.51}$$

P_ℓ^m are associated Legendre functions, given by

$$P_\ell^m(x) = \left(1 - x^2\right)^{|m|/2} \frac{\mathrm{d}^{|m|}}{\mathrm{d}x^{|m|}} P_\ell(x), \tag{1.2.52}$$

where

$$P_\ell(x) = \frac{1}{2^\ell \ell!}\frac{\mathrm{d}^\ell}{\mathrm{d}x^\ell}\left(\left(x^2-1\right)^\ell\right) \tag{1.2.53}$$

are Legendre polynomials. To put them into spherical harmonics, we need $0 \leq \theta < \pi$.

Note that $\mathrm{d}\Omega = \mathrm{d}\cos\theta \mathrm{d}\phi$, $\hat{\mathbf{n}} \cdot \hat{\mathbf{n}}' = \cos\theta$, such that $\hat{\mathbf{n}}$ is a notation for the unit vector specifying a direction.

ℓs are multipole moments running from $\ell \geq 1$, but in practice, especially for data analysis purposes, the dipole moment $\ell = 1$ is often excluded. The reason is that CMB has the largest temperature variation at this dipole, believed to be influenced by its linear dependence on the motion of the observer (Challinor and Peiris, 2009). Since the temperature field is real, $T^*_{\ell m} = (-1)^m T_{\ell,-m}$, this implies that we can adopt the convention $Y^*_{\ell m} = (-1)^m Y_{\ell,-m}$.

The expansion coefficient $T_{\ell m}$ can be found by inversion,

$$T_{\ell m} = \int \mathrm{d}\hat{\mathbf{n}} \frac{\triangle T}{\overline{T}}(\hat{\mathbf{n}}) Y^*_{\ell m}(\hat{\mathbf{n}}). \tag{1.2.54}$$

Note that, as for the case of Fourier transform of the random field in space, the harmonic transformation of $\triangle T/T$ is diagonal, which means off-diagonal correlators of the expansion coefficients $T_{\ell m}$ vanish.

Statistical isotropy for the correlators of $T_{\ell m}$ means

$$\langle T_{\ell m} T_{\ell' m'} \rangle = \delta_{\ell\ell'}\delta_{mm'} C^T_\ell, \tag{1.2.55}$$

where C^T_ℓ is CMB temperature anisotropy angular power spectrum.

This equation signifies that for different values of ℓ and m, there is no correlation between the expansion coefficients, $T_{\ell m}$, and if they are Gaussian, they are also independent. C_ℓ can completely statistically describe the temperature anisotropies. This means we can compute the temperature power spectrum as the squared amplitude of these temperature fluctuations. Mathematically, the temperature power spectrum, C^T_ℓ, is a function of angular scale in the sky or multipole moments, ℓ and is independent for a given realization. This characteristic enables modelling and analysis of the power spectrum in harmonic space.

Let us find how C_ℓ is related to the two-point correlation function. We compute the two-point correlation functions of these spherical harmonics coefficients as

$$\begin{aligned}\left\langle \frac{\triangle T}{\overline{T}}(\hat{\mathbf{n}}) \frac{\triangle T}{\overline{T}}(\hat{\mathbf{n}}') \right\rangle &= \sum_{\ell m}\sum_{\ell' m'} \langle T_{\ell m} T_{\ell' m'}\rangle Y_{\ell m}(\hat{\mathbf{n}}) Y^*_{\ell' m'}(\hat{\mathbf{n}}') \\ &= \sum_\ell C_\ell \sum_{m=-\ell}^{\ell} Y_{\ell m}(\hat{\mathbf{n}}) Y^*_{\ell' m'}(\hat{\mathbf{n}}') \\ &= \frac{1}{4\pi}\sum_\ell (2\ell+1) C_\ell P_\ell(\cos\theta) = C(\theta).\end{aligned} \tag{1.2.56}$$

To get the last equality above, we have applied additional theorem on spherical harmonics:

$$P_\ell(\cos\theta) = \frac{4\pi}{2\ell+1}\sum_{m=-\ell}^{\ell} Y_{\ell m}(\hat{\mathbf{n}}) Y^*_{\ell m}(\hat{\mathbf{n}}'), \tag{1.2.57}$$

where $P_\ell = P_\ell^0$ are Legendre polynomials. The angle brackets denote the average over an ensemble of realizations of the fluctuations (expected values). It is now clear that the two-point correction function (1.2.56) satisfies a statistical isotropy condition, as it only depends on the angle between the two points. The variance of the temperature field is given by

$$C(0) = \sum_\ell \frac{2\ell+1}{4\pi} C_\ell \approx \int \mathrm{dln}\ell \frac{\ell(\ell+1)C_\ell}{2\pi}. \tag{1.2.58}$$

Usually, people conventionally plot the quantity

$$T_\ell = \frac{\ell(\ell+1)}{2\pi} C_\ell \tag{1.2.59}$$

interpreted as the contribution to the variance per logarithmic range in ℓ.

By using the orthogonality of the Legendre polynomials, inversion of the correlation function (1.2.56) gives us the power spectrum:

$$C_\ell = 2\pi \int_{-1}^{1} \mathrm{dcos}\theta C(\theta) P_\ell(\mathrm{cos}\theta). \tag{1.2.60}$$

If we have full sky noise-free measurements of temperature fluctuations, we can estimate the CMB power spectrum by averaging over m for every ℓ as

$$\hat{C}_\ell^T = \frac{1}{2\ell+1} \sum_m |\hat{T}_{\ell m}|^2, \tag{1.2.61}$$

where m ranges from $-\ell$ to ℓ; ℓ is the angular wavenumber, and there are $2\ell+1$ modes for each ℓ. This power spectrum can estimate true ensemble C_ℓ^T without bias; but, since we can only observe finite number $2\ell+1$ of modes, it has cosmic variance that is irremovable. $\hat{C}_\ell^T$ distribution is a χ^2 with $2\ell+1$ degrees of freedom, and the cosmic variance is given by

$$\mathrm{Var}\left(C_\ell^T\right) = \frac{2}{2\ell+1}\left(C_\ell^T\right)^2 \tag{1.2.62}$$

for Gaussian distribution of the temperature anisotropies (Knox (1995); Challinor and Peiris (2009)).

From observational point of view, telescopes in practice observe CMB anisotropies assumed to follow a Gaussian beam function

$$B(\theta) = \mathrm{exp}\left[-\frac{\theta^2}{2\sigma_\mathrm{b}^2}\right], \tag{1.2.63}$$

where the full-width at half-maximum, $\theta_\mathrm{FWHM} \sim \lambda/d$ with d being the aperture size of a telescope such that $\sigma_\mathrm{b} = 2\sqrt{2\mathrm{log}2}\theta_\mathrm{FWHM}$. In this case, a telescope observes temperature anisotropies given by

$$\triangle T_\mathrm{obs}(\theta,\phi) = \sum_{\ell=2}^{\infty} \sum_{m=-\ell}^{m=+\ell} B_\ell T_{\ell m} Y_{\ell m}(\theta,\phi), \tag{1.2.64}$$

where

$$B_\ell = 2\pi \int_0^\pi \mathrm{dsin}\theta P_\ell(\mathrm{cos}\theta) B(\theta) \tag{1.2.65}$$

is the beam profile function ($B(\theta)$) Legendre transform. If the beam profile is Gaussian, the corresponding Legendre transform is given by

$$B_\ell = \exp\left[-\frac{1}{2}\ell(\ell+1)\sigma_{\rm b}^2 \right]. \tag{1.2.66}$$

For observed map, the power spectrum C_ℓ is normally convolved with the beam, so (in Fourier space)

$$C_\ell^{\rm obs} = B_\ell^2 C_\ell. \tag{1.2.67}$$

Conventional plotting of (1.2.59) can follow from neglecting the sky curvature by limiting ourselves to small sections of the sky and transform the spherical harmonic analysis into ordinary two-dimensional Fourier analysis. This limit renders ℓ as the Fourier wavenumber with angular wavelength given by $\theta = 2\pi/\ell$, which means small angular scales correspond to large multipole moments. The variance of the field is

$$\int {\rm d}^2\ell \frac{C_\ell}{(2\pi)^2} \tag{1.2.68}$$

in this limit, with the power spectrum given by

$$(\Delta T)^2 \equiv \frac{\ell(\ell+1)}{2\pi}\left(C_\ell^T\right)^2 \tag{1.2.69}$$

for wavenumber $\ell >> 1$, in practice computed as the power per logarithmic interval which is a representation of the *rms* difference in temperature between two sky positions with angular separation of $\theta = \pi/\ell$ measured in radians.

In summary, the CMB temperature power spectrum has been predicted and measured with great precision over the last decade, see Figure 1.3. The power spectrum is an important result as it contains all the information about the Gaussian isotropic field and we can use measurements of its statistical properties to infer the physics that seeded the first structures in the Universe. Temperature anisotropies in CMB are now one of the powerful cosmological probes in studies of the early universe and its cosmic evolution (Planck Collaboration et al., 2018). What we see in the CMB today helps us to infer the initial conditions of the Universe and constrain some of its very early phenomena. Power spectrum calculations are challenged by a number of real-world complexities; see Efstathiou (2004) for reviews on some practical methods on temperature power spectrum estimation.

1.2.2 Halo Formation and Distribution

Dark matter halo is a theorized component considered to permeate and surround LSSs such as individual galaxies, groups, and clusters of galaxies. The existence of dark matter was first detected through studying the velocities of galaxies in the Coma cluster (see Subsection 1.1.4). Similar dark matter inference was achieved through observations of the velocities of stars and gas in galaxies. Through such studies, it was noted that the amount of ordinary luminous matter

available within disk galaxies was not enough to account for the observed rotation curves. In sum, after a number of observations, it was then concluded that the aforementioned effects could not be reasonably produced by the luminous matter, implying a presence in a significant amount of a mysterious form of an invisible matter-energy called dark matter.

Halos can be thought of as gravitationally bound regions of matter that have decoupled from the Hubble expansion and collapsed (Wechsler and Tinker, 2018). The gravitational instability is responsible for structure collapse that leads to dark matter halos formation. After they are formed, halos can merge with other halos or accrete the neighbouring materials, and thus continue to grow in mass (and size). When halos merge into bigger halos and live as bound objects and survive instabilities, they populate subhalos (Mo et al., 2010). Subhalos may also be remnants of their host halos which survived merging/accretion into big host halos. Subhalos are usually subjected to various forces that try to dissolve them, such as dynamical frictions, impulsive encounters, and tidal forces as they orbit their host halos. Halos develop complex patterns, such as substructures, which seem to be the function of their formation history. Numerous simulations following the advent of fast computers that can handle very large dark matter halo mass and force resolutions have shown that halos that assembled later are both more massive, and have on average a wealthy of substructures than those which formed earlier in the cosmic history.

Galaxies are thought to form through the cooling of gas (baryonic matter) in the centers of collapsed, virialized dark matter halos (White and Rees, 1978), and hence these parent halos are responsible for determining the physical properties of galaxies within them. Descriptions of dark matter gravitational clustering seeded by Gaussian initial fluctuations using linear and higher-order perturbation theory have been provided in Bernardeau et al. (2002). This mass initially thought to be smoothly distributed has evolved into complex structures such as networks of sheets, filaments, and knots. The phrase dark matter halos is often used in place of dense knots (Cooray and Sheth, 2002).

N-body simulations have been frontier approaches to studying the properties of dark matter halos for different cosmological models, such as their evolution with time. Theoretically, high-resolution simulations for relatively small volumes of the Universe have been used to study details of the mass distribution around and inside halos (Navarro et al., 1996; Moore et al., 1999), whereas, low resolution, large volume simulations have been used to study details of their spatial distribution and abundance or dark matter halo mass function (Tinker et al., 2008; Jenkins et al., 2001; Sheth et al., 2001). Therefore, studies in relation to dark matter halos have been conducted, geared to investigating their clustering and evolution, and more attention is now given to using approaches based on virialized halos to understand the properties of dark matter and galaxy power spectrum, mostly, the formation, evolution, and the number and distribution of galaxies that reside within dark matter halos as a function of mass (White et al., 2001). There are other numerous dark matter halo simulations, such as high resolution N-body simulations focusing on halo density profiles (Jing and Suto, 2002), BOLSHOI simulation to

study various halo properties, for example, halo mass function, the halo and subhalo abundances and concentrations, the velocity functions, and the number density profiles of subhalos (Klypin et al., 2011), and halos large-scale bias fitting function numerical calibrations (Tinker et al., 2010).

Although the efficiency of galaxy formation depends on the physics of baryons, the masses and spatial distribution of their host dark matter halos have been found to only rely on dark matter properties and the expansion history of the Universe. These allow for a simple galaxy clustering cosmological model which is clearly separate from the complex physics of baryons. Analytical models for dark matter halos large-scale spatial clustering amplitude as a function of halo mass have been studied by Mo and White (1996); Sheth et al. (2001). These models can then be used to study as a function of scale, both clustering of galaxies and dark matter particles (Seljak, 2000; Peacock and Smith, 2000; Ma and Fry, 2000). For a given cosmological model, a galaxy population clustering can be used to predict the average mass of dark matter halo hosts on some large linear scales.

It has generally been shown through N-body simulations that the statistical clustering of galaxies has an intrinsic connection to the clustering of dark matter halos (Peacock and Smith, 2000). Similarly, galaxy formation efficiency and evolution are correlated to the halo occupation distribution (HOD) and can be a function of a number of properties of galaxy, such as stellar mass, morphology, color, and luminosity (Zehavi et al., 2011). The current understanding of galaxy formation established through high-resolution N-body simulations in conjunction with large surveys of galaxies, such as SDSS, is that each galaxy form inside the dark matter halo and the formation efficiency is strongly a function of halo mass (Mo et al., 2010; Wechsler and Tinker, 2018).

Let us now briefly discuss the halo virial relations. Halos have deep hierarchical structures, where each halo has thousands of subhalos and each subhalo contains small subhalos. It is a standard convention to use respectively, a relation between the mass, radius and the circular velocity of the dark matter halo, called the virial mass, $M_{\rm vir}$, virial radius (the virial radius is defined as the radius of a sphere containing a mean mass overdensity of 200 with respect to the global value (Moore et al., 1998)), $R_{\rm vir}$, and the virial velocity, $V_{\rm vir}$. A usual practice for numerical simulators is to define halo relations between masses and radii specified by a given overdensity

$$\triangle_{\rm vir}\rho_m = \frac{3M_{\rm vir}}{4\pi R_{\rm vir}^3} = \triangle_{\rm vir}(z)\Omega_m(z)\frac{3H^2}{8\pi G}(z), \tag{1.2.70}$$

where for the ΛCDM model of cosmology, overdensity for the dark matter halos is fitted by

$$\triangle_{\rm vir} = \frac{18\pi^2 + 82x - 39x^2}{x+1}, \tag{1.2.71}$$

and $x = \Omega_m(z) - 1$.

The virial mass, virial radius and virial velocity are related as

$$V_{\rm vir} \equiv \sqrt{\frac{GM_{\rm vir}}{R_{\rm vir}}}. \tag{1.2.72}$$

The definition of $\triangle$ varies, and is usually chosen; depending on how it is motivated in the respective literature (Wechsler and Tinker, 2018; Mo et al., 2010). In what follows, we discuss some of the structural properties of the dark matter halos, starting with the halo density profile.

For simplicity, we discuss the modeling of dark matter halo as an approximate spherical object. Neyman, Scot and Shane (1953) (Peacock and Smith, 2000), asserted that a Universe is fragmented into non-linear halos, whose internal density structures determine the observed galaxy correlations. Being non-linear objects, it is possible that halo non-linear collapse has destroyed their primordial historical formation imprints. However, various halo density profiles may have more close connection to the violent relaxation process during a phase of rapid mergers than to initial conditions (Mo et al., 2010). Navarro et al. (1996, 1997) used a suite of simulations for different cosmological models and showed that the density profiles (the internal mass distributions) of dark matter halos for the ΛCDM cosmology can be described by a fitting function (the NFW profile)

$$\rho(R) = \rho_{\rm crt} \frac{\delta_{\rm char}}{(R/R_s)(1+R/R_s)^2}. \tag{1.2.73}$$

Here, R is the radius of the halo mass shell, $\rho_{\rm char}$ is the characteristic overdensity, and R_s is the characteristic scale radius.

The halo virial mass $M_{\rm vir}$ and the concentration parameter defined as $c \equiv R_{\rm vir}/R_s$ or equivalently δchar and $R_{\rm s}$ (Mo et al., 2010), completely characterize the NFW profile, where $R_{\rm vir}$ is the limiting (bounding) radius of the dark matter halo. These quantities are related to the characteristic overdensity as

$$\delta_{\rm char} = \frac{\triangle_{\rm vir}}{3} \frac{c^3}{\ln(1+c) - c(1+c)}. \tag{1.2.74}$$

The corresponding enclosed mass (mass within the mass shell), $M(R)$, of the NFW profile by a shell of radius R is given by

$$M(R) = 4\pi\bar{\rho}\delta_{\rm char}R_{\rm s}^3 \left[\ln(1+cy) - \frac{cy}{1+cy}\right], \tag{1.2.75}$$

where $\bar{\rho}$ is the mean matter density of the Universe, and $y = R/R_{\rm vir}$.

Depending on the chosen definition for $R_{\rm vir}$, we can recover the total mass $M_{\rm vir}$ of the halo by evaluating Equation (1.2.75) at $y = 1$.

Furthermore, the circular velocity of the NFW profile is given by

$$V_{\rm c}(R) = V_{\rm vir}\sqrt{\frac{f(cy)}{yf(c)}}. \tag{1.2.76}$$

There were other proposed halo mass density profile alternatives to NFW profile, see for example Moore et al. (1998); Fukushige and Makino (2001). Navarro and his colleagues established that halos which assembled earlier (they assembled earlier when the Universe was denser) were more concentrated than those which formed later. This relation is in detail surveyed in the literature Wechsler et al. (2002); Zhao et al. (2003). Their findings imply that the characteristic overdensity is closely correlated to the time when the halo formed. They further showed, on average more massive halos form earlier, and are expected to be less concentrated, that is, their masses are inversely proportional to their concentrations. Duffy et al., Duffy et al. (2008); Ma et al. (2015) reported consensus findings, for which through using three cosmological N-body simulations and WMAP5 cosmology, they obtained results which established that dark matter halo concentration parameter c can be well fit by the formula

$$c = \frac{5.72}{(1+z)^{0.71}} \left(\frac{M_{\rm vir}}{10^4 h^{-1} M_\odot} \right)^{-0.081}, \tag{1.2.77}$$

where $M_\odot$ is the solar mass.

However, it was shown earlier through simulations, that concentration is a weakly decreasing function of halo mass (Duffy et al., 2008). A number of researchers were motivated by this and such other findings, and have since then developed an interest to find best estimators of the mean concentration as a function of halo mass through simple models, see for example Bullock et al. (2001); Zhao et al. (2009). Moreover, Duffy et al. (2008) reported discrepancies in the dark matter halo concentrations between the two types of results which respectively, assumed WMAP1 and WMAP5 cosmologies. More recently, Klypin et al. (2016) reports significant dark matter halo concentration evolution deviations from previously established results, especially for massive halos.

1.2.3 The Halo Model

We adapt materials presented by Cooray and Sheth (2002); Mo et al. (2010) to describe the halo model. The halo model can be used to describe analytically the cosmological dark matter density distribution, (as we now know, dark matter is distributed over halos) in the non-linear regime in terms of halo building blocks. In this formalism, we can think of matter field as fragmented, and thus it is a discrete sum of dark matter halos.

We assume sphericity for all dark matter halos, and that their density distribution only depends on halo mass

$$\rho(r|M) = Mu(r|M), \tag{1.2.78}$$

where $u(r|M)$ is the normalized halo density profile:

$$\int \mathrm{d}^3\vec{x} u(\vec{x}|M) = 1. \tag{1.2.79}$$

Let us imagine a vast space split into volumes, $\triangle V_i$ which are very small compared to the whole space and that each of these volumes can only contain a maximum of one halo center. We

currently understand that each galaxy forms within a dark matter halo (Wechsler et al., 2002), so galaxies formation and growth over time are connected to the growth of their host halos. The advent of large-scale high-resolution cosmological simulations and large galaxy surveys have opened a new window that has given us insights on statistical relationships between galaxies, halos and their evolution with time. We have also learned that the efficiency of galaxy formation is highly correlated to the dark matter halo mass of the halo within which they form.

Suppose N_i is the occupation number of dark matter halos in each of these volumes, $\triangle V_i$. Then, we have that N_i is either 0 or 1, and so $N_i = N_i^2 = \ldots = N_i^N$. This formalism provides a way of writing the matter density field as a discrete sum of its components:

$$\rho(\vec{x}) = \sum_i N_i M_i u(\vec{x} - \vec{x}_i | M_i). \tag{1.2.80}$$

This definition denotes the sum of all possible spacial partitions, with and without halos, each multiplied by its respective occupation number, N_i.

The two-point correlation function for the matter density field can then be computed as

$$\begin{aligned} \xi_{\rm mm}(r) &\equiv \langle \delta(\vec{x})\delta(\vec{x}+\vec{r})\rangle \\ &= \frac{1}{\bar{\rho}^2}\langle \delta(\vec{x})\delta(\vec{x}+\vec{r})\rangle - 1, \end{aligned} \tag{1.2.81}$$

where $\delta(\vec{x})$ is the matter field overdensity.

Using (1.2.80), we can expand the correlation function (1.2.81) as

$$\langle \delta(\vec{x})\delta(\vec{x}+\vec{r})\rangle = \Big\langle \sum_i N_i M_i u(\vec{x}_1 - \vec{x}_i | M_i) \sum_j N_j M_j u(\vec{x}_2 - \vec{x}_j | M_j) \Big\rangle, \tag{1.2.82}$$

where $\vec{x}_2 = \vec{x}_1 + \vec{r}$.

Taking summation outside the ensemble average allows us to write (1.2.82) as

$$\langle \delta(\vec{x})\delta(\vec{x}+\vec{r})\rangle = \sum_i \sum_j \Big\langle N_i N_j M_i M_j u(\vec{x}_1 - \vec{x}_i | M_i) u(\vec{x}_2 - \vec{x}_j | M_j) \Big\rangle. \tag{1.2.83}$$

Here, the role of correlation function is simply to count the number of pairs of particles in halos, so we can split the RHS of (1.2.82) into two parties, namely; the one-halo ($i = j$) term, and the two-halo ($i \neq j$) term. The one-halo term basically correlates pairs of particles (galaxies) resulting from the same halo, while the two-halo term, as its name suggests, relates pairs of particles belonging to two different halos.

Considering the one-halo term, $N_i = N_i^2$, so we have

$$\langle \delta(\vec{x})\delta(\vec{x}+\vec{r})\rangle_{\rm 1h} = \sum_i \Big\langle N_i M_i^2 u(\vec{x}_1 - \vec{x}_i | M_i) u(\vec{x}_2 - \vec{x}_i | M_i) \Big\rangle. \tag{1.2.84}$$

Ensemble average can be expressed as an integral over the halo mass function, $n(M)$, and so the above equation becomes,

$$\langle \delta(\vec{x})\delta(\vec{x}+\vec{r})\rangle_{\rm 1h} = \sum_i \int {\rm d}M M^2 n(M) \triangle V_i u(\vec{x}_1 - \vec{x}_i | M) u(\vec{x}_2 - \vec{x}_i | M). \tag{1.2.85}$$

Furthermore, the latter equation can be interpreted as the probability that the halo occupation in the spatial cell of volume $\triangle V_i$ will have the mass M multiplied by the respective volume of that cell. Now, summing these probabilities over all possible spatial volumes, is simply integrating Equation (1.2.85) to have

$$\langle \delta(\vec{x})\delta(\vec{x}+\vec{r})\rangle_{1\mathrm{h}} = \int \mathrm{d}M M^2 n(M) \int \mathrm{d}^3\vec{y} u(\vec{x}_1 - \vec{y}|M) u(\vec{x}_2 - \vec{y}|M). \tag{1.2.86}$$

The term

$$\int \mathrm{d}^3\vec{y} u(\vec{x}_1 - \vec{y}|M) u(\vec{x}_2 - \vec{y}|M) \tag{1.2.87}$$

from Equation (1.2.86) above is called convolution integral. Thus, Equation (1.2.86) is a convolution of the halo profile (mass function) with itself. This is the probability that tells the number of halos of mass M, since one-halo term is a representation of dark matter halo particle pairs distribution within the halo itself.

Now, for the two-halo term, we have

$$\langle \delta(\vec{x})\delta(\vec{x}+\vec{r})\rangle_{2\mathrm{h}} = \Big\langle \sum_i \sum_{i\neq j} \langle N_i N_j M_i M_j u(\vec{x}_1 - \vec{x}_i|M_i) u(\vec{x}_2 - \vec{x}_j|M_j) \Big\rangle. \tag{1.2.88}$$

Making similar analogy as with the one-halo term, we arrive at

$$\begin{aligned} \langle \delta(\vec{x})\delta(\vec{x}+\vec{r})\rangle_{2\mathrm{h}} \quad &= \sum_i \sum_{i\neq j} \int \mathrm{d}M_1 M_1 n(M_1 \int \mathrm{d}M_2 M_2 n(M_2) \triangle V_i \triangle V_j \times \\ &\quad u(\vec{x}_1 - \vec{x}_i|M_1) u(\vec{x}_2 - \vec{x}_j|M_2). \end{aligned} \tag{1.2.89}$$

Equation (1.2.89) cannot correctly describe the two halo-term in its current state, it would only hold if dark matter halos are Poisson distributed (i.e., independent from each other). But dark matter halos are instead have non-zero two-point correlation function, which means they are clustered, so we have to take into account dark matter clustering. Thus, on large (linear) scales, dark matter halos clustering is characterized by halo-halo correlation function

$$\xi_{\mathrm{hh}}(r|M_1, M_2) = b(M_1) b(M_2) \xi^{\mathrm{lin}}_{\mathrm{mm}}(r), \tag{1.2.90}$$

which is the number of pairs in excess of the expected number of pairs that would have Poisson distribution. Here, $b(M)$ is the halo bias function and $\xi^{\mathrm{lin}}_{\mathrm{mm}}(r)$ is a linear matter correlation function. So, Equation (1.2.89) can then be modified by the halo-halo correlation function (1.2.90) to have the two-halo term as

$$\begin{aligned} \langle \delta(\vec{x})\delta(\vec{x}+\vec{r})\rangle_{2\mathrm{h}} \quad &= \sum_i \sum_{i\neq j} \int \mathrm{d}M_1 M_1 n(M_1 \int \mathrm{d}M_2 M_2 n(M_2) \triangle V_i \triangle V_j \times \\ &\quad \left[1 + \xi_{\mathrm{hh}}(\vec{x}_i - \vec{x}_j|M_1, M_2)\right] u(\vec{x}_1 - \vec{x}_i|M_1) u(\vec{x}_2 - \vec{x}_j|M_2). \end{aligned} \tag{1.2.91}$$

On small/medium scales, we will need to consider non-linear correlation functions and other correction terms.

Analogously to the one-halo term, we can further write Equation (1.2.91) as

$$\begin{aligned}\langle\delta(\vec{x})\delta(\vec{x}+\vec{r})\rangle_{2\mathrm{h}} &= \bar{\rho}^2 + \int \mathrm{d}M_1 M_1 n(M_1) \int \mathrm{d}M_2 M_2 n(M_2) \times \\ &\int \mathrm{d}^3\vec{y}_1 \int \mathrm{d}^3\vec{y}_2 u(\vec{x}_1 - \vec{y}_1|M_1) u(\vec{x}_2 - \vec{y}_2)|M_2) \times \\ &\xi_{\mathrm{hh}}(\vec{y}_1 - \vec{y}_2|M_1, M_2).\end{aligned} \tag{1.2.92}$$

By introducing bias and redefining the halo-halo correlation function, we finally have

$$\begin{aligned}\langle\delta(\vec{x})\delta(\vec{x}+\vec{r})\rangle_{2\mathrm{h}} &= \bar{\rho}^2 + \int \mathrm{d}M_1 M_1 b(M_1) n(M_1) \int \mathrm{d}M_2 M_2 b(M_2) n(M_2) \times \\ &\int \mathrm{d}^3\vec{y}_1 \int \mathrm{d}^3\vec{y}_2 u(\vec{x}_1 - \vec{y}_1|M_1) u(\vec{x}_2 - \vec{y}_2)|M_2) \times \\ &\xi^{\mathrm{lin}}_{\mathrm{mm}}(\vec{y}_1 - \vec{y}_2).\end{aligned} \tag{1.2.93}$$

From the above equation, we can again recognize

$$\int \mathrm{d}^3\vec{y}_1 \int \mathrm{d}^3\vec{y}_2 u(\vec{x}_1 - \vec{y}_1|M_1) u(\vec{x}_2 - \vec{y}_2)|M_2) \tag{1.2.94}$$

as convolution function.

Therefore, in a non-linear regime, the correlation function for the halo model in terms of dark matter halos building blocks is expressed as a sum of one-halo term and two-halo term:

$$\xi(r) = \xi^{1\mathrm{h}}(r) + \xi^{2\mathrm{h}}(r), \tag{1.2.95}$$

where

$$\xi^{1\mathrm{h}}(r) = \frac{1}{\bar{\rho}^2} \int \mathrm{d}M M^2 n(M) \int \mathrm{d}^3\vec{y} u(\vec{x} - \vec{y}|M) u(\vec{x} + \vec{r} - \vec{y}|M), \tag{1.2.96}$$

and

$$\begin{aligned}\xi^{2\mathrm{h}}(r) &= \frac{1}{\bar{\rho}^2} \int \mathrm{d}M_1 M_1 b(M_1) n(M_1) \int \mathrm{d}M_2 M_2 b(M_2) n(M_2) \times \\ &\int \mathrm{d}^3\vec{y}_1 \int \mathrm{d}^3\vec{y}_2 u(\vec{x} - \vec{y}_1|M_1) u(\vec{x} + \vec{r} - \vec{y}_2)|M_2) \times \\ &\xi^{\mathrm{lin}}_{\mathrm{mm}}(\vec{y}_1 - \vec{y}_2).\end{aligned} \tag{1.2.97}$$

Halo model parameter values are usually calibrated through N-body numerical simulations, see for example, Tinker et al. (2010).

Next, we consider the halo model in Fourier space. We introduce the notion of convolution, and find how we can transform from real space to Fourier space, and see what advantages this transformation has. The convolution, $c(t)$ of the two functions of t, f and g is a linear function defined by

$$c(t) = f(t) * g(t) \equiv \int_{-\infty}^{\infty} f(x) g(t - x) dx. \tag{1.2.98}$$

We see that, as is the case with our one-halo and two-halo terms above, convolved functions may involve a considerable degree of tedious computations. Luckily, the convolution theorem

tells us that, the convolution of the two functions f and g in real space becomes a product in Fourier space:

$$f(t) * g(t) \longleftrightarrow F(s)G(s) = C(s), \tag{1.2.99}$$

where F and G are respectively, the Fourier transforms of functions f and g.

However, we know that the linear correlation function of the matter is a Fourier transform of the matter power spectrum. More specifically, the Fourier transform of the matter autocorrelation function is the power spectrum, and equivalently, the autocorrelation is the inverse Fourier transform of the matter power spectrum. Therefore, instead of computing the matter linear correlation functions for the one-halo term and the two-halo term of the dark matter halo model, i.e., Equations (1.2.96) and (1.2.97), directly, it is simpler to compute $P(k)$ of the halo model, and then apply Fourier transformation to obtain the linear matter correlation function $\xi(r)$. In this way, we transform the convolution integrals in real space into multiplications in Fourier space.

Therefore, we can write the halo model matter power spectrum as a sum of one-halo term and two-halo term:

$$P(k) = P^{1h}(k) + P^{2h}(k), \tag{1.2.100}$$

where

$$P^{1h}(k) = \frac{1}{\bar{\rho}^2} \int \mathrm{d}M M^2 n(M) |\bar{u}(k|M)|^2, \tag{1.2.101}$$

$$P^{2h}(k) = P^{\mathrm{lin}}(k) \left[\frac{1}{\bar{\rho}} \int \mathrm{d}M M b(M) n(M) \bar{u}(k|M) \right]^2, \tag{1.2.102}$$

such that

$$P^{\mathrm{lin}}(k) = \int \xi^{\mathrm{lin}}_{\mathrm{mm}}(\vec{x}) e^{-i\vec{k}.\vec{x}} \mathrm{d}^3\vec{x} = 4\pi \int_0^\infty \xi^{\mathrm{lin}}_{\mathrm{mm}}(r) \frac{\sin kr}{kr} r^2 \mathrm{d}r \tag{1.2.103}$$

and

$$\bar{u}(\vec{k}|M) = \int u(\vec{x}|M) e^{-i\vec{k}.\vec{x}} \mathrm{d}^3\vec{x} = 4\pi \int_0^\infty u(r|M) \frac{\sin kr}{kr} r^2 \mathrm{d}r. \tag{1.2.104}$$

1.3 21-cm Cosmology

1.3.1 HI Spin-flip Transition

The hyperfine spin-flip transition in neutral hydrogen atom (HI) (Furlanetto et al., 2006b) gives rise to the 21-cm spectral line that can be seen by radio telescopes. Hyperfine spin-flip transition results from the interaction between magnetic moments of electrons and protons. This then leads to the configuration in which the proton and electron spins are in opposite directions;

a configuration with total lower energy than the state in which the two spins are parallel. Thus, a photon having an energy of 5.9×10^{-6}eV equals to the difference in the energies of the two configurations is emitted when the atom flips from the parallel configuration to the antiparallel one. This photon energy corresponds to a wavelength of 21 cm. Modern cosmology large-scale structure surveys of the Universe heavily rely on the analyses of the frequency and the redshifted primordial photon wavelengths to the radio part of the electromagnetic spectrum, and hence the phrase 21-cm cosmology.

1.3.2 HI Intensity Mapping

21-cm cosmology has opened a new window of studying our Universe structure, and together with the potential availability of an enormous amount of data and a promising consistent development of data testable theoretical frameworks underpinning the study, the field of cosmology is progressively becoming more exciting than ever before. As of today, probing the cosmos with 21-cm cosmology is regarded a modern approach (Dodelson, 2003), and undoubtedly presents overwhelming future science prospects.

As opposed to the traditional galaxy redshift survey which focuses to resolve individual galaxies, 21-cm cosmology aims to map out galaxy distribution over large, potentially containing galaxies Universe volumes with 21-cm signal intensity. In particular, the phrase 21-cm cosmology arises from the fact an approach uses the redshifted 21-cm emission line of the neutral hydrogen atom whose wavelength at rest-frame is 21 cm to survey very large cosmic structures. The HI IM (Peterson et al., 2009) survey arguably can collect primordial cosmic information that is several orders of magnitude richer than what CMB measurements could offer (Harper et al., 2018). Direct observations of galaxies to very large distances corresponding to around a billion years Universe age have been carried out by both ground-based optical telescopes such as VLT, Subaru and Keck, and a well known *Hubble Space Telescope*. These telescopes, however, can only see individual galaxies at a time and are limited to observe only the brightest sources since most of the objects of our interest are extremely distant from us. In contrast, 21-cm relies on the analyses of the information encoded in the measurements of the total HI intensity over comparatively large angular scales to efficiently survey extremely large volumes of galaxies. Looking at the advancement trends in the field, we can indisputably predict that HI IM is potentially an extremely important ingredient for imaging the evolving LSSs of our Universe.

From the Big Bang phase to about $400,000$ years later, the initially very hot and dense universe expanded to a size for which the pressure of the gas that filled it dropped significantly. This led to the cooling of the cosmic gas below an order of magnitude from 3000 K. The cooling was sufficient for protons and electrons to detach from a tightly coupled gaseous plasma and combined to form HI. The CMB in the form of minute energy packets of electromagnetic radiation called photons also decoupled from the cosmic gas during this time and free streamed. Thus, the CMB radiation temperature anisotropies of order $\sim 10^{-5}$ can be used to image the primordial universe at distances corresponding to the age of the Universe at recombination ($t \sim 400,000$

years). Similarly, the light emitted by the HI due to the hyperfine spin-flip transition as a result of interaction between magnetic moments of electrons and protons is sufficiently rich in information that we can employ to probe the snapshot of the primordial universe and study how it evolved from such distant past to its current state. At late times, most of the neutral hydrogen content is expected to be confined within galaxies (Visbal et al., 2009; Bull et al., 2015b), and hence this makes it an excellent tracer of galaxy distribution and a probe of the evolutionary Universe since its first stars and galaxies, about the first billion years after the Big Bang. Just as the CMB anisotropies used to probe the cosmos over large scales, the redshifted HI fluctuations will be used to detect all galaxies with HI content. Variations in the intensity of HI can approximate the galaxy power spectrum over sufficiently large angular scales as a function of redshift and cosmic time. Observations with the radio part of the electromagnetic spectrum thus open a new window to the very high redshift universe which is otherwise invisible to traditional optical galaxy redshift surveys (Hall et al., 2013). Optical galaxy redshift surveys can only resolve individual most bright sources and the task becomes extremely challenging at high redshifts since the objects of interest are very far and appear fainter.

By the time the Universe reionized, significant amounts of HI atoms were prevented from reionizing ultraviolet photons since they resided within comparatively large dense clouds (damped Lyα systems) embedded in galaxies (with some of the signal emanating from optically-thin Lyα absorbers in regions of low-density) (Furlanetto et al., 2006b; Morales and Wyithe, 2010; Pritchard and Loeb, 2012; Bull et al., 2015b). Therefore, after the EoR, large amount of hydrogen in the IGM was ionized, but the majority of the HI residing within galaxies was left intact and it is currently the most abundant and ubiquitous element in the Universe (Barkana and Loeb, 2007) mass gas content. Our forecast with the HI IM will illuminate the post-reionization epoch at low redshifts which has some advantages. In contrast to the Epoch of reionization (EoR (Morales and Wyithe, 2010)) observations, the post reionization physics of the 21-cm power spectrum is less complicated in the linear theory and can be well measured (Wyithe and Loeb, 2008, 2009). Due to its sensitivity to the reionization process details (Furlanetto et al., 2006a), modeling of the power spectrum in the EoR is somewhat complicated. However, contaminants such as emission from Galactic synchrotron are significantly suppressed at the post reionization epoch (low redshift) compared to EoR (Battye et al., 2012). Although the foreground will still be several orders of magnitude higher than HI signal, reduced contaminants make the application of any standard algorithm to strip them off a bit easier.

In general, observing using the radio window of the electromagnetic spectrum is thus essentially suitable for HI intensity mapping technique which has a number of advantages over the traditional galaxy redshift survey, as we summarize them below:

- HI IM approach is robust since it allows efficient surveys of extremely large volumes of galaxies without resolving each individual galaxy.
- It produces bright tomographic maps of the HI emission distribution present in the Universe over a large range of angular scales.

- It provides sensitivity to the BAO feature over redshift ranges inaccessible to current galaxy redshift surveys.
- HI IM converts sources redshifts and makes their information readily obtainable via the corresponding observing frequencies. This allows very narrow redshift bins (see advantages Nan et al. (2011); Hall et al. (2013); Xu et al. (2018) of using thin redshift bins) to be used to obtain 3-dimensional tomographic maps, and thus study matter density field evolution and its scale dependence (Hall et al., 2013).
- Furthermore, the significance of the redshift-space distortion (RSD) term is enhanced due to precise redshift information, as opposed to photometric redshifts only optical surveys, in which the RSD term is suppressed due to redshift measurement uncertainties (Hall et al., 2013).

HI IM deploys single-dish telescopes or interferometry arrays which can be cheaply constructed compared to the cost of galaxy redshift survey instruments (Seo et al., 2010; Battye et al., 2012). Large-scale redshifted HI observations will be attainable through the future and near-term HI IM experiments; some of which aim to map out HI at relatively low angular resolution ($\sim 1^{\circ}$) within the HI brightness of galaxies beam fluctuations. With little sacrifice in source resolution, the HI survey technique does not just focus to only resolve individual galaxies or brightest sources but maximizes surveys by efficiently integrating the HI signal from all galaxies at various redshift sliced volumes of the Universe. This is because such telescopes require resolution and sensitivity which can measure large-scale structures of the Universe, such as BAOs wavelengths sufficiently but need no resolution and sensitivity for individual galaxies detection (Peterson et al., 2009). IM is thus an economical and effective strategy to map very large volumes of the Universe efficiently by integrating total emission from many galaxies.

However, 21-cm observations do not only enable us to study the first stars and galaxies, their distribution across the cosmic history, but also provide us with the potential to infer the fundamental physics such as initial conditions of the Big Bang and the various astrophysical effects (Pritchard and Loeb, 2012); carry out forecasts of the cosmological parameters constraints such as dark energy properties to make cosmological inferences (Chang et al., 2008; Visbal et al., 2009), measure BAOs (Masui et al., 2010a; Mao, 2012), and even constrain modified gravity models (Masui et al., 2010b; Brax et al., 2013). Apart from using HI emission line, cumulative emission of other atomic and molecular lines from galaxies can be mapped out using the IM technique provided such spectra lines can be identified and detected (Pritchard and Loeb, 2012). HI IM techniques from radio astronomy surveys thus provide a revolutionary approach to the problem of dark energy and will help to unveil how the Universe evolved since the Big Bang, consequently, giving us the ability to probe and constrain the nature of dark energy that accelerates the Universe's expansion. However, HI IM will also enable us to study properties and effects of dark matter which is currently the second most significant component in the Universe, after dark energy.

1.3.3 Baryonic Acoustic Oscillations

Baryonic acoustic oscillations (BAOs) are the density fluctuations of the luminous ordinary matter that makes up about 4% of the Universe budget. The same comoving BAOs length scale that was triggered by the primordial acoustic waves in the early universe can be observed over many epochs. Such observed angular scale over different redshifts provides a geometric measure of the Universe expansion history. As photons decoupled, they relaxed the cosmos from high pressure that was once exerted by high temperature and clustering of ionized gas. Decoupling left behind at a fixed length scale, the patterns of the oscillatory acoustic waves in the visible baryonic matter density, which are commonly known as baryonic acoustic oscillations (BAOs) (Eisenstein et al., 2005; Bull et al., 2015a). BAOs can be used as statistical standard ruler, to accurately constrain distance measurements and the geometry of the expanding universe. By employing this characteristic acoustic scale, cosmological length scales via measurements of the sound horizon using matter/galaxy clustering and CMB probes can be achieved (Seo and Eisenstein, 2003; Glazebrook and Blake, 2005; Bull et al., 2015a; Abdalla et al., 2015).

However, IM technique can deliver bright tomographic maps of HI emission distribution present in the Universe today over large angular scales and detect/measure BAO scale/signatures through the 21-cm power spectrum (Villaescusa-Navarro et al., 2017).

To see how BAOs is used to measure the length of the sound horizon as a function of cosmic time, suppose that a ruler/intrinsic length l subtends an angle $\Delta\theta$, and these parameters are related to the cosmological angular-diameter distance as (see Xu et al. (2015))

$$\Delta\theta = \frac{l}{d_{\rm A}(1+z)}, \tag{1.3.1}$$

where ($r(z)$ is the co-moving distance)

$$d_{\rm A}(z) = \frac{r(z)}{1+z}, \tag{1.3.2}$$

and the parameter of interest $H(z)$ is obtained via the formula,

$$r(z) = \int_0^z \frac{{\rm d}z'}{H(z')}. \tag{1.3.3}$$

However, we can determine from the measurements the redshift interval, Δz, and use the standard ruler to calculate the Hubble parameter directly as

$$H(z) = \frac{\Delta z}{l}. \tag{1.3.4}$$

This can in turn be used to constrain cosmological parameters, such as dark energy and provide scientific assessment of the accelerated expansion of the Universe (Bull et al., 2015a; Bernal et al., 2019).

1.3.4 The 21-cm Mean Brightness Temperature

We adopt the style and materials presented by Lewis and Challinor (2007); Challinor and Lewis (2011); Hall et al. (2013) to explain the calculations of the 21-cm mean brightness temperature

(Barkana and Loeb, 2007). We represent by $n_{\rm HI}$, the neutral hydrogen atom rest-frame (proper) number density at the redshift z along some line-of-sight. We further denote a fraction of HI number density at the excited triplet states by $n_1/n_{\rm HI}$ and that in the singlet 21-cm hyperfine transition state by $n_0/n_{\rm HI}$. With reference to the gas rest-frame, a propagation in proper time $\mathrm{d}t$ within a solid angle $\mathrm{d}\Omega$ due to 21-cm interactions, will result into the net number of emitted 21-cm photons per unit volume, with energy between E and $E+\mathrm{d}E$:

$$\mathrm{d}n_{\rm emit} = \frac{1}{4\pi}\Big[(n_1-3n_0)N_\gamma + n_1\Big]A_{10}\delta(E-E_{21})\mathrm{d}E\mathrm{d}t\mathrm{d}\Omega, \tag{1.3.5}$$

where N_γ is the photon phase space density controlling stimulated emission, $A_{10}\approx 2.869\times 10^{-15}\ \mathrm{s}^{-1}$ described in Wild (1952) is the coefficient of spontaneous emission, $E_{21}=5.88\ \mu\mathrm{eV}$ is the 21-cm photon rest-frame energy and $\delta(E-E_{21})$ is the difference in energies between the 21-cm rest-frame and the stimulated/excited emission. As you should have already noted, n_0, n_1 are respectively, the number densities of $n_{\rm HI}$ in the singlet and excited triplet states of 21-cm hyperfine transition. Because we are considering large (linear) scales, the HI emission finite line width has been neglected, and we have assumed isotropically populated atomic triplet states (discussed further in Lewis and Challinor (2007)). The spin temperature is defined by population levels by

$$\frac{n_1}{n_0} = 3e^{-T_{21}/T_{\rm s}}, \tag{1.3.6}$$

where for a Boltzmann's constant $k_{\rm B}=1.381\times 10^{-16}\,\mathrm{erg\,K^{-1}}$, $T_{21}=E_{21}/k_{\rm B}=0.068\,\mathrm{K}$. At appropriate frequency range, the radiation field is assumed to consist of the additional photons from the interactions of the 21-cm and the CMB blackbody whose temperature $T_{\rm CMB}\gg T_{21}$. Due to the coupling of spin and gas temperatures by Lyα photons, $T_{\rm s}\gg T_{\rm CMB}$ (Pritchard and Loeb, 2012) at low redshifts, thus we can neglect stimulated emission and absorption lines. This limit reduces Equation (1.3.5) to

$$\mathrm{d}n_{\rm emit} \approx \frac{3}{16\pi}n_{\rm HI}A_{10}\delta(E-E_{21})\mathrm{d}E\mathrm{d}t\mathrm{d}\Omega \tag{1.3.7}$$

(independent of spin temperature). Neglecting the Thomson scattering of the line radiation anisotropies, and since re-absorption is negligible (at $z=2$, the Thomson optical depth is 0.008), summation of all emitted photons is simply a calculation for the brightness temperature. For a line-of-sight direction $\hat{\mathbf{n}}$, collected number of photons of energies between E and $E+\mathrm{d}E$ in proper time $\mathrm{d}t$ in an area $\mathrm{d}A$ which subtends at an observer a solid angle of $\mathrm{d}\Omega$,

$$\mathrm{d}n_{\rm rec} = f(E,\hat{\mathbf{n}})E^2\mathrm{d}E\mathrm{d}\Omega\mathrm{d}A\mathrm{d}t \tag{1.3.8}$$

are the photon numbers received by an observer, where $f(E,\hat{\mathbf{n}})$ is the photon distribution function. Emitted photons are received along the line-of-sight by a four-velocity $u^{\rm a}$ observer, and by considering the propagation of the null geodesics congruence that focus at the observer we can relate Equation (1.3.7) and Equation (1.3.8). Consider that, corresponding to some source position is an affine parameter λ such that the invariant area of the wavefront at λ is

denoted by $\mathrm{d}\tilde{A}$. Then the volume swept out by the wavefront in an interval $\mathrm{d}\lambda$ is $\mathrm{d}\tilde{A}u_{\mathrm{s}}^{\mathrm{a}}k_{\mathrm{a}}\mathrm{d}\lambda$ where $u_{\mathrm{s}}^{\mathrm{a}}$ is the four-velocity of a source and $k^{\mathrm{a}} = \mathrm{d}x^{\mathrm{a}}/\mathrm{d}\lambda$. Now suppose $\mathrm{d}A$ is the detector collecting area, $\mathrm{d}\tilde{\Omega}$ is the sold angle subtended by this area at the source in its rest-frame, then for a solid angle $\mathrm{d}\Omega$ in time $\mathrm{d}t$ at an observer-frame, photons in an energy range $\mathrm{d}E$ around energy E will be collected with number

$$\begin{aligned} \mathrm{d}n_{\mathrm{rec}} &= \frac{3}{16\pi}\int \mathrm{d}\lambda\Big[n_{\mathrm{HI}}A_{10}\delta\left[E(1+z)-E_{21}\right](1+z)\mathrm{d}E\frac{\mathrm{d}t}{1+z}\mathrm{d}\tilde{\Omega}\mathrm{d}\tilde{A}k_{\mathrm{a}}u_{\mathrm{s}}^{\mathrm{a}}\Big] \\ &= \frac{3}{16\pi}n_{\mathrm{HI}}A_{10}(1+z)\left|\frac{\mathrm{d}\lambda}{\mathrm{d}z}\right|\mathrm{d}E\mathrm{d}t\mathrm{d}\tilde{\Omega}\mathrm{d}\tilde{A}, \end{aligned} \tag{1.3.9}$$

where in the first equality above the integral is evaluated along the line-of-sight, and quantities in the second equality are evaluated along the line-of-sight at redshift z for which $1+z = E_{21}/E$. Where $k_{\mathrm{a}}u_{\mathrm{s}}^{\mathrm{a}} = E_{21}$ has been used, integration of the product of $\mathrm{d}n_{\mathrm{emit}}$ from (1.3.7) and the volume element $\mathrm{d}\tilde{A}u_{\mathrm{s}}^{\mathrm{a}}k_{\mathrm{a}}\mathrm{d}\lambda$ along the line-of-sight yields Equation (1.3.9). Using

$$\mathrm{d}\tilde{A}\mathrm{d}\tilde{\Omega} = \frac{\mathrm{d}A\mathrm{d}\Omega}{(1+z)^2} \tag{1.3.10}$$

(the reciprocity relation), and by comparing with Equation (1.3.8), we find

$$f(E,\hat{\mathbf{n}}) = \frac{3}{16\pi}\frac{n_{\mathrm{HI}}A_{10}(1+z)}{E_{21}^2}\left|\frac{\mathrm{d}\lambda}{\mathrm{d}z}\right|. \tag{1.3.11}$$

The photon distribution function $f(E,\hat{\mathbf{n}})$ is related to T_{b}, the 21-cm brightness temperature by

$$k_{\mathrm{B}}T_{\mathrm{b}} = \frac{1}{2}h_{\mathrm{p}}^3Ef(E,\hat{\mathbf{n}}), \tag{1.3.12}$$

where h_{p} is Planck's constant. We finally have

$$T_{\mathrm{b}}(z,\hat{\mathbf{n}}) = \frac{3}{32\pi}\frac{h_{\mathrm{p}}^3n_{\mathrm{HI}}A_{10}}{k_{\mathrm{B}}E_{21}}\left|\frac{\mathrm{d}\lambda}{\mathrm{d}z}\right|. \tag{1.3.13}$$

This equation must include perturbations in $|\mathrm{d}z/\mathrm{d}\lambda|$, and requires evaluation of the perturbed n_{HI} at perturbed positions relevant to z and $\hat{\mathbf{n}}$ if considered in the presence of perturbations (Hall et al., 2013).

For the Hubble parameter $H(z)$, if perturbations

$$\frac{\mathrm{d}z}{\mathrm{d}\lambda} = (1+z)H(z)E_{21} \tag{1.3.14}$$

are initially ignored, the 21-cm mean brightness temperature is

$$\begin{aligned} \overline{T}_{\mathrm{b}} &= \frac{3(h_{\mathrm{p}}c)^3\bar{n}_{\mathrm{HI}}A_{10}}{32\pi k_{\mathrm{B}}E_{21}^2(1+z)H(z)} \\ &= 0.188\ \mathrm{K}\ h\Omega_{\mathrm{HI}}(z)\frac{(1+z)^2}{E(z)}, \end{aligned} \tag{1.3.15}$$

where $\Omega_{\mathrm{HI}}(z)$, calculated in units of the present day critical density is the HI fractional density, $E(z) = H(z)/H_0$ (see Equation (1.1.133) under Subsection 1.1.5) with $H_0 = 100h\,\mathrm{km\,s^{-1}\,Mpc^{-1}}$

being the Hubble constant. Significant evolution in the value of $\Omega_{\rm HI}$ is not expected over the range of considered redshifts (Prochaska and Wolfe, 2009). The local value of $\Omega_{\rm HI}$ found by HIPASS survey (Zwaan et al., 2005) is in consistence with $\Omega_{\rm HI} = 4 \times 10^{-4}$, and can be taken to be constant (Hall et al., 2013). In the linear theory, and by considering the presence of perturbations, including all line-of-sight and relativistic effects, calculations of the 21-cm brightness temperature have been carried in Hall et al. (2013), and the results applied to construct the angular cross-power spectra between redshift windows. An account analogous to Hall et al. (2013) in the context of galaxy surveys applied for the discrete objects such as galaxy number counts calculations is given in Yoo et al. (2009); Bonvin and Durrer (2011); Challinor and Lewis (2011); Jeong et al. (2012).

1.3.5 Spherical Harmonics and Angular Power Spectrum of the HI Signal

The techniques developed for studying CMB anisotropies can be devised to construct the angular power spectrum of HI intensity over a certain frequency range. The 3-dimensional power spectrum of the HI can be computed using the formula (Battye et al., 2013)

$$\Big[\Delta T_{\rm HI}(\vec{k}, z)\Big]^2 = \overline{T}(z)^2 \Big[b(\vec{k}, z)\Big]^2 \frac{k^3 P_{\rm CDM}(\vec{k}, z)}{2\pi^2}, \tag{1.3.16}$$

where $\overline{T}(z)$ is the mean temperature, $b(\vec{k}, z)$ is the bias and $P_{\rm CDM}$ is the power spectrum of the underlying dark matter. At large angular scales, the HI signal has a spectrum $T_{\rm HI} \propto k^2$. The underlying dark matter power spectrum, $P_{\rm CDM}$ can today ($z = 0$) be computed by (Battye et al., 2013)

$$P_{\rm CDM}(\vec{k}) = A \vec{k}^{n_{\rm s}} T^2(\vec{k}) \tag{1.3.17}$$

where $T(\vec{k})$ is the transfer function and $n_{\rm s}$ is the primordial spectral index. The brightness temperature $T_{\rm b}$ is sensitive to cosmology and can act as an indirect thermometer at different redshifts. Its strong coupling with various astrophysical and cosmological effects makes it an excellent probe of various LSS phenomena such as the ionization state of hydrogen at different epochs.

One can follow a procedure outlined in Battye et al. (2013) to compute the 2-dimensional angular power spectrum of the HI by first obtaining the 3-dimensional quantity $\delta\tilde{T}(\vec{r}(z)\hat{\boldsymbol{n}}, z)$ (estimates of sky projection of the temperature perturbation) which can be achieved by replacing the HI density $\rho_{\rm HI}$ with its linear density field $\delta_{\rho_{\rm HI}}$ in equation (8) of Battye et al. (2013).

Here, we adopt a slightly different approach to calculating the HI power spectrum, and start by considering the real-space brightness temperature fluctuation density contrast (as a function of redshift z and position/direction $\hat{\boldsymbol{n}}$ on the sky)

$$\Delta_{T_{\rm b}}(z, \hat{\boldsymbol{n}}) = \delta_n - \frac{1}{\mathcal{H}}\Big[\hat{\boldsymbol{n}} \cdot \Big(\hat{\boldsymbol{n}} \cdot \vec{\nabla}\Big)\, \vec{v}\Big] + \left(\frac{{\rm d}\ln\left(a^3 \bar{n}_{\rm HI}\right)}{{\rm d}\eta} - \frac{\dot{\mathcal{H}}}{\mathcal{H}} - 2\mathcal{H}\right)\delta_\eta + \frac{1}{\mathcal{H}}\Phi + \Psi \tag{1.3.18}$$

where

$$\hat{\boldsymbol{n}} \cdot \left(\hat{\boldsymbol{n}} \cdot \vec{\nabla}\right) \vec{v} = \sum_{i,j} \hat{\boldsymbol{n}}_i \cdot \left(\hat{\boldsymbol{n}}_j \cdot \nabla_j\right) v_i. \tag{1.3.19}$$

From Equation (1.3.18), the first two terms are respectively, the density and the redshift-space distortion (RSD), the third term results from evaluating the zero-order brightness temperature at the perturbed time corresponding to the observed redshift, whereas the fourth term is the integrated Sachs-Wolfe (ISW) effect, and the last term (arises from $|\mathrm{d}\lambda/\mathrm{d}z|$) is a result of conversion between radio distance in gas frame ($\mathrm{d}\lambda$) with increments in redshift (z), see Lewis and Challinor (2007); Challinor and Lewis (2011); Hall et al. (2013) for more details. Note that $\mathcal{H}$ is the conformal Hubble parameter.

Let us transform the density contrast (1.3.18) into the k-space, and then use the results to calculate the angular power spectrum in the ℓ-space. Therefore,

$$\begin{aligned}
\Delta_{T_\mathrm{b}}(z, \hat{\boldsymbol{n}}) &= \int \frac{\mathrm{d}^3\vec{k}}{(2\pi)^{3/2}} \Delta_{T_\mathrm{b}}(z, \vec{k}, \hat{\boldsymbol{n}}) e^{i\vec{k}\cdot\vec{r}(\hat{\boldsymbol{n}},z)} \\
&= \int \frac{\mathrm{d}^3\vec{k}}{(2\pi)^{3/2}} \Delta_{T_\mathrm{b}}(z, \vec{k}, \hat{\boldsymbol{n}}) \left[4\pi \sum_{\ell,m} i^\ell j_\ell(k\chi) Y^*_{\ell m}(\hat{\boldsymbol{k}}) Y_{\ell m}(\hat{\boldsymbol{n}})\right] \\
&= \sum_{\ell,m} \left[\int \frac{\mathrm{d}^3\vec{k}}{(2\pi)^{3/2}} \Delta_{T_\mathrm{b}}(z, \vec{k}, \hat{\boldsymbol{n}}) \left(4\pi i^\ell\right) j_\ell(k\chi) Y^*_{\ell m}(\hat{\boldsymbol{k}})\right] Y_{\ell m}(\hat{\boldsymbol{n}}),
\end{aligned} \tag{1.3.20}$$

and we finally have

$$\Delta_{T_\mathrm{b}}(z, \hat{\boldsymbol{n}}) \equiv \sum_{\ell,m} \left[\left(4\pi i^\ell\right) \int \frac{\mathrm{d}^3\vec{k}}{(2\pi)^{3/2}} \Delta_{T_\mathrm{b},\ell}(z, \vec{k}) Y^*_{\ell m}(\hat{\boldsymbol{k}})\right] Y_{\ell m}(\hat{\boldsymbol{n}}), \tag{1.3.21}$$

where j_ℓ is the spherical Bessel function and $\chi(z)$ is the comoving distance to redshift z.

The equivalence expression (1.3.21) is of our interest; we will apply the Fourier transform and expand the Fourier modes in spherical harmonics, so that the term $\Delta_{T_\mathrm{b},\ell}(z, \vec{k})$ becomes the Fourier space density contrast of ℓ-mode. To do so, each term in Equation (1.3.18) from the first to fifth is Fourier transformed using the general transform

$$\Delta^{(n^\mathrm{th}-\mathrm{term})}_{T_\mathrm{b}}(z, \hat{\boldsymbol{n}}) = \int \frac{\mathrm{d}^3\vec{k}}{(2\pi)^{3/2}} \mathcal{F}\left(n^\mathrm{th}-\mathrm{term}\right) e^{i\vec{k}\cdot\vec{r}(\hat{\boldsymbol{n}},z)}, \tag{1.3.22}$$

and in addition apply the plane-wave expansion

$$e^{i\vec{k}\cdot\vec{r}(\hat{\boldsymbol{n}},z)} = \sum_{\ell,m} \left(4\pi i^\ell\right) j_\ell(k\chi) Y^*_{\ell m}(\hat{\boldsymbol{k}}) Y_{\ell m}(\hat{\boldsymbol{n}}), \tag{1.3.23}$$

where $\mathcal{F}$ represents the Fourier transform of a particular term in Equation (1.3.18). Our final output will then involve summing up the results of each transformation.

We use the notation "$\sim$" to represent the Fourier function, for example $\mathcal{F}(\delta_n) = \tilde{\delta_n}$. Therefore,

the Fourier transform of the first, fourth and fifth terms is

$$\begin{aligned}\Delta_{T_b}^{(1,4,5)}(z,\hat{\boldsymbol{n}}) &= \int \frac{\mathrm{d}^3\vec{k}}{(2\pi)^{3/2}}\mathcal{F}\left[\delta_n + \frac{1}{\mathcal{H}}\dot{\Phi} + \Psi\right]e^{i\vec{k}\cdot\vec{r}(\hat{\boldsymbol{n}},z)} \\ &= \int \frac{\mathrm{d}^3\vec{k}}{(2\pi)^{3/2}}\left[\tilde{\delta_n} + \frac{1}{\mathcal{H}}\tilde{\dot{\Phi}} + \tilde{\Psi}\right]\left[\sum_{\ell,m}\left(4\pi i^\ell\right) j_\ell(k\chi)Y^*_{\ell m}(\hat{\boldsymbol{k}})Y_{\ell m}\right] \\ &= \sum_{\ell,m}\left[\left(4\pi i^\ell\right)\int \frac{\mathrm{d}^3\vec{k}}{(2\pi)^{3/2}}\left(\tilde{\delta_n} + \frac{1}{\mathcal{H}}\tilde{\dot{\Phi}} + \tilde{\Psi}\right)j_\ell(k\chi)Y^*_{\ell m}(\hat{\boldsymbol{k}})\right]Y_{\ell m}(\hat{\boldsymbol{n}}),\end{aligned} \tag{1.3.24}$$

where by comparing the last equality above with (1.3.21), we finally have

$$\Delta_{T_{b,\ell}}^{(1,4,5)}(z,\vec{k}) = \left(\tilde{\delta_n} + \frac{1}{\mathcal{H}}\tilde{\dot{\Phi}} + \tilde{\Psi}\right)j_\ell(k\chi). \tag{1.3.25}$$

For the redshift-space distortion term (second term), we first perform some transformation by defining the velocity field in both real and Fourier space,

$$\vec{v}(\vec{r}) = \int \frac{\mathrm{d}^3\vec{k}}{(2\pi)^{3/2}}\tilde{\boldsymbol{v}}(\vec{k})e^{i\vec{k}\cdot\vec{r}}. \tag{1.3.26}$$

In this case, the dimension of $\vec{v}(\vec{r})$ is $\left[\mathrm{LT}^{-1}\right]$, and thus the dimension of $\tilde{\boldsymbol{v}}(\vec{k})$ is $\left[\mathrm{L}^3\mathrm{T}^{-1}\right]$. We want to preserve the dimension, so, we define the scalar $\tilde{v}(\vec{k})$ to have the same dimension as $\vec{v}(\vec{k})$ according to Hall et al. (2013),

$$\vec{v}(\vec{k}) = -i\hat{\boldsymbol{k}}\tilde{v}(\vec{k}). \tag{1.3.27}$$

Therefore, the Fourier transform of the RSD term is then

$$\begin{aligned}\Delta_{T_b}^{(2)}(z,\hat{\boldsymbol{n}}) &= \int \frac{\mathrm{d}^3\vec{k}}{(2\pi)^{3/2}}\mathcal{F}\left[-\frac{1}{\mathcal{H}}\hat{\boldsymbol{n}}\cdot\left(\hat{\boldsymbol{n}}\cdot\vec{\nabla}\vec{v}\right)\right]e^{i\vec{k}\cdot\vec{r}} \\ &= \int \frac{\mathrm{d}^3\vec{k}}{(2\pi)^{3/2}}\left[-\frac{1}{\mathcal{H}}\left(\hat{\boldsymbol{k}}\cdot\hat{\boldsymbol{n}}\right)^2 k\tilde{v}\left(\vec{k}\right)\right]e^{i\vec{k}\cdot\vec{r}} \\ &= -\frac{1}{\mathcal{H}}\int \frac{\mathrm{d}^3\vec{k}}{(2\pi)^{3/2}}\left(\tilde{v}(\vec{k})\left(\hat{\boldsymbol{k}}\cdot\hat{\boldsymbol{n}}\right)^2 k\right)e^{i\vec{k}\cdot\vec{r}}.\end{aligned} \tag{1.3.28}$$

Note that

$$\frac{\partial e^{i\vec{k}\cdot\vec{r}}}{\partial\chi} = \frac{\partial e^{i(\vec{k}\cdot\hat{\boldsymbol{n}})\chi}}{\partial\chi} = (i\hat{n}^i k_i)e^{i\vec{k}\cdot\vec{r}}, \tag{1.3.29}$$

which implies

$$\frac{\partial^2 e^{i\vec{k}\cdot\vec{r}}}{\partial\chi^2} = -\left(\hat{n}^i k_i\right)\left(\hat{n}^j k_j\right)e^{i\vec{k}\cdot\vec{r}} = -\left(\vec{k}\cdot\hat{\boldsymbol{n}}\right)^2 e^{i\vec{k}\cdot\vec{r}}; \tag{1.3.30}$$

and the last equality of Equation (1.3.28) becomes

$$\begin{aligned}\Delta_{T_b}^{(2)}(z,\hat{\boldsymbol{n}}) &= \frac{1}{\mathcal{H}}\int \frac{\mathrm{d}^3\vec{k}}{(2\pi)^{3/2}}\tilde{v}(\vec{k})\left(k\frac{\partial^2 e^{i\vec{k}\cdot\vec{r}}}{\partial\chi^2}\right) \\ &= \sum_{\ell,m}\left[\left(4\pi i^\ell\right)\int \frac{\mathrm{d}^3\vec{k}}{(2\pi)^{3/2}}\left(\frac{1}{\mathcal{H}}\tilde{v}(\vec{k})kj_\ell''(k\chi)\right)Y^*_{\ell m}(\hat{\boldsymbol{k}})\right]Y_{\ell m}(\hat{\boldsymbol{n}}),\end{aligned} \tag{1.3.31}$$

and thus

$$\Delta^{(2)}_{T_{\mathrm{b},\ell}}(z,\vec{k}) = \frac{1}{\mathcal{H}}\tilde{v}(\vec{k})kj''_\ell(k\chi). \tag{1.3.32}$$

For the third term of Equation (1.3.18) we will consider the equation

$$\mathcal{H}(\bar{\eta}_z)\delta_\eta = \Psi_{\mathrm{A}} - \Psi + \int_{\eta_{\mathrm{A}}}^{\bar{\eta}_z}(\dot{\Phi}+\dot{\Psi})\mathrm{d}\eta' + \hat{\boldsymbol{n}}\cdot(\vec{v}-\vec{v}_{\mathrm{oA}}), \tag{1.3.33}$$

for which the substitution/approximation $\eta \to \bar{\eta}$ has been made (since the difference is second order), where Ψ and Φ are the ISW terms which are functions of spatial hyper-surface $\vec{r}$ at each conformal time $\bar{\eta}$, i.e., $\Psi(\vec{r},\eta)$, $\Phi(\vec{r},\eta)$, so that $\delta\eta$ is both a function of $\hat{\boldsymbol{n}}$ on the sky and a function of redshift z. From Equation (1.3.18), the term in the brackets is a redshift-dependent term, and the spatial dependence is simply encoded in $\delta\eta$, thus using Equation (1.3.33) above, we calculate the Fourier transform of δ_η as

$$\mathcal{F}(\delta_\eta) = \frac{1}{\mathcal{H}(\bar{\eta}_z)}\mathcal{F}\left[\Psi_{\mathrm{A}} - \Psi + \int_{\eta_{\mathrm{A}}}^{\bar{\eta}_z}(\dot{\Phi}+\dot{\Psi})\mathrm{d}\eta' + \hat{\boldsymbol{n}}\cdot(\vec{v}-\vec{v}_{\mathrm{oA}})\right]. \tag{1.3.34}$$

We drop out the two constant terms Φ_{A} and $\vec{v}_{\mathrm{oA}}$, since they only affect the multipole moment $\ell = 1$. For the term Ψ, $\mathcal{F}(\Psi) = \tilde{\Psi}$. The Fourier transform of the velocity term is

$$\mathcal{F}(\hat{\boldsymbol{n}}\cdot\vec{v}) = \hat{\boldsymbol{n}}\cdot\vec{v}(\vec{k}) = -i(\hat{\boldsymbol{k}}\cdot\hat{\boldsymbol{n}})\tilde{v}(\vec{k}). \tag{1.3.35}$$

Carrying similar transformation analogous to the previous ones, we have

$$\Delta_{T_{\mathrm{b},\ell}}(z,\vec{k}) \approx -\tilde{v}(\vec{k})j'_\ell(k\chi). \tag{1.3.36}$$

For the ISW term we neglect higher order perturbation and use $\mathrm{d}\chi = -\mathrm{d}\eta$. Therefore, we have

$$\begin{aligned}
&\int_{\eta_{\mathrm{A}}}^{\bar{\eta}_z}\Big(\dot{\Phi}(\boldsymbol{r'},\eta') + \dot{\Psi}(\boldsymbol{r'},\eta')\Big)\mathrm{d}\eta' \\
&= \int_{\eta_{\mathrm{A}}}^{\bar{\eta}_z}\mathrm{d}\eta'\left[\int\frac{\mathrm{d}^3\vec{k}}{(2\pi)^{3/2}}\Big(\tilde{\dot{\Phi}}(\vec{k},\eta') + \tilde{\dot{\Psi}}(\vec{k},\eta')\Big)e^{i\vec{k}\cdot\boldsymbol{r'}(z',\hat{\boldsymbol{n}})}\right] \\
&= \int_{\eta_{\mathrm{A}}}^{\bar{\eta}_z}\mathrm{d}\eta'\left[\int\frac{\mathrm{d}^3\vec{k}}{(2\pi)^{3/2}}\Big(\tilde{\dot{\Phi}}(\vec{k},\eta') + \tilde{\dot{\Psi}}(\vec{k},\eta')\Big)\left(\sum_{\ell,m}\Big(4\pi i^\ell\Big)\,j_\ell(k\chi')Y^*_{\ell m}(\hat{\boldsymbol{k}})Y_{\ell m}(\hat{\boldsymbol{n}})\right)\right] \\
&= \sum_{\ell m}\left[\Big(4\pi i^\ell\Big)\int\frac{\mathrm{d}^3\vec{k}}{(2\pi)^{3/2}}\left(-\int_0^\chi\mathrm{d}\chi'\Big(\tilde{\dot{\Phi}}(\vec{k},\eta') + \tilde{\dot{\Psi}}(\vec{k},\eta')\Big)j_\ell(k\chi')\right)Y^*_{\ell m}(\hat{\boldsymbol{n}})\right]Y_{\ell m}(\hat{\boldsymbol{n}}),
\end{aligned} \tag{1.3.37}$$

from which we finally get

$$\Delta_{T_{\mathrm{b},\ell}}(z,\vec{k}) \approx -\int_0^\chi\Big(\tilde{\dot{\Phi}} + \tilde{\dot{\Psi}}\Big)\,j_\ell(k\chi')\mathrm{d}\chi'. \tag{1.3.38}$$

In the first line of (1.3.37) above, $\boldsymbol{r'}$ corresponds to the 3-dimensional hypersurface at conformal time η'. The role of the Bessel function is to show how different Fourier modes project onto different angular scales.

Summing all together, the third term in Equation(1.3.18) becomes

$$\Delta^{(3)}_{T_{\mathrm{b},\ell}}(z,\vec{k}) = -\left(\frac{1}{\mathcal{H}}\frac{\mathrm{d}\ln(a^3\bar{n}_{\mathrm{HI}})}{\mathrm{d}\eta} - \frac{\dot{\mathcal{H}}}{\mathcal{H}^2} - 2\right) \times \left[\tilde{\Psi} j_\ell(k\chi) + \tilde{v}(\vec{k}) j'_\ell(k\chi) + \int_0^\chi \left(\dot{\tilde{\Phi}} + \dot{\tilde{\Psi}}\right) j_\ell(k\chi')\mathrm{d}\chi'\right]. \tag{1.3.39}$$

Therefore, the complete $\Delta_{T_{\mathrm{b},\ell}}$ term in Equation (1.3.21) is given by

$$\begin{aligned}\Delta_{T_{\mathrm{b},\ell}}(z,\vec{k}) &= \Delta^{(1)}_{T_{\mathrm{b},\ell}}(z,\vec{k}) + \Delta^{(2)}_{T_{\mathrm{b},\ell}}(z,\vec{k}) + \Delta^{(3)}_{T_{\mathrm{b},\ell}}(z,\vec{k}) + \Delta^{(4)}_{T_{\mathrm{b},\ell}}(z,\vec{k}) + \Delta^{(5)}_{T_{\mathrm{b},\ell}}(z,\vec{k}) \\ &= \left(\tilde{\delta}_n + \frac{1}{\mathcal{H}}\dot{\tilde{\Phi}} + \tilde{\Psi}\right) j_\ell(k\chi) + \frac{1}{\mathcal{H}}\tilde{v}(\vec{k}) k j''_\ell(k\chi) \\ &\quad - \left(\frac{1}{\mathcal{H}}\frac{\mathrm{d}\ln(a^3\bar{n}_{\mathrm{HI}})}{\mathrm{d}\eta} - \frac{\dot{\mathcal{H}}}{\mathcal{H}^2} - 2\right) \times \left[\tilde{\Psi} j_\ell(k\chi) + \tilde{v}(\vec{k}) j'_\ell(k\chi) + \int_0^\chi \left(\dot{\tilde{\Phi}} + \dot{\tilde{\Psi}}\right) j_\ell(k\chi')\mathrm{d}\chi'\right].\end{aligned} \tag{1.3.40}$$

From Equation (1.3.40) above, the physical meanings of the first, second and the third terms (each multiplied with a front factor which is interpreted as $\mathrm{d}\overline{T}_{\mathrm{b}}/\mathrm{d}\eta$) in the square brackets are respectively, the usual contributions from CMB which are the Sachs-Wolfe (SW) effect, Doppler shift, and the Integrated Sachs-Wolfe (ISW) effect contributions. The interpretation of the second term is that the observer knows a photon he collects at some frequency v was emitted at a certain earlier time, provided HI is not moving. However, if HI is moving, then the observer knows that a photon he collects at frequency v was emitted at an earlier or later time. This simply means the signal collected by an observer depends on whether HI is moving or static. The second term arises because, at a certain observed redshift, emitting gas with peculiar velocity lies at a different comoving distance in contrast to FRW prediction. Thus, we actually observe gas at different conformal distances, as we observe at different redshifts the temperature fluctuations across the sky. Although individual terms may be/are gauge-dependent, the sum of all terms in the equation above is gauge-invariant. For the rest of the terms, δ_n is the intrinsic function, the second v term is the familiar RSD term, but the quantity $(\dot{\tilde{\Phi}}/\mathcal{H} + \tilde{\Psi})$ has no usual meaning.

The angular and physical scales should clearly be contrasted. The contribution of the 21-cm angular power spectrum to the large angular part corresponds to small values of ℓ and comes from small physical scales (large values of k).

Once $\Delta_{T_{\mathrm{b},\ell}}(\vec{k}, z)$ is obtained, we can integrate over the frequency band and calculate the projected $\Delta_{T_{\mathrm{b},\ell}}$ for band W (angular window function) for each $\vec{k}$ (see Hall et al. (2013)),

$$\Delta_{T_{\mathrm{b},\ell}}(\vec{k}) = \int \mathrm{d}z W(z) \Delta_{T_{\mathrm{b},\ell}}(\vec{k}, z), \tag{1.3.41}$$

and obtain the power spectrum

$$C_\ell^{WW'} = 4\pi \int \mathrm{d}\ln k P_{\mathcal{R}}(k) \Delta'^{W}_{T_{\mathrm{b},\ell}}(k) \Delta'^{W'}_{T_{\mathrm{b},\ell}}(k), \tag{1.3.42}$$

where

$$\Delta'_{T_{\mathrm{b},\ell}}(k) = \Delta_{T_{\mathrm{b},\ell}}(\vec{k})/\mathcal{R}(\vec{k}). \tag{1.3.43}$$

For very large frequency band width, the RSD term will drop, since the line-of-sight radial integral over many peaks and troughs approximately becomes close to zero. At large angular scales (small ℓ), the 21-cm power spectrum is almost constant.

We can however consider the HI density field $f(\theta, \phi)$ over a sphere which can be expanded in multipoles

$$f(\theta, \phi) = \sum_{\ell m} a_{\ell m} Y_{\ell m}(\theta, \phi), \tag{1.3.44}$$

and calculate the angular power spectrum given by the ensemble average of the expansion coefficients as

$$C_\ell = \langle a_{\ell m} a^*_{\ell m} \rangle \equiv \frac{1}{2\ell + 1} \sum_m |\hat{a}_{\ell m}|^2, \tag{1.3.45}$$

just as discussed under Subsection (1.2.1) for CMB anisotropies.

1.3.6 The EoR Experiments and Cosmic Dawn

Neutral hydrogen is ubiquitous in the Universe and the redshifted 21-cm emission line it emits as photon (or radio wave) due to spin-flip transition (Field, 1958) allows us to trace it. The Hydrogen Epoch of Reionization (EoR) is one of the two major hydrogen phase transitions in the Universe after the recombination phase for which the CMB was emitted. The study of the EoR is crucial and will provide answers to many fundamental questions in cosmology, such as how galaxies, quasars and ultra-low metallicity stars formed. The prospects of detecting the 21-cm signal with various experiments in the EoR have been discussed in Morales and Wyithe (2010) (see also Pritchard and Loeb (2012)). In particular, the EoR is the period when the HI in the intergalactic medium (IGM) - the cosmic gas that fills the vast space between galaxies (Barkana and Loeb, 2007), was reionized by the ultraviolet photons, which are likely to come from the first galaxies (Pober et al., 2014). During this period the cosmic gas went from neutral to ionized. The EoR gives us access to test LSS with more large comoving volumes than the volume accessible for galaxy surveys, hence it will increase our efficiency in surveying the Universe. Numerous current, near-term and next generation 21-cm experiments are targeting the Epoch of reionization (Pober et al., 2014). These experiments include, but are not limited to, Hydrogen Epoch of Reionization Array (HERA) (DeBoer et al., 2017), the Precision Array for Probing the Epoch of Reionization (PAPER) (Parsons et al., 2010; Pober et al., 2013a), the LOw-Frequency ARray (LOFAR) (Yatawatta et al., 2013; van Haarlem et al., 2013), the Murchison Widefield Array (MWA) (Tingay et al., 2013; Bowman et al., 2013), the Baryon Acoustic Oscillation Broadband and Broad-beam (BAOBAB) array (Pober et al., 2013b), and the Giant Metrewave Radio Telescope (GMRT) (Swarup, 1990) which has recently undergone a major upgrade (the uGMRT project) (Gupta et al., 2017).

The redshifted 21-cm line is very sensitive to astrophysics, and using CMB as a backlight, the brightness temperature contrast as a result of the HI emitting or absorbing signal is related to

the CMB temperature $T_{\rm CMB}$, spin temperature of the gas $T_{\rm spin}$, the hydrogen atom abundance $\delta_{\rm b}$ and the fraction of the neutral hydrogen atom $X_{\rm HI}$ as

$$\triangle T_{\rm b} \propto (1+\delta_{\rm b})\, X_{\rm HI}\left(1-\frac{T_{\rm CMB}}{T_{\rm spin}}\right). \tag{1.3.46}$$

Here, $X_{\rm HI} \in [0,1]$, where 0 means neutral and 1 means completely ionized, see full details in Park et al. (2019). Spin temperature controls the ratio of hydrogen atoms in the ground and excited hyperfine levels. For example, if most of the hydrogen atoms are on the ground than in the hyperfine state, it is likely that absorption will occur. Further, the spin temperature depends on the details of the environment the hydrogen atom finds itself in. The relation (1.3.46) is coupled to the hydrogen gas temperature and other contributions, and for completeness it can be written as

$$\begin{aligned}\delta T_{\rm b}(\nu) \approx 27 X_{\rm HI}\,(1+\delta_{\rm b})\left(\frac{H(z)}{{\rm d}\nu_{\rm r}/{\rm d}r + H(z)}\right)\left(1-\frac{T_{\rm CMB}}{T_{\rm spin}}\right)\\ \times\left(\frac{1+z}{10}\frac{0.15}{\Omega_{\rm m}h^2}\right)^{1/2}\left(\frac{\Omega_{\rm b}h^2}{0.023}\right),\end{aligned} \tag{1.3.47}$$

where the offset of the 21-cm brightness temperature, $\delta T_{\rm b}$, with respect to the CMB temperature, $T_{\rm CMB}$, is commonly expressed as the 21-cm temperature, such that all quantities are evaluated at redshift $z = \nu_0/\nu - 1$, with ν_0 being the 21-cm frequency. Furthermore, $\delta_{\rm b} \equiv \rho/\bar{\rho} - 1$ is the gas overdensity, and ${\rm d}\nu_{\rm r}/{\rm d}r$ is the gradient of line-of-sight component of the velocity, see more from Furlanetto (2006); Park et al. (2019). Various quantities in the equation above can be computed by using the semi-numerical simulations, such as 21CMFAST (Mesinger et al., 2011). 21CMFAST uses an initial high resolution Gaussian realization, applying second-order linear perturbation theory (see for example Scoccimarro (1998)) to compute the evolved density and velocity fields. Further explanation on how 21CMFAST is used can be found in Mesinger et al. (2011); Park et al. (2019). Equation (1.3.47) is useful for direct and effective modeling of the EoR.

Experiment to Detect the Global Epoch of Reionization Signature (EDGES) is a radio telescope located at the Murchison Radio-astronomy Observatory (MRO) in a radio-quiet zone in western Australia. EDGES is the most promising high-redshift cosmology (78 GHz, $z = 17.3$) probe that is dedicated to finding imprints of the HI that was ionized by the ultraviolet and X-ray radiation from the first luminous objects in the EoR. As previously stated, EoR is the period in the Universe history timeline during which the IGM that had been predominantly neutral was ionized by the the first luminous objects. Such objects may have been stars, galaxies, quasars, or a combination of some.

The EDGES project's goal is to detect radio emission (HI signal) signatures from EoR, immediately, after the first stars and galaxies came into existence. EDGES is a ground-based antenna system comprised of a low-band (Li and Cai, 2019) and a high-band ((Monsalve et al., 2017, 2019), $90-190$ MHz) instrument, a receiver, and other necessary components, such as spectrometer and a ground plane.

EDGES is dedicated to detect primordial imprints as signatures of the very early stars and galaxies ever to form, as a consequence of evolved soup of gas, mostly HI that began to form about 380,000 years from the Big Bang. The HI soup clumped together and intensified itself over time under the influence of gravity forming the first igniting stars, galaxies and other radiative objects (Springel et al., 2006). As a result, the properties of the primordial gas, mostly composed of hydrogen (75%) and helium (25%) in the IGM, radically altered due to ultraviolet and X-ray radiation produced by the first stars and other stellar remnants. Therefore, the redshifted HI gas once filled the vast space between stars absorbed the primordial CMB photons/radiation, and today the 21-cm hyperfine spin-flip transition provides information which enables us to trace back the ages deep to the cosmic dawn, about 180 million years since the Big Bang.

Recent EDGES results (D. Bowman et al., 2018) detected 21-cm absorption signal whose spectral feature deviates from predictions of standard cosmological models. Such anomaly could hint for new research and has been attributed to physics which could have either increased the background radiation intensity than expected or cooled the hydrogen gas spin temperature (Aristizabal Sierra and Fong, 2018; Barkana, 2018; Feng and Holder, 2018; Ewall-Wice et al., 2018; Fraser et al., 2018; Fialkov and Barkana, 2019). If the hypothesis that the gas might have been cooler in the cosmic dawn is confirmed, the dark matter which theories projected that could have been cooler during the early universe may be the possible candidate responsible for low gas temperature due to its interaction with baryons (Fialkov et al., 2018; Muñoz and Loeb, 2018; Munoz and Loeb, 2018; Muñoz et al., 2018; Barkana, 2018) in the cosmic dawn. The EDGES tentative results may be investigated and confirmed by other experiments such as SARAS, OVRO-LWA, 21CMA, PRIZM, and BIGHORNS (Koopmans et al., 2019). Deep probing of reheating and reionization epochs with sensitive observations of emission and absorption lines will facilitate the detailed study of the matter temperature, density and velocity field which in turn will provide at target redshifts information about large volumes of the Universe. Such information can be used to confine the early history of the structure formation, and the origin of many LSS objects we observe today. Reionization period ended at about $z = 6.5$ (Kashikawa et al., 2006; Keating et al., 2015) which is equivalent to approximately 1 billion years from the Big Bang.

1.4 Radio Telescopes

In this section, we describe various properties of telescopes used by astronomers, challenges faced in designing and calibrating such telescopes and some out of many types of measurements that can be carried out. We further describe various concepts (directly and indirectly) related to intrinsic properties of telescopes in relation to distant objects, and how such knowledge can be used to deduce various parameters, which can then be harmoniously connected to gain insightful information about distant universe, in particular, we give highlights on sensitivity, resolution and resolving power of a telescope.

Sensitivity and resolution are two key properties of any radio/optical telescope (Burke and Graham-Smith, 2009; Cheng, 2009; Chromey, 2010). In astronomy, we are mostly interested in objects that are light years distances from us. Apart from magnification power, astronomical telescopes need to be very sensitive and of reasonable resolution so that they can clearly see fainter distant objects. A light hitting a telescope mirror/detector from a distant source being observed carries encoded information about it. Depending on a telescope design, that light can, for example, be reflected to the secondary mirror, and then to the center of the primary mirror before it is sent to the telescope instrument for digitization. Mirrors used by telescopes are called reflectors and their primary function is to bring light into the focus. Telescopes usually have limits as to how smaller the amount of signal they can measure (Cheng, 2009). Smallest signal from an object a telescope measures determines how fainter a distant object can be before a telescope can see it (Cheng, 2009). Sensitivity can thus be defined as the capability of a telescope to see fainter objects. This property of a telescope is related proportionally to the surface area of its detector/mirror, consequently making large mirrors capable of collecting more light than smaller ones (Burke and Graham-Smith, 2009; Cheng, 2009). Due to this reason, large telescopes such as FAST (Burke and Graham-Smith, 2009; Nan et al., 2011) are very sensitive, and can thus see very faint/dim objects, compared to smaller or medium-sized telescopes.

When looking at distant objects using a telescope there is a limit as to how close apart two adjacent objects can be, in order for the telescope to resolve them as distinct. Below such a limit, two distant objects cannot be seen as separate, instead, they will look as if it is a single object or merged objects to the extent it becomes very difficult to distinguish them. To clearly see distant objects as separate, requires telescopes with high resolutions. Resolution is thus an ability of a telescope to see distant objects that are close as distinct (Cheng, 2009). Just like in the case of sensitivity, the resolution of a telescope increases with the size of its mirror, which means larger telescopes have better overall resolutions than smaller ones (Burke and Graham-Smith, 2009). High-resolution telescopes can for example clearly see (resolve) two distant objects separated by as much small angle as 0.6 seconds of arc at the point of observation as distinct. Interferometry telescopes such as SKA uses many integrated single dishes to get a resolution of a much larger telescope.

In summary, sensitivity is the ability of an optical instrument such as radio telescope to see faint objects, while resolution is the ability of a telescope to distinguish (two) objects which are close to each other. Resolution, in general, can also be defined as the ability of a telescope to discern details on the surface of a distant object. Two close distant sources can be resolved as completely distinct, or just resolved in the sense that the two objects partially overlap to the extent a telescope is unable to distinguish between features/details on their surfaces but can only tell that they are definitely two objects (Chromey, 2010).

Therefore, as we have seen, sensitivity and resolution of a telescope play very important roles in observations. Likewise, resolving power of a telescope can be determined by using particular telescope specifications. The light from an object starts to diffract at the boundary of the

telescope aperture as it goes through it. This behaviour limits the resolution of all telescopes. Again, diffraction of light effect at the boundary of a telescope mirror decreases with an increase in aperture (telescope) size. As a result, resolution of a telescope is proportional to the wavelength λ of the observed signal and inversely proportional to the telescope dish diameter D. Therefore, if we want to see two distinct images of two separate astronomical objects that are close to each other, we need a minimum angle θ (in radians) of separation (the angle that separates beams of light coming from the two sources) between them for the telescope to discern that they are apart (Cheng, 2009). Such minimum angular separation as a diffraction limit of a telescope for a uniformly illuminated aperture is defined as

$$\theta = \frac{1.22\lambda}{D}, \tag{1.4.1}$$

where λ is the observing wavelength, and D is the telescope's primary mirror/lens diameter. Short wavelengths or equivalently large diameters means a telescope can resolve sources that are separated by much smaller angles.

Due to diffraction, the analysis of light signal coming from two distant sources, such as binary stars enters the surface of the detector (circular telescope aperture) creating the disk (the bright source/spot) with rings surrounding it. Such disk is called an "Airy disk", named after the English astronomer Sir George Biddell Airy who in detail modelled its properties mathematically in 1831 (Chromey, 2010). In this context, the formula (1.4.1) is interpreted as the diffraction limit or Rayleigh criterion (Cheng, 2009; Chromey, 2010), and it defines the degree of overlap/separation of two nearby distant sources such as binary stars with two Airy disks for which such sources can be resolved (Cheng, 2009; Chromey, 2010). More specifically, the Rayleigh limit sets the least angular separation for the two light sources to be seen distinct and identifiable images. Since the angle θ (the angular extent) (in radians) is usually sufficiently small, using the small angle approximation, we can define a resolving power of a telescope (angular size) in terms of the physical size of an object l being observed and the physical proximity from observer to the source, d_{A} (usually called the angular diameter distance),

$$\theta = \frac{l}{d_{\mathrm{A}}}. \tag{1.4.2}$$

In this case, the physical distance of an object from the point of observation together with the physical size do not change, but we change our perception and interpretation about them in terms of the angular size.

According to the Rayleigh criterion, the resulting image of a point source such as a star observed through a telescope of circular aperture is usually an Airy disk. Moreover, the circular aperture Fraunhofer diffraction of light produces very faint rings surrounding this disk, for which the irradiance $I(\theta)$ (flux of radiant signal/light energy received by telescope aperture surface per unit area) is defined as

$$I(\theta) = I(0)\left[\frac{2J_1(u)}{u}\right]^2, \tag{1.4.3}$$

where $u = ka\sin\theta$, $I(0)$ is the peak irradiance at the center of the diffraction pattern, $D = 2a$ is the aperture diameter, k is the wavenumber, and $J_1(u)$ is the first-order Bessel function (Cheng, 2009; Chromey, 2010).

Conventionally, in radio astronomy when the observed signal - the Airy disk and the concentric rings surrounding it are modelled, they tend to be a succession of Gaussian distributed profiles that become shallow as we move from the center where the central region/disk has the more pronounced profile, and thus θ can be approximated by the full-width at half-maximum (FWHM) of the respective Gaussian distribution (Burke and Graham-Smith, 2009; Cheng, 2009; Chromey, 2010). Therefore, the Airy disk is basically the central region from the peak to the first minimum and its angular radius is given by

$$\theta \sim \frac{1}{2}\text{FWHM} \cong \frac{1.22\lambda}{d} \cong \frac{\lambda}{d}, \tag{1.4.4}$$

and it provides a minimum angle between two adjacent point sources that can be resolved, where d is the apparent size/diameter of the point-source. Therefore, a pair of adjacent point sources can only be resolved if the peaks at the centers of the two diffraction (irradiance) patterns are separated by a distance of at least the radius of the Airy disk (Cheng, 2009; Chromey, 2010).

Due to all these considerations, designing a telescope that achieves the desired resolution is complicated, other factors such as atmospheric conditions also degrade the resolution. Parallel rays of light from distant sources are slightly deflected on their journey to a telescope as they pass through Earth's turbulent atmosphere. The index of refraction changes on size scales from few centimeters to meters due to atmospheric density and temperature differences. This blurs the view and degrades the resolution. Space telescopes collect light that is not affected (less affected) by atmosphere turbulences, as a result they have better performance/resolution than ground-based telescopes.

However, these are not the only challenges facing astronomers, building a telescope that meets the desired sensitivity and resolution becomes extremely difficult due to very long wavelengths required at some epochs (eg., Dark Ages, $\lambda \approx 7$ to 70 m), problems caused by the ionosphere (that can cause distortion of light even at higher frequencies) which is opaque at frequencies lower than a few MHz, and the situation is made more complex by the foregrounds which are several orders brighter than the light signal we are interested, see Liu and Shaw (2019).

The reflecting dish of the telescope is perhaps the most important part of its design. It essentially plays a crucial role in giving the antenna considerable directionality by focusing radio waves onto the horn from a particular direction. Unfortunately, a radio telescope cannot achieve perfect directionality due to its sensitivity to radiation coming from other directions than the pointing one. Although reflecting dish of a radio telescope can be carefully and maximally designed to minimize radiation contributed by sources outside the field of interest, complete elimination is not possible. Due to such effect, a hypothetical power pattern of a radio telescope, defined to be the measure of the telescope response to a point source as a function of angle, is usually comprised of the largest lobe, called the main beam, and smaller lobes called side lobes (Burke and Graham-Smith, 2009). Such a response is a convolution of the telescope's beam with a

source's signal. Thus during the calibration process, an isolated bright point source can be used to measure the shape of the main beam. In practice, the power pattern is normalized along its most sensitive direction, which ideally corresponds to the direction of the physical axis of the antenna. It turns out that, the size of the main beam is very important since its FWHM approximates the resolution of a telescope. For more detailed presentation on radio telescopes and radio astronomy in general, consult Burke and Graham-Smith (2009); Chromey (2010); Cheng (2009).

1.5 Motivation for this Thesis

The advent of the 21-cm cosmology has pushed the LSS of the Universe survey to an era where its prospects are both fascinating and highly promising. Apart from numerous readily obtainable scientific benefits, LSS surveys of our cosmos are propelled by both our curiosity to understand the nature and evolution of the Universe, and our passion and enthusiasm to provide answers that can unveil various mysteries such as the dark energy phenomenon which keeps the cosmic accelerated expanding. Many cosmological surveys that employ different methodologies/probes (Lahav and Suto, 2004), such as galaxy redshift surveys, cosmic microwave background (CMB), galaxy cluster counts, gravitational lensing and Lyman alpha forest have been in effect for several decades. Techniques such as spectroscopic galaxy redshift surveys have been notably deployed (Giovanelli and Haynes, 1991; Lahav and Suto, 2004) to survey millions of individual galaxies by measuring their redshifts through matching catalogued galaxy SEDs with spectral lines. Although galaxy redshift survey has been successful to some extent, it suffers from limitations, such as resolution and sensitivity required to resolve fainter distant galaxies, and low efficiency, as the approach focuses on resolving individual galaxy at a time (Visbal et al., 2009).

With new more powerful telescope instrumentations coming online, paraded and ready to be commissioned to survey the cosmic structure, a new approach to efficiently survey extremely large volumes of the Universe has been born (invented). This approach is called intensity mapping (IM) and uses the 21-cm line of the neutral hydrogen atom (HI) as a remote messenger for probing the cosmos at different redshifts (Kovetz et al., 2019). The 21-cm cosmology relies on the searches of the redshifted 21-cm line, absorption or emission signatures through HI, which can, in turn, be used as a tracer of the underlying matter distribution over large angular scales and a probe of different properties of the Universe.

The aforementioned postulates motivate us to carry out the forecasts of the observations of the 21-cm cosmology using three radio telescopes which act as a representative sample for many radio astronomy experiments. In particular, the telescopes considered in our study are Five-hundred-meter Aperture Spherical radio Telescope (FAST) and Baryon acoustic oscillations In Neutral Gas Observations (BINGO) single-dish radio experiments, and Square Kilometre Array Phase I (SKA-I) in autocorrelation mode (Bigot-Sazy et al., 2015; Yohana et al., 2019). Together with the HI IM technique, we present with the aid of computer simulations the prospects of

many future and near-term radio telescopes, how stringent will be their constraints on different physical models of dark energy and other cosmological parameters. IM technique is promising, it does not rely on resolving individual bright sources, but traces galaxy distribution by averaging over many objects/sources, that fall inside a single, relatively, large, pixel (Liu and Shaw, 2019). However, IM method is expected to efficiently improve BAOs detection than the traditional galaxy redshift survey (Chang et al., 2008; Masui et al., 2010a; Dickinson, 2014), and one of its great advantages is the capability to probe the integrated/cumulative emission over the entire luminosity function, including the ability to detect photons from very distant and dim objects which would be extremely difficult to detect individually.

Notwithstanding, the 21-cm cosmology studies are impeded by the data analysis challenges. The most obvious of these challenges is the presence of the foreground contaminants from the galaxy and extragalactic point sources which strongly dominate the HI signal (Bigot-Sazy et al., 2015). Therefore, 21-cm experiments' success will depend on the ability to circumvent the foreground challenge, amongst other issues. As a matter of fact, such challenges make 21-cm cosmology inextricably mingled with computer simulations. Our study is thus intended to precede the real experimentation onset and provide an overall picture of these radio experiments' expected performance, which will help them to forge their way forward as they endeavour to fulfill the cosmic survey missions.

All these factors have collectively pushed us to delve into 21-cm cosmology study; and we have therefore employed the neutral hydrogen intensity mapping strategy by developing new tools and deploying a suite of existing ones to build a computationally effective pipeline to remove the foreground contamination from our Milky Way galaxy and extragalactic point sources, and forecast various cosmological constraints with future BINGO, FAST and SKAI-MID (here named SKA-I), 21-cm intensity mapping experiments.

The rest of this thesis is divided into three chapters, organized in sections and subsections. Chapter 2 lays a framework about HI IM cosmological constraints forecast. It starts with a literature review on the current state of the galaxy redshift surveys and 21-cm experiments in Section 2.1, and proceeds to present briefly the preliminary information and tools, in particular, how the huge cosmological data is presented, processed, manipulated and analyzed; from collecting it with experiments to simulations of cosmological parameter constraints and interpretation of results in Section 2.2, the Gaussianity of the maximum likelihood estimation (MLE) in Section 2.3, the Fisher information theory in Section 2.4, and how we can apply them in the modeling of cosmological parameter constraints. We introduce three IM radio experiments, namely, FAST, BINGO and SKA-I, on which our forecast is based in Section 2.5. Under Section 2.6, we discuss and summarize the mathematical derivation of the tomographic angular power spectrum, and introduce the thermal noise and total noise inverse power spectra as residuals of various contaminants after applying foreground removal techniques. This spectrum of noise is related to various observable experimental parameters. We further carry out the calculations involving the noise power spectrum and tomographic power spectrum in computing the Fisher matrix and establish

some framework for the Fisher matrix analyses in relation to parameter constraints. Noise power spectrum together with the tomographic angular power spectrum are prime tools for computing the Fisher matrix via maximum likelihood estimation (Dodelson, 2003; Shaw et al., 2015). We continue with qualitative and quantitative presentations, and statistical analysis of cosmological parameter constraints results in Section 2.7 based on various cosmological parameters of our choice. In this Section, we also define the cosmological parameters implemented and present various FAST, BINGO, and SKA-I experimental parameter specifications. We comparatively summarize our forecasts in Section 2.8. Thereafter, we conclude this chapter in Section 2.9.

Chapter 3 is dedicated to qualitative and quantitative analyses of various contaminants that bury with an overwhelming magnitude the primordial HI signal. It begins with an introductory literature review, Section 3.1, which opens with the description of a selected number of HI IM experiments in light of LSS of Universe surveys and proceeds to reviewing various algorithms and approaches used to clean cosmological data. In Section 3.2, we briefly review the FAST telescope, focusing on its experimental and observational prospects. In Section 3.3, an overview of the signal and various expected foreground contaminants of the radio sky and the instrumental noises is given. Section 3.4 is dedicated to the qualitative and quantitative description of the principal component analysis (PCA) algorithm used for component separation. Section 3.5 presents PCA results and analyses of the recovered 21-cm signal versus the input. We end this chapter in Section 3.6 with some discussion and concluding remarks.

We finally conclude our thesis in Chapter 4 and provide a general outlook: future research avenues and possibilities.

2

Cosmological Forecasts With HI Intensity-Mapping Experiments

2.1 21-cm Experiments Review

Cosmology has improved our understanding of the Universe over the last few decades. Up to this time, study of the Universe has mostly given us a basic picture of how the Universe evolved and formed its large-scale structure (LSS). Many experiments dedicated to studying the Universe throughout its entire history at various epochs have been conducted while others are ongoing or planned to take off in the near future. Some of the most notable surveys targeting the LSS of the Universe include a number of galaxy redshift surveys such as the Two-degree-Field Galaxy Redshift Survey (2dFGRS, Colless et al. (2001)), the WiggleZ Dark Energy Survey (Blake et al., 2008, 2011; Kazin et al., 2014), the Six-degree-Field Galaxy Survey (6dFGS, (Jones et al., 2009; Beutler et al., 2011)), and the Baryon Oscillation Spectroscopic Survey (BOSS, Ross et al. (2012)), which is part of the third stage of the Sloan Digital Sky Survey (SDSS, York et al. (2000); Anderson et al. (2012); Alam et al. (2017)). Recently, the Dark Energy Survey (DES), (Dark Energy Survey Collaboration et al., 2016) reported their cosmological constraints with the 1-year data (Troxel et al., 2017; Camacho et al., 2018). Future optical surveys that aim to utilize larger and more sensitive telescopes at a variety of high redshifts, such as Dark Energy Spectroscopic Instrument (DESI) (Levi et al., 2013; DESI Collaboration et al., 2016), Large Synoptic Survey Telescope (LSST) (Ivezic et al., 2008; LSST Science Collaboration et al., 2009; The LSST Dark Energy Science Collaboration et al., 2018), *Euclid* (Laureijs et al., 2011) and *WFIRST* (Green et al., 2012), have been proposed and some of the constructions are underway. To date, galaxy-redshift surveys have made significant progress in surveying the LSSs of the Universe. To do precision cosmology, one would need to detect sufficiently large samples of galaxies. However, this is a huge task since at higher redshifts the galaxies look essentially very faint (Bull et al., 2015b; Kovetz et al., 2017; Pritchard and Loeb, 2012).

In radio astronomy, observation of the 21-cm spectrum line emitted by neutral hydrogen (HI)

in deep space provides a rich tool for understanding cosmic evolution. After the cosmic reionization, the hydrogen outside galaxies was ionized. However, a massive amount of HI shielded from ionizing ultraviolet photons resided within the dense gas clouds embedded in galaxies as these gas clouds cooled and collapsed to form stars. As a result, the quantity and distribution of HI are related to the evolution of galaxies and cosmic surveys in the radio band, whose origin and evolution are highly related to the structure formation history and nature of cosmic expansion (Pritchard and Loeb, 2012; Kovetz et al., 2017).

At lower redshift, $z \lesssim 0.1$, HI can be detected with the 21-cm emission and absorption lines from its hyperfine splitting. At redshift greater than 2.2, HI can also be detected via optical observation of the Lyα absorption line against bright background sources (Zwaan et al., 2004; Haynes, 2008). At intermediate redshift, the 21-cm emission line of each individual galaxy is too faint to be detected. However, instead of cataloging individual galaxies, the intensity mapping (IM) method measures the total HI flux from many galaxies and can be applied to LSS studies (Chang et al., 2008; Loeb and Wyithe, 2008). With the HI IM method, Chang et al. (2010) first reported the measurements of cross-correlation function between the HI map, observed with the Green Bank Telescope (GBT) and DEEP2 optical redshift survey (Davis et al., 2001). With the extended GBT HI survey and WiggleZ Dark Energy Survey, the cross-power spectrum between HI and optical galaxy survey was also detected (Masui et al., 2013). Recently, another HI survey with the Parkes telescope reported the measurements of the cross-power spectrum with the 2dF optical galaxy survey (Anderson et al., 2017). So far, the auto-power spectrum of the HI IM survey is still not detected (Switzer et al., 2013) because of contamination from the foreground residuals.

There are a number of current and future experiments targeting HI IM. These experiments are increasingly comprised of wide-field and sensitive radio single dishes or interferometers, such as Baryon acoustic oscillations In Neutral Gas Observations (BINGO) (Dickinson, 2014), Canadian Hydrogen Intensity Mapping Experiment (CHIME, Bandura et al. (2014)), Tianlai (Chen, 2012) and Hydrogen Intensity and Real-time Analysis eXperiment (HIRAX, Newburgh et al. (2016)). Besides the specially designed telescopes or interferometers, several larger single-dish telescopes and interferometers, such as the Five-hundred-meter Aperture Spherical radio Telescope (FAST, Nan et al. (2011)), Square Kilometre Array (SKA, Bull et al. (2015a); Santos et al. (2015); Braun et al. (2015)) or MeerKAT (Santos et al., 2017), are also planned for the HI IM survey.

This chapter aims to use the HI IM to forecast how future HI experiments, such as BINGO, FAST and SKA Phase I (SKA-I), will constrain various cosmological parameters.

FAST is the world-largest single-dish telescope and features high resolving power. BINGO is a medium-sized single-dish telescope with a special design (Battye et al., 2016). SKA-I is a telescope array which, in single-dish autocorrelated mode, is suitable for probing large volumes over very large cosmological scales. These experiments are the next-generation LSS surveys, that can be employed to develop and verify excellent techniques for HI IM surveys. Our aim is to simultaneously consider three experiments whose nature and designs categorically represent

Table 2.1: The cosmological parameters in our study as the best-fitting parameters in Planck Collaboration et al. (2016).

Parameter	Fiducial value	Description
$\Omega_{\rm b}h^2$	0.0226	Fractional baryon density today
$\Omega_{\rm c}h^2$	0.112	Fractional cold dark matter density today
w_0	-1.00	Dark energy EoS, from the relationship $w(a) = w_0 + (1-a)w_a$
w_a	0.00	Dark energy EoS, from the relationship $w(a) = w_0 + (1-a)w_a$
$\ln(10^{10}A_{\rm s})$	3.089	Log power of the primordial curvature perturbations, ($k_0 = 0.05$ Mpc^{-1})
H_0	67.30	The Hubble constant (current expansion rate in km s^{-1} Mpc^{-1})
$N_{\rm eff}$	3.046	Effective number of neutrino-like relativistic degrees of freedom
$n_{\rm s}$	0.96	Scalar spectrum power-law index ($k_0 = 0.05$ Mpc^{-1})
$\Sigma m_\nu/94.07$ eV	0.00064	The sum of neutrino masses in eV

many future HI IM probes. We will present a quantitative and qualitative comparison between their future prospects while addressing the range of expected performances, limitations and challenges that may accompany these experiments.

We develop a forecasting framework that is motivated and guided by physical experimental design and set-ups, which can be correctly transformed into mathematics and computer simulations. We believe that this clear scientifically motivated forecast study will substantially provide testable predictions and determine paths and feasibility for future HI IM experiments.

Unless otherwise stated, we adopt a spatially-flat cold dark matter (CDM) cosmology model with a dynamical dark energy content, described by the EoS parameters w_0, w_a, and consider fiducial parameters listed in Table 2.1 (Planck Collaboration et al., 2014, 2016).

2.2 From Time-ordered Data to Cosmological Constraints

A suite of optimal statistical methods and techniques employed to study CMB can also be applied to studying HI IM. In a map-making process (Dodelson, 2003), maps for various sky components are constructed from the time-ordered data points (or data stream), where each data stream corresponds to some particular frequency. The most focal result of such a map-

making process is the two-dimensional fluctuations of the 21-cm signal and power spectrum. What follows from the data stream is the extraction of the frequency-dependent power spectra from the maps and carry out an estimation of the cosmological parameter constraints forecast from such power spectra/band powers and perform various analyses.

In most cases, steps in developing the data manipulation pipeline involve a progressive substantial data reduction/compression in terms of the size and the parameters (number) that describe/represent the data. One such significant data reduction can be seen, for example in the foreground contamination cleaning stage, which involves combining different maps and utilizing spatial and frequency information (see PCA Sections 3.4 and 3.5). However, in real experiments, other steps such as calibration and systematic errors mitigation will be crucial stages applied to the raw data (time-ordered) before proceeding with the data analysis pipeline.

We denote by d_t an experimental data collected at different times, such that the data stream and the underlying HI signal Θ_i are related to the pointing matrix P_{ti} and implicitly to the noise matrix $C_{d,tt'}$ by

$$d_t = P_{ti}\Theta_i + n_t, \tag{2.2.1}$$

where i is the index for the signal pixel positions. Here $C_{d,tt'}$ characterizes the noise covariance in the time stream, such that the implicit summation repeatedly over the index i (Einstein summation convention) is applied, and the data model (2.2.1) is interpreted as the sum of signal and noise. The noise n_t is sampled from a zero-mean Gaussian distribution and the covariance

$$\langle n_t n_{t'} \rangle = C_{d,tt'}. \tag{2.2.2}$$

The simplest form of the pointing matrix, P is composed of rows that are matched to a particular time, where each row has zeros in it with an exception of a single column containing a one. Such a column is related to a specific observed sky pixel at a particular time of interest. In a real observation strategy, a sky pixel is usually scanned more than once which means that a respective column will contain several ones, equivalent to the number of times a pixel is scanned.

We favor a maximum likelihood estimation (MLE) and describe it in the next subsection, as a suitable tool used in the map construction process, and more broadly as applied in the data analysis pipeline development (Tegmark et al., 1997).

2.3 The Maximum Likelihood Estimation

The basic building block of contemporary analysis in cosmology is the MLE, (Dodelson, 2003; Hobson et al., 2014; Trotta, 2017). The MLE builds on the Bayesian methods that we briefly discuss in a sequel. Just as applied in the CMB data analysis for anisotropy searches, MLE function continues to be an indispensable tool for analysis and modeling of HI IM data. The same techniques used to process the CMB data have been adopted to study the three-dimensional distribution (Tegmark et al., 1998) and the two-dimensional distribution (Efstathiou and Moody,

2001; Huterer et al., 2001) galaxy redshift surveys. The approach has as well been extended to other cosmological studies, such as in the Lyman-alpha forest (Hui et al., 2001) and the shear field from the weak gravitational lensing (Hu and White, 2001).

The MLE technique is a consequence of the Bayesian method, which is the natural statistical technique to inference. By inference, we mean reaching a conclusion on the basis of evidence and reasoning. Bayesian inference involves changing one's belief after realizing new evidence. The evidence must be considered, even if it is contrary to what was formerly believed. Therefore, in Bayesian thinking, we re-adjust our beliefs concerning an outcome based on new evidence; unless we have a mechanism in place to rule out all possibilities, rarely can we be certainly conclusive. Therefore, a Bayesian can in most cases be very confident, but can hardly be sure about an outcome, see Ref. Davidson-Pilon (2015).

A Bayesian adopts the philosophy of thinking about probabilities as degrees of beliefs, an experience that is very natural to humans. Thus, to conform to the usual probabilistic notation, we denote with $P(A)$ a belief regarding some event A, the quantity that we call the prior probability. We further use $P(A|X)$, which we think of it as the probability of an event A when the evidence X is given, to denote our new measure of believability.

To illustrate the Bayesian concept quantitatively, suppose we have prior knowledge on the performance of some instrument, and then we decide to conduct an experiment many times with this instrument and record that it passes X tests. Therefore we will need to revise our belief/prior knowledge by incorporating a new piece of evidence. This new belief is called the posterior probability.

We use Bayes' Theorem to update the measure of our believability or confidence:

$$P(A|X) = \frac{P(X|A)P(A)}{P(X)} \propto P(X|A)P(A). \tag{2.3.1}$$

Following a similar analogy as described above, suppose that we have some prior information about the underlying model (a known reality), such that a set of probability distribution parameters, θ, best explains the data D associated to an experiment, therefore

$$\begin{aligned} P(\theta|D) &= \frac{P(D|\theta)P(\theta)}{P(D)} \\ \implies \text{Posterior} &= \frac{\text{Likelihood} \times \text{Prior}}{\text{Evidence}}. \end{aligned} \tag{2.3.2}$$

Our interest is the posterior probability of getting the parameters when provided with the data, $P(\theta|D)$, where θ is the N-dimensional vector of parameter space being varied in the model under consideration. We shall see that, instead of computing this quantity directly, we will bypass the process by considering the MLE approach. Progressing in our formulation, suppose further that, the probabilities are conditional, not just on the data D but also on our assumed model M, and thus we write

$$P(\theta|D, M) = \frac{P(D|\theta, M)P(\theta|M)}{P(D|M)}. \tag{2.3.3}$$

Obtaining an expression for the Bayesian evidence, requires integrating over all θ. Keeping probabilities normalized, while the evidence on the denominator is independent of θ, we have

$$P(D|M) = \int P(D|\theta, M)P(\theta|M)d\theta, \tag{2.3.4}$$

defined as the probability that given a theory/model M, an experiment would get the data D, which then implies

$$\text{Evidence} = \int (\text{Likelihood} \times \text{Prior})d^N\theta. \tag{2.3.5}$$

Prior is what we know (our knowledge) before the data was acquired, usually considered as the degree of belief (Bayesian view) or frequency of occurrence (Frequentists view).

Let us find out what this likelihood function is, by starting with the following assumption: consider a sample of random variables

$$X = \Big(X_1,\ X_2, \ldots,\ X_n\Big), \tag{2.3.6}$$

such that $X \sim f(\mathbf{x}|\theta)$, that is, the probability distribution function (or pmf) of this random variable X is $f(\mathbf{x}|\theta)$, where $\mathbf{x} = (x_1,\ x_2, \ldots,\ x_n)$ and θ is the true unknown parameter, belonging to the parameter space Θ.

The maximum likelihood then chooses as the true value of the unknown parameter θ, the estimator $\hat{\theta}$ that renders the data we are observing most likely describes the underlying model/Theory. In MLE, θ is a point estimate, it is deterministic (not random) but not known, while in Bayesian, θ is assumed to be random. Both Bayesian and MLE look for some parameter θ that is responsible for producing the data which best fits the model.

Thus by definition, the density function

$$\mathcal{L}(\theta|\mathbf{x}) = f(\mathbf{x}|\theta);\ \theta \in \Theta, \tag{2.3.7}$$

considered a function of θ, is called the likelihood, where the MLE is then given by

$$\hat{\theta}(\mathbf{x}) = \arg\ \max_\theta \mathcal{L}(\theta|\mathbf{x}). \tag{2.3.8}$$

Although conceptually clearly understood, there can be many local maxima for this likelihood, thus it can be computationally challenging to find a global maximum. The property for this class of estimators is that $\hat{\theta}$ and $f(\hat{\theta}(\mathbf{x}))$ are, respectively, the maximum likelihood estimates of θ and $f(\theta)$. This holds for the case of the biased estimators, for which ML estimator is one of them.

To that end, we ask ourselves, how constraining will be to the underlying model/theory a given set of measured data? Or in other words, how well will our data fit the theory? In order to answer this question, we consider application of MLE to this likelihood function $\mathcal{L}$, that is, finding the best estimate from the space of parameters that maximizes the likelihood function. This is equivalent to maximizing the probability

$$\mathcal{L} = P(x|\theta) = P(\text{Data}|\text{Theory}), \tag{2.3.9}$$

for a random variable $X \sim f(x|\theta)$, where θ is the true value of the parameter.

The likelihood function describes the probability of observing some data across a given range of parameter values which would represent the model/theory being considered, that can describe physical reality, such as certain Universe measurements we are interested to obtain. We can use the Fisher Matrix to predict the effectiveness of various upcoming 21-cm experiments, particularly, in forecasting the stringentness of bounds such experiments will impose on cosmological parameters upon acquisition of real survey data. Fisher matrix can provisionally provide the best estimates we can expect on the parameter constraints, by maximizing the likelihood function, as we shall see in the subsequent sections.

2.4 Fisher Information Matrix and Cramer-Rao Bound

We proceed in figuring out how to measure the amount of information regarding the unknown parameter θ and establish bounds on the variance/covariance of the estimators and use such variance to find an estimator's sampling distribution, assuming that the estimator is drawn from a large sample.

The virtue of the Fisher information theory is to measure or to determine the amount of information about an unknown parameter that can be estimated from the data sample using the MLE technique. Detailed Fisher information theory analysis tells us that for a random variable $X \sim f(x|\theta)$ described above, the amount of information we can get about the parameter θ increases with an increase in the value of $\left|\partial \log f(x|\theta)/\partial\theta\right| = \left|f'(x|\theta)/f(x|\theta)\right|$ or equivalently $\left[\partial \log f(x|\theta)/\partial\theta\right]^2$. This means, using $\left[\partial \log f(x|\theta)/\partial\theta\right]^2$ enables us to measure the amount of information X provides about parameter θ. Considering the ensemble average, the random variable X contains the Fisher information for a parameter θ given by

$$\begin{aligned}\mathcal{F}_{\alpha\beta}(\theta) &= \mathbb{E}\left[\frac{\partial \ln P(x;\theta)}{\partial\theta_\alpha}\frac{\partial \ln P(x;\theta)}{\partial\theta_\beta}\right] = \left\langle \frac{\partial \ln P(x;\theta)}{\partial\theta_\alpha}\frac{\partial \ln P(x;\theta)}{\partial\theta_\beta}\right\rangle \\ &= \int \frac{\partial \ln P(x;\theta)}{\partial\theta_\alpha}\frac{\partial \ln P(x;\theta)}{\partial\theta_\beta} P(x;\theta)\mathrm{d}^N x,\end{aligned} \tag{2.4.1}$$

where $\mathbb{E}$ stands for expectation, and $P(x;\theta)$ is the probability distribution with respect to parameter θ. Here, θ can be mean, variance, or some other statistic.

Applying

$$\int P(x;\theta)\mathrm{d}^N x = 1, \tag{2.4.2}$$

and differentiating this Equation (2.4.2), we have

$$0 = \int \frac{\partial P(x;\theta)}{\partial\theta_\alpha}\mathrm{d}^N x \equiv \int \frac{\partial \ln P(x;\theta)}{\partial\theta_\alpha} P(x;\theta)\mathrm{d}^N x; \tag{2.4.3}$$

interpreted as the mean value of all the scores, which equals 0.

Let

$$P_{,\alpha} = \frac{\partial P}{\partial \theta_\alpha}, \ (\ln P)_{,\alpha} = \frac{\partial \ln P}{\partial \theta_\alpha}. \tag{2.4.4}$$

We assume we can interchange derivatives and integrals in (2.4.1):

$$\frac{\partial}{\partial \theta_\beta} \int \frac{\partial \ln P(x;\theta)}{\partial \theta_\alpha} P(x;\theta) d^N x = 0, \tag{2.4.5}$$

where multiplying and dividing (2.4.5) by $P(x;\theta)$ implies

$$\int (\ln P)_{,\alpha} (\ln P)_{,\beta} P(x;\theta) \mathrm{d}^N x + \int (\ln P)_{,\alpha\beta} P(x;\theta) \mathrm{d}^N x = 0, \tag{2.4.6}$$

from which we deduce the term

$$\mathcal{F}_{\alpha\beta} = -\int (\ln P)_{,\alpha\beta} P(x;\theta) \mathrm{d}^N x = -\mathbb{E}\left[(\ln P)_{,\alpha\beta}\right] = -\mathbb{E}\left[\frac{\partial^2 \ln P}{\partial \theta_\alpha \partial \theta_\beta}\right], \tag{2.4.7}$$

called the Fisher Matrix. Fisher Matrix is used to form the lower bound on the covariance of any two estimators, $\hat{\theta}_\alpha$ and $\hat{\theta}_\beta$. Thus, the variance of the ML estimator is given by

$$\mathrm{Var}(\hat{\theta}_{\mathrm{MLE}}) = I^{-1}(\theta) = -\left[\mathbb{E}\left[\frac{\partial^2 \mathcal{L}}{\partial \theta^2}\right]\right]^{-1}, \tag{2.4.8}$$

where $\mathcal{L}$ is the log-likelihood function. Uncertainty on the unknown parameter θ value we are estimating is given by $\sqrt{\mathcal{F}^{-1}}$. Therefore, if $C_{\alpha\beta}$ is the covariance matrix, according to the Cramer- Rao bound/inequality,

$$\mathrm{Var}(\theta_\alpha) = C_{\alpha\alpha} \geq \mathcal{F}^{-1}_{\alpha\alpha}. \tag{2.4.9}$$

Fisher Matrix and MLE are important tools in our modeling and analysis. From the MLE technique, we can recover the Fisher matrix for various cosmological parameters which plays a significant role in parameter constraining.

Fisher matrix in this context can be obtained by applying the Taylor expansion to the likelihood function around the maximum value. The better approximation is usually to consider the second derivative of the log-likelihood function. In this way, we approximate our likelihood function as Gaussian. Generally,

$$\frac{\partial^2 \mathcal{L}}{\partial \theta_\alpha \partial \theta_\beta} = -\mathcal{F}, \tag{2.4.10}$$

where $\mathcal{F}$ is the Fisher matrix.

For a Gaussian distributed sample, the Fisher matrix tells us how curved is the likelihood function around the maximum value. The bigger the values in the Fisher matrix, the more curved/peaked it is, meaning the more constraining the data is for that particular parameter.

In our 21-cm HI IM forecasting, we consider the maximum log-likelihood function as follows:

$$\ln \mathcal{L}(\theta) = -\frac{1}{2}\chi^2 = -\frac{1}{2}\sum_\ell \frac{\left(C_\ell^{\mathrm{th}} - C_\ell^{\mathrm{obs}}\right)^2}{(\delta C_\ell)^2}, \tag{2.4.11}$$

where $C_\ell^{\rm th}$ and $C_\ell^{\rm obs}$ can be, respectively, viewed as theoretical and observed tomographic angular power spectrum, and δC_ℓ is the uncertainty measurement of C_ℓ for a given experiment.

Applying and evaluating Taylor expansion to the log-likelihood function (2.4.11) above, around its maxima, say $(\theta_\alpha, \theta_\beta)$, we have the Fisher matrix

$$\mathcal{F}_{\alpha\beta} = \sum_\ell \frac{1}{(\delta C_\ell)^2} \left[\frac{\partial C_\ell^{\rm th}}{\partial \theta_\alpha} \frac{\partial C_\ell^{\rm th}}{\partial \theta_\beta} + (C_\ell^{\rm th} - C_\ell^{\rm obs}) \frac{\partial^2 C_\ell^{\rm th}}{\partial \theta_\alpha \partial \theta_\beta} \right]. \tag{2.4.12}$$

In principle, $(C_\ell^{\rm th} - C_\ell^{\rm obs}) \sim 0$, and therefore

$$\mathcal{F}_{\alpha\beta} = \sum_\ell \frac{1}{(\delta C_\ell)^2} \left[\frac{\partial C_\ell^{\rm th}}{\partial \theta_\alpha} \frac{\partial C_\ell^{\rm th}}{\partial \theta_\beta} \right], \tag{2.4.13}$$

where

$$(\delta C_\ell)^2 = \frac{2}{(2\ell+1) f_{\rm sky}} [C_\ell + N_\ell], \tag{2.4.14}$$

and N_ℓ is the noise power spectrum.

2.5 Intensity Mapping Projects

BINGO, FAST and SKA-I experiments are potentially suitable for surveying HI intensity maps of the Universe and will open avenues for doing a wide range of sciences. In this section, we briefly describe each of these three future experiments for studying the HI IM.

2.5.1 BINGO

The BINGO project is proposed to be built in Brazil and aims to map HI emission at redshift range $0.13 - 0.48$ (960 MHz $\sim$ 1260 MHz). BINGO will map an approximately 15° strip of the sky to measure the HI power spectrum and detect for the first time, baryon acoustic oscillations (BAOs) at radio frequencies. BINGO's expected design is a dual-mirror compact antenna test range telescope with a 40 m primary mirror and an offset focus, which is proposed to have a receiver array containing between $50 - 60$ feed horns, with a 90 m focal length. For more details about the construction of BINGO and its prospective capabilities, please refer to Battye et al. (2013); Bigot-Sazy et al. (2015); Battye et al. (2016).

2.5.2 FAST

FAST is a ground-based radio telescope built within a karst depression in Guizhou province of southwest China. The L-band receiver is designed for 19 beams and the multibeam receiver will increase the survey speed (Nan et al., 2011). FAST is believed to be the most sensitive single-dish telescope currently in existence, covering a wide frequency range from 70 MHz – 3 GHz and a potentially large area of up to $25,000\,{\rm deg}^2$. Here, we consider a survey area of $10,000\,{\rm deg}^2$, approximately equivalent to the one used by Alam et al. (2015). The chosen survey

area reasonably suffices for our current study, and is regarded as moderate considering other experimental parameters and design factors. In addition, this choice is also potentially suitable for any future FAST-SDSS cross-correlation studies. For the HI IM survey with FAST, we consider a frequency range of 950 MHz $\sim$ 1,350 MHz. FAST has a diameter of 500 meters but the illuminated aperture is 300 meters. For full details on FAST engineering and its capabilities please refer to Nan et al. (2011); Smoot and Debono (2017).

2.5.3 SKA-I

The SKA project, currently under development, is basically an interferometry array. The project plans two stages of development, comprising SKA Phase I and SKA Phase II (Bull et al., 2015a; Santos et al., 2015; Braun et al., 2015). The first stage (SKA Phase I) radio astronomy facility is split and shared between South Africa (SKAI-MID) – hosted in the Karoo Desert, and an aperture array in Australia, SKA-LOW Phase I (SKAI-LOW). SKAI-MID plans to build 133 15 m diameter dishes and will incorporate 64 dishes from the MeerKAT array (Santos et al., 2017; Fonseca et al., 2017), each with 13.5 m diameter, that have already been constructed in the Karoo Desert. Note that SKA-I telescope specifications implemented for our study have been subject to changes as the project has gone through various levels of revision (Bull, 2016), see recent updates in Square Kilometre Array Cosmology Science Working Group et al. (2018). Due to the weak resolution requirement for HI IM, we ignore the cross-correlation between dishes, which means the SKAI-MID array is working as 133 single dishes, with an extension of 64 13.5 m MeerKAT array dishes. We, therefore, consider tentative experimentation with SKAI-MID Band 1 (excluding the MeerKAT array), hereafter referred to as SKA-I, at frequencies 350 MHz $\sim$ 1,050 MHz for the full 133 antennae for a total survey area of 10,000 deg^2. However, we make the same choice of survey area as for FAST for similar reasons as explained in Subsection 2.5.2. For full details about BINGO, FAST and SKA-I experimental design, see Table 2.2.

2.6 Method

2.6.1 Tomographic Angular Power Spectrum

In our forecast, we consider the tomographic angular power spectrum of HI for the i-th and j-th redshift bins given by (see Subsection 1.3.5)

$$C_\ell^{ij} = 4\pi T_b^{ij} \int \mathrm{d}\ln k \Delta^2(k) \Delta^W_{T_\mathrm{b},\ell}(k) \Delta^{W'}_{T_\mathrm{b},\ell}(k), \tag{2.6.1}$$

where $\Delta^2(k)$ is the dimensionless power spectrum of primordial curvature perturbations. Here, $T_\mathrm{b}^{ij} = T_\mathrm{b}(z_i)T_\mathrm{b}(z_j)$ is the multiplication of HI mean brightness temperature (Chang et al., 2008) of the i-th and j-th redshift bins, with

$$T_\mathrm{b}(z) = 0.39 \text{ mK} \left(\frac{\Omega_\mathrm{HI}}{10^{-3}}\right) \left(\frac{1+z}{2.5}\right)^{0.5} \left(\frac{\Omega_\mathrm{m} + (1+z)^{-3}\Omega_\Lambda}{0.29}\right)^{-0.5}, \tag{2.6.2}$$

Table 2.2: Experimental parameters for FAST, BINGO and SKA-I. $D_{\rm dish}$ is the illuminated aperture (Li and Ma, 2017).

	FAST	SKA-I	BINGO
$\nu_{\rm min}$[MHz]	950	350	960
$\nu_{\rm max}$[MHz]	1,350	1,050	1,260
$\Delta\nu$[MHz]	10	10	10
$n_\nu(n_z)$	40	70	30
$D_{\rm dish}$[m]	300	15	25
$N_{\rm ant}\times N_{\rm feed}$	1×19	133×1	1×60
$t_{\rm TOT}$[yr]	1	1	1
$T_{\rm rec}$[K]	25	Eq. (2.6.8)	50
$S_{\rm survey}$[deg^2]	10,000	10,000	3,000

where $\Omega_{\rm HI}$ is the fraction of HI density assumed to be 0.62×10^{-3} (Switzer et al., 2013) and $\Delta^W_{T_{\rm b},\ell}(k)\equiv\Delta^W_{T_{\rm b},\ell}(\mathbf{k})/\mathcal{R}(\mathbf{k})$ (Hall et al., 2013). Here, $\mathcal{R}$ is the primordial curvature perturbation. The transfer function is

$$\Delta^W_{T_{\rm b},\ell}(\mathbf{k})=\int_0^\infty {\rm d}z W(z)\Delta_{T_{\rm b},\ell}(\mathbf{k},z), \tag{2.6.3}$$

which is an integration of the temperature fluctuation over the bandwidth $W(z)$. The temperature fluctuation, for each ℓ (projected mode) for each wavenumber $\mathbf{k}$ and redshift bin z is

$$\begin{aligned}\Delta_{T_{\rm b},\ell}(\mathbf{k},z) &= \delta_n j_\ell(k\chi)+\frac{kv}{\mathcal{H}}j_\ell''(k\chi)+\left(\frac{1}{\mathcal{H}}\dot\Phi+\Psi\right)j_\ell(k\chi)\\ &- \left(\frac{1}{\mathcal{H}}\frac{{\rm d}\ln(a^3\bar n_{\rm HI})}{{\rm d}\eta}-\frac{\dot{\mathcal{H}}}{\mathcal{H}^2}-2\right)\left[\Psi j_\ell(k\chi)+vj_\ell'(k\chi)+\int_0^\chi\left(\dot\Psi+\dot\Phi\right)j_\ell(k\chi'){\rm d}\chi'\right].\end{aligned} \tag{2.6.4}$$

This is surely Equation (1.3.40), where j_ℓ is the spherical Bessel function, δ_n is the HI density contrast, and the second term $kvj_\ell''(k\chi)/\mathcal{H}$ is the redshift space distortion term (Hall et al., 2013).

Here, we work in the tomographic power spectrum in ℓ-space of multiple redshift (frequency) slices. We notice that there are several previous works which implemented the forecasts in three-dimensional (3-D) k-space (Bull et al., 2015a,b). There are some advantages that the tomographic two-dimensional power spectrum in $\ell-$space has compared to the 3-D power spectrum in k-space. The three-dimensional power spectrum in k-space has the following disadvantages:

- It assumes plane-parallel conditions, so it cannot encompass wide-angle correlations;

- It cannot include a lensing effect, either;
- In the analysis of 3-D power spectrum, the redshift bins are typically wide, which neglects the evolution of background within bins; and
- It requires a fiducial model which must be assumed to relate redshift to distance.

In addition, the tomographic angular power spectrum can easily be applied to perform cross-correlations between 21-cm images and other LSS tracers at the same redshift. Due to these reasons, our approach thus has some advantages over a 3-D power spectrum, and we find it worth investigating as we have done so in this work. Full details regarding the advantages of using the tomographic angular power spectrum can be referenced in Shaw and Lewis (2008); Di Dio et al. (2014); Tansella et al. (2018); Camera et al. (2018).

2.6.2 Thermal Noise and Fisher Matrix Calculations

Noise for the single-dish IM experiment is given by

$$N_\ell^{ij} = \delta^{ij} N_\ell^{\rm HI} = \frac{\delta^{ij} T_{\rm sys}^2 S_{\rm survey}}{(N_{\rm ant} N_{\rm feed} t_{\rm TOT} \Delta\nu)}, \tag{2.6.5}$$

where $N_{\rm ant}$ is the number of antennae, $N_{\rm feed}$ is the number of feed horns per antenna and $t_{\rm TOT}$ is the total observational time.

BINGO and FAST system temperatures are expressed as

$$T_{\rm sys} = T_{\rm rec} + T_{\rm sky}, \tag{2.6.6}$$

whereas the SKA-I system temperature is modelled by adding ground spill-over (Square Kilometre Array Cosmology Science Working Group et al., 2018)

$$T_{\rm sys} = T_{\rm rec} + T_{\rm spl} + T_{\rm sky}. \tag{2.6.7}$$

Here, $T_{\rm spl} \approx 3$ K is the spill-over contribution.

Furthermore, $T_{\rm rec}$ is the receiver temperature particular to each telescope model. The BINGO and FAST receiver temperatures are presented in Table 2.2, where for SKA-I

$$T_{\rm rec} = 15 \text{ K} + 30 \text{ K}(\nu(\text{GHz}) - 0.75)^2. \tag{2.6.8}$$

Basically, all three telescopes see the same sky, so we model their sky temperature contribution as

$$T_{\rm sky} = T_{\rm gal} + T_{\rm CMB}, \tag{2.6.9}$$

with

$$T_{\rm gal} \approx 25 \text{ K}(408 \text{ MHz}/\nu)^{2.75} \tag{2.6.10}$$

being the contribution from our Milky Way galaxy for a given frequency ν and $T_{\rm CMB} \approx 2.73\,{\rm K}$ is the cosmic microwave background (CMB) temperature. One can refer to Square Kilometre Array Cosmology Science Working Group et al. (2018) for more information regarding system temperature, and Table 2.2 for the detailed list of exact values of each experimental parameters considered in our forecast.

Generally speaking, 21-cm intensity maps highly suffer from contaminations due to foregrounds, such as Galactic synchrotron emission, extragalactic point sources and atmospheric noises. Thus, applications of foreground cleaning techniques are inevitably important in order to mitigate these contaminations. However, there is always some level of contamination residuals after applying such techniques, and therefore, the cross-correlation of noises between different frequency bins may not completely be negligible (Li and Ma, 2017). So the elements of the noise matrix N_ℓ have been treated under some simplified assumptions, such as zero cross-correlated noise residuals.

Next, we perform the Fisher matrix analysis to explore the potential of future HI IM experiments for constraining the cosmological parameters. Assuming that the MLE can be approximated well by a multivariate Gaussian function, the best estimate of the parameter covariance matrix inverse is given by the Fisher matrix $\mathcal{F}$. The Fisher matrix (2.4.13) can be expressed as,

$$\mathcal{F}_{\alpha\beta} = f_{\rm sky} \sum_{\ell_{\rm min}}^{\ell_{\rm max}} \left(\frac{2\ell+1}{2}\right) {\rm tr}\left[C_{\ell,\alpha}\Sigma_\ell C_{\ell,\beta}\Sigma_\ell\right], \tag{2.6.11}$$

in which, the total noise inverse matrix is given by

$$\Sigma_\ell = (C_\ell + N_\ell)^{-1}. \tag{2.6.12}$$

Here, N_ℓ, the noise power spectrum, is an $n_\nu \times n_\nu$ matrix. We assume that noises between the i-th and j-th frequency channels ($i \neq j$) are uncorrelated, and thus N_ℓ is a diagonal matrix. The tomographic angular power spectrum, C_ℓ, is an $n_\nu \times n_\nu$ matrix, and each element of C_ℓ is the HI cross angular power spectrum of the i-th and j-th redshift bins. Furthermore, we multiply C_ℓ with the window function for the i,j-th frequency channels,

$$W_{\ell,ij} = {\rm e}^{-\ell^2(\sigma_i^2+\sigma_j^2)/2}, \tag{2.6.13}$$

which is simply the multiplication of the Fourier space Gaussian beam function at the i-th and j-th frequency channels. In this case,

$$\sigma_i = \theta_{\rm FWHM}/(\sqrt{8\ln(2)}) \simeq 0.4245\theta_{\rm FWHM}, \tag{2.6.14}$$

where $\theta_{\rm FWHM} = 1.22\lambda/D_{\rm dish}$ is the full-width at half-maximum (FWHM) of the beam. The window function (2.6.13) implies that, at large values of ℓ, corresponding to small angular scales, it falls off rapidly as depicted by the HI angular power spectra in Figure 2.1.

For all cosmological constraints, we ignore the monopole and dipole moments, and consider a multipole moment range from $\ell = 2$ to $\ell = 600$ for forecast with BINGO and SKA-I, and $\ell = 2$ to $\ell = 1000$ for FAST. This range of ℓ is chosen for each telescope to ensure that, within each

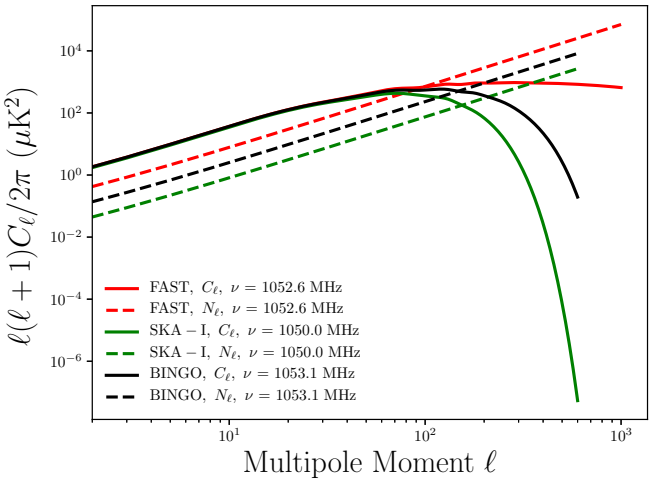

Figure 2.1: The noise power spectra N_ℓ (dashed lines) and beam convolved angular power spectra, C_ℓ (solid lines) for FAST (red), BINGO (black) and SKA-I (green) at approximately overlapped frequencies. As expected, we see that the angular power spectra have almost the same profile at large scales but deviate with increase in number of multipoles, ℓ. Beyond $\ell = 150$, angular power spectra for BINGO and SKA-I more rapidly become insignificant than noise compared to FAST angular power spectrum.

range of ℓ, the signal-to-noise ratio (SNR) is significant, which contributes to the constraints of cosmological parameters. For very high ℓ, the beam function makes the signal be below the noise power spectrum, so adding high ℓ of the power spectrum does not improve the constraints.

Here, we vary nine parameters which are shown in Table 2.1. Therefore, our Fisher matrix (Eq. (2.6.11)) is a 9×9 matrix. To see how we can tighten up constraints with *Planck* satellite data, we utilized the best-fit ΛCDM CMB power spectra from the baseline *Planck* chains, which include TT + TE + EE + lowTEB + BAO + H0 + JLA + lensing, taken from the Planck Legacy Archive website – Cosmology section [1] to compute the *Planck* covariance. We then make an entry-wise addition of the *Planck* Fisher matrix (the inverse of the *Planck* covariance (Planck Collaboration et al., 2016)) for each parameter, to the corresponding parameter entries in the resulting Fisher matrix calculated by applying the formulae (2.6.11) for each particular HI IM experiment. The model cosmological parameters whose values were varied by making entry-wise addition of the *Planck* Fisher matrix correspondingly to BINGO, FAST and SKA-I Fisher matrices are $\Omega_{\rm b}h^2$, $\Omega_{\rm c}h^2$, w_0, w_a, $\ln(10^{10}A_{\rm s})$, H_0 and $n_{\rm s}$. The rest of the HI experiment parameters, namely, $N_{\rm eff}$ and $\Sigma m_\nu/94.07$ eV, were omitted so that we could only consider parameters that conform with the *Planck* chains data set, Planck Collaboration et al. (2016) (believed to set the strongest constraints on cosmological parameters), that we used to compute the *Planck* Fisher matrix under consideration.

[1] https://pla.esac.esa.int/#cosmology

2.7 Results and Discussion

In this section, we present two sets of forecast results, the first one detailing a comparison on various cosmological constraints between FAST, BINGO and SKA-I, and the second one showing relative constraining capabilities by combining each of the three experiments with *Planck*. The *Planck* covariance matrix includes TT + TE + EE + lowTEB + BAO + H0 + JLA + lensing, but throughout this chapter, we will use a shorthand *Planck* to mean *Planck* + TT + TE + EE + lowTEB + BAO + H0 + JLA + lensing. Table 2.3 lists the 1σ errors for the marginalized parameter constraints for each of these experiments. In our simulations, for all the three experiments, we fix the frequency bandwidth to be 10 MHz, unless stated otherwise. More specifically, the frequency (or equivalently redshift) division is done with uniform spacing of channels, each with width 10 MHz or 1 MHz, depending on the tests performed. This means that for standard tests carried out with a channel width of 10 MHz, we included 30 redshift/frequency bins for BINGO, 40 redshift bins for FAST and 70 redshift bins for SKA-I, while for tests carried out with a 1 MHz channel width, we used 300, 400 and 700 redshift bins, respectively, for BINGO, FAST and SKA-I. We have defined significantly narrower channel width compared to most of the previous works, for the motivation described in the later sections. Roughly, the central value of each channel width was used in calculations, which is the sum of the lower and upper margins divided by 2. The central value of the bin is a good approximation for sufficiently narrower bins in that we can neglect evolution of cosmological functions/backgrounds within each redshift bin, because most of the relevant functions coupled in calculations of the angular power spectra vary slowly with redshift; instead, the evolving cosmological functions are fixed to their values at the central redshift of the bin, the choice of which is however motivated by Bull et al. (2015b). Full telescope specifications we implemented for simulations are presented in Table 2.2, and the descriptions of the cosmological parameters utilized in the forecast are given in Table 2.1. We use `Camb_sources` (Challinor and Lewis, 2011) to compute the raw tomographic angular power spectra Equation (2.6.1) and another code that we developed to simulate forecasts of cosmological parameter constraints via the Fisher matrix (Subsection 2.4). We will then compare the forecasted constraints between these different experiments.

2.7.1 Dark Energy Constraints

We present two separate analyses, the first one is to show how FAST, BINGO and SKA-I can comparatively constrain the dark energy equation of state (EoS) in the form of $w(a) = w_0 + w_a(1-a)$ ("Chevallier-Polarski-Linder parametrization" (Chevallier and Polarski, 2001; Linder, 2003)) and the second one is to indicate how each of these experiments, FAST, BINGO and SKA-I plus *Planck* data, can constrain the dark energy EoS. Figure 2.2 demonstrates that FAST will constrain the dark energy EoS better than BINGO, and possibly than many other currently known single-dish HI IM approach counterparts. However, SKA-I puts more stringent constraints on the dark energy EoS than both BINGO and FAST. The 1σ errors from (w_0, w_a) covari-

ance matrices for BINGO, FAST and SKA-I are, respectively, $(0.9293, 3.5792)$, $(0.4083, 1.5878)$ and $(0.3158, 0.4622)$.

To compare the relevant improvement in 1σ errors from BINGO to FAST and SKA-I, we consider the largest error of the three experiments for a particular parameter and find out the fractions of the errors that have been reduced with respect to it. For w_0, the error is reduced by $(0.9293 - 0.4083)/0.9293 = 56.06\%$ and $(0.9293 - 0.3158)/0.9293 = 66.02\%$ for FAST and SKA-I with respect to BINGO, respectively. For w_a, it is reduced by $(3.5792 - 1.5878)/3.5792 = 55.64\%$ and $(3.5792 - 0.4622)/3.5792 = 87.09\%$ for FAST and SKA-I with respect to BINGO, respectively. Therefore, we can see quite a significant improvement of FAST and SKA-I for future constraints on the dark energy EoS. Although the parameters w_0 and w_a have some degeneracy, the joint constraints with *Planck* can significantly improve the constraints.

The fact that FAST will do better than BINGO to constrain the dark energy EoS remains unchanged if each of the experiments is individually combined with *Planck* data, as shown in Figure 2.3. This observation is valid and is supported by Bigot-Sazy et al. (2016), although in their paper they applied a different set of experimental parameters. As previously observed from simulations in Figure 2.2, again, Figure 2.3 demonstrates that SKA-I will put more stringent constraints than both FAST and BINGO when each of the experiment's Fisher matrix is added to the *Planck* Fisher matrix. The 1σ errors for (w_0, w_a), BINGO + *Planck*, FAST + *Planck* and SKA-I + *Planck* covariance matrices are, respectively, $(0.0832, 0.3520)$, $(0.0791, 0.3313)$ and $(0.0678, 0.2679)$, implying (w_0, w_a) constraints improve by $(4.93\%, 5.88\%)$ in error reduction for FAST + *Planck* relative to BINGO + *Planck* and there is an improvement of $(18.51\%, 23.89\%)$ in error reduction when constraining (w_0, w_a) for SKA-I + *Planck* relative to BINGO + *Planck*, see Table 2.3. It is clear that all three experiments improve dark energy constraints tremendously when the *Planck* Fisher matrix is added to each of the respective experiment's Fisher matrix.

To benchmark the performance of each single-dish experiment combined with *Planck* relative to *Planck* alone, we find that the (w_0, w_a) 1σ errors for *Planck*, BINGO + *Planck*, FAST + *Planck* and SKA-I + *Planck* are respectively, $(0.1080, 0.3845)$, $(0.0832, 0.3520)$, $(0.0791, 0.3313)$ and $(0.0678, 0.2679)$. The reduction in (w_0, w_a) 1σ errors for each experiment plus *Planck*, respectively, implies an improvement in the (w_0, w_a) constraints of $(22.96\%, 8.45\%)$, $(26.76\%, 13.84\%)$ and $(37.22\%, 30.33\%)$ for BINGO + *Planck*, FAST + *Planck* and SKA-I + *Planck* relative to *Planck* alone. Table 2.3, Figure 2.11 and Figure 2.13 summarize how the *Planck*-each-single-dish experiment joint constraints improve relative to the *Planck* data constraints alone for all the cosmological parameters considered.

To investigate the optimal survey volume, we consider FAST and SKA-I, and explore the range of survey areas from $2,000\,\mathrm{deg}^2$ to $25,000\,\mathrm{deg}^2$. Considering (w_0, w_a) constraints, we find the optimal survey area is around $16,000\,\mathrm{deg}^2$ for FAST with T_{sys} corresponding to $T_{\mathrm{rec}} = 25\,\mathrm{K}$ and $9,000\,\mathrm{deg}^2$ for a T_{sys} corresponding to $T_{\mathrm{rec}} = 35\,\mathrm{K}$. Results show that SKA-I can survey up to a maximum area of $25,000\,\mathrm{deg}^2$. This reality can be illustrated by the figure of merit (FoM) depicted in Figure 2.4. FoM is defined as (Huterer and Turner, 2001; Albrecht and Bernstein,

Table 2.3: 1σ errors for FAST, BINGO, SKA-I and *Planck* covariance matrices, and those obtained from covariance matrices resulting from a combination of each of the FAST, BINGO and SKA-I experiment's Fisher matrix with *Planck* Fisher matrix.

	FAST	BINGO	SKA-I	*Planck*	FAST + *Planck*	BINGO + *Planck*	SKA-I + *Planck*
$\Omega_{\rm b}h^2$	0.0090	0.0168	0.0072	0.0002	0.0001	0.0001	0.0001
$\Omega_{\rm c}h^2$	0.0061	0.0133	0.0115	0.0014	0.0011	0.0012	0.0008
w_0	0.4083	0.9293	0.3158	0.1080	0.0791	0.0832	0.0678
w_a	1.5878	3.5792	0.4622	0.3845	0.3313	0.3520	0.2679
$\ln(10^{10}A_{\rm s})$	0.1681	0.3217	0.2209	0.0271	0.0240	0.0259	0.0146
H_0	3.6902	6.5433	4.0082	1.0341	0.5288	0.6171	0.5282
$N_{\rm eff}$	1.7016	3.3814	1.2486	$--$	$--$	$--$	$--$
$n_{\rm s}$	0.0201	0.0727	0.0550	0.0046	0.0043	0.0045	0.0039
$\Omega_\nu h^2$	0.0044	0.0048	0.0017	$--$	$--$	$--$	$--$

2007)

$$\text{FoM} \propto [\sigma(w_0)\sigma(w_a)]^{-1} \propto 1/\sqrt{\det\, C(w_0, w_a)}. \tag{2.7.1}$$

We vary the survey area and see which $\Omega_{\rm sur}$ can maximize the FoM. As previously stated, we choose the survey area of $10,000$ deg^2 that was covered by the SDSS (Alam et al., 2015). The choice has the benefit of being fairly moderate and is potentially suitable for comparative and cross-correlation studies involving SDSS-like experiments, FAST and SKA-I. In addition, it is practical to choose this survey area for FAST and SKA-I comparisons because the marginal increase of FAST FoM is quite small if $\Omega_{\rm sur} > 10,000$, so we will use $\Omega_{\rm sur} = 10,000$ in our forecast. BINGO (Bigot-Sazy et al., 2015) can survey an approximate area of $2,500\,\text{deg}^2 - 3,000\,\text{deg}^2$ as reported by Li and Ma (2017); Bigot-Sazy et al. (2016), but for this particular study, we use a survey area of $3,000\,\text{deg}^2$ as was suggested by Bigot-Sazy et al. (2016).

Generally speaking, higher system temperature will result in higher noise spectra, which makes the constraints worse. This is indicated well by the FoM (Fig. 2.4), as signified by the two FAST system temperatures, $T_{\rm sys}$ of 25 K and 35 K. Low values of $1/\sqrt{\det\, C(w_0, w_a)}$ at high system temperature mean that experimental performance decreases with an increase in system temperature. For this reason, it is likely that BINGO is mostly affected because of its high overall system temperature.

There are several reasons why SKA-I performs better than both BINGO and FAST to constrain the dark energy EoS. One of the reasons is SKA-I's wide range of frequency coverage. We split the SKA-I frequency range into lower frequency band 350 MHz $\sim$ 700 MHz and higher

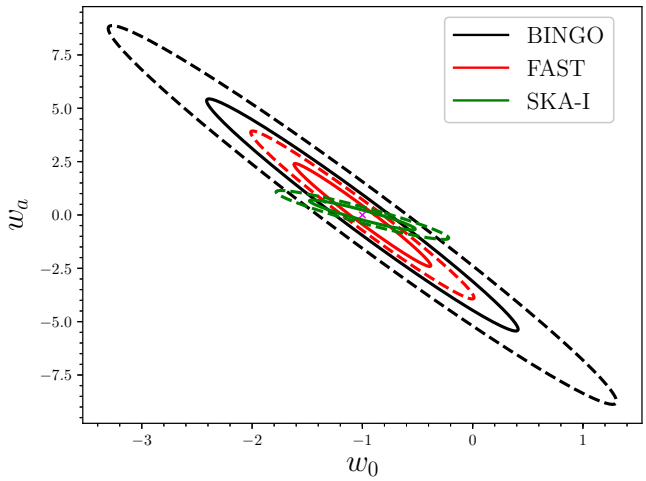

Figure 2.2: w_0 versus w_a, 1σ (solid lines) and 2σ (dashed lines) cosmological constraints for FAST (red), BINGO (black) and SKA-I (green).

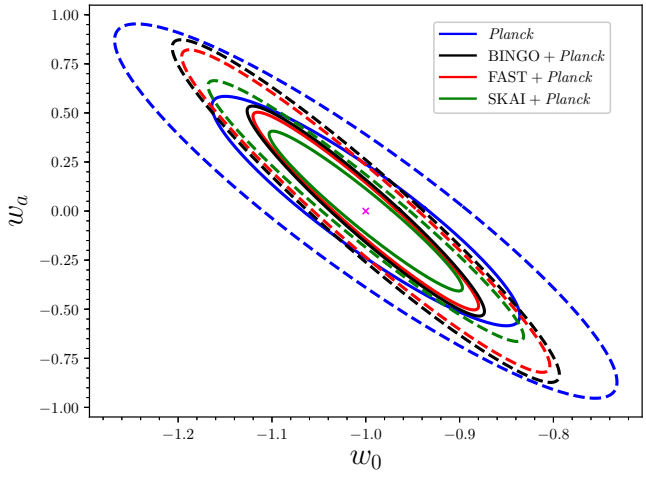

Figure 2.3: w_0 versus w_a, 1σ (solid lines) and 2σ (dashed lines) cosmological constraints for *Planck* (blue), FAST + *Planck* (red), BINGO + *Planck* (black) and SKA-I + *Planck* (green).

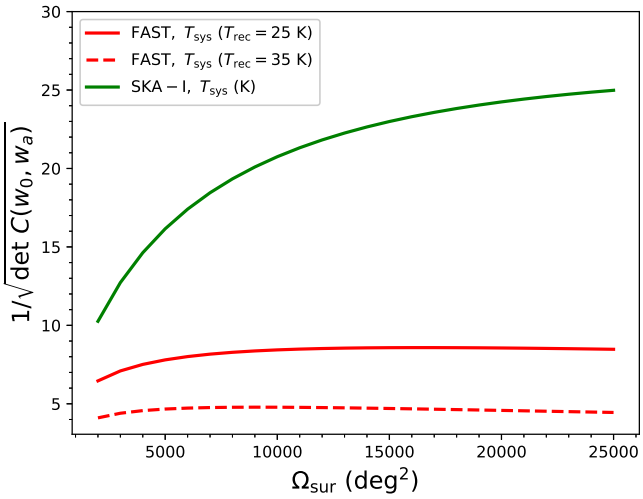

Figure 2.4: FoM: inverse square root of the determinant of w_0, w_a covariance matrix, $1/\sqrt{\det\, C(w_0, w_a)}$ versus survey area, $\Omega_{\rm sur}$ (deg^2) for FAST (red) at system temperatures, $T_{\rm rec}$, of 25 K (solid line) and 35 K (dashed line), and for SKA-I (green) at system temperature, $T_{\rm sys}$ (K) given by Equation (2.6.7).

frequency band 700 MHz $\sim$ 1,050 MHz, and compare them with the full SKA-I frequency range (350 MHz $\sim$ 1,050 MHz). As plotted in Figure 2.5, the full SKA-I range of frequencies proportionately puts more stringent constraints on w_0 and w_a than lower- and upper-frequency bands, and the FoM improves significantly, as illustrated in Figure 2.6. The reason is that the full frequency range of SKA-I includes the measurement of the HI power spectrum at a larger range of redshift evolution, and also includes the information on cross-correlated signals in higher and lower frequency bands. Therefore, it provides tighter constraints than higher and lower redshift bands.

Moreover, as we have previously accounted for BINGO, system temperature seems to be an important nuisance, which if not controlled, will hamper constraints. The less stronger constraints for the lower half of the frequency band of SKA-I compared to the upper band in Figure 2.5 (see also Figure 2.6) are suggestively due to high system temperatures at the corresponding frequencies. The system temperature is somewhat a function of frequency, especially parts of $T_{\rm sys}$ (2.6.7) that vary with it, i.e. Equations (2.6.8) and (2.6.9). As a result, we see that system temperature, $T_{\rm sys}$, is more dominant at low frequencies than at high frequencies, see Figure 2.7. This effect can also be noted for the FAST FoM at different system temperatures, see Figure 2.4.

The current SKA-I experimental design is to have 133 15-meter dishes and 64 13.5-meter MeerKAT dishes. We illustrate the forecast with SKA-I by considering the previous number of dishes, which is 190, and then compare the constraint forecasts with the updated number of dishes, which is 133. The reason for considering the former number of dishes is to illustrate how the change in the number of dishes affects performance and also to form a reference point

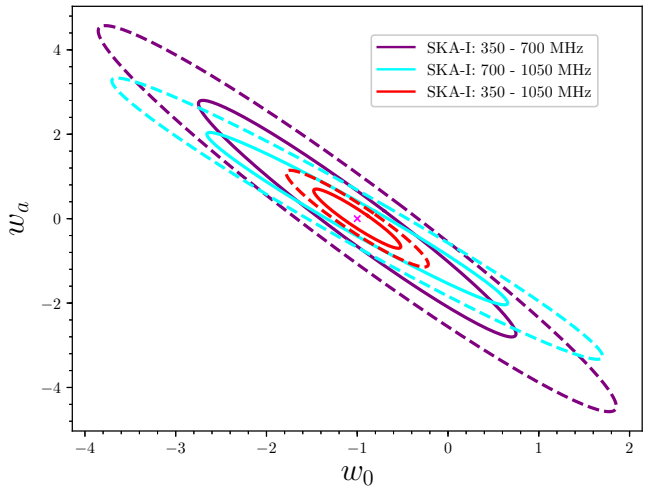

Figure 2.5: w_0 versus w_a, 1σ (solid lines) and 2σ (dashed lines) cosmological constraints for SKA-I split into lower frequency band (purple), high frequency band (cyan) and full range (red) of SKA-I frequencies.

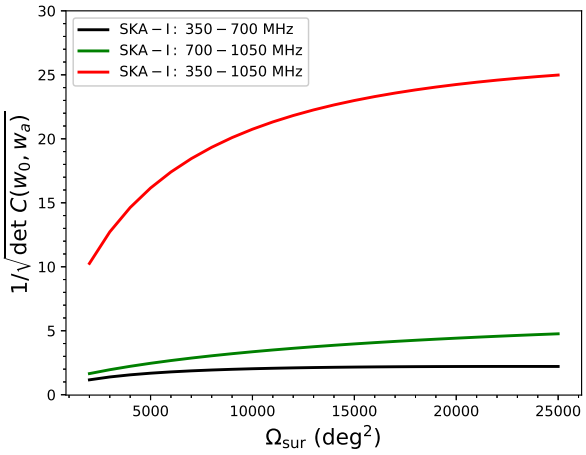

Figure 2.6: FoM: inverse square root of the determinant of w_0, w_a covariance matrix, $1/\sqrt{\det\, C(w_0, w_a)}$ versus survey area, $\Omega_{\rm sur}$ (deg^2) for various SKA-I frequency bands: lower frequency band, $350 - 700$ MHz (black), upper frequency band, $700 - 1,050$ MHz (green) and the full SKA-I frequency range, $350 - 1,050$ MHz (red).

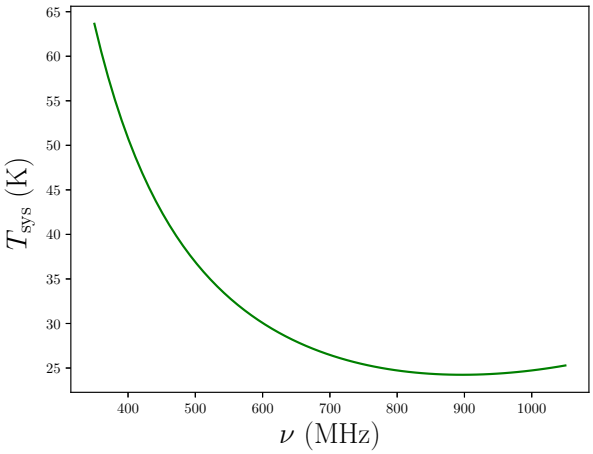

Figure 2.7: SKA-I variation of system temperature, $T_{\rm sys}$ against frequency, ν.

for comparison with previous literature that considered old SKA-I (SKAI-MID) experimental specifications.

We see from Figure 2.8 that constraints do not strongly respond to the number of dishes. The most intrinsic property of a large number of dishes is mapping LSS at very large angular distances/scales by integrating HI emission efficiently over large volumes slices of the sky. One would expect that a large number of dishes would significantly improve cosmological constraints, but if we compare constraints by assuming SKAI-MID 190 and on the other hand 133 single dishes, both in the autocorrelation mode, we notice that there is not much significant difference.

The exact procedure of how to incorporate images from different frequency bands is unknown (Square Kilometre Array Cosmology Science Working Group et al., 2018), but in this forecast, we assume that the SKA-I project incorporates 190 15-meter single-dishes in an autocorrelated mode for HI IM.

2.7.2 Constraints on other Cosmological Parameters

We present the results of our forecast for the nine cosmological parameters in Table 2.1 for the single-dish experiments: FAST (Nan et al., 2011; Bigot-Sazy et al., 2016), BINGO (Bigot-Sazy et al., 2015; Battye et al., 2012) and the SKA-I (Bull et al., 2015a; Santos et al., 2015). Figure 2.9 displays the constraints on various cosmological parameters. For the case of the dark energy EoS, we have seen that SKA-I will give the strongest constraints followed by FAST and then BINGO.

Considering all nine parameters, SKA-I and FAST are competitive in their abilities in constraining cosmological parameters. As illustrated in Figure 2.9, FAST provides stronger constraints on $n_{\rm s}$ because its larger dish can supply more constraints on small-scales of HI power spectra. Interestingly, the marginalized constraints on $n_{\rm s}$ for BINGO and SKA-I do not show much significant difference. FAST will also impose stronger constraints on $\Omega_{\rm c}h^2$, $\ln(10^{10}A_{\rm s})$ and H_0

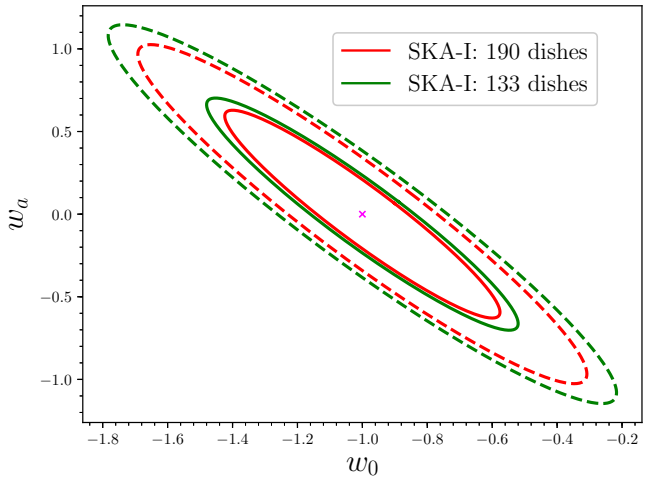

Figure 2.8: 1σ (solid lines) and 2σ (dashed lines) comparisons of SKA-I (SKAI-MID Band I) constraints on the dark energy EoS by considering the early proposition of 190 dishes (red) and the updated (green) 133 dishes.

than both BINGO and SKA-I, but slightly better constraint on H_0 than SKA-I. In comparison, SKA-I will strongly constrain $\Omega_\nu h^2$ in addition to w_a, while slightly better constraining $\Omega_\mathrm{b} h^2$ and w_0 parameters than FAST. Another observation is that SKA-I imposes slightly stronger bounds on both N_eff joint and marginalized constraints than FAST. The corresponding $\Omega_\nu h^2$, N_eff and $\Omega_\mathrm{b} h^2$ 1σ errors for SKA-I, respectively, reduce by 61.36%, 26.62% and 20% relative to FAST. Likewise, the corresponding 1σ errors for the parameters where FAST performs better than SKA-I, n_s, $\Omega_\mathrm{c} h^2$, H_0 and $\ln(10^{10} A_\mathrm{s})$ respectively, are reduced by 63.45%, 46.96%, 7.93% and 23.9% relative to the corresponding SKA-I 1σ errors. These reductions in the errors proportionately imply improvements in constraints as reflected by simulations. In Figure 2.10, we depict the relative constraint improvement in percentage for all parameters and for the three simulated experiments.

The prospective better performance of FAST in constraining particular parameters, as we have seen, is due to its high angular resolving power. FAST has the largest dish diameter of the three telescopes which means its angular resolution is higher than that of SKA-I and BINGO by a factor of 21 and 7.5 respectively, making it very capable of mapping signals at small angular scales. So, it is likely that FAST's performance will be significant at small scales. On the other hand, Figure 2.1 indicates FAST is noise-dominated for $\ell > 100$, because its SNR is less than unity, while SKA-I does not attain SNR<1 until $\ell > 150$. This suggests that SKA-I may better constrain cosmological parameters at some ranges of small angular scales due to its higher SNR compared to FAST on those scales. Although SNR for SKA-I is greater than unity until $\ell > 150$, from this point onwards, SKA-I SNR decreases exponentially, while SNR for FAST decreases gently across the same range of scales. This elucidates another important clue that both FAST and SKA-I can perform relatively well in constraining cosmological parameters sensitive to small

angular scales. As we have previously pointed out, the trade-off on whether FAST or SKA-I can perform better at small scales may not be determined by a single factor but may be influenced by a number of factors, such as, the choice of parameterization.

For the case of dark energy constraints, stringent constraints for SKA-I are due to its wider frequency coverage than FAST and BINGO. BINGO is probably disadvantaged due to its high system/receiver noise temperature.

Figure 2.11 visualizes cosmological constraints for each of these experiments combined with *Planck* by using a Fisher matrix forecast. At this instance, constraints for all the three experiments improve significantly. As we have seen, SKA-I + *Planck* continues to provide better constraints than FAST + *Planck* and BINGO + *Planck* on dark energy EoS parameters w_0 and w_a. In contrast to the previous case involving FAST, BINGO and SKA-I experiments, SKA-I + *Planck* constraints on $\ln(10^{10}A_{\rm s})$ and $\Omega_{\rm c}h^2$ relative to FAST + *Planck* and BINGO + *Planck* experiments are now very significant. Similarly, neither FAST + *Planck* nor SKA-I + *Planck* shows significant improvement in constraining $\Omega_{\rm b}h^2$ compared to BINGO + *Planck*. Therefore, SKA-I + *Planck* imposes strong constraints on $\Omega_{\rm c}h^2$ and $\ln(10^{10}A_{\rm s})$, in addition to w_0, w_a, as we have ascertained previously, relative to FAST + *Planck* and BINGO + *Planck*.

More specifically, SKA-I + *Planck* manifests some significant improvement in constraining $\Omega_{\rm c}h^2$ and $\ln(10^{10}A_{\rm s})$ than FAST + *Planck* and BINGO + *Planck* by respectively, 27.27%, 39.17% and 33.33%, 43.63%. However, SKA-I + *Planck* is slightly better in constraining $n_{\rm s}$ than FAST + *Planck* and BINGO + *Planck* by 9.3% and 13.33% respectively.

In a like manner, FAST + *Planck* exhibits some significant improvement in constraining $\Omega_{\rm c}h^2$, w_0, w_a, $\ln(10^{10}A_{\rm s})$, H_0 and $n_{\rm s}$ than BINGO + *Planck* by 8.33%, 4.93%, 5.88%, 7.34%, 14.31% and 4.44%, respectively.

Though there is significant performance improvement in constraining most of the cosmological parameters for FAST + *Planck* compared to FAST alone, for SKA-I + *Planck* compared to SKA-I alone and for BINGO + *Planck* compared to BINGO alone, there is no improvement for FAST + *Planck* in constraining H_0 relative to SKA-I + *Planck*, see Figures 2.11 and 2.12.

As we have seen from Figures 2.11 and 2.12, SKA-I + *Planck*, followed by FAST + *Planck*, is more competitive in constraining cosmological parameters than BINGO + *Planck*. In any case, *Planck* results have a very significant impact on constraining cosmological parameters when combined with each of the three experiments (Fig. 2.13).

In addition, we have tested using the dark energy EoS and find that, for BINGO, FAST and SKA-I HI IM experiments, the choice of frequency channel width $\Delta\nu = 1\,\mathrm{MHz}$ can significantly improve constraints for all the three HI experiments than larger channel width (Fig. 2.14). This is because a smaller bandwidth can preserve the redshift-space-distortion effect in the radial direction, which makes it less "Limber cancelled" than wider bandwidth (Hall et al., 2013). This is also illustrated in figure 6 of (Xu et al., 2018).

To strike a balance between limitation of foreground techniques to extract HI signal at high

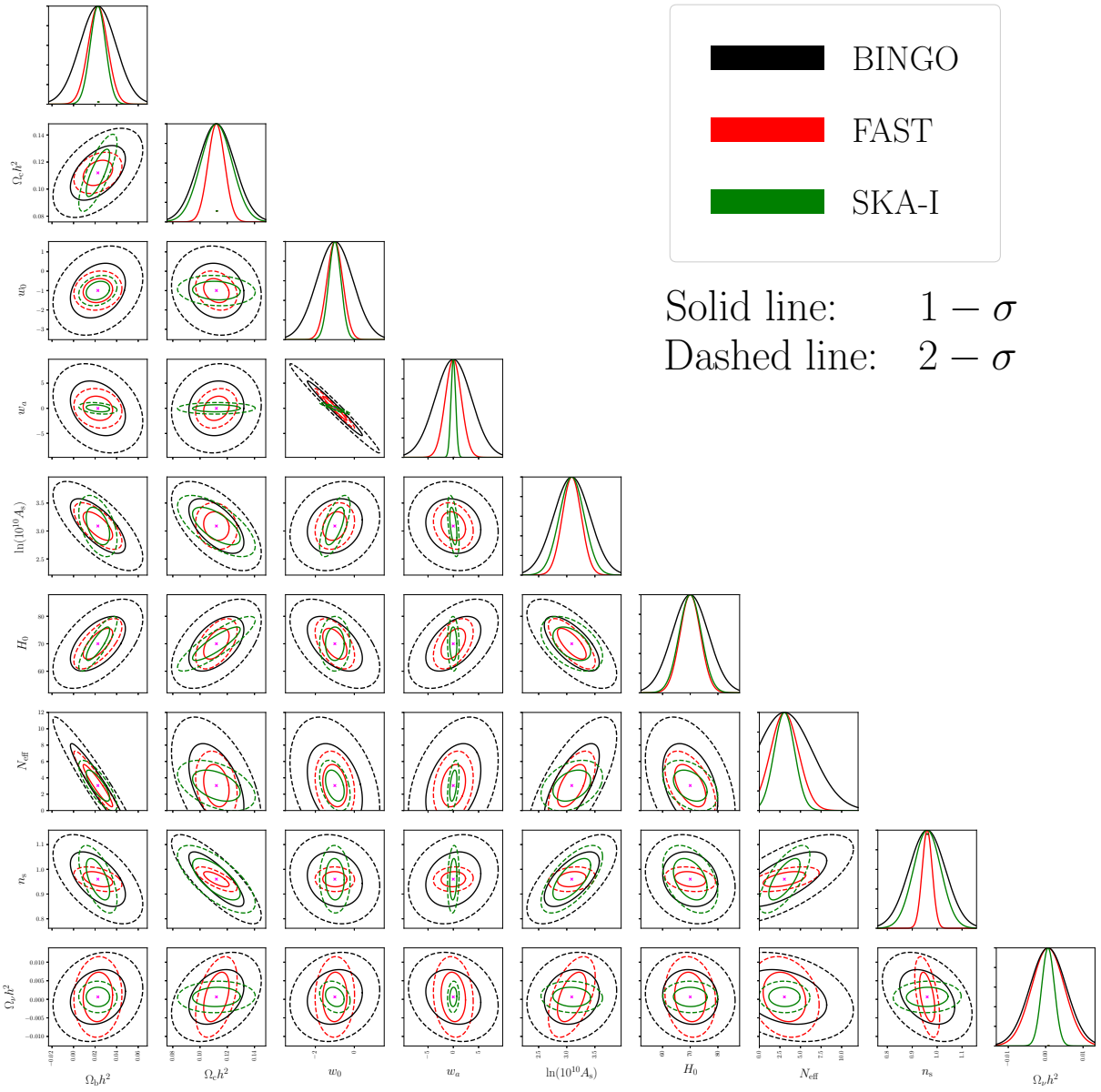

Figure 2.9: Forecasts of cosmological constraints from future observations with FAST, BINGO and SKA-I.

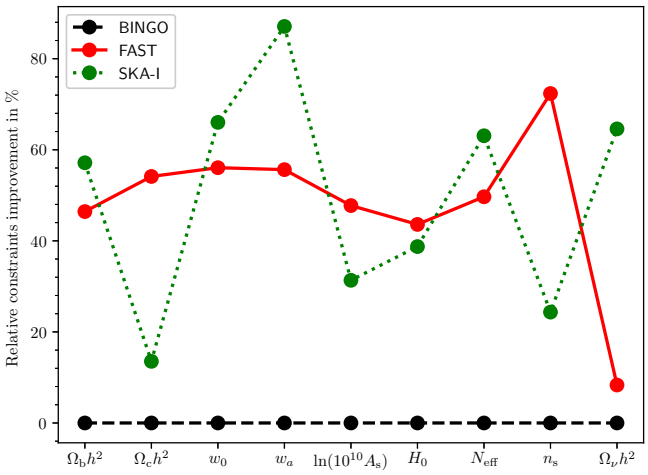

Figure 2.10: The relative percentage improvement for FAST and SKA-I with respect to BINGO in constraining each of the nine cosmological parameters.

angular scales and constraint prospects, as a case study, we simulate new dark energy EoS constraints by ignoring multipole moments at large angular scales, up to $\ell = 9$. The comparisons between Figures 2.2 and 2.3 simulated by considering full multipole range of our interest, and Figures 2.15 and 2.16 where we apply multipole moments cut-off, by considering minimum $\ell = 10$, yield a conflicting scenario between foreground effects if we ignore small ℓ's and optimistic constraint forecast if we include them. Neglecting several values of ℓ corresponding to large angular scales weakens constraints, and the 1σ errors for marginalized (w_0, w_a) constraints change, respectively, for BINGO, FAST and SKA-I from $(0.9293, 3.5792)$, $(0.4083, 1.5878)$, $(0.3158, 0.4622)$ to $(1.0250, 3.9449)$, $(0.4355, 1.6864)$, $(0.4059, 0.5735)$; and from $(0.0832, 0.3520)$, $(0.0791, 0.3313)$, $(0.0678, 0.2679)$ to $(0.0835, 0.3532)$, $(0.0795, 0.3336)$, $(0.0702, 0.2776)$ for BINGO + *Planck*, FAST + *Planck* and SKA-I + *Planck*, as summarized in Table 2.4.

This is a clear illustration of how large angular scales that are more dominated by the foreground contaminations may affect the cosmological constraint forecast analyses. However, we will assume that the ongoing progress in circumventing the foreground challenge and bias at large scales and other systematics at both large and small scales will be successful, and hence allow us to consider the maximum possible range of ℓ's, as we have done in this study.

The subject of foreground in general, its domination and challenges faced when decontaminating the HI signal on certain angular scales have been discussed in Wolz et al. (2014, 2015); Alonso et al. (2015) and the references therein; whereby Planck Collaboration et al. (2018) presents a comparative study on the performance of a number of algorithms for diffuse component separation, just to name a few.

This chapter is primarily focused on the forecast of cosmological parameter constraints with HI IM experiments. To this point, we postpone the in-depth discussion of challenges presented by foregrounds and other issues to the next chapter. Such issues include addressing systematic limitations such as contaminations of single-dish observations by what is so-called $1/f$ noise, a

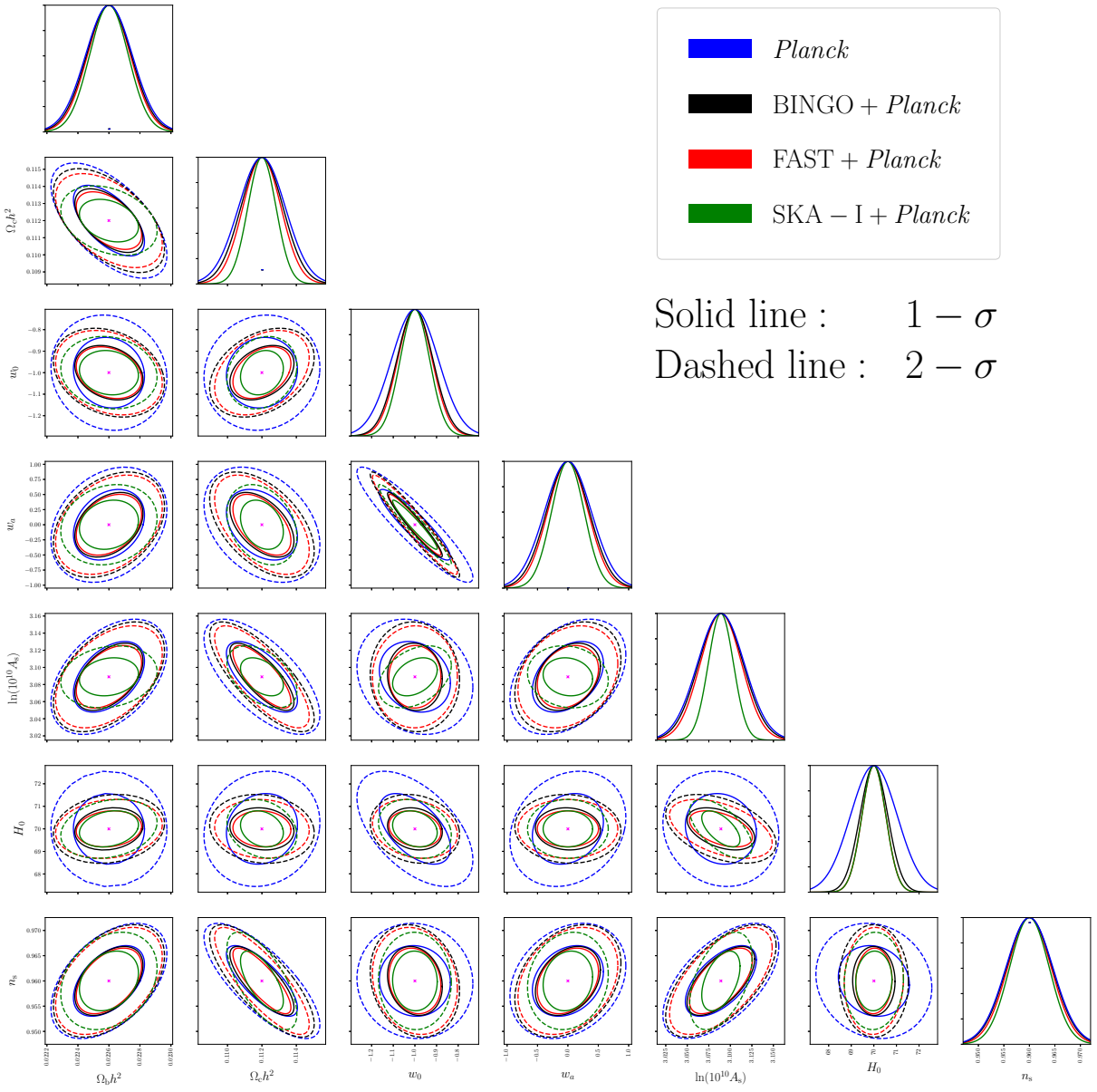

Figure 2.11: Forecasts of joint cosmological constraints with each of the FAST, BINGO and SKA-I experiments plus *Planck* data, compared with *Planck* data constraints alone.

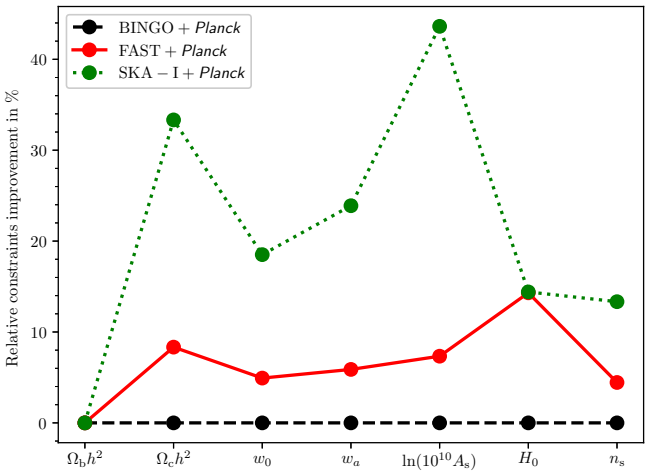

Figure 2.12: The relative percentage improvement for FAST + *Planck* and SKA-I + *Planck* with respect to BINGO + *Planck* in constraining each of the seven cosmological parameters we have considered.

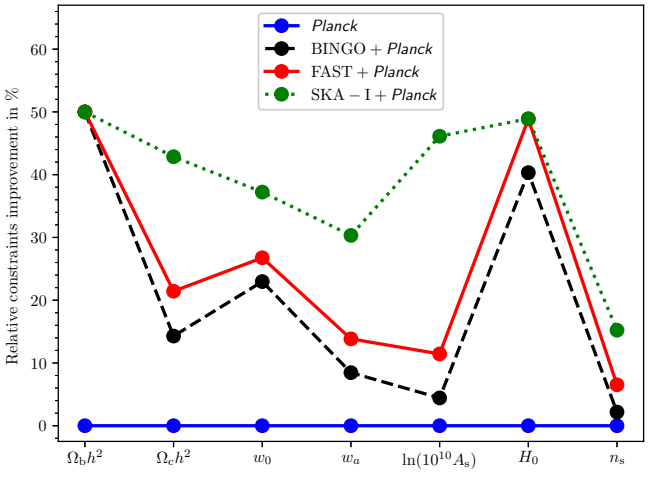

Figure 2.13: The relative percentage improvement for BINGO + *Planck*, FAST + *Planck* and SKA-I + *Planck* with respect to *Planck* alone in constraining each of the seven cosmological parameters we have considered.

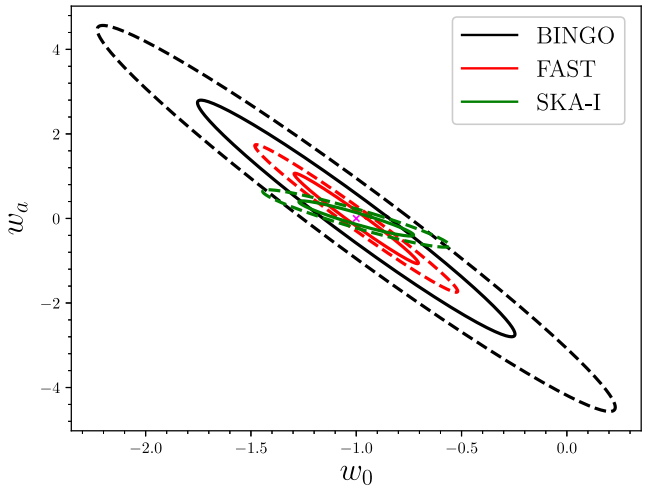

Figure 2.14: Forecasts of cosmological constraints with FAST, BINGO and SKA-I with a frequency channelization of $\Delta\nu = 1\,\mathrm{MHz}$.

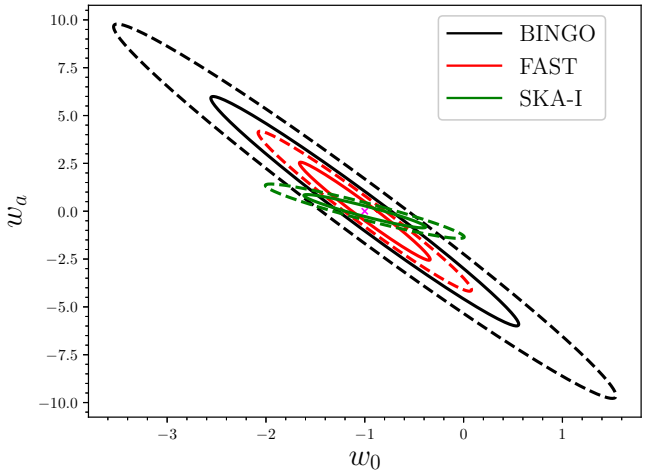

Figure 2.15: w_0 versus w_a, 1σ (solid lines) and 2σ (dashed lines) cosmological constraints for FAST (red), BINGO (black) and SKA-I (green) for minimum multipole moment, $\ell = 10$.

single instrumental systematic, due to frequency correlation, and the correlated gain fluctuations across the receiver bandpass (Harper et al., 2018).

2.8 Comparison with Previous Forecasts of HI IM

This forecast aims to optimize the potential of future 21-cm IM experiments, by providing an in-depth comparative objective study focusing on FAST, BINGO and SKA-I in autocorrelation mode, operating as a collection of independent single-dish (rather than a usual interferometry) telescopes. We use much cleaner and explicit maximum likelihood and Fisher matrix tools to forecast the behavior of these three telescopes by considering a wide range of sensitive exper-

Table 2.4: 1σ errors for FAST, BINGO and SKA-I covariance matrices, and those obtained from covariance matrices resulting from a combination of each of the FAST, BINGO and SKA-I experiment's Fisher matrix with *Planck* Fisher matrix, for minimum multipole moments, $\ell = 2$ and $\ell = 10$. Errors signify that constraints resulting from discarding small values of ℓ, i.e., $2 \leq \ell < 10$, equivalent to large angular scales are weaker than those including small ℓ's.

	FAST	BINGO	SKA-I	FAST + *Planck*	BINGO + *Planck*	SKA-I + *Planck*
$\ell \geq 2$						
w_0	0.4083	0.9293	0.3158	0.0791	0.0832	0.0678
w_a	1.5878	3.5792	0.4622	0.3313	0.3520	0.2679
$\ell \geq 10$						
w_0	0.4355	1.0250	0.4059	0.0795	0.0835	0.0702
w_a	1.6864	3.9449	0.5735	0.3336	0.3532	0.2776

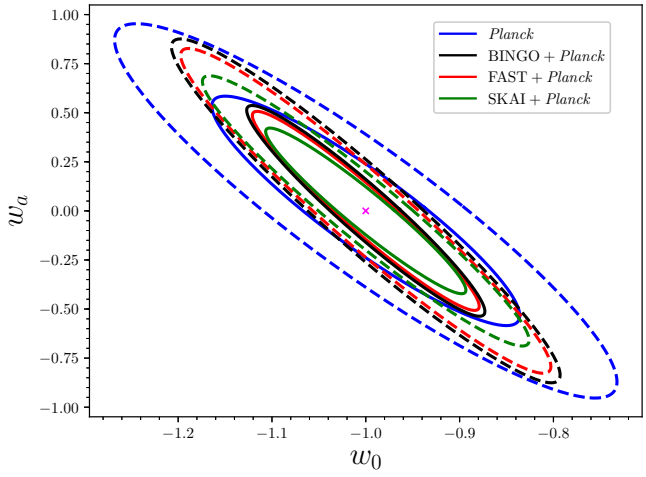

Figure 2.16: w_0 versus w_a, 1σ (solid lines) and 2σ (dashed lines) cosmological constraints for *Planck* (blue) FAST + *Planck* (red), BINGO + *Planck* (black) and SKA-I + *Planck* (green) for minimum multipole moment, $\ell = 10$.

imental analyses aspects, laying the formalism that can be employed to forecast varying sets of cosmological parameter constraints with a diverse range of 21-cm IM experiments. We notice that there are several previous studies that have made cosmological forecasts for HI IM experiments, but our current study has the following distinctive features:

- Extending the work by Bull et al. (2015b) to consider different cosmological parameter set. Bull et al. (2015b) considered a set from the standard ΛCDM model: the Hubble

parameter, $H_0 = 100h$ km s^{-1} Mpc^{-1}, the cosmological constant, Ω_Λ, the baryon density, $\Omega_b h^2$, the linear amplitude of density fluctuations, σ_8, the index of the power spectrum of primordial density fluctuations, n_s, and the optical depth to last scattering, τ. They extended the ΛCDM model with parameters w_0, w_a, Ω_K and the growth index, γ. Here the cosmological constant, Ω_Λ and the curvature parameter, Ω_K are related to the total matter density (cold dark matter + baryons) by $\Omega_M = 1 - \Omega_K - \Omega_\Lambda$. In their forecast, they used varying subsets of the considered parameter set to measure constraints. Their forecast approach included fixing fiducial values of some parameters, marginalizing over the *Planck* priors in the Fisher matrix or over other parameters, and not directly constraining some parameters by assuming their strong correlation with other parameters, such as in the case of *Planck* priors, where *Planck* measurements were combined with a particular experiment. We extended a subset of parameters considered in the aforementioned paper to form a new set, Table 2.1, and carried out Fisher matrix forecast, derived and treated under a somewhat different approach. However, we expanded both cosmological parameters and the HI IM set of experiments compared to such studies as Battye et al. (2013) and Bigot-Sazy et al. (2015, 2016) to form a different forecast portfolio. Forecasting by considering various experimental designs and parameter sets is indispensable, since each set of cosmological parameters when intertwined with a particular experimental design, in principle, characterizes unique prediction results with an intention to harmoniously and comparatively contribute to address caveats and pinpoint prospects as we move towards a more precise and convergent cosmology.

- Furthermore, our forecast incorporates more recent realistic and finalized development and design information because these telescope constructions have been undergoing major updates since the previous forecast results. These revisited experimental update set-ups include the number of beams, dish diameter, frequency bandwidth coverage, survey area for FAST (see FAST included in the early study in Bull et al. (2015b)); and the number of dishes for SKA-I, updated confirmed information about its precursor MeerKAT; and the new approach for modeling system temperatures.

  For example, previous forecasts with SKA-I considered 190 dishes, while we make comparison, for the purpose of illustration examining the case of dark energy EoS (see Fig. 2.8) in terms of SKA-I performance by considering old and updated number of dishes, we use the recently accepted and confirmed dishes for SKA-I from Square Kilometre Array Cosmology Science Working Group et al. (2018) for comparative study with BINGO and FAST.

  However, a number of previous forecasts were limited by the information that had been made publicly available during that time. These updates are crucial because the whole essence of the forecast is to enable the HI IM experiments to optimize their performances by considering each aspect and every single detail of their experimental designs and specifications to find out how each experiment is sensitive to various variables.

- We use reasonably narrow and computationally effective frequency channelization, each

with a bandwidth channel of 10 MHz, in contrast to previous forecasts, such as Bull et al. (2015b) which considered 60 MHz for all experiments. Our consideration accounts for the role of narrower channel bandwidths, as expected for modern radio receivers (Bull et al., 2015b) in tightening the constraints.

- We forecast for an even narrower frequency channel width of 1 MHz. This choice is close to the expected channelization of the future real HI IM surveys (Nan et al., 2011; Bigot-Sazy et al., 2016).

- To break degeneracies and improve precision of cosmological constraints, we include *Planck* 2015 CMB prior measurements and additional non-CMB data (TT + TE + EE + lowTE + BAO + H0 + JLA + lensing) that have been rigorously tested and improved. They include CMB lensing reconstruction, TT, TE, EE *Planck* CMB (Bennett et al. (2013)) power spectra, where TT represents temperature power spectrum, TE is temperature-polarization cross-spectrum, and EE is polarization power spectrum. In addition, lowTEB is low-ℓ CMB joint TT, EE, BB, and TE spectra, BAO is baryonic acoustic oscillation data, H0 is Hubble measurements, and JLA is the "Joint Light-curve Analysis supernovae (SNeIa) data". This aspect was not objectively considered by previous forecasts such as those that tried to include as many experiments as possible.

- We have provided more extensive quantification of cosmological constraint forecast in regard to these representative telescopes of our choice focusing on HI IM surveys. Other related works, such as Villaescusa-Navarro et al. (2017), studied the BAO measurements through single-dish HI IM observations in the post-reionization epoch in light of SKAI-MID. Shaw et al. (2014, 2015) alternatively addressed forecast of cosmological constraints, HI power spectrum estimation and measurement analyses of wide-field transient telescopes such as CHIME by an approach of what they call m-mode formalism. Furthermore, Pourtsidou et al. (2017) forecasted HI evolution with redshift and selected a subset of model-independent cosmological parameters focusing on the performance of the SKA and its precursor MeerKAT HI IM surveys (Pourtsidou, 2017), proposing their cross-correlation with optical galaxy surveys. With different settings, constraints on the dark energy parameters by cross-correlating/combining SKA-like HI IM and LSST-like surveys have been calculated by Pourtsidou et al. (2015).

  The essence of cross-correlating HI IM or 21-cm maps in general with galaxy redshift surveys is that contaminants, such as foregrounds, various noises, and systematics between the maps from two types of surveys are largely expected to be uncorrelated in frequency; this is in contrast to an HI signal that is correlated in respective frequency bands. Therefore, cross-correlation will not only statistically boost the abundance and the amplitude of HI signal, but will also statistically cancel out relevant foregrounds and systematics, thus increasing HI signal detection, and consequently improving constraints on the estimated values of the cosmological and astrophysical parameters. Constraints on $\Omega_{\rm HI} b_{\rm HI} r$ have a

direct link on future IM survey capabilities and the prospective science outputs. These surveys heavily depend on the qualitative and quantitative measurements (such as shape and amplitude) of HI signal. Cross-correlation will thus aggregate more HI signal information than any individual experiments, yielding robust and precise cosmological measurements (Pourtsidou, 2017). Pourtsidou et al. (2017), for example, have reported improvement to about a factor ~ 3 by considering Stage IV spectroscopic galaxy survey (similar to *Euclid*) and MeerKAT with an overlap area of $500\,\mathrm{deg}^2$ in constraining the amplitude of the quantity $\Omega_{\mathrm{HI}} b_{\mathrm{HI}} r$, where r is a correlation coefficient that accounts for possible stochasticity in the galaxy and HI tracers (Pourtsidou, 2017). Similarly, with an overlap area of $4000\,\mathrm{deg}^2$, the cross-correlation between MeerKAT and Stage III photometric optical galaxy survey measured/constrained $\Omega_{\mathrm{HI}} b_{\mathrm{HI}} r$ at the ~ 5 percent level across a wide range of redshifts compared to the autocorrelated MeerKAT constraints. According to them, these improvements were better than autocorrelation results they could achieve. The fact that the cross-correlated power spectrum will be less susceptible to contaminations can be used to identify systematics in 21-cm maps (Wolz et al., 2016; Pourtsidou et al., 2017; Carucci et al., 2017). Cross-correlation could be less susceptible to systematic contaminants (Pourtsidou et al., 2015), hence both foregrounds and systematics are expected to be highly suppressed, making their removal and control much easier.

Furlanetto and Lidz (2007) have laid down several advantages of cross-correlation, and two of them are as follows: first, the SNR resulting from cross-correlating 21-cm experiments and galaxy redshift surveys exceeds that of the individual 21-cm power spectrum by a factor of a few, further asserting that this may allow probing of smaller spatial scales and possibly more efficient detection of inhomogeneous reionization, and second, the approach highly reduces the required level of foreground cleaning for the 21-cm signal/maps. The HI IM and galaxy redshift survey cross-correlation approach to suppress foregrounds and systematics has also been motivated, explored and echoed using simulations by a number of other authors, such as Wolz et al. (2016); Carucci et al. (2017); Cunnington et al. (2019). This observation is also supported by Pen et al. (2009); Chang et al. (2010); Switzer et al. (2013); Masui et al. (2013); Anderson et al. (2017) who achieved the detection of HI by cross-correlating the HI IM and optical galaxy redshift surveys. Synergized cross-correlation between these two types of surveys has mutual benefits, which make them complement each other in alleviating survey-specific systematic effects and boost HI signal detection.

Other forecasts include CMB bounds on f_{NL} by combining information from SKA Phase I and *Euclid*/LSST-like photometric galaxy surveys using multi-tracer approaches, contrasting with respective single-tracer measurements (Fonseca et al., 2015); and an extension of this approach for HI IM with MeerKAT and photometric galaxy survey to constrain f_{NL} and a number of other parameters (Fonseca et al., 2017).

- Although combination of different subsets of cosmological parameters and experimental

designs largely characterizes future telescope performances, this study has singled out those features that are intrinsic to the particular experiment and are likely to determine their performance reliability, consistency, and stability in benchmarking with other similar surveys.

Therefore, in this chapter we have addressed forecasts of cosmological constraints for the three HI IM experiments under consideration, while including issues previously not given significant attention, updating the forecasts to suit the upgrades undergone by the considered telescopes and individually and simultaneously comparatively assessing the three telescope performances while laying down a basis for any other forecast of cosmological constraints with HI IM experiments, as we prepare for real survey take-off with these next generation instruments. A great deal of such useful information that we aggregate through our research plays a complementary role in building a scientific body of knowledge that can be maximally deployed to continually study the Universe.

2.9 Summary

We have conducted forecasts for cosmological constraints (Figures. 2.2, 2.3, 2.9 and 2.11) for a set of nine cosmological parameters (Table 2.1) and compared performance for three different proposed future survey projects, FAST, BINGO, and SKA-I. Our results, with a prescribed choice of experimental parameter set (Table 2.2), demonstrate that the FAST experiment will have better performance compared to BINGO, particularly in constraining dark energy EoS. Overall, SKA-I will put more stringent constraints on the dark energy EoS than both FAST and BINGO. We notice that there is a trade-off between SKA-I and FAST in constraining cosmological parameters, with each experiment being superior in constraining a particular set of parameters.

We point out that narrower frequency bandwidth such as 1 MHz (see Fig. 2.14) greatly improves constraints because the redshift-space-distortion effect suffers less cancellation if the frequency band becomes narrower (Hall et al., 2013; Xu et al., 2018). In fact, this requires more computer resources in terms of memory (RAM) for intermediate storage and speed for the reasonable computational time. This challenge can be addressed by advancing computing resources and modeling strategy. We postulate that high frequency-resolution needs one to take into account correlated noise residues at i-th and j-th frequency bins which would become noticeable due to many frequency channels being correlated, otherwise ignoring noise residues would be significant and in some way would impact the results. Real instrumentation will use a much narrower frequency bandwidth which would facilitate radio frequency interference excision (Nan et al., 2011).

We conclude that for a single-dish approach, BINGO, FAST and SKA-I will progressively provide stronger constraints on the dark energy EoS and other cosmological parameters. The constraints can be further improved by combining with a CMB experiment such as *Planck* data.

We performed HI IM Fisher matrix forecast for BINGO, FAST and SKA-I radio telescopes, and extended similar comparative analysis for each of the three experiments' data, combined with *Planck* chains, (Planck Collaboration et al., 2014) which have considerably tightened the cosmological constraints. This substantial and objective comparative analysis of simulated forecast results provides a benchmark on the relative expected performances of BINGO, FAST and SKA-I experiments under relatively similar settings in constraining an extended number of cosmological parameters in Table 2.1. FAST, BINGO, SKA-I and many other telescopes are suitable for HI IM, and some will even do a wider range of sciences (Nan et al., 2011) than others. Our aim is not to show the superiority or inferiority of these experiments against each other but to illustrate a global picture of their relative prospects. Our results can, however, signal/hint the need for adjustment, revision of specification configurations, or for further calibration where there is a possibility to rectify and optimize capabilities so that these telescopes can fulfill their promise.

This chapter sets an important mark for our series of works to study IM surveys with HI. Future proceedings will feature applicability and quantification of this novel but promising approach by developing the IM pipeline to simulate sky maps for various sky emissions, addressing and testing different foreground cleaning methods, and investigating and quantifying various calibration issues. These realistic issues include bandpass calibration, systematics and other uncertainty measurements, studying and developing a solid knowledge of polarization purity, and measuring BAO wiggles from HI power spectrum and consequently developing more stringent constraints on dark energy, dark matter, and other cosmological parameters.

3

Foreground Subtraction from Contaminated HI Maps

3.1 Literature Review

Large-scale structures of the Universe can be efficiently surveyed by the neutral hydrogen (HI) intensity mapping (IM) technique that employs the 21-cm emission line of neutral atomic hydrogen (HI). The HI IM technique is novel but a promising approach that measures the collective HI emission intensity over the physical volume of a few tens of Mpc, to efficiently survey extremely large volumes of galaxies without focusing to resolve each individual sources (Pritchard and Loeb, 2012; Battye et al., 2013; Bull et al., 2015b; Kovetz et al., 2017). Although the 21-cm emission signal is weak, observations over a large number of sky pixels through IM can greatly resolve HI signal detection and sensitivity requirements. The main advantage of using single-dish HI IM is to increase the HI surface brightness temperature sensitivity and sample the fluctuations on large angular scales.

A number of near-term and future radio experiments are being constructed with priority to apply HI IM to probe large volumes of the Universe, in an effort to constrain cosmological and astrophysical parameters. In our series of intensity-mapping with HI studies, we have prioritized to work with some of such single-dish radio telescopes, namely; FAST (Nan et al., 2011; Li and Pan, 2016; Li et al., 2018), BINGO (Battye et al., 2012, 2013; Dickinson, 2014; Bigot-Sazy et al., 2015; Battye et al., 2016), MeerKLASS (Santos et al., 2017); and SKA-MID (Santos et al., 2015; Bull et al., 2015a; Braun et al., 2015; Square Kilometre Array Cosmology Science Working Group et al., 2018) in a single-dish imaging mode (Yohana et al., 2019). For instance, FAST can offer a high resolving power since it is currently the largest single-dish telescope in the world (Peng et al., 2009). Being a medium-sized telescope with special design (Battye et al., 2016), BINGO is optimized to detect at radio frequencies the Baryon Acoustic Oscillations (BAO), which would, in turn, be useful for measurements of the dark energy. SKA-MID telescope array is suitably optimized to probe over cosmological scales, large chunks of the Universe volume. It is, however,

worth conducting studies with MeerKLASS since it is the SKA's precursor, which will pave the road for SKA-MID success. These next-generation experiments for LSS surveys of the Universe are suitable laboratories to learn various HI IM techniques. In this study, we will focus on FAST, which has already been commissioned for initial tests, and prior data for 20 hours of integration time is already available. Focusing our studies on FAST is intended for the immediate application of our mock simulations to real-data being delivered by this telescope.

IM approach is unquestionably promising, but the approach shifts the observational problem from that of weak HI detection to that of foreground contamination. The performance of HI IM surveys in detecting and extracting HI signal will, therefore, depend on the successful removal of foregrounds and other contaminants, calibration of instruments and mitigation of several problems on very large scales (Pourtsidou et al., 2017). Luckily, total foreground contaminants are expected to have a smooth frequency dependence (Liu and Tegmark, 2011; Alonso et al., 2015; Bigot-Sazy et al., 2015; Olivari et al., 2016; Villaescusa-Navarro et al., 2017; Cunnington et al., 2018), whereas the underlying 21-cm signal varies in frequency and sky position. Smoothness property means foreground modes are in some way correlated in frequency (Santos et al., 2005), and hence can be clustered in the direction of maximum variance and stripped out by appropriate methods. Large parts of noise and systematics are expected to be spectrally uncorrelated, except for the correlated $1/f$ noise (Harper et al., 2018).

A number of approaches to address the foreground cleaning have been tested and presented in the literature so far. These include the line-of-sight fitting method (Wang et al., 2006; Liu and Tegmark, 2011), line-of-sight and Wiener filter (Gleser et al., 2008), and the method of foregrounds signal frequency bins cross-correlation (Santos et al., 2005). More recently, Robust Principal Component Analysis (RPC), Independent Component Analysis (ICA) techniques (Chapman et al., 2012; Wolz et al., 2014, 2015; Alonso et al., 2015), extended ICA (Zhang et al., 2016), Singular Value Decomposition (SVD) (Paciga et al., 2011; Masui et al., 2013), correlated component analysis (CCA) (Bonaldi et al., 2006), Principal Component Analysis (Masui et al., 2013; Villaescusa-Navarro et al., 2017; Bigot-Sazy et al., 2015; Alonso et al., 2015) and methods that assume some physical properties of the foregrounds, such as polynomial/parametric-fitting (Bigot-Sazy et al., 2015; Alonso et al., 2015) have been widely deployed. Other approaches, for example, quadratic estimation (Switzer et al., 2015) and inverse variance (Liu and Tegmark, 2011) are also being discussed and investigated. These foreground contaminant subtraction algorithms are somehow successful but still have issues, such as biased results and an inability to mitigate various systematics. For example, FASTICA (Chapman et al., 2012; Wolz et al., 2014) seems to succeed in removing dominant foreground contaminants, especially, resolved point sources and diffuse frequency-dependent components on large scales but fails to mitigate systematics on smaller scales dominated by thermal noise (Wolz et al., 2015).

We forecast the potential detection of 21-cm intensity maps of China's Five-hundred-meter Aperture Spherical radio Telescope (FAST), by developing a model for these foreground components and a cleaning method for removing these foregrounds. We consider 1-year observational time

with the survey area of $20,000\,\mathrm{deg}^2$ to capture significant variations of the foregrounds across both the sky position and angular scales relative to the HI signal. Our intention is to investigate the capability of using FAST to conduct the HI IM survey. We will simulate the 21-cm sky and various foregrounds using FAST telescope parameter specifications, and apply the PCA foreground cleaning technique to the map. Although the PCA approach is a general dimensionality reduction or a component separation approach to subtraction of the foregrounds for various contaminated models, each experiment is unique in its specification so a demonstration on how to apply it to subtract the foreground for FAST is worth investigating. At the time of writing this chapter, a similar but different study of forecasting HI galaxy power spectrum and IM are conducted in Hu et al. (2019). Hu et al. (2019) made a simulation-based foreground impact study on the measurements of the 21-cm power spectrum with FAST, and calculated the expected cosmological parameter precision based on the Fisher matrix with Gaussian instrumental noise. In this chapter, we are taking the foreground problem with FAST IM observations, critically further, starting with the modeling and analyses of various sky components, and adding a more complete package of foreground contaminants and confusion components such as $1/f$ noise, which challenges the component separation techniques. With more detailed and sophisticated input of HI IM foreground and instrumental noise, as well as considering a wide FAST sky strip, our approach is a "closer to reality" forecast for FAST HI IM study.

Throughout the chapter, while computing the theoretical 21-cm power spectra at different frequencies, we adopt a spatially-flat ΛCDM cosmology model with best-fitting parameters fixed to *Planck* 2013 results, i.e. $\Omega_\mathrm{b}h^2 = 0.02205$, $\Omega_\mathrm{c}h^2 = 0.1199$, $n_\mathrm{s} = 0.9603$, and $\ln(10^{10}A_\mathrm{s}) = 3.089$ (Planck Collaboration et al., 2014).

3.2 FAST TELESCOPE

The Five-hundred-meter Aperture Spherical radio Telescope (FAST) (Peng et al., 2009; Nan et al., 2011; Li and Pan, 2016; Li et al., 2018) is a multi-beam radio telescope potentially suitable for 21-cm IM surveys. The construction was completed in 2016 and the commissioning phase was completed in 2018. This telescope can map the large-scale cosmic structures and deliver the redshifted 21-cm sky intensity of temperature maps over a wide range of redshifts. Using simple drift-scan (preferred for better spatial sampling) designated as a Commensal Radio Astronomy FasT Survey (CRAFTS) (Li et al., 2018), and a transverse set of beams, FAST can survey a broad strip of the sky. With CRAFTS observations using an L-band array of 19 feed-horns (and $1.05 - 1.45$ GHz), data from different pointings or beams can be combined to construct a high-quality HI image. In terms of sensitivity, FAST will be more sensitive within its frequency band than any single-dish telescope; its design and features supersedes the 300-meter post-Gregorian upgrade Arecibo Telescope and 100-meter Green Bank Telescope (GBT). FAST is expected to have approximately twice and ten times, respectively, the collecting areas of Arecibo and GBT (Li and Pan, 2016), and will deliver 10% of the SKA collecting area (Li et al., 2018).

In Table 3.1, we list all the necessary instrumental parameters of the current FAST telescope. We consider the proposition of parameters and strategy to work with the FAST 19-beam (feed-horns) L-band ($1.1 - 2$ GHz) focal plane array (which is a primary FAST survey instrument) covering the frequency range from $1,050\,\mathrm{MHz}$ to $1,450\,\mathrm{MHz}$ ($0.0 < z < 0.35$) with a system (receiver) temperature of $20\,\mathrm{K}$. The dish has a diameter of $500\,\mathrm{m}$ but the illuminated aperture is $300\,\mathrm{m}$. Each of the feed horn has the beam size (FWHM) of $2.94'$, and forming an L-band 19-beam feed-horn array field of view (FOV) diameter of $26'$. Here we consider a survey by FAST conducted in the drift scan mode, which is operationally simple and stable. Similar to the BINGO experiment (Battye et al., 2012, 2016), as an example, we consider a survey comparable to the one presented in the CRAFTS proposal, which will scan a $26'$ wide strip along the Right Ascension direction for each sidereal day, expected to cover the northern/FAST sky between $-14°$ and $+66°$ of declination in about 220 full days (Li et al., 2018). Being a parabolic dish, its beam size can be estimated as FWHM $= \lambda/D$, where D is the dish aperture. More detailed FAST technical design description, its survey strategies, capabilities, science potentials, and expected substantial challenges, such as complexities in the system control (real-time precision control), RFI mitigation, and big data challenges associated to FAST petascale astronomy, are presented in Nan et al. (2011); Li and Pan (2016); Li et al. (2018).

3.3 HI Signal, Noise and Foreground

3.3.1 HI Signal

HI Brightness Temperature

The observed effective HI signal brightness temperature is (Bull et al., 2015b; Smoot and Debono, 2017)

$$T_{\rm b} = \overline{T}_{\rm b}(1 + \delta_{\rm HI}), \tag{3.3.1}$$

which consists of homogeneous and fluctuating parts, for which the fluctuating part in a voxel (an individual volume element) is given by

$$\delta T^{\rm S}(\boldsymbol{\theta}_i, \nu_i) = \overline{T}_{\rm b}(z)\delta_{\rm HI}(\mathbf{r}_i, z), \tag{3.3.2}$$

where

$$\overline{T}_{\rm b}(z) = \frac{3}{32\pi}\frac{h_{\rm p}c^3 A_{10}}{k_{\rm B}m_{\rm p}^2\nu_{21}^2}\frac{(1+z)^2}{H(z)}\Omega_{\rm HI}(z)\rho_{\rm c,0} \tag{3.3.3}$$

is the mean brightness temperature. Here, i labels the volume element (voxel) given by a 2-dimensional angular direction, $\boldsymbol{\theta}_i$, and frequency ν_i (Bull et al., 2015b); $\mathbf{r}_i$ is the comoving distance to the voxel i. $h_{\rm p}$ is the Planck constant, $m_{\rm p}$ is the mass of the proton, $k_{\rm B}$ is the Boltzmann constant, and c is the speed of light. $A_{10} \approx 2.869 \times 10^{-15}\ \mathrm{s}^{-1}$ is the Einstein's coefficient for spontaneous emission, which is a measure of probability per unit time that a

Table 3.1: FAST instrumental and survey parameters (Nan et al., 2011; Bigot-Sazy et al., 2016; Li and Pan, 2016; Smoot and Debono, 2017; Li et al., 2018; Hu et al., 2019).

Parameter description	Value
Instrumental Parameters	
Dish/aperture diameter	500 m
illuminated aperture	$D = 300\,\mathrm{m}$
Frequency coverage	$\nu = 1,050$–$1,450\,\mathrm{MHz}$
Survey redshift range	$0 < z < 0.35$
Receiver temperature	$T_{\mathrm{rec}} = 20\,\mathrm{K}$
Number of L-band receivers	$n_{\mathrm{f}} = 19$
L-band sensitivity (antenna effective area per system noise temperature)	$A_{\mathrm{eff}}/T_{\mathrm{sys}} = 2,000\,\mathrm{m^2\,K^{-1}}$
Survey Parameters	
Sky coverage	$\Omega_{\mathrm{sur}} = 20,000\,\mathrm{deg^2}$
Total integration time	1 year
Opening angle	$100^\circ - 120^\circ$ (112.8°)
Zenith angle (sky coverage)	$26.4^\circ - 40^\circ$ (with max 18% gain loss), 26.4° (full gain)
Declination	$-14^\circ 12' - 65^\circ 48'$
Pointing accuracy	8 arcsec
Tracking range	$4 - 6$ hours
Telescope positions [latitude, longitude]	North $25^\circ 48'$, East $107^\circ 21'$
Slew time between sources	$1.5 - 10$ minutes (for a maximum slew of up to 80°)
FWHM at reference frequency ($1,420\,\mathrm{MHz}$)	2.94 arcmin
Frequency bandwidth (Number of channels)	$\Delta\nu = 10\,\mathrm{MHz}$ ($N_\nu = 40$)

photon with an energy $E_1 - E_0 = h_p\nu$ is emitted by an electron in state 1 with energy E_1, decaying spontaneously to state 0 with energy E_0; $\nu_{21} \simeq 1420\,\mathrm{MHz}$ is the 21-cm rest-frame emission frequency, $H(z)$ is the Hubble rate as a function of redshift, and

$$\Omega_{\rm HI} = \frac{\rho_{\rm HI}}{\rho_{\rm c,0}} \tag{3.3.4}$$

is the neutral hydrogen fraction such that $\rho_{\rm c,0} = 3H_0^2/8\pi G$ is the critical density today. Equation (3.3.3) can be further simplified to an expression related to cosmological parameters (Battye et al., 2013; Hall et al., 2013; Bigot-Sazy et al., 2016),

$$\begin{aligned}\overline{T}_{\rm b}(z) &= 0.188\mathrm{K}\,(\Omega_{\rm HI}(z)h)\,\frac{(1+z)^2}{E(z)} \\ &= 0.127\left(\frac{h}{0.7}\right)\left(\frac{\Omega_{\rm HI}(z)}{10^{-3}}\right)\left(\frac{(1+z)^2}{E(z)}\right)\mathrm{mK},\end{aligned} \tag{3.3.5}$$

where $E(z) \equiv H(z)/H_0 = \sqrt{\Omega_{\rm m}(1+z)^3 + \Omega_\Lambda}$ is the redshift-dependent part of Hubble parameter.

Power Spectrum

Since most of the HI are locked within galaxies at low-redshift universe, it is expected that HI signal (21-cm brightness temperature) will be a biased tracer of underlying matter fluctuations, naturally characterized by the angular power spectrum (Lewis and Challinor, 2007; Datta et al., 2007). Thus the HI density contrast, $\delta_{\rm HI}$ is expressed as a convolution of the HI bias, $b_{\rm HI}$ and the total matter density perturbation/contrast, $\delta_{\rm m}$:

$$\delta_{\rm HI} = b_{\rm HI} * \delta_{\rm m}. \tag{3.3.6}$$

Assuming the peculiar velocity v gradients and v/c terms are small for these pixels (which are in practice large (Bull et al., 2015b; Smoot and Debono, 2017)), for a given frequency ν, a solid angle $\Delta\Omega$ of a considered spatial volume element and a frequency interval $\Delta\nu$, we have

$$T_{\rm b}(\nu, \Delta\Omega, \Delta\nu) \approx \overline{T}_{\rm b}(z)\left[1 + b_{\rm HI}\delta_{\rm m}(z) - \frac{1}{H(z)}\frac{{\rm d}v}{{\rm d}s}\right], \tag{3.3.7}$$

where ${\rm d}v/{\rm d}s$ is the proper gradient of the perpendicular velocity along the line of sight, which accounts for the peculiar velocity effect, and $\Omega_{\rm HI}(z) = (1+z)^{-3}\rho_{\rm HI}(z)/\rho_{\rm c,0}$ is the HI fractional density. We then use these relations to calculate in a more consistent manner the redshift evolution of HI density, 21-cm brightness temperature, and HI bias, see also Bull et al. (2015b); Smoot and Debono (2017).

Instead of carrying out exact calculations of the angular power spectrum, 21-cm cosmological signal simulations are performed by generating Gaussian realizations from the flat-sky approximation (found to be accurate to 1% level for $\ell > 10$, see Datta et al. (2007)) angular power spectrum,

$$C_\ell(z, z') = \frac{1}{\pi\chi\chi'}\int_0^\infty {\rm d}k_\parallel \cos\left(k_\parallel\Delta\chi\right) P_{T_{\rm b}}(\mathbf{k}; z, z'), \tag{3.3.8}$$

where χ and χ' are comoving distances to redshifts z and z', $\Delta\chi = \chi - \chi'$, and $\mathbf{k}$ is the vector with components $k_\parallel$ and $\ell/\bar{\chi}$, in the direction parallel and perpendicular to the line of sight respectively (Shaw et al., 2014; Bigot-Sazy et al., 2015). It follows that,

$$P_{T_\mathrm{b}}(\mathbf{k}; z, z') = \overline{T}_\mathrm{b}(z)\overline{T}_\mathrm{b}(z') \left(b + f\mu^2\right)^2 P_\mathrm{m}(k; z, z') \tag{3.3.9}$$

is the power spectrum of the 21-cm brightness temperature.

Defining terms from Equation (3.3.9), b is the bias which is unity on large scales,

$$f = \frac{\mathrm{d}\log D}{\mathrm{d}\log a} \tag{3.3.10}$$

is the linear growth rate, where ($D(z)$ is the growth factor. Finally, the real-space matter power spectrum is given by (Shaw et al., 2014; Bull et al., 2015b; Bigot-Sazy et al., 2015)

$$P_\mathrm{m}(k; z, z') = P(k)D(z)D(z'). \tag{3.3.11}$$

For flat-sky approximation (Limber approximation/projection (Limber, 1954)), $\mu \sim k_\parallel/k$.

To calculate the covariance matrix of the angular power spectrum (C_ℓ) through simulations, we calculate the 3-dimensional angular power spectra of the 21-cm tomography error covariance matrix

$$M = \langle nn^t \rangle, \tag{3.3.12}$$

over $N = 100$ samples of HI sky map realizations. We compute this covariance of errors by

$$M_{\ell\ell'} = \frac{1}{N}\sum_{i=1}^{N}\left(C_\ell^{(i)} - \overline{C}_\ell\right)\left(C_{\ell'}^{(i)} - \overline{C}_{\ell'}\right), \tag{3.3.13}$$

where C_ℓ averaging is performed over a particular frequency for all simulated maps:

$$\overline{C}_\ell = \frac{1}{N}\sum_{i=1}^{N} C_\ell^{(i)}. \tag{3.3.14}$$

In Figure 3.4, we plot the averaged HI signal power spectrum at the frequency of $1,255\,\mathrm{MHz}$, and the sample variance of the power spectrum from simulation. As one can see, due to the cosmic variance on large angular scales, the intrinsic dispersion at low-ℓ is considerably larger.

3.3.2 Noise

Thermal Noise

We model the thermal noise as a white noise caused by the telescope receiver's temperature. Thermal noise is related to the telescope receiver system noise temperature, and for each pixel, can well be approximated as Gaussian white noise with *rms* amplitude (Wilson et al., 2009) by

$$\sigma_\mathrm{pix} = \frac{T_\mathrm{rec}}{\sqrt{\Delta\nu t_\mathrm{pix}}}, \tag{3.3.15}$$

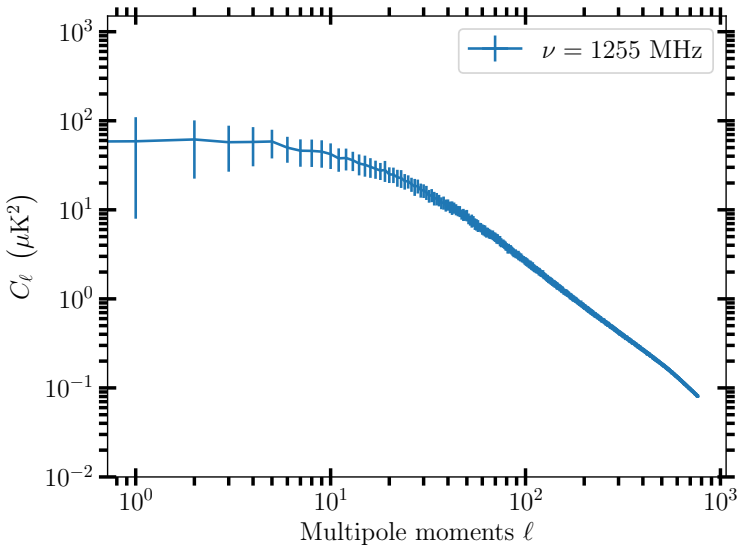

Figure 3.1: The averaged HI signal power spectrum at the frequency $1,255\,\mathrm{MHz}$ (median frequency of $1,050 - 1,450\,\mathrm{MHz}$), and its intrinsic dispersion $\Delta C_\ell = \sqrt{M_{\ell\ell}}$ calculated via Eqs. (3.3.13) and (3.3.14).

where $T_{\rm rec}$ is the receiver system temperature, $t_{\rm pix}$ is the integration time for each pixel and $\triangle\nu$ is the frequency bandwidth (frequency resolution).

A pixel size is given by its FWHM

$$\theta_{\rm FWHM} = \frac{1.22\lambda_\nu}{D}. \tag{3.3.16}$$

Here λ_ν is the wavelength corresponding to a particular frequency ν, and D is the telescope's illuminated aperture.

FAST telescope full illuminated aperture at any time as the telescope tracks objects has been designed to be 300 m, thus considering the redshifted observations of the 21-cm signal, the FAST beam size is

$$\begin{aligned} \theta_{\rm FWHM} &= 1.22\frac{21\ \mathrm{cm}(1+z)}{300\ \mathrm{m}} \\ &= 2.94\left(\frac{\nu_{21}}{\nu}\right)\ \mathrm{arcmin}, \end{aligned} \tag{3.3.17}$$

where $\nu_{21} = 1,420\,\mathrm{MHz}$ is the rest-frame frequency of 21-cm emission. We consider a practically tested pixelization (Bigot-Sazy et al., 2015) to simulate FAST instrumental thermal noise. The integration time for each pixel, $t_{\rm pix}$, for the total observational time $t_{\rm obs} = 1\,\mathrm{year}$, the number of feed horns, $n_{\rm f} = 19$, and the FAST survey area, $\Omega_{\rm sur} = 20,000\ \mathrm{deg}^2$ is then given by

$$\begin{aligned} t_{\rm pix} &= n_{\rm f} t_{\rm obs}\frac{\Omega_{\rm pix}}{\Omega_{\rm sur}} \\ &= 71.98 \times \left[\frac{1420\,\mathrm{MHz}}{\nu}\right]^2\ \mathrm{s}, \end{aligned} \tag{3.3.18}$$

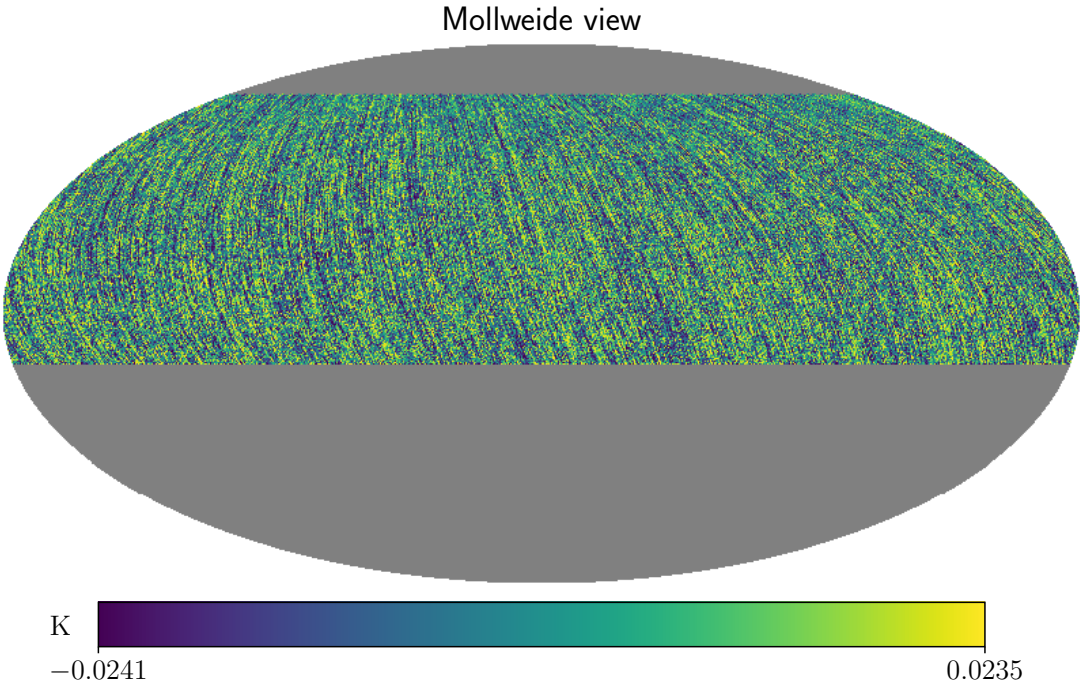

Figure 3.2: FAST mollweide projection of the $1/f$ noise at frequency, $\nu = 1,250\,\mathrm{MHz}$, for parameters $\beta = 0.25$, $\alpha = 1.0$ and a knee frequency $f_\mathrm{k} = 1.0\,\mathrm{Hz}$.

where $\Omega_\mathrm{pix} \equiv \theta^2_\mathrm{FWHM}$ is the beam area. We can therefore calculate the *rms* by substituting t_pix values into Equation (3.3.15). We will use the Python Healpy to generate the noise maps at different frequencies, taking into consideration a particular number of sky pixels ($N_\mathrm{side} = 256$).

$1/f$ Noise

$1/f$ noise is an effect separate from a well known instrumental thermal noise. This is a form of correlated noise across frequency bands, and to a large extent affects radio receiver systems, revealing itself as small gain fluctuations (Harper et al., 2018). Binning $1/f$ noise on the sky map results into spatial distributions that resemble the large-scale fluctuations which can easily be confused with the true HI signal, see Figure 3.2. We summarize some of the observations and the analyses of $1/f$ noise (Seiffert et al., 2002; Bigot-Sazy et al., 2015; Smoot and Debono, 2017; Harper et al., 2018) (also known as single instrumental systematic in the total power spectrum) to discuss its inclusion in our foreground subtraction process.

The power spectral density (PSD) for the thermal and $1/f$ noises contaminated receiver that takes into account the impact of frequency correlations of the $1/f$ noise (in the spectroscopic receivers) assumes a decoupled power-law and takes the two-dimensional form:

$$\mathrm{PSD}(f) = \frac{T^2_\mathrm{sys}}{\Delta\nu}\left[1 + C(\beta, N_\nu)\left(\frac{f_\mathrm{k}}{f}\right)^\alpha \left(\frac{1}{\omega\Delta B}\right)^{\frac{1-\beta}{\beta}}\right]. \tag{3.3.19}$$

Here, T_sys is the receiver system temperature, $\Delta\nu$ is the frequency channel bandwidth, f_k is

the knee frequency, and α is the spectral index of temporal fluctuations. The unity term in Equation (3.3.19) describes the contribution by the thermal noise, and the reciprocal power-law $(f_k/f)^\alpha$ (from which the term $1/f$ noise is derived) describes the $1/f$ noise. When $\alpha > 0$, it implies that the power gained is proportional to time-scale fluctuations. Furthermore, different values of the spectral index α characterize several variations in the names of $1/f$ noise, in particular, pink noise, brown noise, and red noise are respectively characterized by $\alpha = 1$, $\alpha = 2$, and generally for any value of $\alpha > 0$.

Moreover, ω is the inverse spectroscopic frequency wavenumber, ΔB is the total receiver bandwidth, β is the PSD spectral index parametrization parameter, and $C(\beta, N_\nu)$ is a constant, described in detail by Harper et al. (2018). $0 < \beta < 1$ is the limit for which the spectral index of the frequency correlation is defined, where small values of β indicates high correlations, such that $\beta = 0$ implies identical $1/f$ noise across different frequency channels, and $\beta = 1$ would describe independent $1/f$ noise in every frequency channel. For a complete detailed account of $1/f$ noise including its modeling, we refer the interested reader to Harper et al. (2018).

Generation of $1/f$ noise has been carried out using the end to end simulations (simulations assume that $1/f$ noise fluctuations have some Gaussian properties) described in Harper et al. (2018) as would be required by most of the time-dependent systematics. This approach of modeling sky signal, however, intends to account for the maximum impact of $1/f$ noise for a particular telescope model on the recovery of the HI signal spectrum using component separation techniques.

3.3.3 Foreground Templates

It is a common understanding that the biggest challenge of using the 21-cm IM technique is to develop a computationally effective strategy to remove the foreground contaminants. The foreground challenge is due to a number of contaminants, which include, but not limited to, Galactic synchrotron emission, emitted by electrons spiraling in Galactic magnetic field (Pacholczyk, 1970; Banday and Wolfendale, 1990, 1991); emission from the background of extragalactic point/radio sources (unresolved foreground) that includes a mixture of radio galaxies, quasars and other objects; and free-free radio emission produced by free electrons that encounter ions and scattering off them without being captured. Among these foregrounds, Galactic synchrotron emission is the most notable and overshadows the HI signal of our interest to several orders of magnitude (Bigot-Sazy et al., 2015). There is however thermal/white noise and an instrumental $1/f$ noise (see Subsections 3.3.2, 3.3.2), radio frequency interference (RFI), time-variable noise induced as the signal propagates through the atmosphere which additionally contributes to the $1/f$ noise of the instrument, and atmospheric effects caused by absorption or scattering of signals and fluctuations arising from the turbulence in the emission of the water vapour (Bigot-Sazy et al., 2015). We explain some of these contaminants in the subsequent subsections.

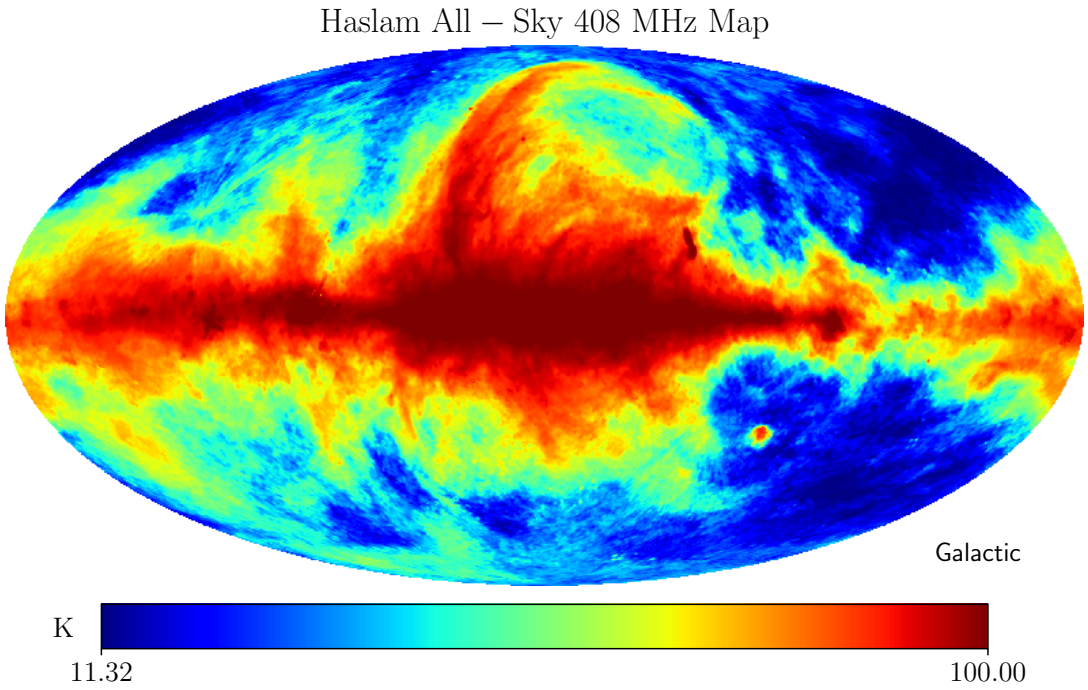

Figure 3.3: The destriped and desourced all-sky 408 MHz Haslam map (Haslam et al., 1982), produced by the *WMAP* team using data from the National Center for Supercomputing Applications (NCSA) ADIL. The colour scale (truncated to 50 K) follows the rainbow order, where red is the highest, purple the lowest, and grey is being an indication of no data.

Galactic Synchrotron Emission

Across the sky on very large scales, the Galactic synchrotron emission is predicted to vary, characterized in the observations by large quadrupole features and additional signal on the Galactic plane, and due to the Galactic foreground signal, (slightly) higher temperature at lower frequencies is expected (Smoot and Debono, 2017).

A template for Galactic synchrotron sky emission can be generated by extrapolating/interpolating at appropriate frequencies the all-sky 408 MHz continuum and reprocessed Haslam maps. To date, these maps, especially, the processed all-sky 408 MHz map (Fig. 3.3) which is publicly available (Haslam et al., 1982), and the reprocessed and improved 408 MHz all-sky map continue to offer the best approximation and characterization of the diffuse Galactic synchrotron emission.

Following the framework presented in Shaw et al. (2014), the global sky map (de Oliveira-Costa et al., 2008) generated by compiling maps from 10 MHz to 94 GHz is used to generate sky temperature maps at frequencies 400 MHz and 1420 MHz. These maps are then used for the calculation of an effective spectral index at each sky location, $\hat{\mathbf{n}}$, estimated as

$$\alpha(\hat{\mathbf{n}}) = \frac{\log T_{1420}(\hat{\mathbf{n}}) - \log T_{400}(\hat{\mathbf{n}})}{\log 1420 - \log 400}. \tag{3.3.20}$$

The spectral index is used in combination with the 408 MHz Haslam et al. (1982) map to

extrapolate sky temperature maps at different frequencies using the power law (de Oliveira-Costa et al., 2008; Bigot-Sazy et al., 2015; Olivari et al., 2016):

$$T(\hat{\mathbf{n}}, \nu) = T_{408}(\hat{\mathbf{n}}) \left(\frac{\nu}{408 \text{ MHz}} \right)^{\alpha(\hat{\mathbf{n}})} . \tag{3.3.21}$$

The Galactic synchrotron model simulated by Shaw et al. (2015) is suitably calibrated for both Galactic plane and low frequencies, and the resulted model has been transitioned from low to higher frequencies as described in Shaw et al. (2014) to make the angular power law applicable for HI IM simulations.

Previously, many cosmologists have simply been extrapolating 408 MHz Haslam maps to lower/upper frequencies by ignoring any spectral variations across the sky that have been predicted. Although Galactic synchrotron emission is expected to dominate at low frequencies, it has been observed that its dependence on frequency is not a perfect power-law, instead, the slope of the Galactic synchrotron emission progressively steepens with an increase in frequency, at the same time other Galactic contaminants such as free-free and dust emissions noticeably start to trickle in. Due to the fact that this power-law extrapolation (Eq. (3.3.21)) does not take into account any spectral variations, the resultant maps lack the small scale angular fluctuations because of the limited resolution of the Haslam map template used (Shaw et al., 2014). These missing expected real sky components have been included for realistic foreground model tests as described in Shaw et al. (2014, 2015).

Following this observation, we use the Cosmology in the Radio Band (CORA) code developed by Shaw et al. (2015) which takes into account the radio emission spectral variations and small-scale angular fluctuations to simulate Galactic synchrotron emission templates (point sources and 21-cm as well) for our foreground removal with PCA.

Extragalactic Point Sources

We summarize the analysis by Shaw et al. (2014, 2015), where the extragalactic point sources are assumed to be an isotropic field modelled as the power law in both frequency and multipole moment, ℓ,

$$C_\ell(\nu, \nu') = A \left(\frac{100}{\ell} \right)^{\alpha} \left(\frac{\nu\nu'}{\nu_0^2} \right)^{-\beta} \exp\left[-\frac{1}{2\xi_\ell^2} \ln^2 \left(\frac{\nu}{\nu'} \right) \right], \tag{3.3.22}$$

which was originally described by Santos et al. (2005) and applied to low frequencies during the Epoch of Reionization, and later modified in Shaw et al. (2014, 2015) to suit high frequencies and the full-sky intensity mapping regime. Here C_ℓ is the angular power spectrum, and ν, ν' represent two different frequency bands with ν_0 being a pivot frequency.

The approach uses simulated maps of the point sources which are composed of two different populations. The first population is constructed directly following the point sources distribution by Di Matteo et al. (2002) and forms a population of bright and isolated point sources with a flux $S > 0.1$ Jy at 151 MHz, and the second one is a continuum/background of dimmer unresolved

point sources (whose flux $S < 0.1\,\mathrm{Jy}$), simulated by drawing random realization (Gaussian random field) from Equation (3.3.22) by adopting parametrization from Shaw et al. (2014), where $A = 3.55 \times 10^{-4}\,\mathrm{K}^2$, $\alpha = 2.1$, and the spectral index $\beta = 1.1$. Here, the parameter ξ_ℓ measures the foreground frequency coherence/correlation. Two limits of this parameter $\xi \to 0$ and $\xi \to \infty$, respectively, means completely foreground-frequency incoherence and perfectly foreground-frequency coherence (Tegmark et al., 2000; Santos et al., 2005). This foreground-frequency correlation length parameter ξ can be determined in terms of the spectral index β as described in detail by Tegmark (1998); Tegmark et al. (2000); Santos et al. (2005). Such treatment is important because it takes into account possible changes of the foregrounds with the observed direction/position on the sky, and the relative power ratio between various sky components which may also vary with the angular scales (Olivari et al., 2016).

In the former population (Di Matteo et al., 2002), sources are randomly distributed over the sky, where a pure power-law emission is assumed to model each source with a randomized spectral index (Shaw et al., 2015).

In practice, the brightest radio sources ($S > 10\,\mathrm{Jy}$) above the threshold flux are usually subtracted or masked. In order for the Di Matteo model (Di Matteo et al., 2002) point sources distribution to be useful in a range of higher frequencies, and also to be able to adjust the maximum flux of sources (that were not subtracted) from 0.1 mJy to 0.1 Jy, the pivot frequency is changed from 150 MHz to Haslam 408 MHz frequency, and the amplitude A rescaled.

Free-free Emission

Free-free emission arises due to the interaction, in the ionized medium between ions and free electrons. The term free-free follows from the nature of the emission, in which electrons are free before they encounter ions and thereafter scatter off ions and remain free again (Rybicki and Lightman; Olivari et al., 2016). These electrons as seen in radio frequencies, are said to originate from warm ionized gas whose temperature $T_\mathrm{e} \simeq 10^4\,\mathrm{K}$ (Olivari et al., 2016).

According to Dickinson et al. (2003) and Olivari et al. (2016), in an electrically charged medium of ions and electrons, free-free emission generates the brightness temperature given by

$$T_\mathrm{ff} \approx 90\ \mathrm{mK}\left(\frac{T_\mathrm{e}}{\mathrm{K}}\right)^{-0.35}\left(\frac{\nu}{\mathrm{GHz}}\right)^{\beta}\left(\frac{\mathrm{EM}}{\mathrm{cm}^{-6}\mathrm{pc}}\right), \tag{3.3.23}$$

where ν is frequency, and $\mathrm{EM} = \int n_\mathrm{e}^2 \mathrm{d}\ell$ is called emission measure, interpreted as the integral of the electron density squared along the line of sight (Olivari et al., 2016), and $\beta \sim -2.1$ is the spectral index. We estimate the emission measure (EM) and generate the Galactic free-free temperature maps by using the base Wisconsin H-Alpha Mapper (WHAM) survey maps, where we have considered an electron temperature, $T_\mathrm{e} = 7000\,\mathrm{K}$.

We present in Figure 3.4 the power spectra for some of these notable contaminants as we have already discussed; these components are simulated by assuming a full-sky approximation.

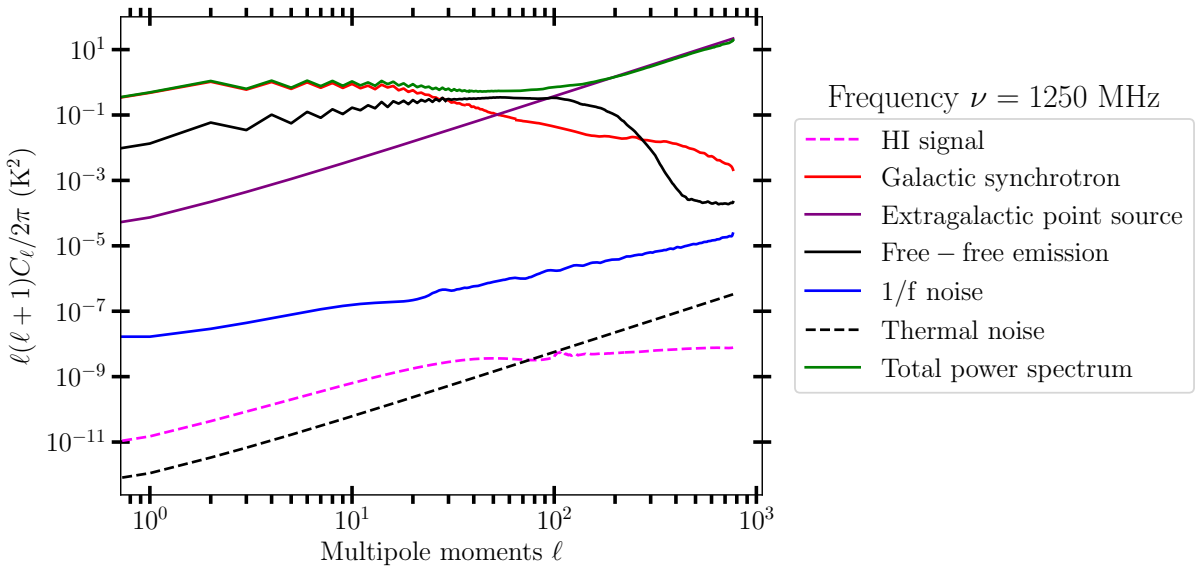

Figure 3.4: FAST full-sky approximation power spectra for Galactic synchrotron, extragalactic point sources, $1/f$ noise, free-free emission and HI signal simulated at the FAST bandwidth mid-range frequency, $\nu = 1.25\,\mathrm{GHz}$.

3.3.4 Sky Area

We use the Equatorial Coordinate System: right ascension (RA) and declination (DEC) to specify points/direction on the celestial sphere in this coordinate system.

We consider the FAST maximum declination range $[-14°, 65°]$, which means we utilize the full sky region that is potentially surveyable by FAST telescope, as shown in Figure 3.5.

3.4 Principal Component Analysis

To illustrate foreground subtraction algorithm capability and capture various effects for a wide range of frequency variation, we will perform foreground subtraction over the full FAST frequency bandwidth, $1,050 - 1,450\,\mathrm{MHz}$, but report results for the middle $(1,250\,\mathrm{MHz})$ frequency (or equivalently an average frequency in the band). Principal component analysis (PCA) is a non-parametric method for extracting useful information from a high-dimensional data set. The method is a multivariate statistical procedure that finds the direction of maximum variance by orthogonally transforming a possibly correlated high-dimensional data set of observations into a low-dimensional linearly-uncorrelated subspaces called principal components.

This process involves compressing a lot of data by projecting it into a smaller dimensional subspace while retaining the essence of the original data. In our case, we will apply PCA to transform noisy data into a subspace that consists of two measurement object patterns, one composed of dominant components (the foregrounds) and the other one consisting of the complementary component, i.e. the HI signal. The scientific information that will be collected by

the radio telescopes is expected to be highly contaminated, and thus devising means to subtract foregrounds and noises from HI signal is essentially very important at this radio astronomy developmental stage.

We encode our total emission sky data set as a matrix X with dimensions $N_\nu \times N_\mathrm{p}$, where N_ν is the number of frequency channels, and N_p is the number of pixels of the temperature fluctuation map. We can think of this matrix as composed of N_ν samples and N_p pixelized temperature measurements of the brightness temperature, $T(\nu, \hat{n}_\mathrm{p})$, corresponding to the frequency ν, and along the direction of the line of sight $\hat{n}_\mathrm{p}$ (Bigot-Sazy et al., 2015). To distinguish the frequency with spatial indices, we use Greek symbol for frequency index, and Latin symbol to denote spatial index.

We can then compute the covariance matrix as

$$C = (N_p - 1)^{-1} X X^T. \tag{3.4.1}$$

The $\alpha\beta^{\mathrm{th}}$ entry of the product $(N_\mathrm{p} - 1)^{-1} X X^T$, which we call $\sigma_{\alpha\beta}$ is expressed as the dot product of the α^{th} and β^{th} columns of the data matrix X, respectively, denoted by $x_{\cdot,\alpha}$ and $x_{\cdot,\beta}$. Thus, for the zero-centered (column means have been subtracted) data set, the α^{th} value of this covariance matrix is calculated as

$$\sigma_{\alpha\beta} = \frac{1}{N_\mathrm{p} - 1} x_{\cdot,\alpha} \cdot x_{\cdot,\beta} = \frac{1}{N_\mathrm{p} - 1} \sum_{i=1}^{N_\mathrm{p}} x_{i\alpha} x_{i\beta}, \tag{3.4.2}$$

where $\alpha = \beta$ implies the covariance of the variable with itself that gives us the variance of the data along the β^{th} coordinate axis, and we have the measure of how much the two coordinates covary if $\beta \neq \alpha$. Considering the N_ν-dimensional non-zero mean column vector

$$\bar{x} = \frac{1}{N_\mathrm{p}} \sum_{i=1}^{N_\mathrm{p}} x_i = \frac{1}{N_\mathrm{p}} \left(\sum_{i=1}^{N_\mathrm{p}} x_{1i}, \sum_{i=1}^{N_\mathrm{p}} x_{2i}, \ldots, \sum_{i=1}^{N_\mathrm{p}} x_{N_\nu i} \right)^{\mathrm{T}} \tag{3.4.3}$$

in our calculations, we can explicitly write the covariance element of the covariance matrix (Eq. (3.4.1)) as

$$\sigma_{\alpha\beta} = \frac{1}{N_\mathrm{p} - 1} \sum_{i=1}^{N_\mathrm{p}} (x_{i\alpha} - \bar{x}_\alpha)(x_{i\beta} - \bar{x}_\beta), \tag{3.4.4}$$

which enables us to further contract the covariance matrix as

$$C = \frac{1}{N_\mathrm{p}} \left((X - \mu) (X - \mu)^T \right), \tag{3.4.5}$$

where μ is the population mean. Scaling observations by $N_\mathrm{p} - 1$ is usually considered as a correction for the bias introduced when the sample mean is used instead of the population mean.

Next, we can normalize the covariance matrix (Eq. (3.4.5)) by calculating the correlation matrix entries between each pair of frequency channels

$$r_{\alpha\beta} = \frac{\sigma_{\alpha\beta}}{\sqrt{\sigma_{\alpha\alpha}} \sqrt{\sigma_{\beta\beta}}}, \tag{3.4.6}$$

where $\sigma_{\alpha\alpha} \equiv \sigma_\alpha^2$ is the variance (covariance of a variable with itself). $r_{\alpha\beta}$ are entries of the dimensionless correlation matrix, $R_{\alpha\beta}$, such that $-1 \leq r_{\alpha\beta} \leq 1$, $r_{\alpha\alpha} = 1$, and can be interpreted as correlation coefficients between frequency pairs. The quantities σ_α characterize the *rms* fluctuations at each frequency.

The eigenvectors of a correlation (or equivalently covariance) matrix (Eq. (3.4.6)) form a basis for the principal component analysis. The eigenvectors in the reduced subspace determine the new axis direction, and the magnitudes of their corresponding eigenvalues describe the variance of the data of the resulting subspace axis. Therefore, PCA requires that we perform the eigendecomposition on the correlation matrix (Eq. (3.4.6)) or the covariance matrix (Eq. (3.4.5)). Similarly, PCA can be carried out after performing SVD (singular vector/value decomposition) on the correlation/covariance matrix for the sake of computational efficiency and numerical robustness.

However, the magnitude of the eigenvalues can give us clues on which eigenvectors (principal axes) correspond to the dominant foregrounds. This can easily be seen by ranking the eigenvectors in the decreasing order of their corresponding eigenvalues (see the left panel of Figure. 3.7). Usually, the first few principal components can be attributed to the dominant variance (information) – the foregrounds.

As previously stated, the eigendecomposition can be carried on either the covariance matrix or correlation matrix, depending on which one is preferred for PCA. Here, we illustrate these cases by proceeding with the diagonalization of the covariance matrix,

$$C = W^T \Lambda' W, \tag{3.4.7}$$

where $WW^T = W^T W = I$, implying that W is orthogonal matrix, whose columns are the principal axes/directions (eigenvectors) (see the right panel of Figure. 3.7), and the diagonal matrix of the corresponding eigenvalues is given by $\Lambda'_{\alpha\beta} = \delta_{\alpha\beta}\lambda_\alpha$. After identifying the principal axes, we next compose an $N_\nu \times k$ ($k < N_\nu$) matrix, W', called the projection matrix, a matrix whose columns are made up of the first k columns of W, that will form the dominant principal components by projecting the data matrix X onto them.

Finally, we project our data matrix X onto a new subspace by using the projection matrix W' via the equations

$$U = W'^T \cdot X, \tag{3.4.8}$$

$$V = W' \cdot U, \tag{3.4.9}$$

and recover the HI signal as

$$S_{\rm HI} = X - V, \tag{3.4.10}$$

where V is the map of the reconstructed foreground. Lastly, we project the patch of the cleaned HI signal pixels into the correct position in the sky map.

More often, singular value decomposition (SVD) is favored, applied just in the same way as PCA to a real or complex rectangular matrix, but with more computational power. SVD decomposes a data matrix X in the form

$$X = W^{*}\Sigma R, \tag{3.4.11}$$

where W^{*} and R are unitary matrices, i.e. $WW^{*} = I$, $RR^{*} = I$, and they are respectively, called left and right singular vectors; Σ is a rectangular diagonal matrix of singular values. In the form (Eq. (3.4.11)), W is generally complex-valued matrix and $*$ denotes conjugate transpose. Since we are dealing with a real data matrix X, the resulting unitary matrices will be real, and thus (Eq. (3.4.11)) takes the form

$$X = W^{T}\Sigma R. \tag{3.4.12}$$

With SVD, we bypass calculations of the covariance matrix, by looking for something equivalent to it in a computationally efficient way. This requires application of SVD on the covariance matrix C as

$$\begin{aligned} C &= \frac{XX^{\mathrm{T}}}{N_{\mathrm{p}} - 1} \\ &= \frac{(W^{T}\Sigma R)(W^{\mathrm{T}}\Sigma R)^{\mathrm{T}}}{N_{\mathrm{p}} - 1} \\ &= \frac{W^{\mathrm{T}}\Sigma^{2}W}{N_{\mathrm{p}} - 1} \\ &= \frac{W^{-1}\Sigma^{2}W}{N_{\mathrm{p}} - 1}, \end{aligned} \tag{3.4.13}$$

where the last equality follows from the fact that W is unitary.

We see that the result takes the form of the eigendecomposition (Eq. (3.4.7)), and we can easily notice the relationship between the eigenvalues $\Lambda^{'}$ and the singular values Σ, where we establish that

$$\Lambda^{'} = \frac{\Sigma^{2}}{N_{\mathrm{p}} - 1}, \tag{3.4.14}$$

implying $\lambda_{\alpha} = \sigma_{\alpha}^{2}/N_{p} - 1$ for $\lambda_{\alpha} \in \Lambda^{'}$ and $\sigma_{\alpha} \in \Sigma$. Principal components are given by $WX = WW^{\mathrm{T}}\Sigma R = \Sigma R$, and singular values can be arranged in decreasing order $\sigma_{1} > \sigma_{2} > \sigma_{3} \ldots$, such that the first column of the principal components ΣR corresponds to the first singular value, and so on. Thereafter, PCA can be performed under this new transformation. In this work, we will favor PCA over covariance matrix (Eq. (3.4.5)) for very rapid convergence of the HI signal recovery process, but this is only true if the foreground is not too complicated as we shall see in the subsequent sections.

We describe the performance of PCA results in Section 3.5, obtained by applying the algorithm to subtract foregrounds for the FAST telescope specifications.

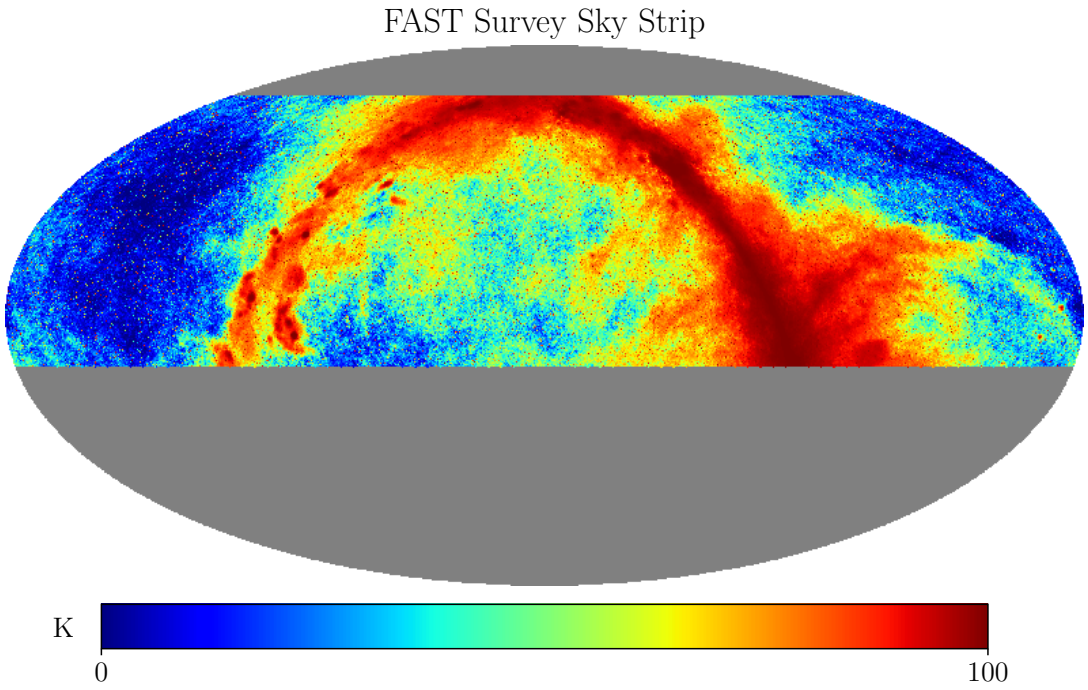

Figure 3.5: Sky map containing anticipated components that are significant, within the FAST survey sky strip (Galactic synchrotron + extragalactic point sources + free-free emission + HI signal + $1/f$ noise), simulated for FAST telescope specifications at frequency 1.25 GHz.

3.5 PCA Results

This section is intended to fairly treat the foreground challenge, and provide an overview of this mammoth task which we need to undertake if we want enormous HI IM experiments that are being put in place to succeed.

To help to maximize the scientific impact of the future 21-cm experiments we apply PCA to model simulations as described in the previous section. We carry out PCA tests by considering the input sky strip depicted by Figure 3.5 which is the whole region expected to be surveyed by the FAST telescope.

To realize the effect of the foreground contamination, we generate and visualize the assumed superimposed sky maps for Galactic synchrotron, extragalactic point sources, thermal noise and 21-cm in a frequency range of our interest. The combined sky component models, indeed, show that the foreground contaminants whose brightness temperatures are very high compared to that of HI signal, will overshadow the HI signal to about $4-5$ orders of magnitude (Battye et al., 2013; Bigot-Sazy et al., 2015) (Fig. 3.5).

We considered the sky strip between declinations of $[-14°, 65°]$ that the FAST telescope is expected to survey, by masking out unrequired patches of the sky from full simulated sky maps. We choose a single frequency channel centered at 1.25 GHz, which is the mid-range frequency in the FAST radio band, to demonstrate the foreground cleaning process applied to contaminated

angular power spectra of the sky maps and visualize both the resulting power spectra and the HI maps.

We first apply PCA to sky components without including the thermal noise; where in this case we consider the multipole moments up to $\ell = 768$ to cover the smallest angular scales. Thereafter, we include the thermal noise; the purpose here is to show separately how the noise power impacts the foreground subtraction process. This is because the FAST thermal noise is very strong at small scales, and will progressively significantly affect the HI recovery towards low multipoles.

Our first category of results with the omission of the thermal noise is reported in Figure 3.8. HI decontamination under this approach is equivalent to removing principal eigenmodes that correspond to the higher-order components, the foregrounds, and the procedure is greatly favored by the fact that the foreground is expected to be smooth in frequency (Fig. 3.6). This smoothness is also illustrated in the right panel of Figure 3.7 since the first three principal axes vary smoothly with frequency. We, however, notice increasing non-linearity in the principal axes in the corresponding order of decreasing eigenvalues. The first few smooth principal axes exhibit the property of the foreground which is expected to be smooth and dominant than HI signal. These principal axes pick out the dominant components when projected onto the data matrix X.

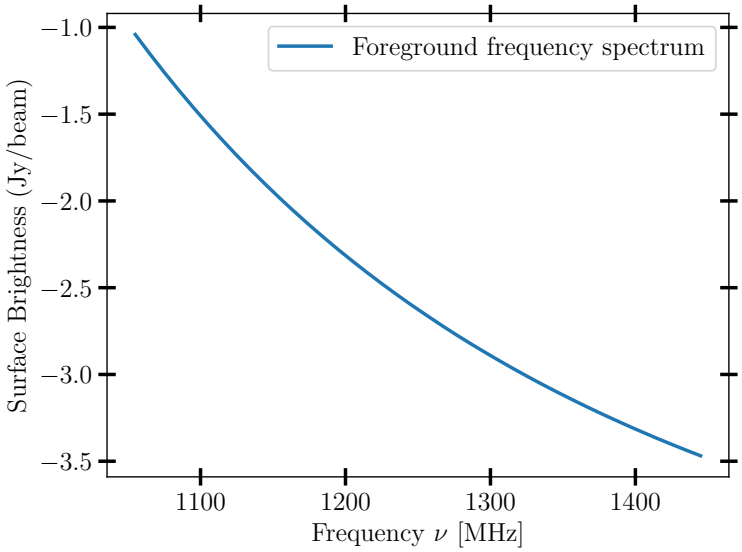

Figure 3.6: FAST telescope smooth foreground (Galactic synchrotron + extragalactic point sources + free-free emission) frequency spectrum, that is, the temperature flux at a given pixel. Foreground spectral smoothness feature greatly favors the process of decontaminating HI signal. High temperatures at lower frequencies are expected due to the Galactic foreground (mostly Galactic synchrotron) signal domination (Smoot and Debono, 2017).

It is clear from the results illustrated in Figure 3.8 that PCA is able to completely separate contaminants and recover HI signal at some relevant scales. The left panel of Figure 3.7 gives us

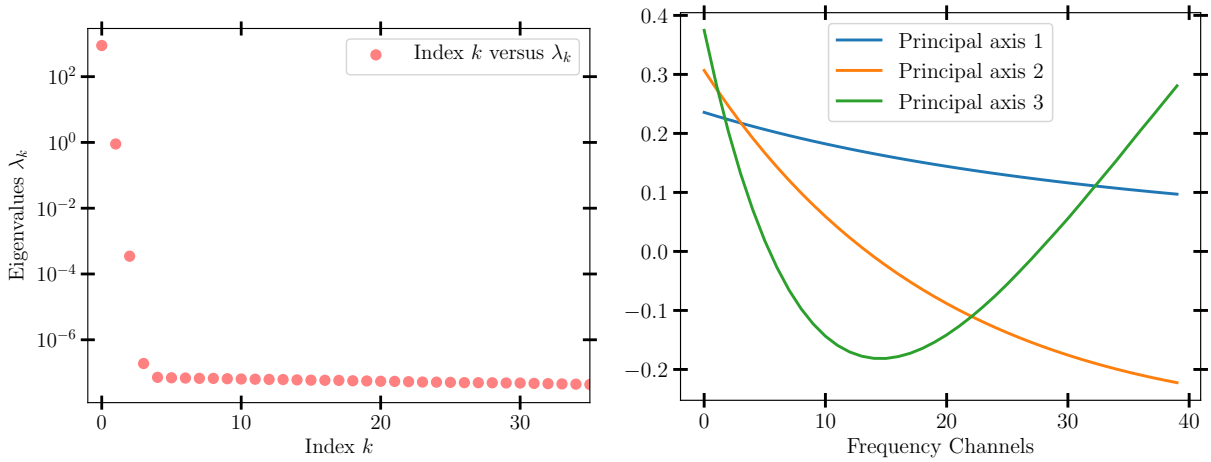

Figure 3.7: *Left:* – The eigenvalues profile corresponding to the $N_\nu \times N_\nu$ matrix of eigenvectors, used for PCA with FAST. *Right:* – The principal axes corresponding to the first three eigenvalues of this matrix. Because the foreground dominates the sky map, it is represented by the largest principal components; in this case, the first four principal components contain more than 99% of the total foreground information.

a clue as to how many eigenmodes we need to remove in order to recover the HI signal. It also tells us how much of the particular sky information is contained in each of the principal components, whereby in our case almost more than 99% of the dominant information is constrained within the first four principal components. PCA is greatly promising, as we can see, we fairly accurately recovered the signal just after removing 4 eigenmodes.

Figure 3.10 shows the linear relation between the input HI signal versus the recovered HI signal, a profile that is to be expected (Bigot-Sazy et al., 2015). This figure provides more information on PCA performance as we consider the mean deviation between the input and the recovered HI temperature maps,

$$\Delta T = \sqrt{\frac{1}{N}\sum_i \left(T_i^{\rm in} - T_i^{\rm out}\right)^2}, \tag{3.5.1}$$

where N is the number of pixels in the map.

We calculate the mean deviation (mean scatter) from the best fit at frequency $1,250\,\mathrm{MHz}$ and find $\Delta T = 0.034\,\mathrm{mK}$. This deviation is slightly higher at lower frequencies, due to the fact that Galactic synchrotron more dominates at lower frequencies than higher frequencies. Such contamination makes the algorithm struggle to clean dirty HI sky maps efficiently, and more contributions arguably come from high angular scales (low-ℓ).

Next, we include the thermal noise, and report our PCA results in Figure 3.9 for the multipole range up to $\ell = 150$. It is possible to reduce the thermal noise by altering some FAST telescope survey parameters, such as reducing the survey area and increasing the total observational time, but we decide not to do so in order to account for the largest possible survey region under a reasonable optimal observational time and other parameters. We, however, choose these survey

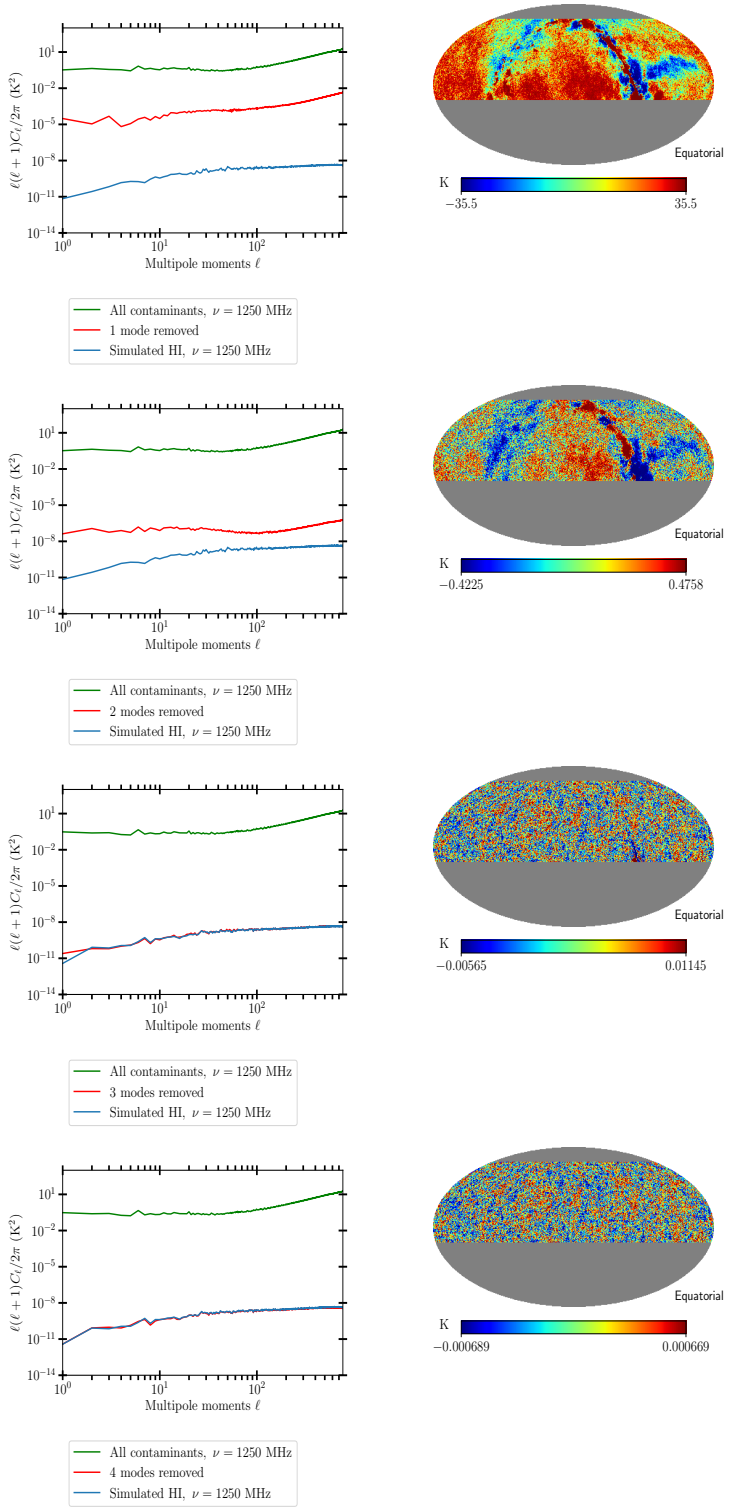

Figure 3.8: Noise-free simulations of contaminated power spectra and the corresponding Healpix maps at frequency 1.25 GHz and for the maximum multipole range $\ell = 768$, to show the evolution of HI signal recovery as we progressively remove the principal eigenmodes using PCA from the input map (Fig. 3.5) (All contaminants – Galactic synchrotron + extragalactic point sources + free-free emission + $1/f$ noise) – green line. The evolving recovery of HI signal (red lines) is indicated, respectively, from top to bottom with 1, 2, 3 and 4 modes removed.

parameters to include the significant impact of the thermal noise and make our PCA reports close to reality.

We see that the progressive increase in the thermal noise amplitude towards small angular scales causes the less accurate reconstruction of the HI power spectrum (see also (Olivari et al., 2016)). Under this consideration, beyond $\ell = 150$, it becomes increasingly difficult for PCA to recover the HI signal. This is because beyond this point thermal noise quickly increases than HI signal. Thermal noise has similar Gaussianity property like HI, thus the algorithm cannot easily identify the thermal noise and strip it out. Although various noises and systematics complicate the foreground removal across all frequencies, with known problems at high and small angular scales, the situation may become much more complicated. Foreground emissions without noises and systematics can be detected and stripped out easily since they significantly depart from Gaussianity compared to the HI signal. Therefore, we notice that instrumental thermal (and also $1/f$ noise) create more confusion to the PCA algorithm, hampering its performance. But on average, PCA is promising and can redeem HI signal from contaminants. We emphasize that it is important for telescopes to be designed in such a way the intrinsic artifacts such as thermal noise, $1/f$ noise and other systematics are optimally mitigated.

3.6 Discussion and Summary

We presented a detailed study of the Principal Component Analysis framework for subtraction of the foregrounds, that predictions have shown to overwhelmingly bury the HI signal. We described and analyzed succinctly some of the logically-connected finer details that have been overlooked in most of the literature, and visualized both mathematical and algorithmic flow of PCA, providing a clear linkage between input and results. We show how the PCA reliably handles, processes and manipulates data, transforming it into various quantitative parametric relationships to optimize its performance and achieve the desired end. The principal component analysis can to a large extent redeem HI signal from the contaminations that overshadow it. We see that, with the removal of 4 (see Figures 3.8 and 3.9) principal components, we can recover the HI signal to a very significant accuracy. Removal of fewer than this number of principal components would be possible to accurately recover the signal if the only contaminant present is Galactic synchrotron. But, as we include free-free emission, extragalactic point sources, noise components, such as thermal noise and spectrally varying $1/f$ noise, and allow synchrotron spatial/frequency variation, total foreground information becomes spread across more principal components. We find that PCA robustness increases with strength in the frequency correlation between foreground components. The results we get are visually promising and have a virtue of unveiling the HI cosmological information that is buried under $\sim 10^4$ times larger in magnitude foreground emissions. There may however be a number of challenges, especially, at large-angular scales (small ℓ's), PCA may be unable to completely recover the HI signal accurately. However, $1/f$ noise, especially, for values of β that significantly decorrelates it in frequency, imposes challenges to PCA by complicating HI signal-background/foreground confusion, causing the

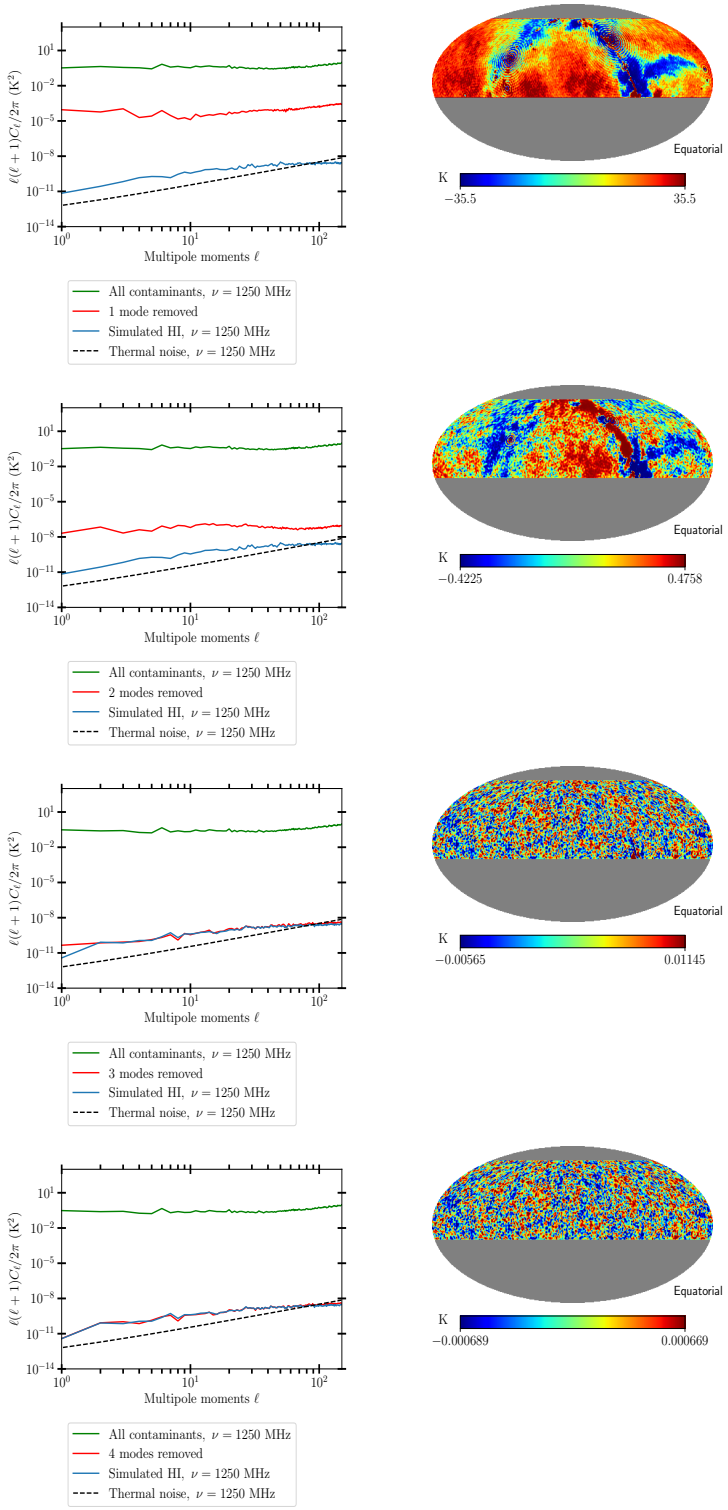

Figure 3.9: Simulations of contaminated power spectra and the corresponding Healpix maps at frequency 1.25 GHz and for the maximum multipole range $\ell = 150$, to show the evolution of HI signal recovery as we progressively remove the principal eigenmodes using PCA from the input map (Fig. 3.5) (All contaminants – Galactic synchrotron + extragalactic point sources + free-free emission + $1/f$ noise) + thermal noise – green line. The evolving recovery of HI signal (red lines) is indicated, respectively, from top to bottom with 1, 2, 3 and 4 modes removed.

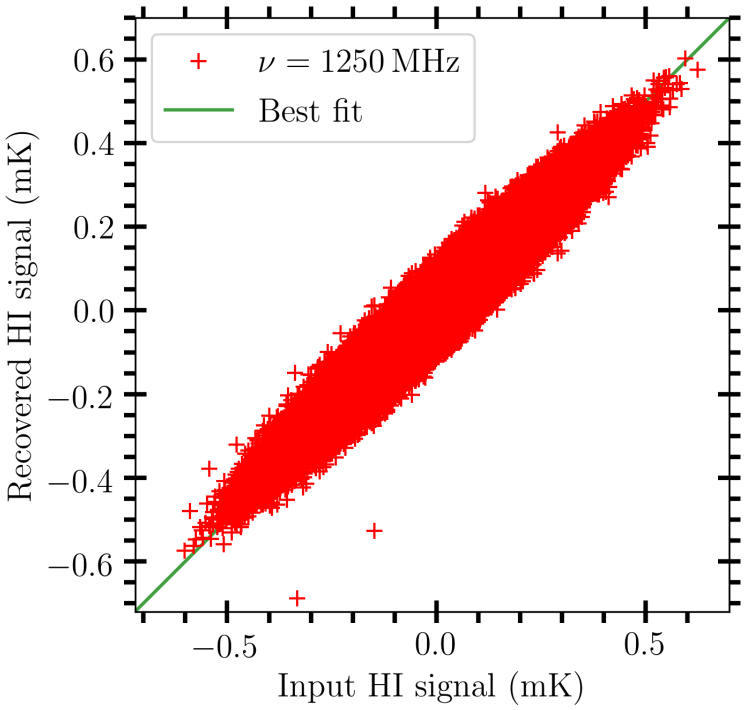

Figure 3.10: Comparison between the input (simulated) HI signal map, versus output (recovered) HI signal map, showing the unbiased results of PCA analysis without the thermal noise inclusion in the foregrounds. The standard dispersion between input and output signals is $\Delta T \equiv \sqrt{\sum_i \left(T_i^{\rm in} - T_i^{\rm out}\right)^2 / N} = 0.034\,\mathrm{mK}$, indicating the robustness of PCA reconstruction.

PCA algorithm to easily wrongly interpret $1/f$ noise which is uncorrelated in frequency as HI signal.

It is important to point out that the level of thermal noise will be critical for successful foreground separation and HI recovery with PCA for FAST and other single-dish IM experiments. We notice that, for a fixed survey area, the thermal noise level is sensitive to the observational time, and hence the integration time per pixel. Thus below some $t_{\rm pix}$ threshold, it may be difficult for PCA to recover HI signal effectively, especially, at small angular scales. To illustrate this argument further, we vary the total observational time, which will automatically result to changes in the integration time per pixel and thus affect the HI signal-to-noise ratio power. We compute the standard deviations, ΔT for the HI sky temperature fluctuations using Equation (3.5.1), where $T_i^{\rm in}$ and $T_i^{\rm out}$ are respectively, the input and output temperature fluctuations at a particular sky pixel. We plot the observational time $t_{\rm obs}$ (years) against these standard deviations as shown in Figure 3.11. The figure clearly illustrates how PCA HI recovery improves with the increase in the observational time. This is correspondingly reflected by the decrease in ΔT.

The eigenmode-based analysis demonstrates that the essential HI eigenmode is just less than 1 percent level comparing to the foreground. Although PCA may be biased in the sense that the same number of principal components is subtracted across the whole range of angular scales (ℓ) by assuming a relatively uniform ratio between the foreground power spectrum and the HI signal

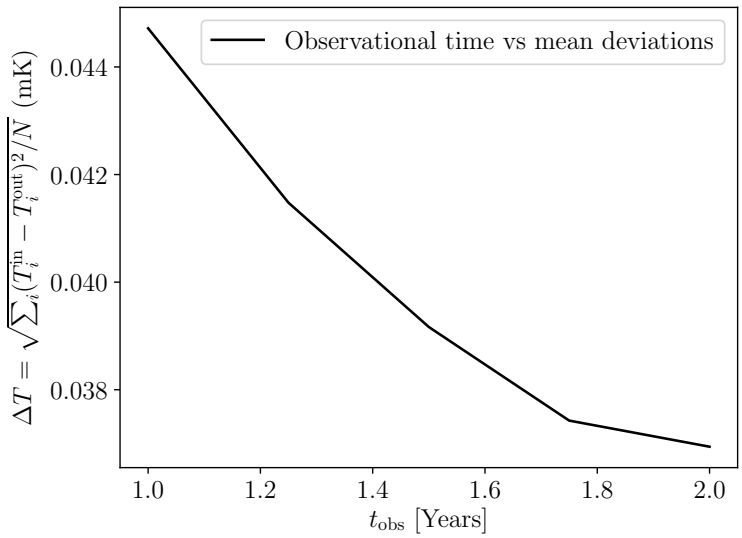

Figure 3.11: Observational time $t_{\rm obs}$ versus the standard dispersion, $\Delta T \equiv \sqrt{\sum_i \left(T_i^{\rm in} - T_i^{\rm out}\right)^2 / N}$, between input and output HI signals. PCA recovery precision improves with the increase in the observational time, while the rest of the experimental and survey parameters are held constant.

power spectrum (Olivari et al., 2016) (and hence PCA may possibly cause a relatively similar effect independent of scales), it has the power and carries the promise to significantly recover the HI signal for FAST and other single-dish intensity mapping experiments.

In spite of the fact that PCA is a blind approach and assumes nothing/little about the underlying physics of the sky components, its results may unveil encoded physical information of the underlying problem. PCA is simplistic but efficient in the sense that it is an approach where the data is maneuvered and projected into axes that cleverly select an optimally parametrized frequency dependence form that is the representation of the original data, making significant information available in the fewest possible parameters and principal components. We have an intuitive grasp that, PCA can be more effective and accurate if there is a mechanism in place to process data and remove the obvious artifacts. Although we have applied PCA to uniquely clean simulated FAST HI IM data, our approach has considered both standard and non-standard procedures and provides a roadmap for a seamless extension to problems beyond astronomy.

Further tests with PCA or other algorithms, will need to take into account many more artifacts, such as uncorrelated offsets, calibration errors, other systematic effects and any components which are non-signal, present in the sky maps. With consideration of such more contaminants, PCA can be hybridized with other algorithms, modified or applied in multi-stage with other methods for more reliable and appealing results. Indeed, there is no hesitation for combining or testing PCA with other algorithms, since the literature has already detailed a number of promising approaches.

4

Conclusion and Outlook

This thesis begins with a review and outline in Chapter 1 of theoretical cosmology in the content from homogeneous and isotropic universe, to its large-scale structure surveys, dark matter halos and the 21-cm cosmology. We have presented a number of mathematical and physical fundamentals underpinning modern cosmology studies. We also briefly reviewed technical design and characterization of radio telescopes, highlighting their most intrinsic property requirements that make them capable of probing very distant, essentially fainter sources. We provided in Chapter 2 derivations of statistical and mathematical frameworks for cosmological parameter constraints forecast, and presented quantitative and qualitative analyses of our simulations and results. This chapter has established a foundation for future studies with real survey data from the upcoming 21-cm experiments. Chapter 3 addressed the challenge of the HI signal domination by the foregrounds; we presented studies of properties of various sky components and developed the modelling strategy, which is chiefly based on the frequency-dependent behaviours of such components across differing sky regions. However, we qualitatively and quantitatively described the capabilities of the PCA-based algorithm, and implemented it; the results we obtained show a promising potential to reconstruct the underlying 21-cm signal from BINGO, FAST and SKA-I telescopes. This presumably solid foundation has unveiled a number of future potential studies for 21-cm cosmology.

Building on top of success we reported in the modeling of the Gaussian distribution of sky maps and telescope beams, we plan to generalize such findings, especially, in testing real cosmological models for detectability of the non-Gaussianity (NoG) (Camera et al., 2013, 2015; Bull et al., 2015b; Li and Ma, 2017) emergence and evolution of the primordial cosmologies, for example, on such observables as the angular power spectrum, and quantify how NoG fluctuations may affect LSS of the Universe modeling, and possibly in inferring the inflationary model of the early universe. Primordial non-Gaussianity is a particular model of structure formation, a possible candidate useful in probing large-scale structure scale-dependent bias (Camera et al., 2013; Bull et al., 2015b); in identifying on large scales, distinctive relic structures; and even probing relativistic effects on such scales (Camera et al., 2013). Non-Gaussianity properties of initial fluctuations, supposedly to have come into effect on extremely large scales might have

effected vast cosmic structures. Such primordial curvature fluctuations have been predicted by the alternative models of single-field slow-roll inflation to have deviations from Gaussian distribution (Li and Ma, 2017). PNG-induced scale-dependent bias effects can be traced using the large-scale galaxy bias and HI distribution. More specifically, PNG via the induced bias exhibits characteristic features on the very large scales of the 21-cm power spectrum, the galaxy power spectrum, the bispectrum, and even high modes (Camera et al., 2015; Li and Ma, 2017). Statistical properties of the PNG could be described sufficiently by the power spectrum in the Fourier space (the two-point correlation function), only if the primordial fluctuations were Gaussian (Li and Ma, 2017). But, the deviation from Gaussian as predicted by inflationary models, requires higher-order statistics beyond the power spectrum, at least a three-point function (bispectrum), in order to extract more useful PNG fluctuations information. This deviation from Gaussianity is described by the parametrization (Camera et al., 2015; Li and Ma, 2017)

$$\Phi = \Psi + f_{\rm NL}\Big(\Psi^2 - \langle\Psi^2\rangle\Big), \tag{4.0.1}$$

where Φ is a gauge-invariant Bardeen's potential, Ψ is a linear Gaussian random field potential, and $f_{\rm NL}$ is a dimensionless parameter describing the PNG magnitude. Studies proposing IM surveys to efficiently constrain the NoG parameter, $f_{\rm NL}$ through HI signal detection have been conducted by Camera et al. (2013); Li and Ma (2017). Similar studies on PNG constraints with galaxy redshift surveys in conjunction with SKAI experiment, and taking fully into account relativistic effects have been made by Camera et al. (2015). In the latter reference, it has been concluded that, HI galaxy redshift survey with the full SKA deployment, and in combination with CMB measurements are able to detect PNG signal and deliver tight constraints on the NoG parameter, $f_{\rm NL}$. Early best constraint estimates on PNG were made using CMB measurements by *Planck* (Planck Collaboration et al., 2014). However, Xu et al. (2015) discussed 21-cm IM with Tianlai Cylinder Array to constrain the PNG via scale-dependent bias in the power spectrum, or by using the bispectrum, and Xu et al. (2016) proposed 21-cm IM to detect imprints of oscillatory features in the primordial power spectrum and bispectrum during inflation. These study frameworks on PNG laid down by others, will serve as a building block and enable us to further such studies on various PNG inflationary models, and more interestingly, test the postulates with real survey data.

Also, we desire to study and apply other algorithms such as Generalized Needlet Internal Linear Combination (GNILC) (Olivari et al., 2016) and Fast Independent Component Analysis (FASTICA) (Wolz et al., 2014, 2015; Cunnington et al., 2019) to separate sky components and recover the HI signal. GNILC is a non-parametric approach that can be used to separate components from sky intensity maps. It deploys both spatial (different directions on the sky) and angular scale information and has shown some promise in recovering HI signal from the observed/simulated HI intensity mapping data. The method can extract from the observed data the emission information of spatially correlated multidimensional components (Olivari et al., 2016). GNILC is an extension of the Internal Linear Combination (ILC) technique (originally applied to CMB data by the *WMAP* team (Bennett et al., 2003)) in wavelet space by Remazeilles

et al. (2011). GNILC involves several steps whose target is to perform a wavelet (needlet) decomposition of the data to estimate locally the signal-to-noise ratio in both pixel and harmonic spaces (with angular scale and location on the sky) (Olivari et al., 2016).

On the other hand, FASTICA is an independent component analysis (ICA) technique; whereas just like PCA, it does not assume any foreground-specific parametric model, but depends on the observed data by identifying components with strong spectral correlation, cluster them and then subtract them from the data to recover the HI signal. ICA is closely analogous to the method known as blind source separation, where the source here means an original signal and blind signifies we have very limited knowledge of the mixing matrix (Wolz et al., 2014, 2015), and thus we can only make a very little assumption on the original signal (data). Mathematically, FASTICA is formulated as a linear combination problem, see more (Wolz et al., 2014, 2015). Our intentions and attempts extend to studying the cosmic, test further cosmological constraint forecasts, and overcome the foreground contamination challenge by considering machine learning (Arjona and Nesseris, 2019) techniques and algorithms. We, therefore aim to test these algorithms and techniques as alternative and complementary approaches in enhancing the expectations and outcomes of our component separation process, from simulations to working with real intensity mapping experiments data.

This means, the recent real observational test data obtained, in particular, 20 hours and 5 nights observational data, respectively, with MeerKLASS and FAST, have created an opportunity to test both our parameter constraints forecast and the foreground subtraction algorithms with real observations. We will also apply our models, to substantially numerous amount of existing or newly upcoming real data, such as data from GBT (Masui et al., 2013) and Parkes (Anderson et al., 2017) radio telescope surveys, and other datasets which we hope will be made available soon from a number of ongoing experiments. Furthermore, our plan extends to deploying the data surveyed by these telescopes to investigate and constrain HI galaxy filaments/profiles in the intergalactic media (Tramonte et al., 2019). Studying in detail, the modeling of $1/f$ noise across frequency band correlations is also of great interest to us. We plan to carry out large-scale structure cross-correlation studies between different 21 cm intensity mapping and galaxy redshift surveys, typically, between SKA-like and SDSS-like experiments, however studying other cosmological probes, including, but not limited to, the Sunyaev-Zeldovich (S-Z) effect.

Bibliography

F. B. Abdalla, P. Bull, S. Camera, et al. Cosmology from HI galaxy surveys with the SKA. In *Advancing Astrophysics with the Square Kilometre Array (AASKA14)*, page 17, April 2015.

S. Alam, F. D. Albareti, C. Allende Prieto, et al. The Eleventh and Twelfth Data Releases of the Sloan Digital Sky Survey: Final Data from SDSS-III. *The Astrophysical Journal Supplement Series*, 219:12, July 2015. doi: 10.1088/0067-0049/219/1/12.

S. Alam, M. Ata, S. Bailey, et al. The clustering of galaxies in the completed SDSS-III Baryon Oscillation Spectroscopic Survey: cosmological analysis of the DR12 galaxy sample. *Monthly Notices of the Royal Astronomical Society*, 470:2617–2652, September 2017. doi: 10.1093/mnras/stx721.

A. Albrecht and G. Bernstein. Evaluating dark energy probes using multidimensional dark energy parameters. *Physical Review D*, 75(10):103003, May 2007. doi: 10.1103/PhysRevD.75.103003.

D. M. Alexander, J. P. Stott, Ryan C. Hickox, et al. The LABOCA survey of the Extended Chandra Deep Field-South: clustering of submillimetre galaxies. *Monthly Notices of the Royal Astronomical Society*, 421(1):284–295, 03 2012. ISSN 0035-8711. doi: 10.1111/j.1365-2966.2011.20303.x. URL https://doi.org/10.1111/j.1365-2966.2011.20303.x.

D. Alonso, P. Bull, P. G. Ferreira, et al. Blind foreground subtraction for intensity mapping experiments. *Monthly Notices of the Royal Astronomical Society*, 447:400–416, February 2015. doi: 10.1093/mnras/stu2474.

H. Andernach and F. Zwicky. English and Spanish Translation of Zwicky's (1933) The Redshift of Extragalactic Nebulae. *arXiv e-prints*, November 2017.

C. J. Anderson, N. J. Luciw, Y.-C. Li, et al. Lack of clustering in low-redshift 21-cm intensity maps cross-correlated with 2dF galaxy densities. *ArXiv e-prints*, October 2017.

L. Anderson, E. Aubourg, S. Bailey, et al. The clustering of galaxies in the SDSS-III Baryon Oscillation Spectroscopic Survey: baryon acoustic oscillations in the Data Release 9 spectroscopic galaxy sample. *Monthly Notices of the Royal Astronomical Society*, 427:3435–3467, December 2012. doi: 10.1111/j.1365-2966.2012.22066.x.

D. Aristizabal Sierra and Chee Sheng Fong. The EDGES signal: An imprint from the mirror world? *Physics Letters B*, 784:130–136, Sep 2018. doi: 10.1016/j.physletb.2018.07.047.

Rubén Arjona and Savvas Nesseris. What can Machine Learning tell us about the background expansion of the Universe? *arXiv e-prints*, art. arXiv:1910.01529, October 2019.

A. J. Banday and A. W. Wolfendale. Fluctuations in the cosmic microwave background. *Monthly Notices of the Royal Astronomical Society*, 245:182–191, July 1990.

A. J. Banday and A. W. Wolfendale. Fluctuations in the galactic synchrotron radiation. I - Implications for searches for fluctuations of cosmological origin. *Monthly Notices of the Royal Astronomical Society*, 248:705–714, February 1991. doi: 10.1093/mnras/248.4.705.

Kevin Bandura, Graeme E. Addison, Mandana Amiri, et al. Canadian Hydrogen Intensity Mapping Experiment (CHIME) pathfinder. In *Proceedings of SPIE*, volume 9145 of *Society of Photo-Optical Instrumentation Engineers (SPIE) Conference Series*, page 914522, Jul 2014. doi: 10.1117/12.2054950.

James M. Bardeen, Paul J. Steinhardt, and Michael S. Turner. Spontaneous creation of almost scale-free density perturbations in an inflationary universe. *Physical Review D*, 28: 679–693, Aug 1983. doi: 10.1103/PhysRevD.28.679. URL https://link.aps.org/doi/10.1103/PhysRevD.28.679.

Rennan Barkana. Possible interaction between baryons and dark-matter particles revealed by the first stars. *Nature*, 555(7694):71–74, Mar 2018. doi: 10.1038/nature25791.

Rennan Barkana and Abraham Loeb. The physics and early history of the intergalactic medium. *Reports on Progress in Physics*, 70(4):627–657, Apr 2007. doi: 10.1088/0034-4885/70/4/R02.

R. A. Battye, M. L. Brown, I. W. A. Browne, et al. BINGO: a single dish approach to 21cm intensity mapping. *ArXiv e-prints*, September 2012.

R. A. Battye, I. W. A. Browne, C. Dickinson, et al. HI intensity mapping: a single dish approach. *Monthly Notices of the Royal Astronomical Society*, 434:1239–1256, September 2013. doi: 10.1093/mnras/stt1082.

Richard Battye, Ian Browne, Tianyue Chen, et al. Update on the BINGO 21cm intensity mapping experiment. *arXiv e-prints*, art. arXiv:1610.06826, Oct 2016.

C. L. Bennett, M. Halpern, G. Hinshaw, et al. First-Year Wilkinson Microwave Anisotropy Probe (WMAP) Observations: Preliminary Maps and Basic Results. *The Astrophysical Journal Supplement Series*, 148:1–27, September 2003. doi: 10.1086/377253.

C. L. Bennett, D. Larson, J. L. Weiland, et al. Nine-year Wilkinson Microwave Anisotropy Probe (WMAP) Observations: Final Maps and Results. *The Astrophysical Journal Supplement Series*, 208(2):20, Oct 2013. doi: 10.1088/0067-0049/208/2/20.

José Luis Bernal, Patrick C. Breysse, and Ely D. Kovetz. The Cosmic Expansion History from Line-Intensity Mapping. *arXiv e-prints*, art. arXiv:1907.10065, Jul 2019.

F. Bernardeau, S. Colombi, E. Gaztañaga, et al. Large-scale structure of the Universe and cosmological perturbation theory. *Physics Reports*, 367:1–248, Sep 2002. doi: 10.1016/S0370-1573(02)00135-7.

J. Bernstein. *KINETIC THEORY IN THE EXPANDING UNIVERSE*. Cambridge Monographs on Mathematical Physics. Cambridge University Press, Cambridge, U.K., 1988. ISBN 9780511564185. doi: 10.1017/CBO9780511564185.

F. Beutler, C. Blake, M. Colless, et al. The 6dF Galaxy Survey: baryon acoustic oscillations and the local Hubble constant. *Monthly Notices of the Royal Astronomical Society*, 416:3017–3032, October 2011. doi: 10.1111/j.1365-2966.2011.19250.x.

M.-A. Bigot-Sazy, C. Dickinson, R. A. Battye, et al. Simulations for single-dish intensity mapping experiments. *Monthly Notices of the Royal Astronomical Society*, 454:3240–3253, December 2015. doi: 10.1093/mnras/stv2153.

M.-A. Bigot-Sazy, Y.-Z. Ma, R. A. Battye, et al. HI Intensity Mapping with FAST. In L. Qain and D. Li, editors, *Frontiers in Radio Astronomy and FAST Early Sciences Symposium 2015*, volume 502 of *Astronomical Society of the Pacific Conference Series*, page 41, February 2016.

C. Blake, S. Brough, W. Couch, et al. The WiggleZ Dark Energy Survey. *Astronomy and Geophysics*, 49(5):5.19–5.24, October 2008. doi: 10.1111/j.1468-4004.2008.49519.x.

C. Blake, E. A. Kazin, F. Beutler, et al. The WiggleZ Dark Energy Survey: mapping the distance-redshift relation with baryon acoustic oscillations. *Monthly Notices of the Royal Astronomical Society*, 418:1707–1724, December 2011. doi: 10.1111/j.1365-2966.2011.19592.x.

A. Bonaldi, L. Bedini, E. Salerno, et al. Estimating the spectral indices of correlated astrophysical foregrounds by a second-order statistical approach. *Monthly Notices of the Royal Astronomical Society*, 373(1):271–279, 10 2006. ISSN 0035-8711. doi: 10.1111/j.1365-2966.2006.11025.x. URL https://doi.org/10.1111/j.1365-2966.2006.11025.x.

W. B. Bonnor. Jeans' formula for gravitational instability. *Monthly Notices of the Royal Astronomical Society*, 117:104, 1957. doi: 10.1093/mnras/117.1.104.

Camille Bonvin and Ruth Durrer. What galaxy surveys really measure. *Physical Review D*, 84(6):063505, Sep 2011. doi: 10.1103/PhysRevD.84.063505.

J. D. Bowman, I. Cairns, D. L. Kaplan, et al. Science with the Murchison Widefield Array. *Publications of the Astronomical Society of Australia*, 30:e031, April 2013. doi: 10.1017/pas.2013.009.

R. Braun, T. Bourke, J. A. Green, et al. Advancing Astrophysics with the Square Kilometre Array. In *Advancing Astrophysics with the Square Kilometre Array (AASKA14)*, page 174, April 2015.

Philippe Brax, Sébastien Clesse, and Anne-Christine Davis. Signatures of modified gravity on the 21 cm power spectrum at reionisation. *Journal of Cosmology and Astro-Particle Physics*, 2013(1):003, Jan 2013. doi: 10.1088/1475-7516/2013/01/003.

N. Bretón, J. L. Cervantes-Cota, and M. Salgad. The Early Universe and Observational Cosmology. In *The Early Universe and Observational Cosmology*, volume 646 of *Lecture Notes in Physics, Berlin Springer Verlag*, 2004. doi: 10.1007/b97189.

P. Bull. Extending Cosmological Tests of General Relativity with the Square Kilometre Array. *The Astrophysical Journal*, 817:26, January 2016. doi: 10.3847/0004-637X/817/1/26.

P. Bull, S. Camera, A. Raccanelli, et al. Measuring baryon acoustic oscillations with future SKA surveys. In *Advancing Astrophysics with the Square Kilometre Array (AASKA14)*, page 24, April 2015a.

P. Bull, P. G. Ferreira, P. Patel, et al. Late-time Cosmology with 21 cm Intensity Mapping Experiments. *The Astrophysical Journal*, 803:21, April 2015b. doi: 10.1088/0004-637X/803/1/21.

J. S. Bullock, T. S. Kolatt, Y. Sigad, et al. Profiles of dark haloes: evolution, scatter and environment. *Monthly Notices of the Royal Astronomical Society*, 321:559–575, March 2001. doi: 10.1046/j.1365-8711.2001.04068.x.

Bernard F. Burke and Francis Graham-Smith. *An Introduction to Radio Astronomy*. Cambridge University Press, Fourth edition (2019), 2009.

H. Camacho, N. Kokron, F. Andrade-Oliveira, et al. Dark Energy Survey Year 1 Results: Measurement of the Galaxy Angular Power Spectrum. *ArXiv e-prints*, July 2018.

S. Camera, M. G. Santos, P. G. Ferreira, et al. Cosmology on Ultralarge Scales with Intensity Mapping of the Neutral Hydrogen 21 cm Emission: Limits on Primordial Non-Gaussianity. *Physical Review Letters*, 111(17):171302, October 2013. doi: 10.1103/PhysRevLett.111.171302.

S. Camera, M. G. Santos, and R. Maartens. Probing primordial non-Gaussianity with SKA galaxy redshift surveys: a fully relativistic analysis. *Monthly Notices of the Royal Astronomical Society*, 448:1035–1043, April 2015. doi: 10.1093/mnras/stv040.

Stefano Camera, José Fonseca, Roy Maartens, et al. Optimized angular power spectra for spectroscopic galaxy surveys. *Monthly Notices of the Royal Astronomical Society*, 481(1):1251–1261, Nov 2018. doi: 10.1093/mnras/sty2284.

Sean M. Carroll. *Spacetime and Geometry: An Introduction to General Relativity*. Pearson, San Francisco, USA, 2003.

Isabella P. Carucci, Francisco Villaescusa-Navarro, and Matteo Viel. The cross-correlation between 21 cm intensity mapping maps and the Lyα forest in the post-reionization era. *Journal of Cosmology and Astroparticle Physics*, 2017(4):001, Apr 2017. doi: 10.1088/1475-7516/2017/04/001.

Anthony Challinor and Antony Lewis. Linear power spectrum of observed source number counts. *Physical Review D*, 84(4):043516, Aug 2011. doi: 10.1103/PhysRevD.84.043516.

Anthony Challinor and Hiranya Peiris. Lecture notes on the physics of cosmic microwave background anisotropies. In Mario Novello and Santiago Perez, editors, *American Institute of Physics Conference Series*, volume 1132 of *American Institute of Physics Conference Series*, pages 86–140, May 2009. doi: 10.1063/1.3151849.

T.-C. Chang, U.-L. Pen, K. Bandura, et al. An intensity map of hydrogen 21-cm emission at redshift $z \approx 0.8$. *Nature*, $466 : 463 - -465, July2010. doi : .$

Tzu-Ching Chang, Ue-Li Pen, Jeffrey B. Peterson, et al. Baryon Acoustic Oscillation Intensity Mapping of Dark Energy. *Physical Review Letters*, 100(9):091303, Mar 2008. 10.1103/PhysRevLett.100.091303.

E. Chapman, F. B. Abdalla, G. Harker, et al. Foreground removal using FASTICA: a showcase of LOFAR-EoR. *Monthly Notices of the Royal Astronomical Society*, 423:2518–2532, July 2012. 10.1111/j.1365-2966.2012.21065.x.

X. Chen. The Tianlai Project: a 21CM Cosmology Experiment. In *International Journal of Modern Physics Conference Series*, volume 12 of *International Journal of Modern Physics Conference Series*, pages 256–263, March 2012. 10.1142/S2010194512006459.

Yun Chen, Suresh Kumar, and Bharat Ratra. Determining the Hubble Constant from Hubble Parameter Measurements. *The Astrophysical Journal*, 835:86, Jan 2017. 10.3847/1538-4357/835/1/86.

Jingquan Cheng. The principles of astronomical telescope design. *Springer*, 360, Jan 2009. 10.1007/b105475.

Michel Chevallier and David Polarski. Accelerating Universes with Scaling Dark Matter. *International Journal of Modern Physics D*, 10(2):213–223, Jan 2001. 10.1142/S0218271801000822.

Frederick R. Chromey. *To Measure the Sky: An Introduction to Observational Astronomy*. Cambridge University Press; First edition (July 2010), Jan. 2010. 10.1017/CBO9780511794810.

Alison L. Coil. *The Large-Scale Structure of the Universe*, volume 6, page 387. Springer Science+Business Media, 2013. 10.1007/978-94-007-5609-0_8.

Alison L. Coil, Marc Davis, Darren S. Madgwick, et al. The DEEP2 Galaxy Redshift Survey: Clustering of Galaxies in Early Data. *The Astrophysical Journal*, 609(2):525–538, Jul 2004. 10.1086/421337.

P. Coles and F. Lucchin. *Cosmology: The Origin and evolution of cosmic structure*. Chichester, UK: Wiley, 1995.

M. Colless, G. Dalton, S. Maddox, et al. The 2dF Galaxy Redshift Survey: spectra and redshifts. *Monthly Notices of the Royal Astronomical Society*, 328:1039–1063, December 2001. 10.1046/j.1365-8711.2001.04902.x.

Asantha Cooray and Ravi Sheth. Halo models of large scale structure. *Physics Reports*, 372: 1–129, Dec 2002. 10.1016/S0370-1573(02)00276-4.

S. Cunnington, I. Harrison, A. Pourtsidou, et al. HI Intensity Mapping for Clustering-Based Redshift Estimation. *Monthly Notices of the Royal Astronomical Society*, October 2018. 10.1093/mnras/sty2928.

Steven Cunnington, Laura Wolz, Alkistis Pourtsidou, et al. Impact of Foregrounds on HI Intensity Mapping Cross-Correlations with Optical Surveys. *Monthly Notices of the Royal Astronomical Society*, page 1847, Jul 2019. 10.1093/mnras/stz1916.

Judd D. Bowman, Alan E. E. Rogers, Raul A. Monsalve, et al. An absorption profile centred at 78 megahertz in the sky-averaged spectrum. *Nature*, 555:67–70, 03 2018. 10.1038/nature25792.

Dark Energy Survey Collaboration, T. Abbott, F. B. Abdalla, et al. The Dark Energy Survey: more than dark energy - an overview. *Monthly Notices of the Royal Astronomical Society*, 460: 1270–1299, August 2016. 10.1093/mnras/stw641.

Kanan K. Datta, T. Roy Choudhury, and Somnath Bharadwaj. The multifrequency angular power spectrum of the epoch of reionization 21-cm signal. *Monthly Notices of the Royal Astronomical Society*, 378(1):119–128, Jun 2007. 10.1111/j.1365-2966.2007.11747.x.

Cameron Davidson-Pilon. *Bayesian Methods for Hackers: Probabilistic Programming and Bayesian Inference*. Addison-Wesley Professional, First edition, 2015. ISBN 0133902838, 9780133902839.

M. Davis, J. A. Newman, S. M. Faber, et al. The DEEP2 Redshift Survey. In S. Cristiani, A. Renzini, and R. E. Williams, editors, *Deep Fields*, page 241, 2001. 10.1007/10854354_66.

A. de Oliveira-Costa, M. Tegmark, B. M. Gaensler, et al. A model of diffuse Galactic radio emission from 10 MHz to 100 GHz. *Monthly Notices of the Royal Astronomical Society*, 388: 247–260, July 2008. 10.1111/j.1365-2966.2008.13376.x.

J. G. de Swart, G. Bertone, and J. van Dongen. How dark matter came to matter. *Nature Astronomy*, 1:0059, Mar 2017. 10.1038/s41550-017-0059.

David R. DeBoer, Aaron R. Parsons, James E. Aguirre, et al. Hydrogen Epoch of Reionization Array (HERA). *Publications of the Astronomical Society of the Pacific*, 129(974):045001, Apr 2017. 10.1088/1538-3873/129/974/045001.

DESI Collaboration, A. Aghamousa, J. Aguilar, et al. The DESI Experiment Part I: Science,Targeting, and Survey Design. *ArXiv e-prints*, October 2016.

Enea Di Dio, Francesco Montanari, Ruth Durrer, et al. Cosmological parameter estimation with large scale structure observations. *Journal of Cosmology and Astroparticle Physics*, 2014 (1):042, Jan 2014. 10.1088/1475-7516/2014/01/042.

Tiziana Di Matteo, Rosalba Perna, Tom Abel, et al. Radio Foregrounds for the 21 Centimeter Tomography of the Neutral Intergalactic Medium at High Redshifts. *The Astrophysical Journal*, 564(2):576–580, Jan 2002. 10.1086/324293.

C. Dickinson. BINGO - A novel method to detect BAOs using a total-power radio telescope. *ArXiv e-prints*, May 2014.

C. Dickinson, R. D. Davies, and R. J. Davis. Towards a free-free template for CMB foregrounds. *Monthly Notices of the Royal Astronomical Society*, 341(2):369–384, May 2003. 10.1046/j.1365-8711.2003.06439.x.

S. Dodelson. *Modern cosmology*. Academic Press, An Imprint of Elsevier, 2003.

Mauro D'Onofrio and C. Burigana. *Questions of Modern Cosmology: Galileo's Legacy*. Springer; 2009 edition, November, 2014. 10.1007/978-3-642-00792-7.

A. G. Doroshkevich, S. F. Shandarin, and E. Saar. Spatial structure of protoclusters and the formation of galaxies. *Monthly Notices of the Royal Astronomical Society*, 184:643–660, September 1978. 10.1093/mnras/184.3.643.

Alan R. Duffy, Joop Schaye, Scott T. Kay, et al. Dark matter halo concentrations in the Wilkinson Microwave Anisotropy Probe year 5 cosmology. *Monthly Notices of the Royal Astronomical Society*, 390(1):L64–L68, Oct 2008. 10.1111/j.1745-3933.2008.00537.x.

William E. East, Matthew Kleban, Andrei Linde, et al. Beginning inflation in an inhomogeneous universe. *Journal of Cosmology and Astro-Particle Physics*, 2016(9):010, Sep 2016. 10.1088/1475-7516/2016/09/010.

G. Efstathiou. Myths and truths concerning estimation of power spectra: the case for a hybrid estimator. *Monthly Notices of the Royal Astronomical Society*, 349:603–626, April 2004. 10.1111/j.1365-2966.2004.07530.x.

G. Efstathiou and S.J. Moody. Maximum likelihood estimates of the two- and three-dimensional power spectra of the APM Galaxy Survey. *Monthly Notices of the Royal Astronomical Society*, 325(4):1603–1615, 08 2001. ISSN 0035-8711. 10.1046/j.1365-8711.2001.04575.x. URL https://doi.org/10.1046/j.1365-8711.2001.04575.x.

J. Einasto, M. Gramann, E. Saar, et al. Power spectrum of the matter distribution in the universe on large scales. *Monthly Notices of the Royal Astronomical Society*, 260:705–716, February 1993. 10.1093/mnras/260.4.705.

D. J. Eisenstein, I. Zehavi, D. W. Hogg, et al. Detection of the Baryon Acoustic Peak in the Large-Scale Correlation Function of SDSS Luminous Red Galaxies. *The Astrophysical Journal*, 633:560–574, November 2005. 10.1086/466512.

A. Ewall-Wice, T. C. Chang, J. Lazio, et al. Modeling the Radio Background from the First Black Holes at Cosmic Dawn: Implications for the 21 cm Absorption Amplitude. *The Astrophysical Journal*, 868(1):63, November 2018. 10.3847/1538-4357/aae51d.

S. M. Faber and J. S. Gallagher. Masses and mass-to-light ratios of galaxies. *Annual Review of Astronomy and Astrophysics*, 17:135–187, 1979. 10.1146/annurev.aa.17.090179.001031.

Benoît Famaey and Stacy S. McGaugh. Modified Newtonian Dynamics (MOND): Observational Phenomenology and Relativistic Extensions. *Living Reviews in Relativity*, 15(1):10, Sep 2012. 10.12942/lrr-2012-10.

Chang Feng and Gilbert Holder. Enhanced Global Signal of Neutral Hydrogen Due to Excess Radiation at Cosmic Dawn. *Astrophysical Journal Letters*, 858(2):L17, May 2018. 10.3847/2041-8213/aac0fe.

Anastasia Fialkov and Rennan Barkana. Signature of excess radio background in the 21-cm global signal and power spectrum. *Monthly Notices of the Royal Astronomical Society*, 486(2): 1763–1773, 03 2019. ISSN 0035-8711. 10.1093/mnras/stz873. URL https://doi.org/10.1093/mnras/stz873.

Anastasia Fialkov, Rennan Barkana, and Aviad Cohen. Constraining baryon–dark-matter scattering with the cosmic dawn 21-cm signal. *Physical Review Letters*, 121:011101, Jul 2018. 10.1103/PhysRevLett.121.011101. URL https://link.aps.org/doi/10.1103/PhysRevLett.121.011101.

G. B. Field. Excitation of the Hydrogen 21-CM Line. *Proceedings of the IRE*, 46:240–250, January 1958. 10.1109/JRPROC.1958.286741.

D. J. Fixsen, E. S. Cheng, J. M. Gales, et al. The Cosmic Microwave Background Spectrum from the Full COBE FIRAS Data Set. *The Astrophysical Journal*, 473:576, December 1996. 10.1086/178173.

José Fonseca, Stefano Camera, Mário G. Santos, et al. Hunting Down Horizon-scale Effects with Multi-wavelength Surveys. *Astrophysical Journal Letters*, 812(2):L22, Oct 2015. 10.1088/2041-8205/812/2/L22.

José Fonseca, Roy Maartens, and Mário G. Santos. Probing the primordial Universe with MeerKAT and DES. *Monthly Notices of the Royal Astronomical Society*, 466(3):2780–2786, Apr 2017. 10.1093/mnras/stw3248.

Sean Fraser, Andi Hektor, Gert Hütsi, et al. The EDGES 21 cm anomaly and properties of dark matter. *Physics Letters B*, 785:159–164, October 2018. 10.1016/j.physletb.2018.08.035.

Wendy L. Freedman, Barry F. Madore, Brad K. Gibson, et al. Final Results from the Hubble Space Telescope Key Project to Measure the Hubble Constant. *The Astrophysical Journal*, 553: 47–72, May 2001. 10.1086/320638.

Wendy L. Freedman, Barry F. Madore, Dylan Hatt, et al. The Carnegie-Chicago Hubble Program. VIII. An Independent Determination of the Hubble Constant Based on the Tip of the Red Giant Branch. *arXiv e-prints*, art. arXiv:1907.05922, Jul 2019.

K. C. Freeman. On the Disks of Spiral and S0 Galaxies. *The Astrophysical Journal*, 160:811, June 1970. 10.1086/150474.

Toshiyuki Fukushige and Junichiro Makino. Structure of Dark Matter Halos from Hierarchical Clustering. *The Astrophysical Journal*, 557:533–545, Aug 2001. 10.1086/321666.

Steven R. Furlanetto. The global 21-centimeter background from high redshifts. *Monthly Notices of the Royal Astronomical Society*, 371(2):867–878, Sep 2006. 10.1111/j.1365-2966.2006.10725.x.

Steven R. Furlanetto and Adam Lidz. The Cross-Correlation of High-Redshift 21 cm and Galaxy Surveys. *The Astrophysical Journal*, 660(2):1030–1038, May 2007. 10.1086/513009.

Steven R. Furlanetto, Matthew McQuinn, and Lars Hernquist. Characteristic scales during reionization. *Monthly Notices of the Royal Astronomical Society*, 365(1):115–126, Jan 2006a. 10.1111/j.1365-2966.2005.09687.x.

Steven R. Furlanetto, S. Peng Oh, and Frank H. Briggs. Cosmology at low frequencies: The 21 cm transition and the high-redshift Universe. *Physics Reports*, 433(4-6):181–301, Oct 2006b. 10.1016/j.physrep.2006.08.002.

A. Georgakakis, B. Mobasher, L. Cram, et al. The Phoenix radio survey: The angular correlation function. *Astronomy and Astrophysics Supplement*, 141:89–101, Jan 2000. 10.1051/aas:2000111.

Riccardo Giovanelli and Martha P. Haynes. Redshift surveys of galaxies. *Annual Review of Astronomy and Astrophysics*, 29:499–541, January 1991. 10.1146/annurev.aa.29.090191.002435.

K. Glazebrook and C. Blake. Measuring the Cosmic Evolution of Dark Energy with Baryonic Oscillations in the Galaxy Power Spectrum. *The Astrophysical Journal*, 631:1–20, September 2005. 10.1086/432497.

L. Gleser, A. Nusser, and A. J. Benson. Decontamination of cosmological 21-cm maps. *Monthly Notices of the Royal Astronomical Society*, 391:383–398, November 2008. 10.1111/j.1365-2966.2008.13897.x.

J. Green, P. Schechter, C. Baltay, et al. Wide-Field InfraRed Survey Telescope (WFIRST) Final Report. *ArXiv e-prints*, August 2012.

Yashwant Gupta, B Ajithkumar, H.S. Kale, et al. The upgraded GMRT: Opening new windows on the radio Universe. *Current Science*, 113:707–714, 01 2017. 10.18520/cs/v113/i04/707-714.

A. H. Guth. Inflationary universe: A possible solution to the horizon and flatness problems. *Physical Review D*, 23:347–356, January 1981. 10.1103/PhysRevD.23.347.

Alan H. Guth and So-Young Pi. Fluctuations in the new inflationary universe. *Physical Review Letters*, 49:1110–1113, Oct 1982. 10.1103/PhysRevLett.49.1110. URL https://link.aps.org/doi/10.1103/PhysRevLett.49.1110.

A. Hall, C. Bonvin, and A. Challinor. Testing general relativity with 21-cm intensity mapping. *Physical Review D*, 87(6):064026, March 2013. 10.1103/PhysRevD.87.064026.

S. E. Harper, C. Dickinson, R. A. Battye, et al. Impact of simulated 1/f noise for HI intensity mapping experiments. *Monthly Notices of the Royal Astronomical Society*, 478:2416–2437, August 2018. 10.1093/mnras/sty1238.

E. R. Harrison. Fluctuations at the threshold of classical cosmology. *Physical Review D*, 1:2726–2730, May 1970. 10.1103/PhysRevD.1.2726. URL https://link.aps.org/doi/10.1103/PhysRevD.1.2726.

C. G. T. Haslam, C. J. Salter, H. Stoffel, et al. A 408 MHz all-sky continuum survey. II - The atlas of contour maps. *Astronomy and Astrophysics Supplement*, 47:1, January 1982.

S. W. Hawking. The Development of Irregularities in a Single Bubble Inflationary Universe. *Advanced Series in Astrophysics and Cosmology*, 8:144–146, June 1993. 10.1142/9789812384935_0010.

M. P. Haynes. HI Cosmology in the Local Universe with ALFALFA. In A. H. Bridle, J. J. Condon, and G. C. Hunt, editors, *Frontiers of Astrophysics: A Celebration of NRAO's 50th Anniversary*, volume 395 of *Astronomical Society of the Pacific Conference Series*, page 125, August 2008.

G. Hinshaw, J. L. Weiland, R. S. Hill, et al. Five-Year Wilkinson Microwave Anisotropy Probe Observations: Data Processing, Sky Maps, and Basic Results. *The Astrophysical Journal Supplement Series*, 180:225–245, February 2009. 10.1088/0067-0049/180/2/225.

M. P. Hobson, A. H. Jaffe, A. R. Liddle, et al. *Bayesian Methods in Cosmology*. Cambridge University Press, Cambridge, UK, February 2014.

Wayne Hu and Martin White. Power Spectra Estimation for Weak Lensing. *The Astrophysical Journal*, 554(1):67–73, Jun 2001. 10.1086/321380.

Wenkai Hu, Xin Wang, Fengquan Wu, et al. Forecast for FAST: from Galaxies Survey to Intensity Mapping. *arXiv e-prints*, art. arXiv:1909.10946, Sep 2019.

E. Hubble. A Relation between Distance and Radial Velocity among Extra-Galactic Nebulae. *Proceedings of the National Academy of Science*, 15:168–173, March 1929. 10.1073/pnas.15.3.168.

Lam Hui, Scott Burles, Uroš Seljak, et al. On estimating the QSO transmission power spectrum. *The Astrophysical Journal*, 552(1):15–35, May 2001. 10.1086/320436. URL https://doi.org/10.1086%2F320436.

D. Huterer and M. S. Turner. Probing dark energy: Methods and strategies. *Physical Review D*, 64(12):123527, December 2001. 10.1103/PhysRevD.64.123527.

Dragan Huterer, Lloyd Knox, and Robert C. Nichol. The Angular Power Spectrum of Edinburgh/Durham Southern Galaxy Catalogue Galaxies. *The Astrophysical Journal*, 555(2): 547–557, Jul 2001. 10.1086/323328.

Z. Ivezic, J. A. Tyson, B. Abel, et al. LSST: from Science Drivers to Reference Design and Anticipated Data Products. *ArXiv e-prints*, May 2008.

A. Jenkins, C. S. Frenk, S. D. M. White, et al. The mass function of dark matter haloes. *Monthly Notices of the Royal Astronomical Society*, 321:372–384, February 2001. 10.1046/j.1365-8711.2001.04029.x.

Donghui Jeong, Fabian Schmidt, and Christopher M. Hirata. Large-scale clustering of galaxies in general relativity. *Physical Review D*, 85(2):023504, Jan 2012. 10.1103/PhysRevD.85.023504.

Y. P. Jing and Yasushi Suto. Triaxial modeling of halo density profiles with high-ResolutionN-body simulations. *The Astrophysical Journal*, 574(2):538–553, aug 2002. 10.1086/341065. URL https://doi.org/10.1086%2F341065.

D. H. Jones, M. A. Read, W. Saunders, et al. The 6dF Galaxy Survey: final redshift release (DR3) and southern large-scale structures. *Monthly Notices of the Royal Astronomical Society*, 399:683–698, October 2009. 10.1111/j.1365-2966.2009.15338.x.

Nobunari Kashikawa, Kazuhiro Shimasaku, Matthew A. Malkan, et al. The End of the Reionization Epoch Probed by Lyα Emitters at z = 6.5 in the Subaru Deep Field. *The Astrophysical Journal*, 648(1):7–22, September 2006. 10.1086/504966.

A. Kashlinsky. Constraints on the power spectrum of the primordial density field from large-scale data - Microwave background and predictions of inflation. *Astrophysical Journal Letters*, 387:L1–L5, March 1992. 10.1086/186292.

E. A. Kazin, J. Koda, C. Blake, et al. The WiggleZ Dark Energy Survey: improved distance measurements to z = 1 with reconstruction of the baryonic acoustic feature. *Monthly Notices of the Royal Astronomical Society*, 441:3524–3542, July 2014. 10.1093/mnras/stu778.

Laura C. Keating, Martin G. Haehnelt, Sebastiano Cantalupo, et al. Probing the end of reionization with the near zones of $z \geq 6$ QSOs. *Monthly Notices of the Royal Astronomical Society*, 454(1):681–697, 09 2015. ISSN 0035-8711. 10.1093/mnras/stv2020. URL https://doi.org/10.1093/mnras/stv2020.

Claus Kiefer and David Polarski. Why do cosmological perturbations look classical to us? *arXiv e-prints*, art. arXiv:0810.0087, Oct 2008.

Anatoly Klypin, Gustavo Yepes, Stefan Gottlöber, et al. MultiDark simulations: the story of dark matter halo concentrations and density profiles. *Monthly Notices of the Royal Astronomical Society*, 457(4):4340–4359, 02 2016. ISSN 0035-8711. 10.1093/mnras/stw248. URL https://doi.org/10.1093/mnras/stw248.

Anatoly A. Klypin, Sebastian Trujillo-Gomez, and Joel Primack. DARK MATTER HALOS IN THE STANDARD COSMOLOGICAL MODEL: RESULTS FROM THE BOLSHOI SIMULATION. *The Astrophysical Journal*, 740(2):102, oct 2011. 10.1088/0004-637x/740/2/102. URL https://doi.org/10.1088%2F0004-637x%2F740%2F2%2F102.

Lloyd Knox. Determination of inflationary observables by cosmic microwave background anisotropy experiments. *Physical Review D*, 52:4307–4318, Oct 1995. 10.1103/PhysRevD.52.4307. URL https://link.aps.org/doi/10.1103/PhysRevD.52.4307.

Lev Kofman, Andrei Linde, and Viatchesiav Mukhanov. Inflationary Theory and Alternative Cosmology. *Journal of High Energy Physics*, 2002(10):057, Oct 2002. 10.1088/1126-6708/2002/10/057.

Edward W. Kolb and Michael S. Turner. The Early Universe. *Front. Phys.*, 69:1–547, 1990.

Leon Koopmans, Rennan Barkana, Mark Bentum, et al. Peering into the Dark (Ages) with Low-Frequency Space Interferometers. *arXiv e-prints*, art. arXiv:1908.04296, August 2019.

Ely Kovetz, Patrick C. Breysse, Adam Lidz, et al. Astrophysics and Cosmology with Line-Intensity Mapping. , 51(3):101, May 2019.

Ely D. Kovetz, Marco P. Viero, Adam Lidz, et al. Line-Intensity Mapping: 2017 Status Report. *arXiv e-prints*, art. arXiv:1709.09066, Sep 2017.

Ofer Lahav and Yasushi Suto. Measuring our universe from galaxy redshift surveys. *Living Review Relativity*, 7:8, 2004. 10.12942/lrr-2004-8.

R. Laureijs, J. Amiaux, S. Arduini, et al. Euclid Definition Study Report. *ArXiv e-prints*, October 2011.

M. Levi, C. Bebek, T. Beers, et al. The DESI Experiment, a whitepaper for Snowmass 2013. *ArXiv e-prints*, August 2013.

Antony Lewis and Anthony Challinor. 21cm angular-power spectrum from the dark ages. *Physical Review D*, 76(8):083005, Oct 2007. 10.1103/PhysRevD.76.083005.

Chunlong Li and Yi-Fu Cai. Searching for the dark force with 21-cm spectrum in light of EDGES. *Physics Letters B*, 788:70–75, Jan 2019. 10.1016/j.physletb.2018.11.011.

D. Li, P. Wang, L. Qian, et al. FAST in Space: Considerations for a Multibeam, Multipurpose Survey Using China's 500-m Aperture Spherical Radio Telescope (FAST). *IEEE Microwave Magazine*, 19:112–119, April 2018. 10.1109/MMM.2018.2802178.

Di Li and Zhichen Pan. The Five-hundred-meter Aperture Spherical Radio Telescope Project. *Radio Science*, 51:1060–1064, Jul 2016. 10.1002/2015RS005877.

Y.-C. Li and Y.-Z. Ma. Constraints on primordial non-Gaussianity from future Hi intensity mapping experiments. *Physical Review D*, 96(6):063525, September 2017. 10.1103/PhysRevD.96.063525.

A. R. Liddle and D. H. Lyth. *Cosmological Inflation and Large-Scale Structure*. Cambridge University Press, Cambridge, UK, June 2000.

D. N. Limber. The Analysis of Counts of the Extragalactic Nebulae in Terms of a Fluctuating Density Field. II. *The Astrophysical Journal*, 119:655, May 1954. 10.1086/145870.

A. D. Linde. A new inflationary universe scenario: A possible solution of the horizon, flatness, homogeneity, isotropy and primordial monopole problems. *Physics Letters B*, 108:389–393, February 1982. 10.1016/0370-2693(82)91219-9.

Andrei Linde. Towards inflation in string theory. In *Journal of Physics Conference Series*, volume 24 of *Journal of Physics Conference Series*, pages 151–160, Jan 2005a. 10.1088/1742-6596/24/1/018.

Andrei Linde. Particle Physics and Inflationary Cosmology. *arXiv e-prints*, art. hep-th/0503203, Mar 2005b.

Eric V. Linder. Exploring the Expansion History of the Universe. *Physical Review Letters*, 90 (9):091301, Mar 2003. 10.1103/PhysRevLett.90.091301.

A. Liu and M. Tegmark. A method for 21 cm power spectrum estimation in the presence of foregrounds. *Physical Review D*, 83(10):103006, May 2011. 10.1103/PhysRevD.83.103006.

Adrian Liu and J. Richard Shaw. Data Analysis for Precision 21 cm Cosmology. *arXiv e-prints*, art. arXiv:1907.08211, Jul 2019.

A. Loeb and J. S. B. Wyithe. Possibility of Precise Measurement of the Cosmological Power Spectrum with a Dedicated Survey of 21cm Emission after Reionization. *Physical Review Letters*, 100(16):161301, April 2008. 10.1103/PhysRevLett.100.161301.

LSST Science Collaboration, P. A. Abell, J. Allison, et al. LSST Science Book, Version 2.0. *ArXiv e-prints*, December 2009.

Chung-Pei Ma and J. N. Fry. Deriving the nonlinear cosmological power spectrum and bispectrum from analytic dark matter halo profiles and mass functions. *The Astrophysical Journal*, 543(2):503–513, nov 2000. 10.1086/317146. URL https://doi.org/10.1086%2F317146.

Yin-Zhe Ma, Ludovic Van Waerbeke, Gary Hinshaw, et al. Probing the diffuse baryon distribution with the lensing-tSZ cross-correlation. *Journal of Cosmology and Astro-Particle Physics*, 2015(9):046, Sep 2015. 10.1088/1475-7516/2015/09/046.

S. J. Maddox, G. Efstathiou, W. J. Sutherland, et al. Galaxy correlations on large scales. *Monthly Notices of the Royal Astronomical Society*, 242:43P–47P, January 1990. 10.1093/mnras/242.1.43P.

Philip D. Mannheim. Alternatives to dark matter and dark energy. *Progress in Particle and Nuclear Physics*, 56(2):340–445, Apr 2006. 10.1016/j.ppnp.2005.08.001.

Xiao-Chun Mao. Measuring Baryon Acoustic Oscillations on 21 cm Intensity Fluctuations at Moderate Redshifts. *The Astrophysical Journal*, 752(2):80, Jun 2012. 10.1088/0004-637X/752/2/80.

K. W. Masui, E. R. Switzer, N. Banavar, et al. Measurement of 21 cm Brightness Fluctuations at z ˜ 0.8 in Cross-correlation. *Astrophysical Journal Letters*, 763:L20, January 2013. 10.1088/2041-8205/763/1/L20.

Kiyoshi Wesley Masui, Patrick McDonald, and Ue-Li Pen. Near-term measurements with 21 cm intensity mapping: Neutral hydrogen fraction and BAO at $z < 2$. *Physical Review D*, 81 (10):103527, May 2010a. 10.1103/PhysRevD.81.103527.

Kiyoshi Wesley Masui, Fabian Schmidt, Ue-Li Pen, et al. Projected constraints on modified gravity cosmologies from 21 cm intensity mapping. *Physical Review D*, 81(6):062001, Mar 2010b. 10.1103/PhysRevD.81.062001.

J. C. Mather, E. S. Cheng, D. A. Cottingham, et al. Measurement of the cosmic microwave background spectrum by the COBE FIRAS instrument. *The Astrophysical Journal*, 420:439–444, January 1994. 10.1086/173574.

Andrei Mesinger, Steven Furlanetto, and Renyue Cen. 21CMFAST: a fast, seminumerical simulation of the high-redshift 21-cm signal. *Monthly Notices of the Royal Astronomical Society*, 411(2):955–972, Feb 2011. 10.1111/j.1365-2966.2010.17731.x.

M. Milgrom. A modification of the Newtonian dynamics as a possible alternative to the hidden mass hypothesis. *The Astrophysical Journal*, 270:365–370, July 1983a. 10.1086/161130.

M. Milgrom. A modification of the Newtonian dynamics - Implications for galaxies. *The Astrophysical Journal*, 270:371–389, July 1983b. 10.1086/161131.

M. Milgrom. A Modification of the Newtonian Dynamics - Implications for Galaxy Systems. *The Astrophysical Journal*, 270:384–389, July 1983c. 10.1086/161132.

H. Mo, F. C. van den Bosch, and S. White. *Galaxy Formation and Evolution*. Cambridge University Press, Cambridge, UK, May 2010.

H. J. Mo and S. D. M. White. An analytic model for the spatial clustering of dark matter haloes. *Monthly Notices of the Royal Astronomical Society*, 282:347–361, Sep 1996. 10.1093/mnras/282.2.347.

Raul A. Monsalve, Alan E. E. Rogers, Judd D. Bowman, et al. Results from EDGES High-band. I. Constraints on Phenomenological Models for the Global 21 cm Signal. *The Astrophysical Journal*, 847(1):64, Sep 2017. 10.3847/1538-4357/aa88d1.

Raul A. Monsalve, Anastasia Fialkov, Judd D. Bowman, et al. Results from EDGES High-Band. III. New Constraints on Parameters of the Early Universe. *The Astrophysical Journal*, 875(1):67, Apr 2019. 10.3847/1538-4357/ab07be.

B. Moore, F. Governato, T. Quinn, et al. Resolving the Structure of Cold Dark Matter Halos. *Astrophysical Journal Letters*, 499:L5–L8, May 1998. 10.1086/311333.

B. Moore, T. Quinn, F. Governato, et al. Cold collapse and the core catastrophe. *Monthly Notices of the Royal Astronomical Society*, 310:1147–1152, Dec 1999. 10.1046/j.1365-8711.1999.03039.x.

Miguel F. Morales and J. Stuart B. Wyithe. Reionization and Cosmology with 21-cm Fluctuations. *Annual Review of Astronomy and Astrophysics*, 48:127–171, Sep 2010. 10.1146/annurev-astro-081309-130936.

Julian B. Muñoz and Abraham Loeb. Insights on Dark Matter from Hydrogen during Cosmic Dawn. *arXiv e-prints*, art. arXiv:1802.10094, Feb 2018.

Julian B. Muñoz, Cora Dvorkin, and Abraham Loeb. 21-cm Fluctuations from Charged Dark Matter. *Physical Review Letters*, 121(12):121301, Sep 2018. 10.1103/PhysRevLett.121.121301.

V. F. Mukhanov, H. A. Feldman, and R. H. Brandenberger. Theory of cosmological perturbations. *Physics Reports*, 215:203–333, June 1992. 10.1016/0370-1573(92)90044-Z.

Julian Munoz and Abraham Loeb. A small amount of mini-charged dark matter could cool the baryons in the early universe. *Nature*, 557, 05 2018. 10.1038/s41586-018-0151-x.

R. Nan, D. Li, C. Jin, et al. The Five-Hundred Aperture Spherical Radio Telescope (fast) Project. *International Journal of Modern Physics D*, 20:989–1024, 2011. 10.1142/S0218271811019335.

J. F. Navarro, C. S. Frenk, and S. D. M. White. The Structure of Cold Dark Matter Halos. *The Astrophysical Journal*, 462:563, May 1996. 10.1086/177173.

J. F. Navarro, C. S. Frenk, and S. D. M. White. A Universal Density Profile from Hierarchical Clustering. *The Astrophysical Journal*, 490:493–508, December 1997. 10.1086/304888.

L. B. Newburgh, K. Bandura, M. A. Bucher, et al. HIRAX: A probe of dark energy and radio transients. In *Ground-based and Airborne Telescopes VI*, volume 9906 of *Proceedings of SPIE*, page 99065X, August 2016. 10.1117/12.2234286.

J. Neyman and E. L. Scott. A Theory of the Spatial Distribution of Galaxies. *The Astrophysical Journal*, 116:144, July 1952. 10.1086/145599.

L. C. Olivari, M. Remazeilles, and C. Dickinson. Extracting HI cosmological signal with generalized needlet internal linear combination. *Monthly Notices of the Royal Astronomical Society*, 456:2749–2765, March 2016. 10.1093/mnras/stv2884.

A. G. Pacholczyk. *Radio astrophysics: Nonthermal processes in galactic and extragalactic sources*. A Series of books in astronomy and astrophysics. W. H. Freeman, 1970.

G. Paciga, T.-C. Chang, Y. Gupta, et al. The GMRT Epoch of Reionization experiment: a new upper limit on the neutral hydrogen power spectrum at $z \approx 8.6$. *Monthly Notices of the Royal Astronomical Society*, 413:1174–1183, May 2011. 10.1111/j.1365-2966.2011.18208.x.

Jaehong Park, Andrei Mesinger, Bradley Greig, et al. Inferring the astrophysics of reionization and cosmic dawn from galaxy luminosity functions and the 21-cm signal. *Monthly Notices of the Royal Astronomical Society*, 484(1):933–949, Mar 2019. 10.1093/mnras/stz032.

A. R. Parsons, D. C. Backer, G. S. Foster, et al. The Precision Array for Probing the Epoch of Re-ionization: Eight Station Results. *The Astronomical Journal*, 139:1468–1480, April 2010. 10.1088/0004-6256/139/4/1468.

J. A. Peacock. *Cosmological Physics*. Cambridge University Press, 1998. 10.1017/CBO9780511804533.

J. A. Peacock and D. Nicholson. The large-scale clustering of radio galaxies. *Monthly Notices of the Royal Astronomical Society*, 253:307–319, November 1991. 10.1093/mnras/253.2.307.

J. A. Peacock and R. E. Smith. Halo occupation numbers and galaxy bias. *Monthly Notices of the Royal Astronomical Society*, 318:1144–1156, November 2000. 10.1046/j.1365-8711.2000.03779.x.

P. J. E. Peebles and J. T. Yu. Primeval Adiabatic Perturbation in an Expanding Universe. *The Astrophysical Journal*, 162:815, December 1970. 10.1086/150713.

Ue-Li Pen, Lister Staveley-Smith, Jeffrey B. Peterson, et al. First detection of cosmic structure in the 21-cm intensity field. *Monthly Notices of the Royal Astronomical Society*, 394(1):L6–L10, Mar 2009. 10.1111/j.1745-3933.2008.00581.x.

B Peng, Chengjin Jin, Qiming Wang, et al. Preparatory study for constructing fast, the world's largest single dish. *Proceedings of the IEEE*, 97:1391 – 1402, 09 2009. 10.1109/JPROC.2009.2013563.

S. Perlmutter, S. Gabi, G. Goldhaber, et al. Measurements of the Cosmological Parameters Ω and Λ from the First Seven Supernovae at z $\geq=$ 0.35. *The Astrophysical Journal*, 483:565–581, July 1997. 10.1086/304265.

S. Perlmutter, G. Aldering, G. Goldhaber, et al. Measurements of Ω and Λ from 42 High-Redshift Supernovae. *The Astrophysical Journal*, 517:565–586, Jun 1999. 10.1086/307221.

Jeffrey B. Peterson, Roy Aleksan, Réza Ansari, et al. 21-cm Intensity Mapping. In *astro2010: The Astronomy and Astrophysics Decadal Survey*, volume 2010, page 234, Jan 2009.

Planck Collaboration, P. A. R. Ade, N. Aghanim, et al. Planck 2013 results. XVI. Cosmological parameters. *Astronomy and Astrophysics*, 571:A16, November 2014. 10.1051/0004-6361/201321591.

Planck Collaboration, P. A. R. Ade, N. Aghanim, et al. Planck 2015 results. XIII. Cosmological parameters. *Astronomy and Astrophysics*, 594:A13, September 2016. 10.1051/0004-6361/201525830.

Planck Collaboration, N. Aghanim, Y. Akrami, et al. Planck 2018 results. VI. Cosmological parameters. *ArXiv e-prints*, July 2018.

Moritz Platscher, Juri Smirnov, Sven Meyer, et al. Long range effects in gravity theories with Vainshtein screening. *Journal of Cosmology and Astro-Particle Physics*, 2018(12):009, Dec 2018. 10.1088/1475-7516/2018/12/009.

Jonathan C. Pober, Aaron R. Parsons, James E. Aguirre, et al. Opening the 21 cm Epoch of Reionization Window: Measurements of Foreground Isolation with PAPER. *The Astrophysical Journal*, 768(2):L36, May 2013a. 10.1088/2041-8205/768/2/L36.

Jonathan C. Pober, Aaron R. Parsons, David R. DeBoer, et al. The Baryon Acoustic Oscillation Broadband and Broad-beam Array: Design Overview and Sensitivity Forecasts. *The Astronomical Journal*, 145(3):65, Mar 2013b. 10.1088/0004-6256/145/3/65.

Jonathan C. Pober, Adrian Liu, Joshua S. Dillon, et al. What Next-generation 21 cm Power Spectrum Measurements can Teach us About the Epoch of Reionization. *The Astrophysical Journal*, 782(2):66, Feb 2014. 10.1088/0004-637X/782/2/66.

Marc Postman, Tod R. Lauer, István Szapudi, et al. Clustering at High Redshift: Precise Constraints from a Deep, Wide-Area Survey. *The Astrophysical Journal*, 506(1):33–44, Oct 1998. 10.1086/306245.

A. Pourtsidou, D. Bacon, and R. Crittenden. Cross-correlation cosmography with HI intensity mapping. *ArXiv e-prints*, June 2015.

A. Pourtsidou, D. Bacon, and R. Crittenden. H I and cosmological constraints from intensity mapping, optical and CMB surveys. *Monthly Notices of the Royal Astronomical Society*, 470: 4251–4260, October 2017. 10.1093/mnras/stx1479.

Alkistis Pourtsidou. HI Intensity Mapping with MeerKAT. *arXiv e-prints*, art. arXiv:1709.07316, Sep 2017.

J. R. Pritchard and A. Loeb. 21 cm cosmology in the 21st century. *Reports on Progress in Physics*, 75(8):086901, August 2012. 10.1088/0034-4885/75/8/086901.

J. Xavier Prochaska and Arthur M. Wolfe. On the (Non)Evolution of H I Gas in Galaxies Over Cosmic Time. *The Astrophysical Journal*, 696(2):1543–1547, May 2009. 10.1088/0004-637X/696/2/1543.

C. Quigg. *Gauge Theories of the Strong, Weak, and Electromagnetic Interactions*. EBSCO ebook academic collection. Princeton University Press, 2013. ISBN 9780691135489. URL https://books.google.co.za/books?id=kXiWmwEACAAJ.

Mathieu Remazeilles, Jacques Delabrouille, and Jean-François Cardoso. Foreground component separation with generalized Internal Linear Combination. *Monthly Notices of the Royal Astronomical Society*, 418(1):467–476, Nov 2011. 10.1111/j.1365-2966.2011.19497.x.

Adam G. Riess, Alexei V. Filippenko, Peter Challis, et al. Observational Evidence from Supernovae for an Accelerating Universe and a Cosmological Constant. *The Astronomical Journal*, 116(3):1009–1038, Sep 1998. 10.1086/300499.

Adam G. Riess, Stefano Casertano, Wenlong Yuan, et al. Large Magellanic Cloud Cepheid Standards Provide a 1% Foundation for the Determination of the Hubble Constant and Stronger Evidence for Physics beyond ΛCDM. *The Astrophysical Journal*, 876(1):85, May 2019. 10.3847/1538-4357/ab1422.

N. P. Ross, A. D. Myers, E. S. Sheldon, et al. The SDSS-III Baryon Oscillation Spectroscopic Survey: Quasar Target Selection for Data Release Nine. *The Astrophysical Journal Supplement Series*, 199:3, March 2012. 10.1088/0067-0049/199/1/3.

V. C. Rubin and W. K. Ford, Jr. Rotation of the Andromeda Nebula from a Spectroscopic Survey of Emission Regions. *The Astrophysical Journal*, 159:379, February 1970. 10.1086/150317.

George B. Rybicki and Alan P. Lightman. *Radiative Processes in Astrophysics*. Wiley-VCH; Revised edition, March, 1985.

M. Santos, P. Bull, D. Alonso, et al. Cosmology from a SKA HI intensity mapping survey. In *Advancing Astrophysics with the Square Kilometre Array (AASKA14)*, page 19, April 2015.

M. G. Santos, A. Cooray, and L. Knox. Multifrequency Analysis of 21 Centimeter Fluctuations from the Era of Reionization. *The Astrophysical Journal*, 625:575–587, June 2005. 10.1086/429857.

M. G. Santos, M. Cluver, M. Hilton, et al. MeerKLASS: MeerKAT Large Area Synoptic Survey. *ArXiv e-prints*, September 2017.

P. Schneider. *Extragalactic Astronomy and Cosmology: An Introduction*. Springer, 2006. ISBN 9783540331742. URL https://books.google.co.za/books?id=uP1Hz-6sHaMC.

P. Schneider, J. Ehlers, and E. E. Falco. *Gravitational Lenses*. Springer-Verlag, Berlin, Heidelberg, New York, 1992. 10.1007/978-3-662-03758-4.

R. Scoccimarro. Transients from initial conditions: a perturbative analysis. *Monthly Notices of the Royal Astronomical Society*, 299:1097–1118, October 1998. 10.1046/j.1365-8711.1998.01845.x.

M. Seiffert, A. Mennella, C. Burigana, et al. 1/f noise and other systematic effects in the Planck-LFI radiometers. *Astronomy and Astrophysics*, 391:1185–1197, September 2002. 10.1051/0004-6361:20020880.

U. Seljak. Analytic model for galaxy and dark matter clustering. *Monthly Notices of the Royal Astronomical Society*, 318:203–213, October 2000. 10.1046/j.1365-8711.2000.03715.x.

H.-J. Seo and D. J. Eisenstein. Probing Dark Energy with Baryonic Acoustic Oscillations from Future Large Galaxy Redshift Surveys. *The Astrophysical Journal*, 598:720–740, December 2003. 10.1086/379122.

Hee-Jong Seo, Scott Dodelson, John Marriner, et al. A Ground-based 21 cm Baryon Acoustic Oscillation Survey. *The Astrophysical Journal*, 721(1):164–173, Sep 2010. 10.1088/0004-637X/721/1/164.

J. R. Shaw and A. Lewis. Nonlinear redshift-space power spectra. *Physical Review D*, 78(10): 103512, November 2008. 10.1103/PhysRevD.78.103512.

J. R. Shaw, K. Sigurdson, U.-L. Pen, et al. All-sky Interferometry with Spherical Harmonic Transit Telescopes. *The Astrophysical Journal*, 781:57, February 2014. 10.1088/0004-637X/781/2/57.

J. Richard Shaw, Kris Sigurdson, Michael Sitwell, et al. Coaxing cosmic 21 cm fluctuations from the polarized sky using m-mode analysis. *Physical Review D*, 91(8):083514, Apr 2015. 10.1103/PhysRevD.91.083514.

R. K. Sheth, H. J. Mo, and G. Tormen. Ellipsoidal collapse and an improved model for the number and spatial distribution of dark matter haloes. *Monthly Notices of the Royal Astronomical Society*, 323:1–12, May 2001. 10.1046/j.1365-8711.2001.04006.x.

G. F. Smoot, C. L. Bennett, A. Kogut, et al. Structure in the COBE differential microwave radiometer first-year maps. *Astrophysical Journal Letters*, 396:L1–L5, September 1992. 10.1086/186504.

George F. Smoot and Ivan Debono. 21 cm intensity mapping with the Five hundred metre Aperture Spherical Telescope. *Astronomy and Astrophysics*, 597:A136, Jan 2017. 10.1051/0004-6361/201526794.

D. N. Spergel, R. Bean, O. Doré, et al. Three-Year Wilkinson Microwave Anisotropy Probe (WMAP) Observations: Implications for Cosmology. *The Astrophysical Journal Supplement Series*, 170(2):377–408, Jun 2007. 10.1086/513700.

Volker Springel, Carlos S. Frenk, and Simon D. M. White. The large-scale structure of the Universe. *Nature*, 440(7088):1137–1144, April 2006. 10.1038/nature04805.

Square Kilometre Array Cosmology Science Working Group, D. J. Bacon, R. A. Battye, et al. Cosmology with Phase 1 of the Square Kilometre Array; Red Book 2018: Technical specifications and performance forecasts. *ArXiv e-prints*, November 2018.

A. A. Starobinsky. Dynamics of phase transition in the new inflationary universe scenario and generation of perturbations. *Physics Letters B*, 117:175–178, November 1982. 10.1016/0370-2693(82)90541-X.

G. Swarup. Giant metrewave radio telescope (GMRT) - Scientific objectives and design aspects. *Indian Journal of Radio and Space Physics*, 19:493–505, December 1990.

E. R. Switzer, K. W. Masui, K. Bandura, et al. Determination of $z \sim 0.8$ neutral hydrogen fluctuations using the 21cm intensity mapping autocorrelation. *Monthly Notices of the Royal Astronomical Society*, 434:L46–L50, Jul 2013. 10.1093/mnrasl/slt074.

E. R. Switzer, T. C. Chang, K. W. Masui, et al. Interpreting the Unresolved Intensity of Cosmologically Redshifted Line Radiation. *The Astrophysical Journal*, 815(1):51, Dec 2015. 10.1088/0004-637X/815/1/51.

Vittorio Tansella, Camille Bonvin, Ruth Durrer, et al. The full-sky relativistic correlation function and power spectrum of galaxy number counts. Part I: theoretical aspects. *Journal of Cosmology and Astroparticle Physics*, 2018(3):019, Mar 2018. 10.1088/1475-7516/2018/03/019.

Max Tegmark. Removing Real-World Foregrounds from Cosmic Microwave Background Maps. *The Astrophysical Journal*, 502(1):1–6, Jul 1998. 10.1086/305905.

Max Tegmark, Andy N. Taylor, and Alan F. Heavens. Karhunen-Loève Eigenvalue Problems in Cosmology: How Should We Tackle Large Data Sets? *The Astrophysical Journal*, 480(1):22–35, May 1997. 10.1086/303939.

Max Tegmark, Andrew J. S. Hamilton, Michael A. Strauss, et al. Measuring the Galaxy Power Spectrum with Future Redshift Surveys. *The Astrophysical Journal*, 499(2):555–576, May 1998. 10.1086/305663.

Max Tegmark, Daniel J. Eisenstein, Wayne Hu, et al. Foregrounds and Forecasts for the Cosmic Microwave Background. *The Astrophysical Journal*, 530(1):133–165, Feb 2000. 10.1086/308348.

The LSST Dark Energy Science Collaboration, R. Mandelbaum, T. Eifler, et al. The LSST Dark Energy Science Collaboration (DESC) Science Requirements Document. *ArXiv e-prints*, September 2018.

S. J. Tingay, R. Goeke, J. D. Bowman, et al. The Murchison Widefield Array: The Square Kilometre Array Precursor at Low Radio Frequencies. *Publications of the Astronomical Society of Australia*, 30:e007, January 2013. 10.1017/pasa.2012.007.

Jeremy Tinker, Andrey V. Kravtsov, Anatoly Klypin, et al. Toward a Halo Mass Function for Precision Cosmology: The Limits of Universality. *The Astrophysical Journal*, 688(2):709–728,

Dec 2008. 10.1086/591439.

Jeremy L. Tinker, Brant E. Robertson, Andrey V. Kravtsov, et al. The Large-scale Bias of Dark Matter Halos: Numerical Calibration and Model Tests. *The Astrophysical Journal*, 724 (2):878–886, Dec 2010. 10.1088/0004-637X/724/2/878.

Denis Tramonte, Yin-Zhe Ma, Yi-Chao Li, et al. Searching for H I imprints in cosmic web filaments with 21-cm intensity mapping. *Monthly Notices of the Royal Astronomical Society*, 489(1):385–400, Oct 2019. 10.1093/mnras/stz2146.

V. Trimble. Existence and nature of dark matter in the universe. *Annual Review of Astronomy and Astrophysics*, 25:425–472, 1987. 10.1146/annurev.aa.25.090187.002233.

Roberto Trotta. Bayesian Methods in Cosmology. *arXiv e-prints*, art. arXiv:1701.01467, Jan 2017.

M. A. Troxel, N. MacCrann, J. Zuntz, et al. Dark Energy Survey Year 1 Results: Cosmological Constraints from Cosmic Shear. *ArXiv e-prints*, August 2017.

S. Tsujikawa. Introductory review of cosmic inflation. *arXiv High Energy Physics - Phenomenology e-prints*, April 2003.

M. P. van Haarlem, M. W. Wise, A. W. Gunst, et al. LOFAR: The LOw-Frequency ARray. *Astronomy and Astrophysics*, 556:A2, August 2013. 10.1051/0004-6361/201220873.

Francisco Villaescusa-Navarro, David Alonso, and Matteo Viel. Baryonic acoustic oscillations from 21 cm intensity mapping: the Square Kilometre Array case. *Monthly Notices of the Royal Astronomical Society*, 466(3):2736–2751, Apr 2017. 10.1093/mnras/stw3224.

Eli Visbal, Abraham Loeb, and Stuart Wyithe. Cosmological constraints from 21cm surveys after reionization. *Journal of Cosmology and Astro-Particle Physics*, 2009(10):030, Oct 2009. 10.1088/1475-7516/2009/10/030.

X. Wang, M. Tegmark, M. G. Santos, et al. 21 cm Tomography with Foregrounds. *The Astrophysical Journal*, 650:529–537, October 2006. 10.1086/506597.

Risa H. Wechsler and Jeremy L. Tinker. The Connection Between Galaxies and Their Dark Matter Halos. *Annual Review of Astronomy and Astrophysics*, 56:435–487, Sep 2018. 10.1146/annurev-astro-081817-051756.

Risa H. Wechsler, James S. Bullock, Joel R. Primack, et al. Concentrations of Dark Halos from Their Assembly Histories. *The Astrophysical Journal*, 568:52–70, Mar 2002. 10.1086/338765.

S. Weinberg. *Gravitation and Cosmology: Principles and Applications of the General Theory of Relativity*. John Wiley Sons, Inc.; First edition, July 1972.

M. White, D. Scott, and J. Silk. Anisotropies in the Cosmic Microwave Background. *Annual Review of Astronomy and Astrophysics*, 32:319–370, 1994. 10.1146/annurev.astro.32.1.319.

Martin White, Lars Hernquist, and Volker Springel. The Halo Model and Numerical Simulations. *The Astrophysical Journal*, 550:L129–L132, Apr 2001. 10.1086/319644.

S. D. M. White and M. J. Rees. Core condensation in heavy halos - A two-stage theory for galaxy formation and clustering. *Monthly Notices of the Royal Astronomical Society*, 183:341–358, May 1978. 10.1093/mnras/183.3.341.

Lawrence M. Widrow, Pascal J. Elahi, Robert J. Thacker, et al. Power spectrum for the small-scale Universe. *Monthly Notices of the Royal Astronomical Society*, 397(3):1275–1285, August 2009. 10.1111/j.1365-2966.2009.15075.x.

J. P. Wild. The Radio-Frequency Line Spectrum of Atomic Hydrogen and its Applications in Astronomy. *The Astrophysical Journal*, 115:206, March 1952. 10.1086/145533.

M. L. Wilson and J. Silk. On the anisotropy of the cosmological background matter and radiation distribution. I - The radiation anisotropy in a spatially flat universe. *The Astrophysical Journal*, 243:14–25, January 1981. 10.1086/158561.

R. W. Wilson and A. A. Penzias. Measurement of the Flux of Five Sources at 4080 Mc/sec. *The Astronomical Journal*, 70:697, November 1965. 10.1086/109803.

T. L. Wilson, K. Rohlfs, and S. Hüttemeister. *Tools of Radio Astronomy*. Springer-Verlag, Berlin, Germany, 2009. 10.1007/978-3-540-85122-6.

L. Wolz, F. B. Abdalla, C. Blake, et al. The effect of foreground subtraction on cosmological measurements from intensity mapping. *Monthly Notices of the Royal Astronomical Society*, 441 (4):3271–3283, Jul 2014. 10.1093/mnras/stu792.

L. Wolz, C. Blake, F. B. Abdalla, et al. Erasing the Milky Way: new cleaning technique applied to GBT intensity mapping data. *arXiv e-prints*, art. arXiv:1510.05453, Oct 2015.

L. Wolz, C. Tonini, C. Blake, et al. Intensity mapping cross-correlations: connecting the largest scales to galaxy evolution. *Monthly Notices of the Royal Astronomical Society*, 458(3): 3399–3410, May 2016. 10.1093/mnras/stw535.

J. Stuart B. Wyithe and Abraham Loeb. Fluctuations in 21-cm emission after reionization. *Monthly Notices of the Royal Astronomical Society*, 383(2):606–614, Jan 2008. 10.1111/j.1365-2966.2007.12568.x.

J. Stuart B. Wyithe and Abraham Loeb. The 21-cm power spectrum after reionization. *Monthly Notices of the Royal Astronomical Society*, 397(4):1926–1934, Aug 2009. 10.1111/j.1365-2966.2009.15019.x.

X. Xu, Y.-Z. Ma, and A. Weltman. Constraining the interaction between dark sectors with future HI intensity mapping observations. *Physical Review D*, 97(8):083504, April 2018. 10.1103/PhysRevD.97.083504.

Yidong Xu, Xin Wang, and Xuelei Chen. Forecasts on the Dark Energy and Primordial Non-Gaussianity Observations with the Tianlai Cylinder Array. *The Astrophysical Journal*, 798(1):

40, January 2015. 10.1088/0004-637X/798/1/40.

Yidong Xu, Jan Hamann, and Xuelei Chen. Precise measurements of inflationary features with 21 cm observations. *Physical Review D*, 94(12):123518, December 2016. 10.1103/PhysRevD.94.123518.

S. Yatawatta, A. G. de Bruyn, M. A. Brentjens, et al. Initial deep LOFAR observations of epoch of reionization windows. I. The north celestial pole. *Astronomy and Astrophysics*, 550: A136, February 2013. 10.1051/0004-6361/201220874.

Elimboto Yohana, Yi-Chao Li, and Yin-Zhe Ma. Forecasts of cosmological constraints from HI intensity mapping with FAST, BINGO & SKA-I. *arXiv e-prints*, art. arXiv:1908.03024, Aug 2019.

Jaiyul Yoo, A. Liam Fitzpatrick, and Matias Zaldarriaga. New perspective on galaxy clustering as a cosmological probe: General relativistic effects. *Physical Review D*, 80(8):083514, Oct 2009. 10.1103/PhysRevD.80.083514.

D. G. York, J. Adelman, J. E. Anderson, Jr., et al. The Sloan Digital Sky Survey: Technical Summary. *The Astronomical Journal*, 120:1579–1587, September 2000. 10.1086/301513.

Idit Zehavi, Zheng Zheng, David H. Weinberg, et al. The Luminosity and Color Dependence of the Galaxy Correlation Function. *The Astrophysical Journal*, 630(1):1–27, Sep 2005. 10.1086/431891.

Idit Zehavi, Zheng Zheng, David H. Weinberg, et al. Galaxy Clustering in the Completed SDSS Redshift Survey: The Dependence on Color and Luminosity. *The Astrophysical Journal*, 736: 59, Jul 2011. 10.1088/0004-637X/736/1/59.

Y. B. Zeldovich. A hypothesis, unifying the structure and the entropy of the Universe. *Monthly Notices of the Royal Astronomical Society*, 160:1P, 1972. 10.1093/mnras/160.1.1P.

L. Zhang, E. F. Bunn, A. Karakci, et al. Bayesian Semi-blind Component Separation for Foreground Removal in Interferometric 21 cm Observations. *The Astrophysical Journal Supplement Series*, 222:3, January 2016. 10.3847/0067-0049/222/1/3.

D. H. Zhao, H. J. Mo, Y. P. Jing, et al. The growth and structure of dark matter haloes. *Monthly Notices of the Royal Astronomical Society*, 339:12–24, February 2003. 10.1046/j.1365-8711.2003.06135.x.

D. H. Zhao, Y. P. Jing, H. J. Mo, et al. Accurate Universal Models for the Mass Accretion Histories and Concentrations of Dark Matter Halos. *The Astrophysical Journal*, 707:354–369, Dec 2009. 10.1088/0004-637X/707/1/354.

M. A. Zwaan, M. J. Meyer, R. L. Webster, et al. The HIPASS catalogue - II. Completeness, reliability and parameter accuracy. *Monthly Notices of the Royal Astronomical Society*, 350: 1210–1219, June 2004. 10.1111/j.1365-2966.2004.07782.x.

M. A. Zwaan, M. J. Meyer, L. Staveley-Smith, et al. The HIPASS catalogue: Ω_{HI} and environmental effects on the HI mass function of galaxies. *Monthly Notices of the Royal Astronomical Society*, 359(1):L30–L34, May 2005. 10.1111/j.1745-3933.2005.00029.x.

F. Zwicky. Die Rotverschiebung von extragalaktischen Nebeln. *Helvetica Physica Acta*, 6: 110–127, 1933.

F. Zwicky. On the Masses of Nebulae and of Clusters of Nebulae. *The Astrophysical Journal*, 86:217, October 1937. 10.1086/143864.